Designing $Mg_3(Sb,Bi)_2$ and MgAgSb for Low- and Mid-Temperature Thermoelectric Applications

by

Melis Özen

A Dissertation Submitted to the
Graduate School of Sciences and Engineering
in Partial Fulfillment of the Requirements for
the Degree of

Doctor of Philosophy

in

Materials Science and Engineering

KOÇ ÜNİVERSİTESİ

September 27, 2024

Designing $Mg_3(Sb,Bi)_2$ and MgAgSb for Low- and Mid-Temperature Thermoelectric Applications

Koç University

Graduate School of Sciences and Engineering

This is to certify that I have examined this copy of a doctoral dissertation by

Melis Özen

and have found that it is complete and satisfactory in all respects,
and that any and all revisions required by the final
examining committee have been made.

Committee Members:

Assoc. Prof. Umut Aydemir (Advisor)

Assoc. Prof. Uğur Ünal

Asst. Prof. Enes Kılınç

Assoc. Prof. Safacan Kölemen

Prof. Dr. Yaşar İslamoğlu

Date: Sep 27, 2024

To my lovely family…

ABSTRACT

Designing $Mg_3(Sb,Bi)_2$ and MgAgSb for Low- and Mid-Temperature Thermoelectric Applications

Melis Özen

Doctor of Philosophy in Materials Science and Engineering

Sep 27, 2024

Over the past few decades, concerns about environmental pollution, global warming, and greenhouse gas emissions have intensified. Therefore, many countries have committed to achieving net-zero emissions, implementing climate policies, and integrating green energy systems by 2050. Given that about 60% of energy produced is lost as waste heat from industries, transportation etc., harnessing this waste heat for alternative energy could be a highly effective way to improve overall energy efficiency and reduce greenhouse gas emissions. Thermoelectric materials offer a potential solution due to their ability to convert heat into electricity. However, while high-quality waste heat (above 573 K) is easier to recover, low-grade waste heat, which constitutes about 90% of the available source, poses a challenge due to its lower energy density. Besides the ability of energy production, thermoelectric materials also offer an environmentally friendly, noise and vibration free solution for solid-state coolers with no-moving parts and hazardous gas emissions. To achieve high output from both electric energy production and cooling purposes through thermoelectric materials, the conversion efficiency should be enhanced which is related to the dimensionless thermoelectric figure of merit $zT = S^2\sigma T/(\kappa_l+\kappa_e)$, where S, σ, κ_l, κ_e and T are the Seebeck coefficient, electrical conductivity, lattice thermal conductivity, electronic thermal conductivity and temperature, respectively. Because of the interdependence of these transport properties, achieving optimum values of zT is challenging. Currently, the thermoelectric market especially for low temperature applications is dominated by Bi_2Te_3-based materials, but concerns about the diminishing availability and toxicity of the element tellurium are driving the search for alternative materials. There is growing interest in Mg_3Sb_2 and Mg_3Bi_2-based compounds as *n*-type thermoelectric materials, offering promising substitutes for Bi_2Te_3 in low- and mid-temperature applications. Similarly, MgAgSb is emerging as a potential *p*-type material, serving as a counterpart to the *n*-type Mg_3Sb_2 and Mg_3Bi_2-based materials. This thesis focuses on the synthesis, characterization, and evaluation of the thermoelectric transport properties of *n*-type Mg_3Sb_2-Mg_3Bi_2 solid solutions and *p*-type MgAgSb.

In this study, Mg_3Sb_2-Mg_3Bi_2 solid solutions were prepared via mechanochemical synthesis, with a higher proportion of Mg_3Bi_2 selected to enhance low-temperature performance. The $Mg_3(Sb,Bi)_2$ system was further modified through the incorporation of Nb to investigate grain boundary complexion phenomena and its effects on transport properties. This modification led to a dramatic reduction in the resistivity of the grain boundaries. The combined effects of low thermal conductivity, reduced resistivity, and elevated carrier mobility contributed to achieving high zT values, particularly in low-

temperature regimes. Notably, a record-high zT of 1.15 at 330 K was achieved for $Mg_{3.1}Nb_1(Sb_{0.3}Bi_{0.7})_{1.996}Te_{0.004}$, underscoring the competitive performance of these materials.

For mid-temperature applications, $Mg_3(Sb,Bi)_2$ system with higher amount of Mg_3Sb_2 was studied. The effectiveness of MgB_2 incorporation on the thermoelectric properties of $Mg_{3.2}Sb_{1.5}Bi_{0.49}Te_{0.01}$ was investigated, inspired by the energy filtering effect. MgB_2 nanoparticles were dispersed in the $Mg_{3.2}Sb_{1.5}Bi_{0.49}Te_{0.01}$ matrix to enhance the charge carrier scattering. As a result, alterations in the microstructure and transport properties of the $Mg_3(Sb,Bi)_2$ system have been observed. By adjusting the carrier scattering without changing the carrier concentration, a significant increase in the Seebeck coefficient of composite materials was observed, attributed to energy filtering where carriers are selectively scattered. The achievement of a high Seebeck coefficient, coupled with low thermal conductivity, led to an impressive zT value of 1.9 at 673 K for 0.1 wt.% MgB_2 incorporated $Mg_{3.2}Sb_{1.5}Bi_{0.49}Te_{0.01}$ sample.

Polycrystalline thermoelectric materials with nominal compositions of $MgAg_{0.97}Sb_x$ (x=1, 0.995, and 0.975) were synthesized through mechanical alloying to explore *p*-type counterparts. The phase transition behavior of MgAgSb-based materials was investigated using differential scanning calorimetry (DSC), revealing phase transitions at approximately 588 K (α- to β-MgAgSb) and 655 K (β- to γ-MgAgSb). The purity of synthesized $MgAg_{0.97}Sb$ materials were investigated by X-ray diffraction (XRD), scanning electron microscopy (SEM), and wavelength-dispersive X-ray spectroscopy (WDS) measurements. To eliminate the observed β-MgAgSb phase, an additional annealing step was incorporated into the synthesis methodology, resulting a significant difference in XRD patterns. Subsequently, the effect of Sb content on the purity and transport properties of $MgAg_{0.97}Sb$ was investigated. Based on the assessment of electronic transport properties, it was deduced that variations in the quantities of secondary phases significantly influence the transport characteristics. Optimal electronic transport properties were attained with the nominal composition of $MgAg_{0.97}Sb$.

In order to obtain a reliable thermoelectric performance and stable crystal structure, sintering and annealing parameters were investigated for $MgAg_{0.97}Sb$ thermoelectric materials. The phase transition behavior of MgAgSb-based materials was investigated by DSC measurements for both heat treated and pristine sample. The effect of Mg-Ag anti-site defects observed for MgAgSb phases were discussed. The strain-induced defects were examined with external heat applied to promote strain defect formation. From the Seebeck coefficient and electrical resistivity values, a change in the behavior was observed at low temperatures. As a result, high Seebeck coefficient of 243 μV/K, high Hall and weighted mobilities of 116 and 200 $cm^2V^{-1}s^{-1}$ were achieved. Combining these properties with a low lattice thermal conductivity of 0.57 $Wm^{-1}K^{-1}$ resulted in a high zT of 0.82 at 330 K after heat treatment.

To investigate the effect of carrier concentration on the thermoelectric performance of $MgAg_{0.97}Sb$, an extensive examination was performed through different dopant elements like Y and Nb elements on the Mg site, Zn and Co elements on the Ag site, and finally Ge and Te elements on the Sb site. The role of Ag atoms on electron donation was discussed based on electrical transport properties. Attempts to dope the Mg site led to the formation of secondary phases and poorer thermoelectric properties due to decreased Mg content. The most significant improvement was achieved with Ge doping on the Sb site.

ÖZETÇE

Düşük ve Orta Sıcaklık Termoelektrik Uygulamalarına Yönelik $Mg_3(Sb,Bi)_2$ ve MgAgSb Malzemelerinin Tasarımı

Melis Özen

Malzeme Bilimi ve Mühendisliği, Doktora

27 Eylül 2024

Son birkaç on yılda, çevre kirliliği, küresel ısınma ve sera gazı emisyonlarına dair endişeler giderek artmaktadır. Bu nedenle, birçok ülke 2050 yılına kadar net sıfır emisyon hedefine ulaşmayı, iklim politikalarını uygulamayı ve yeşil enerji sistemlerini entegre etmeyi taahhüt etmiştir. Üretilen enerjinin yaklaşık %60'ının sanayi, ulaşım vb. alanlardan atık ısı olarak kaybedildiği düşünüldüğünde, bu atık ısının alternatif enerji için kullanılması, genel enerji verimliliğini artırmak ve sera gazı emisyonlarını azaltmak için son derece etkili bir yol olabilir. Termoelektrik malzemeler, ısıyı elektriğe dönüştürme yetenekleri nedeniyle potansiyel bir çözüm sunmaktadır. Ancak, yüksek kaliteli atık ısının (573 K'nin üzerinde) geri kazanılması daha kolayken, mevcut kaynağın yaklaşık %90'ını oluşturan düşük kaliteli atık ısı, daha düşük enerji yoğunluğu nedeniyle zorluk teşkil etmektedir. Enerji üretme yeteneklerinin yanı sıra, çevreci, hareketli parça içermeyen ve tehlikeli gaz emisyonu yaratmayan termoelektrik malzemeler, gürültü ve titreşimden arınmış bir katı hal soğutma çözümü de sunmaktadır. Termoelektrik malzemelerle hem elektrik enerjisi üretimi hem de soğutma uygulamalarında yüksek verim elde etmek için dönüşüm verimliliği artırılmalıdır, bu da boyutsuz termoelektrik değer katsayısı, $zT = S^2\sigma T/(\kappa_l+\kappa_e)$ ile ilişkilidir. Burada S, σ, κ_l, κ_e ve T sırasıyla Seebeck katsayısı, elektrik iletkenliği, kafes ısıl iletkenliği, elektronik ısıl iletkenliği ve sıcaklıktır. Bu iletim özelliklerinin birbirine bağımlılığı nedeniyle, optimum zT değerlerine ulaşmak zorlayıcı olmaktadır. Şu anda, özellikle düşük sıcaklık uygulamaları için termoelektrik pazarı, Bi_2Te_3 temelli malzemeler tarafından domine edilmektedir, ancak tellür elementinin azalan bulunabilirliği ve toksisitesi, alternatif malzemelerin aranmasına yol açmaktadır. Mg_3Sb_2 ve Mg_3Bi_2 temelli malzemelere *n*-tipi termoelektrik malzeme olarak artan bir ilgi bulunmaktadır. Bu alternatifler, düşük ve orta sıcaklık uygulamaları için dikkat çekmekte ve Bi_2Te_3 malzemesine alternatif olarak umut vaadetmektedir. Bunun yanı sıra, MgAgSb malzemesi, Mg_3Sb_2 ve Mg_3Bi_2 temelli malzemelere karşılık gelen bir *p*-tipi malzeme olarak ortaya çıkmaktadır. Bu tez çalışması, *n*-tipi Mg_3Sb_2-Mg_3Bi_2 ve *p*-tipi MgAgSb malzemelerinin sentezi, karakterizasyonu ve termoelektrik iletim özelliklerine odaklanmaktadır.

Mg_3Sb_2-Mg_3Bi_2 alaşımları mekanik alaşımlama yöntemi ile başarılı bir şekilde sentezlenmiştir. Düşük sıcaklık uygulamaları için, yüksek miktarda Mg_3Bi_2 içeren faz ana faz olarak seçilmiştir. $Mg_3(Sb,Bi)_2$ sistemi, Nb katkısı ile modifiye edilmiştir. Tane sınırı kompleksleşme fenomeni ve bunun iletim özelliklerine etkisi tartışılmıştır. Nb ekleme sonrasında, tane sınırlarının direnci önemli ölçüde azalmaktadır. Düşük termal iletkenlik ile birlikte düşük direnç değerleri ve artan taşıyıcı mobilitesi, özellikle düşük sıcaklıklarda

yüksek *zT* değerlerine ulaşılmasına katkıda bulunmuştur. 330 K'de 1.15 gibi rekor bir *zT* değeri elde edilmiş ve rekabetçi bir performans sergilenmiştir.

Orta sıcaklık uygulamaları için, daha yüksek Mg_3Sb_2 miktarına sahip $Mg_3(Sb,Bi)_2$ sistemi incelenmiştir. MgB_2 katkısının, $Mg_{3.2}Sb_{1.5}Bi_{0.49}Te_{0.01}$ malzemesinin termoelektrik özellikleri üzerindeki etkisi, enerji filtreleme etkisinden ilham alınarak araştırılmıştır. MgB_2 nanopartikülleri, yük taşıyıcı saçılmasını destekleyecek şekilde $Mg_{3.2}Sb_{1.5}Bi_{0.49}Te_{0.01}$ matrisinde dağılmıştır. Sonuç olarak, $Mg_3(Sb,Bi)_2$ sisteminin mikro yapısındaki ve iletim özelliklerindeki değişiklikler gözlemlenmiştir. Taşıyıcı konsantrasyonunu değiştirmeden taşıyıcı saçılma davranışının düzenlenmesi ile, Seebeck katsayısında önemli bir artış gözlemlenmiştir. Bu fenomen, taşıyıcıların seçici olarak saçıldığı enerji filtreleme stratejisinden kaynaklanmaktadır. Yüksek Seebeck katsayısının elde edilmesi, düşük ısıl iletkenliği ile beraber, 673 K'de 1.9 *zT* değerinin elde edilmesini sağlamıştır.

Nominal bileşimleri $MgAg_{0.97}Sb_x$ (x=1, 0.995 ve 0.975) olan polikristalin termoelektrik malzemeler, mekanik alaşımlama yöntemiyle sentezlenmiştir. MgAgSb bazlı malzemelerin faz geçiş davranışı, diferansiyel taramalı kalorimetri ölçümleriyle incelenmiş ve 588 K'de (α'dan β-MgAgSb'ye) ve 655 K'de (β'dan γ-MgAgSb'ye) faz geçişleri tespit edilmiştir. Sentezlenen $MgAg_{0.97}Sb$ malzemelerinin saflığı XRD, SEM ve WDS ölçümleriyle araştırılmıştır. Gözlemlenen β-MgAgSb fazını ortadan kaldırmak için sentez metodolojisine ek bir tavlama adımı eklenmiştir. Tavlama işlemi sonrasında, XRD örneklerinde önemli bir fark gözlemlenmiştir. Ardından, Sb miktarının $MgAg_{0.97}Sb$'nin saflığı ve iletim özellikleri üzerindeki etkisi araştırılmıştır. Elektronik iletim özellikleri incelenerek, ikincil faz miktarındaki değişikliklerin iletim özellikleri üzerinde etkili olduğu görülmüştür. En iyi elektronik iletim özellikleri, $MgAg_{0.97}Sb$ nominal bileşimi ile elde edilmiştir.

Güvenilir bir termoelektrik performans ve stabil kristal yapı elde etmek amacıyla $MgAg_{0.97}Sb$ termoelektrik malzemeleri için sinterleme, tavlama, ısıl işlem parametreleri araştırılmıştır. Hem ısıl işlem uygulanmış hem de ana örnek olan $MgAg_{0.97}Sb$ malzemelerinin faz geçiş davranışı DSC ölçümleriyle incelenmiştir. MgAgSb fazları için gözlemlenen Mg-Ag ters konum kusurlarının etkisi tartışılmıştır. Dışarıdan ısı uygulanarak gerinim kusur oluşumu zorlanmıştır. Seebeck katsayısı ve elektrik direnci değerlerinden, düşük sıcaklıklarda bir davranış değişikliği olduğu gözlemlenmiştir. Sonuç olarak, 243 μV/K yüksek Seebeck katsayısı, sırayla 116 ve 200 $cm^2V^{-1}s^{-1}$ yüksek Hall ve ağırlıklı mobiliteler elde edilmiştir. Ayrıca, 0.57 $Wm^{-1}K^{-1}$ düşük kafes ısıl iletkenliği ile birlikte, 330 K'de 0.82 *zT* değeri elde edilmiştir.

Taşıyıcı konsantrasyonunun $MgAg_{0.97}Sb$'nin termoelektrik performansı üzerindeki etkisini araştırmak amacıyla farklı katkı elementleri (Mg konumunda Y ve Nb elementleri, Ag konumunda Zn ve Co elementleri, son olarak Sb konumunda Ge ve Te elementleri gibi) üzerine kapsamlı bir inceleme yapılmıştır. Elektriksel iletim özellikleri ile Ag atomlarının elektron bağışlama davranışı üzerindeki rolü tartışılmıştır. Mg konumunun katkılandırılabilirliği araştırılmıştır. Ancak, ikincil fazlar gözlemlenmiştir. Mg miktarındaki azalma, zayıf termoelektrik özelliklere sebep olmuştur. En umut verici sonuç, Sb yerine Ge katkılandırılmasıyla elde edilmiştir.

ACKNOWLEDGEMENTS

I would like to thank all the supportive people for the motivation and belief during my academic studies. This thesis would not have been possible without their support in various ways.

I am deeply grateful to everyone who offered their encouragement and belief in me throughout my academic journey. This thesis would not have been achievable without their support in countless ways.

First, I would like to express my sincere gratitude to my supervisor, Assoc. Prof. Dr. Umut Aydemir, for his invaluable guidance and unwavering support. His encouragement and the opportunities he provided were instrumental throughout the course of my thesis.

I would like to express my sincere thanks to my thesis committee members, Assoc. Prof. Dr. Uğur Ünal, Assoc. Prof. Dr. Safacan Kölemen, Asst. Prof. Dr. Enes Kılınç and Prof. Dr. Yaşar İslamoğlu for their valuable comments and discussions. Special thanks to Assoc. Prof. Dr. Uğur Ünal for his guidance and support. He always motivated me with his positive attitude during the hardest times.

I am deeply thankful to all my group members. Special thanks to Müjde Yahyaoğlu for being my side from the beginning of my M.Sc. study, she is like a sister, friend, colleague for me. She provided all kind of supports during this journey, I have learned lots of things from her. I want to thank Arda Baran Burçak, for his discussions, support and friendship. His curiosity to explore enlarged and forced my studies as well. I want to thank Saba Sepahban Shahgoli, her positive attitude encouraged me to complete some parts of this thesis study, her contribution is very valuable. She is always open to discuss, research and support people around her.

I would like to express my gratitude to Prof. G. Jeffrey Snyder for all the scientific discussions, and guidance. I want to thank Assoc. Prof. Hyun-Sik Kim, we had chance to discuss scientific topics, he is always accessible to support researches. I would like to thank also Dr. Ulrich Burkhardt from Max-Planck Institute CPfS for the collaborating on the main part of this research for his collaboration and WDX-SEM analysis. I would like to also thank KUYTAM, especially Dr. Barış Yağcı, for SEM and EDX analysis.

I want to thank TÜBİTAK BİDEB 2214/A financial support for my attendance to European Confenrence on Thermoelectrics. It has assisted to share our academic

discoveries with several researchers around the world, extended my network and provided opportunity to collaborate in detailed scientific studies.

I am lucky to have my special, thoughtful, intelligent friends from different periods of my life. It was a difficult time to handle both academic and industrial career, in different cities with a complete new life. I could not manage it without their support, encouragement and love throughout my life.

Finally, I am very lucky and grateful for having a lovely family with endless support. I am thankful to my thoughtful parents, Hatice & Mesut Özen and my lovely sister, Merve Nurseli Özen for their constant presence, steadfast belief and boundless patience with me. And many thanks to Uğur Dinç, who consistently eases difficulties and provides support in any way without hesitation.

TABLE OF CONTENTS

LIST OF TABLES

LIST OF FIGURES

ABBREVIATIONS

BM	Ball Milling
BSE	Backscattered Electron
CBM	Conduction Band Minimum
COP	Coefficient of Performance
DFT	Differential Functional Theory
DOS	Density of States
DSC	Differential Scanning Calorimetry
EDS	Energy Dispersive X-ray Spectroscopy
EDX	Energy Dispersive X-ray
HP	Hot Pressing
HR-TEM	High Resolution Transmission Electron Microscopy
HT	Heat Treated
IR	Infrared
LFA	Laser Flash Apparatus
OM	Optical Microscopy
PF	Power Factor
PGEC	Phonon-Glass Electron-Crystal
SAED	Selected Area Electron Diffraction
SEM	Scanning Electron Microscopy
SPS	Spark Plasma Sintering
STEM	Scanning Transmission Electron Microscope
TE	Thermoelectric
TEM	Transmission Electron Microscopy
TG	Thermogravimetric Analysis
VBM	Valence Band Maximum
WDS	Wavelength Dispersive X-ray
XRD	X-ray Diffraction

Chapter 1

INTRODUCTION

In this thesis, a detailed investigation into the synthesis, materials characterization, and thermoelectric transport properties of materials for low- and mid-temperature applications is conducted. For *n*-type thermoelectric materials, Mg_3Sb_2 and Mg_3Bi_2 were investigated through various doping and energy filtering strategies. Additionally, the thermoelectric properties of the *p*-type material MgAgSb were thoroughly examined. The theoretical background of thermoelectricity and the experimental methods employed are presented in **Chapters 2** and **3**, respectively. Subsequently, detailed theoretical investigations and experimental studies on the *n*-type Mg_3Sb_2-Mg_3Bi_2 system and *p*-type MgAgSb are presented.

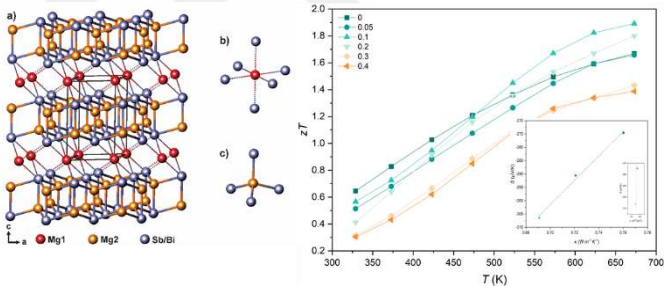

Chapter 4 presents the study of the effect of MgB_2-addition (0.05, 0.1, 0.2, 0.3 and 0.4 wt. %) on the transport properties of $Mg_{3.2}Sb_{1.5}Bi_{0.49}Te_{0.01}$. Specifically, the chapter discusses the energy filtering effect induced by MgB_2 addition and how the enhancement of the power factor is achieved by modifying scattering mechanisms.

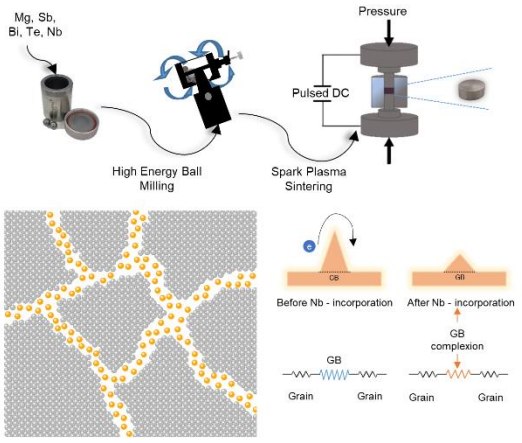

Chapter 5 explores the theoretical background of Mg_3Sb_2-Mg_3Bi_2 systems. The chapter provides a detailed discussion on the effect of Nb-incorporation on the thermoelectric properties of the compounds $Mg_{3.2-x}Nb_x(Sb_{0.3}Bi_{0.7})_{1.996}Te_{0.004}$ (x = 0, 0.025, 0.05, 0.1 and 0.15) synthesized by high-energy ball milling and spark plasma

sintering. The concept of grain boundary complexion and its influence on transport properties are thoroughly discussed.

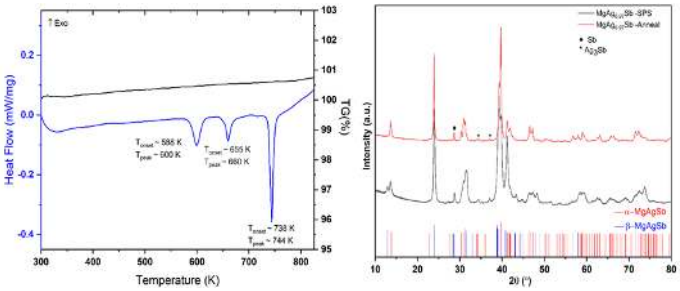

Chapter 6 focuses on the investigation of the crystal structure, thermal properties, and electrical properties of MgAgSb. The chapter examines the effects of synthesis parameters on the material's characteristics, with particular attention to the phase transitions of MgAgSb. These transitions include the half-Heusler γ phase at high temperatures (630−700 K), Cu_2Sb-related β phase at intermediate temperatures (560−630 K), and tetragonal structure α phase at low temperatures (RT ~ 560 K). Additionally, the presence of impurity phases and their impact on the thermoelectric transport properties are discussed in detail.

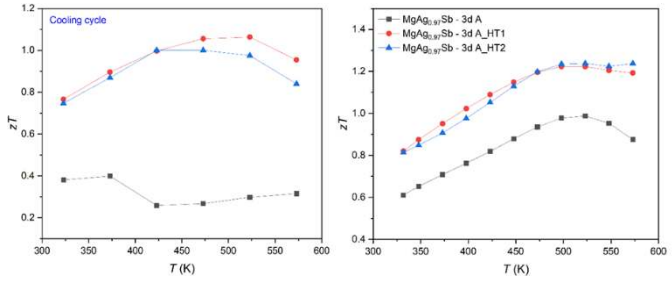

Chapter 7 focuses on optimizing the synthesis parameters like sintering duration, temperature, and annealing time to enhance and stabilize the thermoelectric properties of *p*-type $MgAg_{0.97}Sb$. The formation of anti-site defects in the crystal structure through heat treatment is examined, along with their impact on the thermoelectric properties.

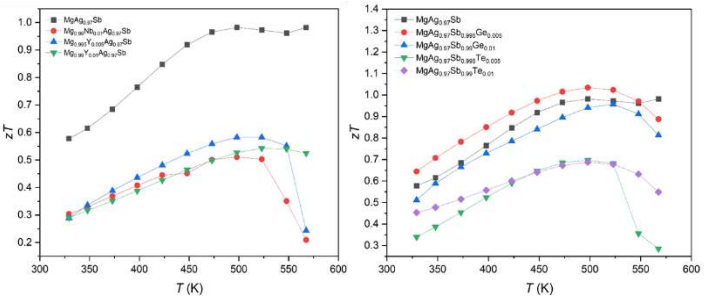

Chapter 8 investigates the synthesis of MgAgSb doped with various elements including Nb, Y, Ge, Te, Zn and Co on different lattice sites (Mg-site, Sb-site, and Ag-site). The chapter explores how doping MgAgSb with these elements at specific sites affects its thermoelectric properties.

Chapter 2

THEORY OF THERMOELECTRICS

2.1 Thermoelectric Concept

Concerns about environmental pollution, global warming, and greenhouse gas emissions have grown over the past decades. As a result, many countries have committed to achieving net-zero emissions, implementing climate policies, and integrating green energy systems by 2050[1]. Since over half of the energy from industry, transportation, and daily activities is wasted as heat, harnessing this waste heat for alternative energy offers a promising solution. This approach can significantly reduce greenhouse gas emissions and overall energy consumption with notable efficiency.

The thermoelectric effect involves converting temperature differences into electricity and vice versa. Thermoelectric devices distinguish themselves from other heat recovery systems with several unique features. These include low cost, zero emissions, no moving parts, solid-state construction, noiseless operation, durability, and being maintenance-free. Additionally, they are compact and versatile, making them suitable for a wide range of applications. While recovering high-quality waste heat (above 573 K) is relatively straightforward, capturing low-grade waste heat, which accounts for about 90% of the total, is more challenging due to its lower energy density[2-4].

Depending on the operational conditions, waste heat capacity varies as a function of temperature. Conversely, in cooling applications, the heat removal requirements fluctuate based on the necessary cooling capacity. Thermoelectric technology can convert waste heat into useful electrical energy by selecting the most suitable materials for the operating temperature range. This technology is versatile, covering a wide temperature range from 100 °C to 1000 °C, depending on the waste heat potential and the specific processes involved. Figure 2.1. represents the optimal materials according to different temperature ranges[5].

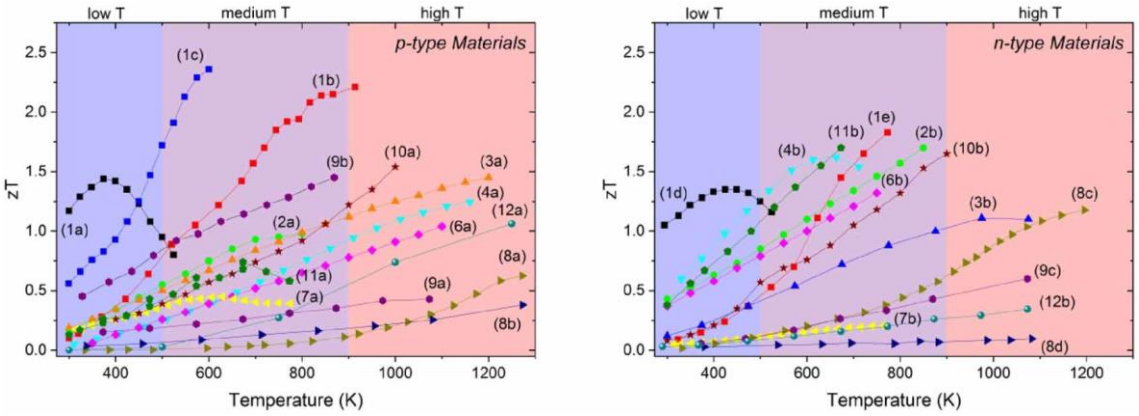

Figure 2.1. Thermoelectric figure of merit (zT) as a function of temperature for the families of materials. Details: (1) tellurides, (2) skutterudites, (3) half Heuslers, (4) Zintls (6) clathrates, (7) $FeGa_3$-type materials, (8) actinides and lanthanides, (9) oxides, (10) sulfides and selenides, (11) silicides, (12) borides and carbides.

The fundamental theory of thermoelectric effect is originating from the migration of charge carriers from hot side to cold side when a temperature gradient is applied at two different junctions, resulting in a current flow and a small voltage. This phenomenon is known as the Seebeck effect or thermopower, named after Thomas Johann Seebeck[6, 7]. The generated voltage is proportional to the temperature difference, and the Seebeck coefficient (S), which is material-specific, is the ratio of the generated voltage to the temperature difference ($\Delta V/\Delta T$). Reversely, an applied current causes charge carriers to migrate from cold side to hot side, forming an intentional temperature gradient, known as the Peltier effect, which is named by Jean Peltier[8, 9]. Figure 2 illustrates the two distinct modes of the thermoelectric module: The Seebeck effect, used for power generation (Figure 2.2a), and the Peltier effect, used for cooling.

Another common effect thermoelectric effect is Thomson effect, which refers to the heating or cooling that occurs in a current-carrying conductor with a temperature gradient. As a result of the electric current through a circuit composed of a single material, evolution or absorption of heat occurs.

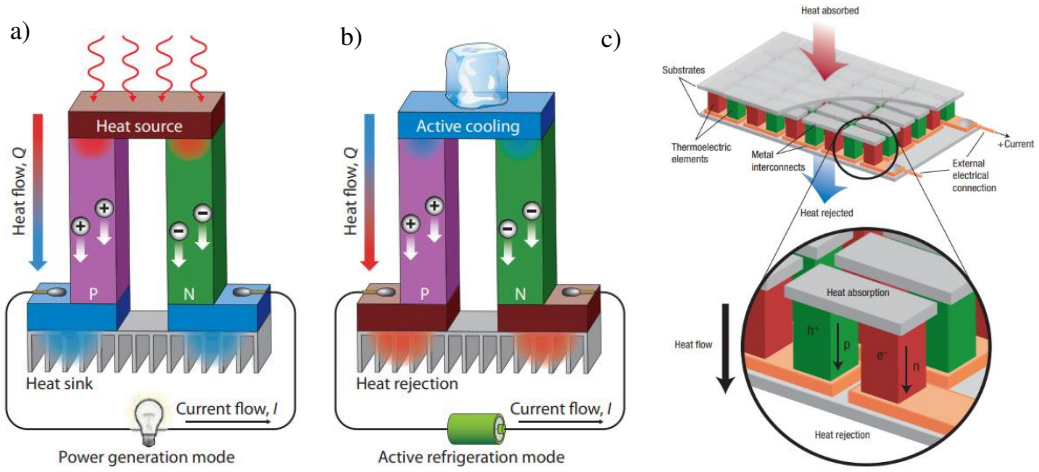

Figure 2.2. Schematic view of a thermoelectric module a) power generation (Seebeck eff ect), b) active refrigeration (Peltier effect)[10] and c) module consisting of n and *p*-type thermoelectric legs that connected electrically in series and thermally in parallel[11].

2.2 Transport Properties

The thermoelectric properties of the materials are in relation with the transport properties such as: electrical conductivity, seebeck coefficient, thermal conductivity, carrier mobility etc.

2.2.1 Seebeck Coefficient

In metals and degenerate semiconductors, the Seebeck coefficient can be expressed using the Mott formula, which correlates the charge carrier concentration and the effective mass relationship into account[12].

$$S = \frac{8\pi^2 {k_B}^2}{3eh^2} m^* T \left(\frac{\pi}{3n}\right)^{\frac{2}{3}} = \frac{\pi^2 k^2 T}{3e} \frac{d \ln \sigma(E)}{dE} \tag{2.1}$$

where k_B is the Boltzman constant, m^* is the density of states effective mass, n is the carrier concentration, e is per electron charge, h is the Planck constant and $\sigma(E)$ is the electronic conductivity as a function of the band filling or Fermi energy, E_F[6, 13]. To reduce the dependence between S and σ, various strategies have been explored over the years, such as optimizing the ideal crystal structure and band configurations in thermoelectric

materials. The $\sigma(E)$ is directly proportional to the density of states (DOS) when electronic scattering is energy-independent. According to Equation 2.1, an increase in the $d\ln\sigma(E)/dE$ value results in a higher Seebeck coefficient and power factor. Figure 2.3 illustrates two different hypothetical electronic DOS diagrams. Based on Equation 2.1, a system similar to Figure 2.3a exhibits a higher Seebeck coefficient.

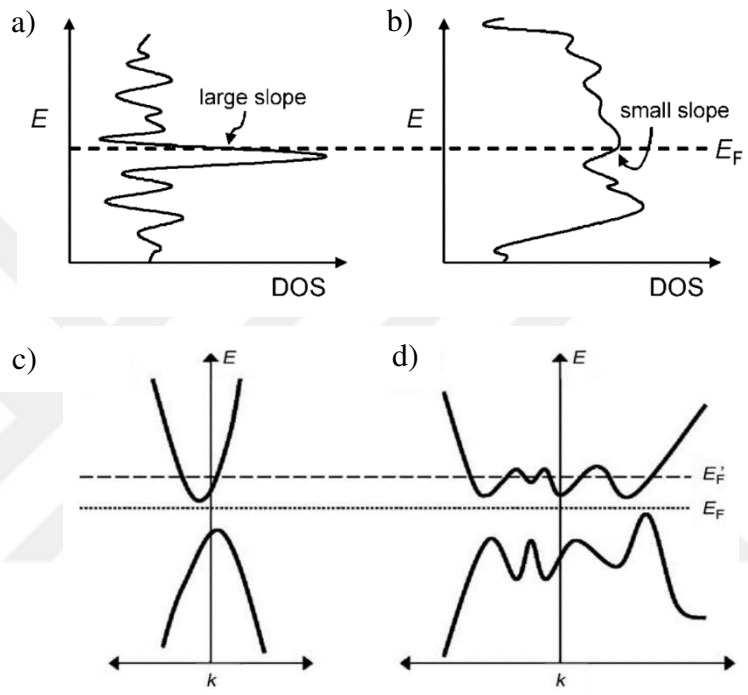

Figure 2.3. Hypothetical density of states with a) large slope $d\ln\sigma(E)/dE$ and b) small slope near EF, and hypothetic electronic band structures with c) single valley and d) multi valley valence and conduction band systems[13].

Figure 2.3c shows a system with a single band valley in both the valence and conduction bands, whereas Figure 2.3d depicts a system with multiple band valleys in both bands. Because the power factor is influenced by the number of populated valleys, the system illustrated in Figure 2.3d is expected to have a higher power factor[13].

2.2.2 Electrical Conductivity

The general expression of the electrical conductivity can be given as;

$$\sigma = nq\frac{v}{E} \tag{2.2}$$

where n is the carrier concentration, q is the charge of the carrier and $(\frac{v}{E})$ represents the mobility of carriers (either holes or electrons). For conductive materials such as metals, electrical conductivity is significantly influenced by mobility. In contrast, for semiconductors, the number of charge carriers is more crucial than mobility.

In the presence of an electric field, electrons tend to move preferentially in a specific direction, resulting in an average velocity[14]. In that case, the electrical conductivity can be expressed as;

$$\sigma = \frac{ne^2\tau}{m} \tag{2.3}$$

where m is the electron mass and τ is the relaxation time which is the expression of average time between two collisions of electrons while moving through the solid. Thus, it can be deduced that the charge carriers, the mass of the charges, and the scattering mechanisms within the material play an effective role on the electrical conductivity of materials[14].

2.2.3 Thermal Conductivity

The thermal conductivity is the heat transfer in the materials through carriers under the presence of a temperature gradient. Two main components; carrier and phonons (lattice vibrations) are responsible for total heat conduction. The total thermal conductivity is given by the sum of electronic thermal conductivity(κ_e) and phonon thermal conductivity (κ_l)[15].

$$\kappa = \kappa_e + \kappa_l \tag{2.4}$$

In metals, the electronic contribution is more effective than the phonon contribution, generally. However, the movement of phonons become dominant for the thermal conductivity in case of degenerate semi-conductors and for the materials with the bands with non-parabolicity. Through the classic kinetic theory, the phonon thermal conductivity of a solid can be examined as,

$$\kappa_l = \frac{1}{3} c_v v_s l = \frac{\pi^2 n k_B^2 T \tau}{3 m_e} \tag{2.5}$$

where c_v is the specific heat capacity for a constant volume, v_s is the velocity of sound, and l is the mean free path of phonons. According to the equation above, the change in the phonon mean free path is an effective strategy for adjusting the lattice thermal conductivity. In such a way, the total thermal conductivity can be decreased while keeping the electrical contribution same. The possible phonon scattering mechanisms are atomic defects to scatter the short wavelength phonons, and larger defects such as precipitations of nanoparticles, interfaces and grain boundaries for scattering mid and long wavelength phonons[16]. Figure 2.4 represents the defects in relation with the scattered phonons.

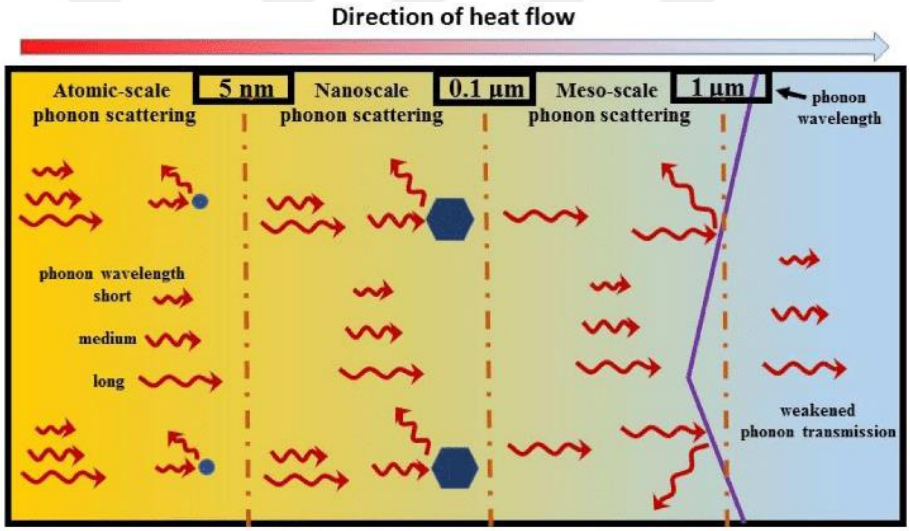

Figure 2.4. The schematic illustration of phonon scattering[17].

Since the phonon scattering is minimal due to the low number of phonon excitations and long wavelengths, the lattice thermal conductivity follows the Debye T^3 law for heat capacity (c_v) at low temperatures. At high temperatures, exceeding the Debye temperature, the velocity of sound and the heat capacity of the solid in most materials remain relatively constant. Consequently, at higher temperatures, the lattice thermal conductivity is influenced by the mean free path of phonons. In real crystals, various scattering mechanisms significantly reduce thermal conductivity. These mechanisms involve the scattering of both carriers and phonons. The major phonon-scattering

mechanisms are phonon-phonon scattering, phonon-boundary scattering, and phonon-defect scattering.

By dividing the Equation 2.5 and Equation 2.3 Wiedemann-Franz Law can be achieved as,

$$\frac{\kappa_e}{\sigma T} = \frac{\pi^2}{3}\left(\frac{k_B}{e}\right)^2 \tag{2.6}$$

the ratio ($\frac{\kappa_e}{\sigma T}$) in the above equation, is known as the Lorenz number and is equal to 2.45 x10^{-8} WΩ K^{-2}. Wiedemann-Franz Law shows that the proportion of thermal conductivity to the electrical conductivity is not related to the phonon parameters[18]. Therefore, the electronic thermal conductivity can be defined as,

$$\kappa_e = L\sigma T \tag{2.7}$$

2.3 Thermoelectric Figure-of-Merit

The dimensionless thermoelectric figure of merit, *zT*, which defines the ability of a material to convert the heat to the electricity defined as,

$$zT = \frac{S^2\sigma T}{\kappa} \tag{2.8}$$

where *S* is the Seebeck coefficient, σ is electrical conductivity, κ is the total thermal conductivity and *T* is absolute temperature[7, 11]. To enhance the efficiency of a thermoelectric generator or a cooler, a material with high *zT* value is necessary. Therefore, with large Seebeck coefficient, high electrical conductivity, and low thermal conductivity, the requirement of high *zT* can be fulfilled. However, the inter-relationship between thermoelectric properties (*S,* σ and κ) is the main challenge for optimization of *zT*. As discussed before, according to Wiedemann-Franz law (κ_e=$L\sigma T$) the electronic thermal conductivity (κ_e) is proportional to the electrical conductivity. And, both electrical conductivity and Seebeck coefficient dependent carrier concentration. Hence, optimization of the carrier concentration is significant rather than achieving high carrier concentration.

Figure 2.5a shows the inter-relationship between different physical parameters (α, σ and κ, $S^2\sigma$, and zT) and carrier concentration. As seen, the increase in the carrier concentration increases both thermal conductivity and electrical conductivity, while diminishes the Seebeck coefficient. The combination of those physical properties led to a low power factor and hence reduces zT value with high carrier concentration. On the other hand, significantly high Seebeck coefficient and low thermal and electrical conductivity results in a low power factor with low zT in the low carrier concentration zone[19]. The maximum zT value can be achieved when the carrier concentration is between 10^{19}-10^{20} cm^{-3}. Thus, heavily doped semiconducting materials are more appealing for thermoelectric applications compared to insulators and metals. While it is challenging to reduce thermal conductivity without affecting electrical conductivity, it is achievable by targeting the phonon component of thermal conductivity. As illustrated in Figure 2.5b, if the lattice thermal conductivity can be reduced without altering the carrier concentration, the zT value can be improved[11].

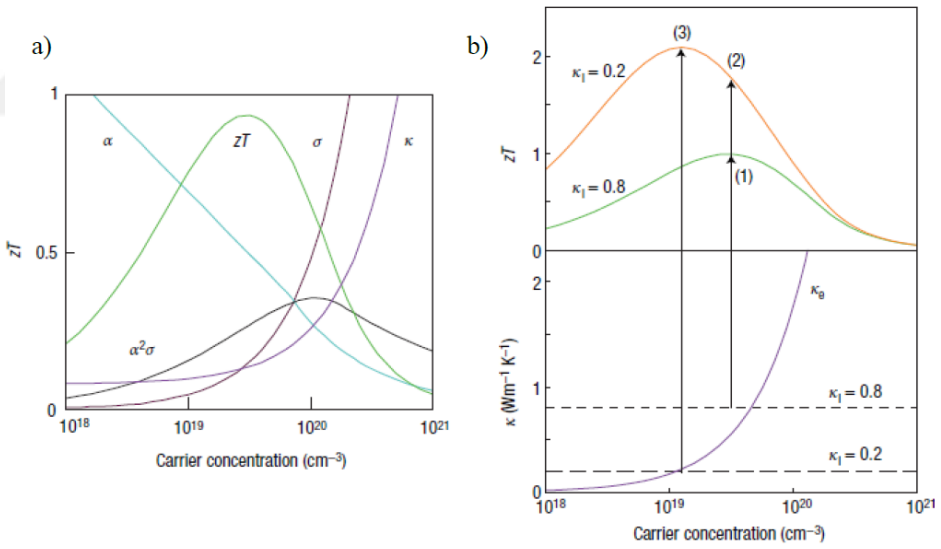

Figure 2.5. The relation between carrier concentration and transport properties, b) the dependence of zT to lattice thermal conductivity with the same amount of carrier concentration[11].

2.4 Thermoelectric Devices

Thermoelectric devices composed of *n*- and *p*-type legs that are electrically connected in series and thermally connected in parallel, as shown in Figure 2.6. The

purpose of the devices can be either generation of power or cooling. These legs are connected by electrically conductive shunts, for instance by copper. Additionally, the module includes a heat sink to sustain the temperature difference between the top and bottom sides for effective application[20].

The efficiency of thermoelectric devices is determined by the ratio of the electrical power supplied to the load to the heat absorbed at the hot junction, as given[21],

$$\eta = \frac{w}{Q} = \frac{I^2 R_l}{K(T_h - T_c) + SIT_h} \tag{2.9}$$

In case of dimensionless figure-of-merit, the efficiency of a thermoelectric power generator primarily depends on the zT value and the thermoelectric quality factor, given as,

$$\eta_{max} = \frac{T_H - T_C}{T_H} \times \frac{\sqrt{1 + \overline{ZT_m}} - 1}{\sqrt{1 + \overline{ZT_m}} + \frac{T_C}{T_H}} \tag{2.10}$$

the term $(T_H - T_C/T_H)$ above represents the Carnot efficiency, where ZT_m is the average ZT value between the hot and cold temperatures[22].

For the thermoelectric coolers, the cooling efficiency is defined by the coefficient of performance (COP_{max}), as follow[23],

$$COP_{max} = \frac{T_C}{T_H - T_C} \frac{\sqrt{1 + \overline{ZT}} - \frac{T_H}{T_C}}{\sqrt{1 + \overline{ZT}} + 1} \tag{2.11}$$

where $\overline{ZT}$ is the average ZT. Thermoelectric quality factor (B factor) can be defined by the relation of the band structure and transport properties as given,

$$B \propto \frac{\mu_c {m_*}^{1.5} T^{2.5}}{\kappa_L} \tag{2.12}$$

where m^*, κ_L, μ_c and T are the effective mass, lattice thermal conductivity, carrier mobility and specific temperature at the nondegenerate limit, respectively[22].

Figure 2.6 presents the efficiency of a thermoelectric device as a function of various zT values with the changing temperature difference between source and sink[24]. For a comparison, the efficiency of a thermoelectric generator reaching about 35% at a temperature difference of 500 K and a ZT value of ~10, which is comparable to a steam engine[25]. On the other hand, with a maximum zT of 2.6, a thermoelectric material provides less efficiency than other energy-conversion technologies[26].

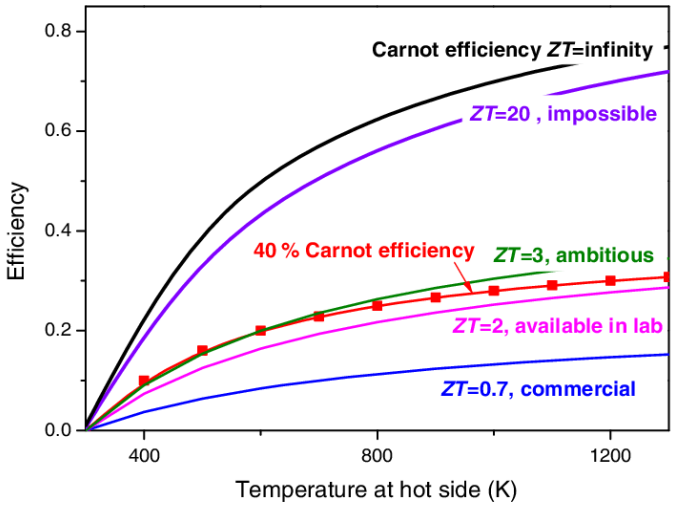

Figure 2.6. Conversion efficiency of thermoelectric materials as a function of temperature difference with different ZT values (the cold side temperature is taken as 300 K)[24].

Chapter 3

EXPERIMENTAL METHODS & CHARACTERIZATION OF THERMOELECTRIC MATERIALS

The raw material storage, weighing and preparation steps were performed under inert Ar atmosphere in a glove box (MBraun) because of the air sensitive character of some starting materials. Mainly, the thermoelectric material synthesis has been conducted through mechanical alloying method.

3.1 Chemicals

The starting chemicals used in this study are listed in the Table 3.1. All elements with fine particle sizes were used as it is without a requirement for further purification.

Table 3.1. Starting chemicals with specifications.

Chemical	**Physical State**	**Melting Point**	**Company**
Magnesium	Powder	650 °C	Pavezyum
Antimony	Powder	630 °C	Alfa Aesar
Bismuth	Powder	271°C	Alfa Aesar
Tellurium	Pieces	449.51 °C	Alfa Aesar
Niobium	Pieces	2468°C	Sigma Aldrich
Silver	Powder	961.8°C	Nanografi
MgB_2	Powder	830 °C	Pavezyum

3.2 Sample Preparation Methods

In this study, mechanical alloying used for synthesis of the desired chemical compounds. To consolidate the as-prepared powders with desired compositions, spark plasma sintering applied for further characterizations and physical measurements.

3.2.1 Mechanical Alloying

High-energy ball milling is a mechanical alloying technique that can produce homogeneously reacted powders by mixing starting elements in a closed vial. This method offers an advantage over conventional solid-state synthesis by allowing better control over the stoichiometry of highly volatile reactants.

Mechanical alloying reactions and doping studies are employed using a two-clamp high-energy ball milling device (SpexSamplePrep 8000D). This device can accommodate two grinding vials simultaneously, which are secured between clamps that operate at a speed of 875 cycles per minute. In this study, hardened steel vials with a maximum capacity of approximately 10 grams and half-inch stainless steel balls were utilized. In this process, the clamps holding the vials shake back and forth with slight lateral movements, causing the solid powders to react under the influence of G-forces aided by the stainless-steel balls. To prevent oxidation of the activated sample surfaces during milling, the preparation steps inside the stainless-steel jars were always conducted within an Ar-filled glovebox. A schematic of the SPEX 8000D is shown in Figure 3.1.

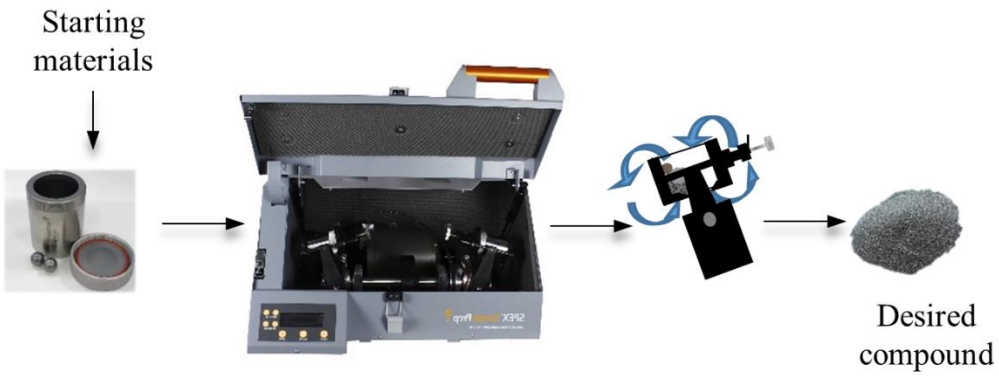

Figure 3.1. Schematic view of high energy ball milling process.

3.2.2 Spark Plasma Sintering

High-energy ball milling is a mechanical alloying technique that can produce homogeneously reacted powders by mixing starting elements in a closed vial. This method offers an advantage over conventional solid-state synthesis by allowing better control over the stoichiometry of highly volatile reactants. The spark plasma sintering (SPS) method was utilized for the densification of powder samples using AGUS-PECS SPS-320Sx from SUGA Co., Ltd. (Figure 3.2). This technique involves passing an electrical current through a graphite die containing the powder samples, leading to rapid heating and short processing times, known as spark plasma sintering. The system comprises a vacuum chamber controlled by a vacuum pump and inert gas lines for creating desired atmospheric conditions, a sintering component where axial pressure is applied via electrode punches, and a DC pulse power supply that manages the sintering process with temperature measurements from a thermocouple or IR camera. The advantages of the SPS technique such as short processing times and well-controlled grain sizes and microstructures stem from various phenomena, including plasma generation, joule heating (heat generated through electrical resistance), the electro-plastic effect, electro-migration under pulsed electric currents, and the application of mechanical pressure.

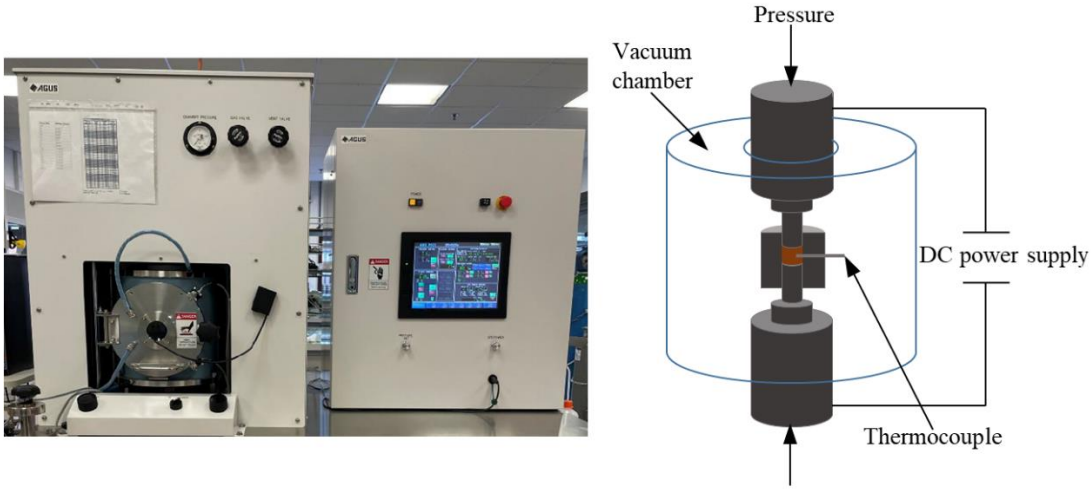

Figure 3.2. (a) Spark plasma sintering (SPS) devices used in this study and (b)schematic view of SPS with the graphite dies and sample inserted in the vacuum chamber.

In principle, powders are placed inside a graphite die, between graphite punches and graphite foils. By applying DC pulses, the temperature can be rapidly increased to between 1000-2500 °C. The combination of pressure and high temperature allows the SPS system to produce highly compacted, dense samples. The SPS process leverages various effects, such as plasma generation, joule heating, the electro-plastic effect, electro-migration due to the pulsed current, and mechanical pressure[27]. Figure 3.3 represents these effects on neck formation by SPS.

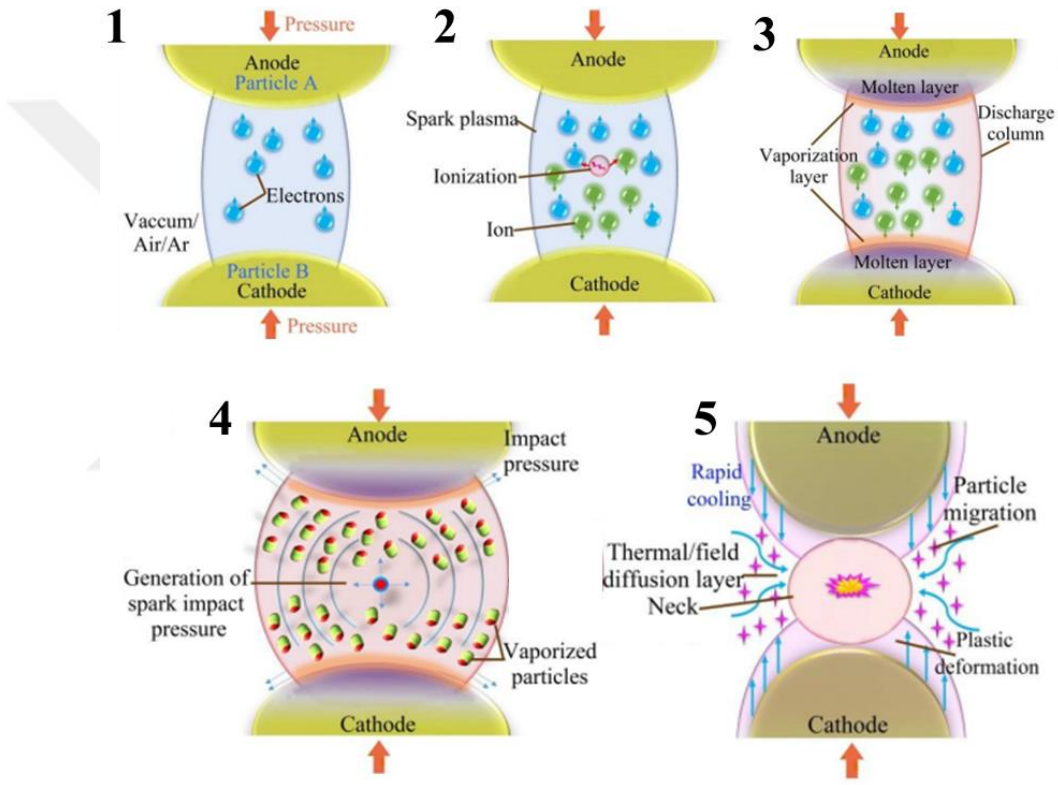

Figure 3.3. The formation mechanism of neck by SPS[28].

Unlike conventional systems, the SPS technique heats the sample both externally and internally using pulsed direct currents passing through the graphite dies and the sample itself. When an electrical potential is applied to the system, sparks at the contact points generate electron flow and plasma discharges between the particles. These sparks cause the local temperature to rise instantly to several thousand degrees Celsius. This rapid heating, due to joule heating, leads to evaporation and melting on the particle surfaces, resulting in immediate neck formation (Figure 3.3). Additionally, the electro-plastic

effect, which reduces the yield strength of metals when an electric field is applied, aids in the plastic deformation mechanism and accelerates the densification process[27-29].

For densification of powders, graphite dies with an inner diameter of 10 mm is used with graphite punches. Initially, the inside of the graphite dies was lined with graphite foil to facilitate the easy removal of the consolidated samples and prevent any cross-contamination. The powder is then placed into the graphite die between the graphite punches, with additional graphite layers (10 mm in diameter) positioned between the powder and the punches under Ar atmosphere for obstruction of any trapped oxygen during the process. The loaded graphite dies are inserted between punch electrodes where current and pressure are applied in a vacuum chamber. Then the chamber is evacuated. According to the materials being studied, the sintering time, applied axial pressure, and duration is set to the sintering program. During the process, temperature readings are taken using a K-type thermocouple inserted into the die's hole, or an IR camera is used when sintering temperatures exceed 850 °C to avoid thermocouple failure.

3.2.3 Diamond Wire Saw Cutting

A specific shape is necessary to measure the physical properties of thermoelectric materials. As presented in Figure 3.4, a diamond wire saw was used to cut the as-prepared pellets (shaped cylindrically with a height of 4-5 mm and a diameter of 10 mm). Based on the diffusivity range of the samples, the disc thickness should generally be between 1-2 mm for the thermal diffusivity measurements using a Laser Flash Apparatus (LFA). For electrical resistivity and Seebeck coefficient measurements the samples should ideally be rectangular with the desired dimensions of at least 2 mm width and depth, with a height of at least 6 mm. The achieved disc shaped pellets by SPS is glued on its side to a ceramic or Teflon surface using polymer wax to cut into a disc approximately 1-1.5 mm thick for LFA. The remaining 2.5 mm thick disc is then glued on its round surface to be cut into a rectangular bar shape for ZEM-3 measurements. Water with addition of a lubricant was used as coolant to enhance the efficiency of process.

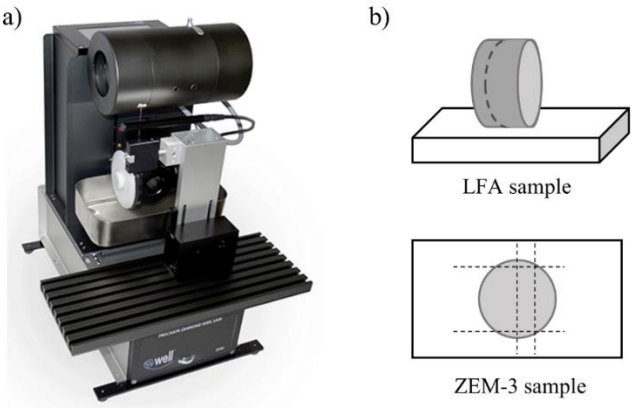

Figure 3.4. a) Diamond wire saw cutting device (b) cutting directions of samples.

3.3 Characterization Techniques

3.3.1 X-ray Diffraction

A specific shape is necessary to measure the physical properties of thermoelectric materials. X-ray diffraction (XRD) is used to determine the structure and composition of materials, providing details about lattice parameters, grain sizes, and crystallinity. X-rays are generated by an electron bombardment of a target material (such as Cu, Fe, Mo, or Cr) in a cathode ray tube. These X-rays are then filtered and collimated to produce monochromatic radiation. When the monochromatic X-rays strike the sample, result in a constructive or destructive interference by scattering from the periodic lattice. The constructive interference results in a diffraction pattern, only if the conditions of Bragg's Law are fulfilled. The Bragg's Law is given as,

$$n\lambda = 2\mathrm{d}\ \sin\theta \tag{3.1}$$

where where n is the order of reflection, λ is the X-ray wavelength, d is the inter-planar spacing of the crystal, and θ is the angle between the Bragg plane and the incident X-ray[30]. Since the diffraction pattern is unique for each crystal, the chemical identity of the samples can be defined by comparing the patterns with the database.

Powder and bulk samples were characterized using a Rigaku MiniFlex XRD with Cu K_α radiation (λ = 1.540598 Å) as the X-ray source, operating at 40 kV and 15 mA. The

measurements were conducted over a range of $10° \leq 2\theta \leq 90°$, with a step size of $\Delta 2\theta = 0.02°$. STOE WinXPOW software was used to analyse the X-ray powder diagrams through using crystallographic data from the ICSD database. Lattice parameter refinements were performed using LaB_6 as a correction standard to accurately determine peak positions, and WinCSD program package was used to calculate the unit cell parameters through least-square refinement using the[31].

3.3.2 Scanning Electron Microscopy

Scanning electron microscopy (SEM) is a highly effective multifunctional characterization technique used to determine the morphology of microstructures and chemical compositions (if equipped with WDX or EDX). SEM works by detecting signals generated from the interactions between the sample and an electron beam.

The SEM setup includes an electron gun, condenser lenses, an objective lens, electron detectors, and a vacuum system. The electron gun emits electrons and accelerates them, which then pass through electromagnetic lenses to form a small, focused electron spot on the sample. These processes occur under a high vacuum to prevent electron scattering by air. When electrons hit the sample, they cause various signals due to excitation within the sample. Different interactions between the sample and the electron beam produce various signals, including secondary electrons, backscattered electrons, Auger electrons, characteristic X-rays, and cathodoluminescence.

The most commonly used signal is from secondary electrons, which are generated by the ionization of atoms following interaction with primary electrons. Secondary electrons, with their low energy (around 5 eV), provide detailed information about the specimen's topography, resolving surface structures down to 10 nm. Bright areas in the SEM image result from unhindered electrons where brightness is determined by the number of electrons, while blocked electrons create darker images. Backscattered electron signals offer both topographic and compositional information. After elastic collisions, primary electron beams reflect from the sample, retaining 60-80% of their energy. These backscattered signals vary based on the atomic number, with higher atomic numbers producing more backscattered electrons due to increased positive charge[32, 33].

In this study, SEM measurements were performed using a Zeiss Ultra Plus Field Emission Scanning Electron Microscope. Both fine powder and bulk samples were placed on carbon tape before being loaded into the vacuum chamber. The bulk samples were finely polished using the Tegramin 30 Struers automatic sample polisher system after being mounted with the Citopress 30 Struers mounting press. Elemental composition and distribution were examined using the elemental mapping feature with Energy Dispersive X-ray Spectroscopy (EDS) and Wavelength-Dispersive X-ray Spectroscopy (WDS, Cameca SX 100, tungsten cathode). Microstructure analysis was conducted using optical microscopy (OM, Zeiss Axioplan).

3.3.3 Transmission Electron Microscopy (TEM)

Transmission electron microscopy provides detailed information about the electron diffraction patterns and crystalline properties of materials, in addition to highly magnified images at magnifications ranging from 10^3 to 10^6.[34] During measurements, electron beams with energies between 60-150 keV are directed at the sample. The electron beams are generated in an electron gun and focused onto the sample using condenser lenses, which determine the exposed area. After the sample is exposed to the electron beams, a subsequent lens system projects an image of the electron intensity distribution onto a fluorescent screen[35].

In this thesis, TEM experiments were conducted using the Talos F200S scanning/transmission electron microscope (S/TEM) operating with a maximum acceleration voltage of 200 kV.

3.3.4 Thermal Analysis

Differential scanning calorimetry (DSC) is used to evaluate the reaction temperatures, phase changes (both physical and chemical), and enthalpy of samples as a function of temperature by measuring the heat flow difference between a sample and a reference. The temperature difference between the sample and the reference side, which is typically an empty pan, is recorded by sensors, connected to thermocouples.

The thermal stability of the samples was assessed using the Netsch STA 449 F3 Jupiter, equipped with thermos-gravimetric analysis (TG). All measurements were performed under an inert atmosphere by flowing nitrogen (N_2).

3.4 Physical Property Measurements

3.4.1 Thermal Diffusivity and Thermal Conductivity

The laser flash method is employed through the Netsch LFA 467 HT Hyper Flash instrument (Figure 3.5) to measure the thermal diffusivity of samples across a specified temperature range under controlled argon flow. In this method, a brief energy pulse from a Xenon lamp heats the lower surface of the sample causing a temperature change. This temperature variation on the upper surface is then detected by an infrared (IR) InSb detector. Since LFA is an optical technique, prior to measurement, samples were coated with a thin layer of graphite to minimize reflection and improve absorption and emission properties, thereby enhancing the signal-to-noise ratio. The thermal diffusivity(α) value is calculated by the equation,

$$\alpha = 0.1388 \times \frac{d^2}{t_{\frac{1}{2}}} \tag{3.2}$$

where d is the thickness of the sample, and $t_{1/2}$ is the half-time at half-signal height.

The laser flash technique was operated between the specific temperature range depending on the material characteristics. The thermal conductivities of samples are calculated by using α as follow;

$$\kappa(T) = d(T) \times c_p(T) \times \alpha(T) \tag{3.3}$$

where κ is the thermal conductivity (W/K·m), d is the density (g/cm^3), α is the thermal diffusivity (mm^2/s) and c_p is the specific heat (J/g·K).

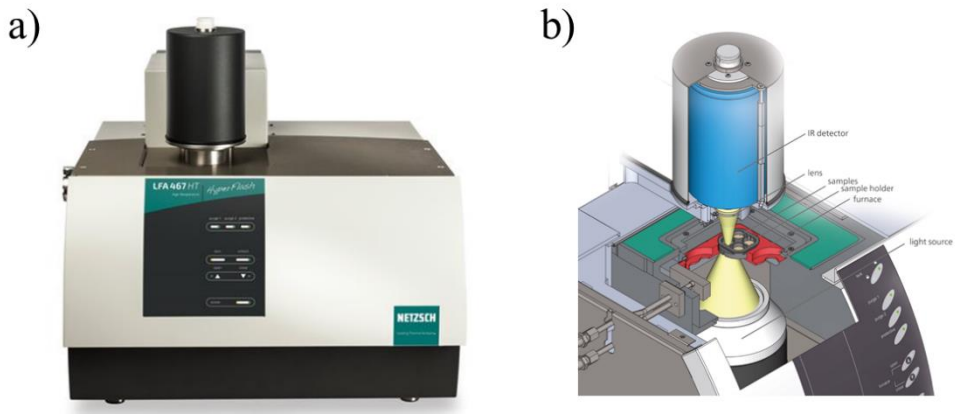

Figure 3.5. a) LFA 467 HyperFlash and b) the schematic representation of the instrument parts.

3.4.2 Thermal Analysis

The specific heat capacity, c_p, can be determined by DSC using the ratio method, with sapphire as the reference material. c_p represents the amount of heat needed to raise the temperature of a given mass of material by one degree. In DSC, signals at various temperatures are recorded and compared to those of a reference material simultaneously. In this study, the reference used is a sapphire sample with a known c_p and mass. The c_p of the sample is calculated using the ratio method, as evaluated by the software, as follow,

$$c_{p,sample} = \frac{m_{sapp}}{m_{sample}} \frac{DSC_{sample} - DSC_{baseline}}{DSC_{sapp} - DSC_{baseline}} c_{p,sapp} \tag{3.4}$$

where m_{sample} is the sample mass, DSC_{sample}, $DSC_{baseline}$, *and* DSC_{sapp} are signals achieved from sample, baseline, and sapphire reference, respectively.

The Dulong-Petit law can also be applied to calculate c_p by considering the vibrational degrees of freedom of the atoms. Each atom vibrates in three dimensions, resulting in an energy of $3k_BT$ per atom, or $3k_BTN_A$ per mole of atoms, where k_B is Boltzmann's constant and N_A is Avogadro's number. The c_p can then be calculated as given,

$$c_p = \frac{3NR}{M} \tag{3.5}$$

where N is the total number of atoms in the chemical formula, R is the gas constant (equal to $k_B N_A$, and M is the molar mass of the compound.

3.4.3 Electrical Resistivity and Seebeck Coefficient

The electrical resistivity(ρ) and Seebeck coefficient (S) values were measured by ULVAC ZEM-3 Seebeck Coefficient/Electrical Resistance Measurement System (Figure 3.6), through a four-point probe method. This method is using to minimize/eliminate the contact effect while measuring the resistivity of semi-conductors. Using ZEM-3 measurement, the sample geometry and dimensions should be 2-3 mm width and depth to a height of 6-8 mm with a rectangular shape. For prevention of any contamination and to protect the probes and electrodes, graphite sheets were placed between the touching surfaces of the sample. Inside the furnace chamber, the sample were placed between the lower and upper electrodes, vertically. Before the measurement, an evacuation process is taken into account in every 15 minutes or cycles for at least three times by refilling with He in each. In the end, to maintain the conductive environment a small amount of He is kept inside the chamber.

The software of the system controlled the electrical current for the determination of resistivity. The electrodes applied the constant current during the measurements, while a temperature gradient of 10, 20 and 30K was created on the sample through a heater in the lower block at elevated temperatures. Thermocouples measured the electromotive force dE and the temperature difference. Through the static DC method, Seebeck coefficient was measured given as,

$$S = \frac{\Delta V}{\Delta T} \tag{3.5}$$

where S, ΔV, and ΔT are Seebeck coefficient (V/K), the voltage difference and the temperature difference.

DC-four terminal method is used for measurement of the electrical resistivity. The voltage drops are detected between the thermocouples while a current is applied from

upper and lower electrodes. The electrical resistivity can be determined by the relation as given,

$$\rho = \frac{dV}{dI}\frac{A}{d} \tag{3.6}$$

where ρ is the resistivity, $\frac{dV}{dI}$ is the slope of V-I plot giving the resistance (R), A is the cross-sectional area of the sample, and d is the distance between the thermocouple probes.

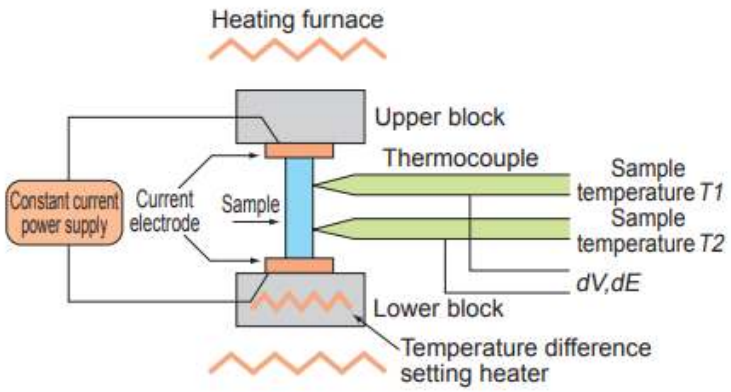

Figure 3.6. Schematic view of the electrical resistivity and seebeck coefficient measurement system.

3.4.4 Hall Effect

The charge carrier concentration with a determination of carrier type either as negative for electron or as positive for holes, and the carrier mobility can be measured effectively by Hall effect. These properties are engaged to predict the carrier scattering mechanism and the band effective mass of a material.

When a sample subjected to a magnetic field B, where an electric current flows through, a transverse voltage, V_H, which is also named as the Hall effect, is produced by the diversion of the paths of the charge carriers to the sides. Via the formulation given below, the hall constant, R_H, can be calculated as,

$$R_H = \frac{V_H A}{IdB} = \frac{\rho_H}{B}, \quad R_H = -\frac{1}{n_e}(electron)\ ,\ R_H = -\frac{1}{n_p}(hole) \tag{3.7}$$

where I is the current, d is the transverse dimension of the sample, ρ_H is the Hall resistivity, n_e and n_p, are the electron and hole concentration. The Hall mobility, μ_H, can be calculated followed as,

$$n_H = \frac{1}{R_H|e|}, \quad \mu_H = \frac{R_H}{\rho} \tag{3.8}$$

A home built system was used to measure the Hall effect through 4-point probe Van der Pauw (VdP), via a magnetic field of 2 T with pressure-assisted tungsten electrodes in Northerstern University. Dense samples are set on an alumina holder with a heater inside. To eliminate the contact resistance between the sample and probes, four molybdenum probes on the sample tightened with screws. The sample holder is protected via a radiation shield and located inside the vacuum chamber. To minimize oxidation, the chamber is evacuated to a pressure of 10^{-5} Torr using turbo pumps.

3.4.5 Vickers Hardness

The micro-hardness of the samples is identified using Shimadzu HMV-G Series Micro Vickers Hardness Tester. First, to achieve a flat surface, a surface preparation is applied. To be able to determine the appropriate load, various loads (0.1, 0.01, 0.05 HV) are applied to the material.

In principle, to apply force on the surface a pyramidal shaped diamond indenter is utilized and held there without any vibrations or strikes for 10-15 seconds. After picking up the indenter, a mark with diagonals are achieved on the surface. The Vickers hardness is calculated by using these diagonals given in the equation[36],

$$HV = 2000L \sin\frac{\frac{a}{2}}{d^2} = \frac{1854.5L}{d^2} \tag{3.9}$$

where L and d represents the load in kgf and the arithmetic mean of the two diagonals in mm, respectively.

Chapter 4

INVESTIGATING THERMOELECTRIC PERFORMANCE OF *N*-TYPE $Mg_{3.2}Sb_{1.5}Bi_{0.49}Te_{0.01}$ THROUGH MgB_2 INCORPORATION

4.1 Introduction

Enhancement on the zT is necessary for improvement of the conversion efficiency of thermoelectric devices. However, the parameters affecting zT values such α, σ, κ_l, $\kappa_{e,}$ are interdependent, and it is challenging to optimize these parameters. Zintl phases are promising for efficient thermoelectric devices, because of their inherently low lattice thermal conductivities in addition to the tunable electronic transport[37, 38]. As be discussed in the crystal structure, the covalently bonded network composing of complex anions with ionically weakly bonded cations, Zintl phases present a phonon-glass, electron crystal concept (PGEC)[39, 40]. Although, most of the Zintl phases show *p*-type characteristic, achievability of *n*-type Zintl compounds with higher thermoelectric performances is displayed in the last decade[41-44].

It is a well-known fact that for Mg_3Sb_2, Mg vacancies tend to form stemming from the high vapor pressure and reactivity of Mg, resulting in electron acceptors during the synthesis[45, 46]. As a result of the moving of the chemical potential to valence bands, *p*-type conduction characteristic has been observed for Mg_3Sb_2. Therefore, excess amount of Mg in the nominal composition have been a strategy for suppressing the creation of Mg vacancies. That strategy triggered the achievement of very high zT values ~1.5 near 800 K with the optimized thermoelectric properties[46]. Therefore, *n*-type Mg_3Sb_2-based materials obtained a great attention to enhance transport properties further with various strategies, like tuning scattering mechanism, carrier concentration optimization, optimization of grain size, annealing, orbital engineering, band structure modification, doping, energy filtering etc[4, 47-57]. Especially, through the alloying with Mg_3Bi_2 thermoelectric efficiency is remarkably enhanced via advanced band structure and

modified scattering mechanism[58-64]. Therefore, further studies mostly have been conducted on Mg_3Sb_2-Mg_3Bi_2 systems. Besides, grain boundary and microstructure engineering stand out for enhanced electrical conductivity, specifically at low temperatures. Several methods such as annealing, adjusting synthesis temperatures and creating wetting phases, have been studied to increase grain sizes to diminish grain boundaries with suppression of possible carrier scatterings[51, 65-69].

Along with the strategies focused on reduced lattice thermal conductivity and increased electrical conductivity, mobility, energy filtering effect also discovered as a significant approach for improved Seebeck coefficients with consistent electrical conductivities through selective filtering of the carriers according to the energy spectrums[70]. The contribution of low energy electrons to the Seebeck coefficient is smaller for the *n*-type thermoelectric materials[71, 72]. Therefore, through suppression of low energy electrons by an energy barrier, Seebeck coefficient can be increased[73]. One option to obtain energy filtering effect is creating interfaces like grain boundaries as energy barriers. Although it is effective to reduce lattice thermal conductivity by scattering phonons, and enhance the Seebeck coefficient, it also led to a decrease in the electrical conductivity. It is difficult to achieve an astonishing improvement in the *zT,* since the enhancement in the Seebeck coefficient should repay any reduction in the electrical conductivity. Therefore, only a few study has successfully employed energy filtering to improve thermoelectric efficiency[74, 75]. To maximize the effect of secondary phases such as grain boundary, while blocking the low energy carriers, generated phonon scattering centers should reduce the κ_l. Some of the studies succeeded in reducing thermal conductivity without affecting the conductivity and charge mobility through inserting carbon additives such as graphene and carbon nanotubes[73, 76-78]. Through tunnelling barriers composite structures with interfaces between participations and semi-conductors, energy filtering effect can enhance the power factor ($\sigma\alpha^2$). Several studies successfully enhanced the power factor through composite structures like Y_2O_3 incorporation in BiSbTe, SiO_2 in BiSbTe, Al_2O_3 in $Bi_2Se_{0.3}Te_{2.7}$, SiC in $Bi_{0.3}Sb_{1.7}Te_3$, ZnO in $Bi_{0.5}Sb_{1.5}Te_3$, InSb in $Bi_2Te_{0.7}Se_{0.3}$, Sb_2O_3 in $Bi_{0.5}Sb_{1.5}Te_3$ and Zn_4Sb_3 in $Bi_{0.4}Sb_{1.6}Te_3$[79-86].

In this chapter, the effectiveness of MgB_2 incorporation on the thermoelectric properties of $Mg_{3.2}Sb_{1.5}Bi_{0.49}Te_{0.01}$ is investigated by the inspiration of the energy filtering effect. MgB_2 nanoparticles are dispersed in the $Mg_{3.2}Sb_{1.5}Bi_{0.49}Te_{0.01}$ matrix supporting

the charge carrier scattering. As a consequence of Hall measurements the difference of charge carriers observed as negligible with the MgB_2 addition. Besides, an enhancement in Seebeck coefficient with a reduction in thermal conductivity is achieved, resulting in a high zT of 1.9 at high temperatures.

4.2 Crystal Structure

The Mg_3Sb_2 adopts the trigonal layered $CaAl_2Si_2$ structure with space group of P-3m1. Three individual atom sites are present in the asymetric unit cell as Mg1 (0, 0, 0), Mg2 ($^1/_3$, $^2/_3$, 0.6339), and Sb ($^1/_3$, $^2/_3$, 0.2283)[87]. The Mg atoms placed in two individual Wyckoff positions; first are positioned at the 1a site which represent the interlayer Mg1 atoms octahedrally coordinated with six neighbouring Sb atoms, sustaining a bond distance of 3.12 Å. Second, the Mg2 atoms located at the 2d site surrounded by four Sb atoms within a distorted tetrahedral environment with bond distances of 2.82-2.86 Å elongated along the z-direction, slightly[88, 89]. While the Mg2 atoms forms an anionic $[Mg_2Sb_2]^{2-}$ layer with Sb atoms, Mg1 atoms forms a cationic Mg^{2+} layer between the anionic frameworks as presented in the Figure 4.1[53, 57, 90-92]. In this case, the frameworks are responsible for the complex crystal structure with high hole mobility, while cation layers providing the low thermal conductivity combined with a good tunability. These behaviors result in phonon glass and electron-crystal structure together called as phonon-glass electron crystal concept (PGEC).

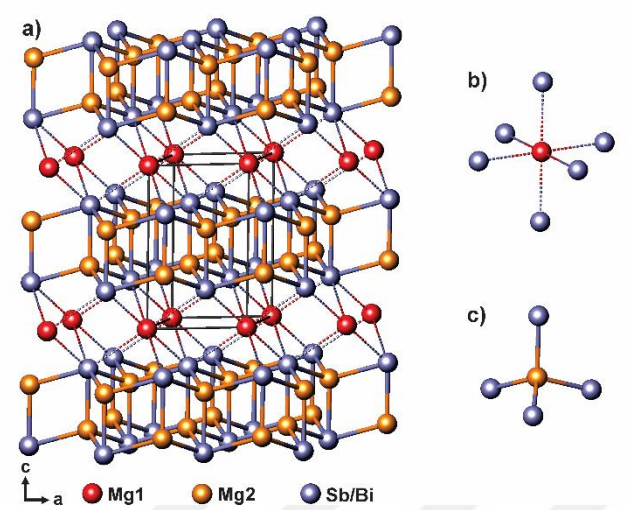

Figure 4.1.The crystal structure of Mg_3Sb_2 with $Mg1^{2+}$ cationic layer and $[Mg2_2Sb_2]^{2-}$ with the ionic interaction between them. B) Octahedral coordination of Mg1 with six equal Mg1-Sb bonds, almost perfectly. c) Slightly distorted tetrahedral coordination of Mg2 with three long and one short Mg2-Sb bonds.

4.3 Phase Diagram and Defect Mechanism

The binary phase diagram of Mg-Sb system with two polymorphs; α-Mg_3Sb_2 and β-Mg_3Sb_2 is presented in Figure 4.2a. The phase transition from α-Mg_3Sb_2 phase to β- Mg_3Sb_2 occurs at 1198.15 ± 5 K[93]. In the case of α-Mg_3Sb_2 the elemental Mg and α-Mg_3Sb_2 phase exist together for Mg-rich region, while the Sb-rich region is characterized by the presence of elemental Sb and α-Mg_3Sb_2. The stability of the system against the precipitation of elemental Sb and Mg as well as the conditions of the crystal-grown mechanism determine the lower and upper boundaries of the chemical potential (μ_i)[91].

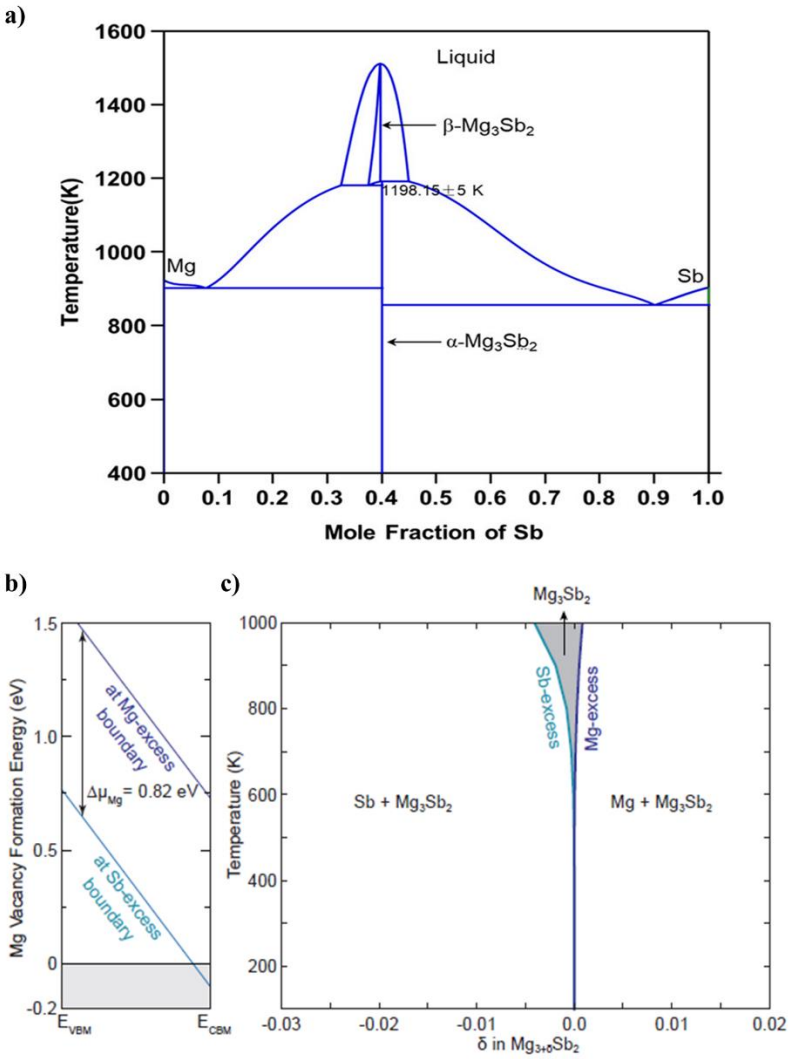

Figure 4.2. a) The phase diagram of Mg-Sb system, b) The formation energy of Mg vacancies showing that in the Sb-excess region blocking effect of Mg vacancies to bring the fermi level to the conduction band related to negative formation energy and high formation energy on the Mg-excess region, c) The phase diagram of Mg-Sb and phase boundaries with Sb-excess and Mg-excess solubility limits.

Figure 4.2b and c shows the phase diagram near α- phase Mg_3Sb_2 and its effect on the defect formation. The phase boundaries and stoichiometry determine the formation of defects at thermodynamics equilibrium conditions[94]. Mg_3Sb_2 can either have Sb vacancies or Mg vacancies depending on the stoichiometry. When the Mg vacancy is the dominant defect, V_{Mg}^{2-} ($Mg_{Mg} \Rightarrow V_{Mg}^{2-} + 2h^+$) acts as electron acceptor and results in excess holes h^+. As given in Figure 4.2b, the formation energy of V_{Mg}^{2-} defects becomes more

negative with increase in the Fermi level. When the formation energy becomes negative, the defect forms spontaneously. Even with *n*-type doping strategy to increase Fermi level led to formation of vacancies as electron acceptor. Therefore, the material behave like *p*-type all the time, as observed before for Mg_3Sb_2. As presented in Figure 4.2c, although it is expected to achieve a line Mg_3Sb_2 phase, in reality, due to the Mg vacancies, Mg_3Sb_2 phase is expanded the narrow compositional range. Because of the higher defect energy of Mg interstitials, the extension is less at the Mg-excess region. Since the Mg vacancy defect is more favourable around the Sb-excess boundary compared to the Mg-excess boundary, starting with excess amount of Mg in the stoichiometry can restrict the formation of vacancies with positive formation energy[45, 90].

Several studies have been investigated the reason behind the formation of *n*-type Mg_3Sb_2. The defect energy estimations revealed that the Mg vacancy suppress instead of Mg interstitials[89]. To achieve a good thermoelectric performance, it is significant to achieve high carrier concentration, which can be obtained through elevated Fermi level, E_F toward the conduction band edge, E_{CBM}. Figure 4.3 represents the defect formation energies of different defects calculated by differential functional theory (DFT) with Te doping. As shown, for both Sb and Mg-excess cases, the Fermi level becomes higher with Te doping. However, because of the defect formation it is pinned in a lower level in case of Sb-excess condition. On the other hand, with the increase in V_{Mg} defect, formation of Mg vacancy restrained, and lead to increase in E_F and Te concentration[45]. Therefore, it enhances the *n*-type thermoelectric properties. Another study[91] has been discussed the reason behind the *n*-type character through offsetting the electronic charge of the defect complex $(V_{Mg2} + Mg_i)^{1-}$.

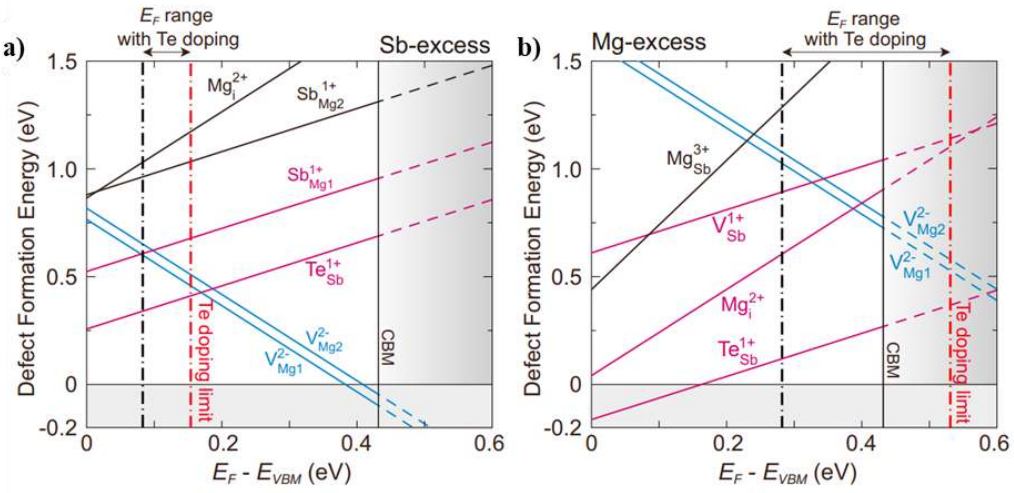

Figure 4.3. a) Defect formation energies of intrinsic point defects as well as the extrinsic defect Te-Sb under Sb-excess (ΔμSb¼ 0) and b) Mg-excess conditions[89].

4.4 Band Structure and Electronic Properties

The electrical transport properties are significantly dependent on the band structure, band degeneracy and band effective mass. The electronic band structure of Mg_3Sb_2 has been studied by several groups through DFT calculations. Figure 4.4a represents the density of states and the electronic band structure of Mg_3Sb_2[88]. The band gap is realized as 0.6 eV with the conduction band minimum at the CB1 point and at the K point, while valence band maximum at the Γ point[95]. On the other hand, the band gap is estimated as 0.5 eV through mBJ functional as several studies claimed[54, 96, 97]. According to the DFT calculation Sb-s and Sb-p character is responsible from the occupied states from -10 eV to E_F. And, Mg2-p orbitals are also contributing to the valence band. On the other hand, Mg s and p orbitals are mainly determining the conduction band, above the E_F with some mixing Sb-p orbitals. The contribution of mixing orbitals both in conduction and valence bands is coming from the covalent relations in between Sb and Mg atoms [88]. As shown in Figure 4.4a, CB_1 point along the M^* and L^*, which is called U^*corresponds to the conduction band minimum (CBM)[42] and the valence band maximum(VBM) is located at the Γ point with orbital splitting[53, 98]. While the U^* point is a low symmetry point with six-fold degeneracy N_v=6, the Γ point with high symmetry shows low degeneracy with N_v=1[99, 100]. Therefore, while *n*-type Mg_3Sb_2 is more promising to control the

thermoelectric properties, *p*-type counterpart of Mg_3Sb_2 presents weaker transport properties. Both the experimental and theoretical studies have been revealed the valley degeneracy of *n*-type and *p*-type Mg_3Sb_2[46, 101, 102]. Figure 4.4b displays the schematic illustration of the complex Fermi surfaces both on CBM with six valley degeneracy for *n*-type Mg_3Sb_2 and on VBM with one valley degeneracy for *p*-type Mg_3Sb_2.

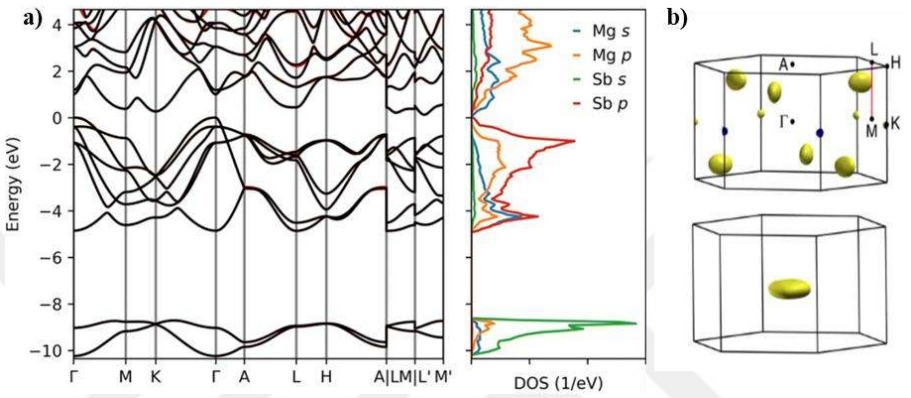

Figure 4.4. a) Electronic band structure and density of states (DOS) of Mg_3Sb_2 and b) schematic view of the complex Fermi surfaces for both *n*-type (on CBM with six valley degeneracy) and *p*-type (on VBM with one valley degeneracy) Mg_3Sb_2.

As discussed in the theory, the electronic transport properties are related to curvatures of bands at the band edges and degeneracy. Both Seebeck coefficient and weighted mobility values ($\mu(m_d^*/m_e)^{3/2}$, where m_e is the electron mass, are dependent on the density states of effective mass m_d^* which is directly proportional to valley degeneracy, N_v[103]. To understand the electronic transport characteristic of Mg_3Sb_2, the valley degeneracy should be considered. For *n*-type Mg_3Sb_2, conduction band valley engineering and for *p*-type valence band valley engineering can be studied[54]. Figure 4.5a shows the Mg1-s, Mg2-s, and Sb-p orbitals on the band structure of Mg_3Sb_2 conduction band minimum. As shown, the dependency of Mg2-s orbitals on the K-point is higher than the dependency of Mg1-s orbitals, and Mg2-s Sb-p bonding mainly effect the first CBM. Hence, the CBM on the first level can be controlled by changing the bond character[42, 54]. Through reducing the crystal lattice by substituting the Sb with isoelectronic elements, the band strength can be enhanced. Another way is to tune the CBM via introducing of ionic dopants in Mg site[53].

In case of *p*-type Mg_3Sb_2, by decreasing the crystal field splitting energy which is defined as $\Delta = E(\Gamma(px,y)) - E(\Gamma(pz))$, the electronic transport properties can be enhanced

through orbital engineering or valence band engineering theory. Figure 4.5b illustrates the crystal field splitting effect and orbital engineering on the valence band maximum for $CaAl_2Si_2$ structure likewise Mg_3Sb_2. The interlayer distances, length and the angle of the bonds, lattice parameters are effective on the crystal field splitting energy. Therefore, several strategies such as alloying, solid solution formations and doping can be applied to adjust the splitting energy [104].

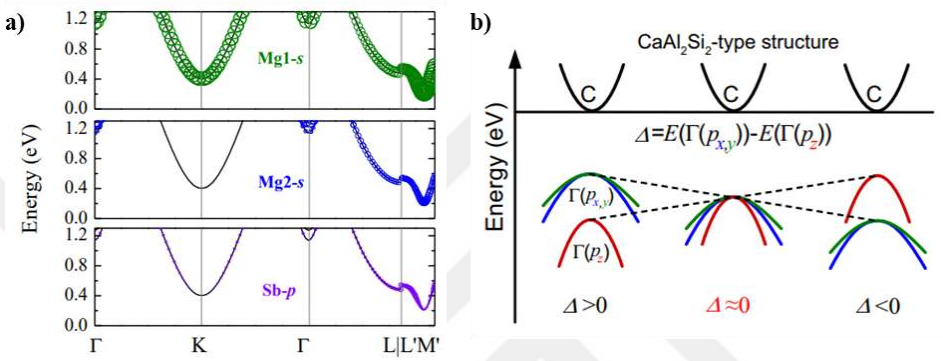

Figure 4.5. a) The CBM of Mg_3Sb_2 with detailed band structures, where circles representing the characteristic weight of Mg1-s, Mg2-s, and Sb-p orbitals, and b) schematic view of crystal field splitting effect on the p orbitals at the Γ point[54, 104].

4.5 Thermal Properties

In contrast to electrical conductivity, a low thermal conductivity is significant to achieve good thermoelectric properties. One way to decrease thermal conductivity without affecting the electrical conductivity is diminishing the lattice thermal conductivity. Low lattice thermal conductivity is obtainable via strong lattice anharmonicity, which is related to weak chemical bonding[105, 106].

Zhang et al., have shown that the lattice thermal conductivity of Mg_3Sb_2 is almost isotropic along with similar thermal conductivity values along a and c axes. When the response of phonon frequencies to volume change is investigated, a ratio of 1.2 is observed along the a and c axes[92].

Another reason of the low lattice thermal conductivity is low phonon velocity, v, and lower phonon relaxation time, τ[107, 108]. The phonon velocities can be determined by the speed of sound or calculated phonon dispersion. The atom projected density of states

(DOS) and the phonon dispersions of Mg_3Sb_2 is given in Figure 4.6. Stemming from the two different Mg sites, a significant difference is observable in local bonding environment. Coming from the low phonon frequencies of octahedrally coordinated Mg-1 atoms, it can be assumed the bond between Mg-1 and Sb is softer than the bond between Mg-2 and Sb. The Umklapp scattering and point defect scattering which are estimated as $\tau \propto \frac{1}{\omega^2}$, and, $\tau \propto \frac{1}{\omega^4}$, are strongly dependent on the phonon frequencies[109]. Therefore, low frequency phonons led to long mean free paths[110].

The lattice thermal conductivity can be optimized through nanoscale participations, boundary scattering defects and introducing atomic scale defects for mid, low and high frequency phonons[111]. As given in Figure 4.6a, Mg_3Sb_2 has soft transverse acoustic phonon modes at the M (~0.71 THz), L (~0.81 THz), and A (~1.04 THz) points with large mode Grüneisen parameters[89, 112]. There are studies focusing on the softening of phonon modes to reduce the phonon velocity resulting in a low lattice thermal conductivity[113].

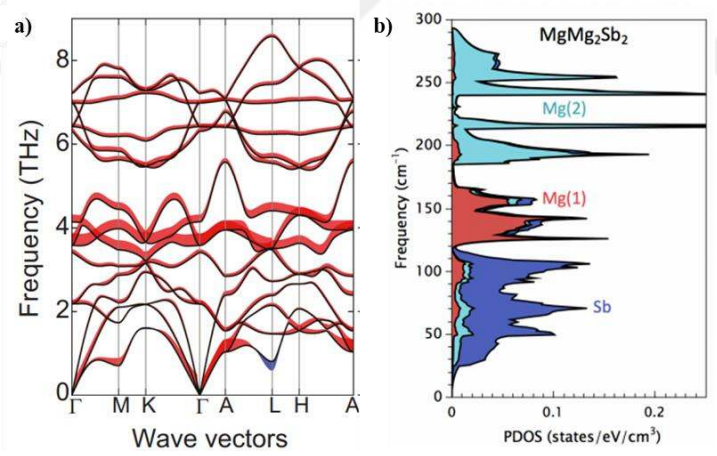

Figure 4.6. a) Calculated phonon dispersion with a curve width colored in red and blue showing the positive and negative mode Grüneisen parameters showing the relative magnitude of the mode Grüneisen parameter and b) DOS of Mg_3Sb_2[89].

From the phonon spectrum and DOS, the lattice thermal conductivity can be driven as,

$$\kappa_l = A\frac{\bar{M}{\Theta_D}^3 {V_{per}}^{1/3}}{\gamma^2 n^{2/3} T} \tag{4.1}$$

where A is a physical constant 3.1×10^{-6}, $\bar{M}$, Θ_D, V_{per} , n and γ are the average atomic mass, the Debye temperature, the volume per atom, the number of atoms in the primitive cell and the Grüneisen parameter, respectively. γ is a significant parameter for estimating the lattice thermal conductivity, increasing the γ result in a decrease in κ_l. It is mostly contributed the low κ_l of Mg_3Sb_2[114]. Through taking the derivative of the phonon frequencies regarding the volume, Grüneisen parameters which reveals the anharmonicity can be achieved[98].

4.6 Sample Preparation

In this chapter, intermetallic compounds of $Mg_{3.2}Sb_{1.5}Bi_{0.49}Te_{0.01}$ were synthesized by high energy ball mill (SPEX 8000D Mixer/Mill, 1425 rpm) utilizing mechanical alloying. Throughout the synthesis and sintering procedures, all sample manipulations were performed within an Ar-filled glove box to prevent oxidation. All the high purity raw materials of magnesium powder (Mg, 99.8%; Alfa Aesar), bismuth pieces (Bi, 99.999%; Alfa Aesar), antimony shots (Sb, 99.999%; Alfa Aesar), tellurium pieces (Te, 99.9999%; AlfaAesar) were used without further purification. Stoichiometric proportions of these elements regarding the nominal composition were loaded into a stainless steel vial along with two half-inch stainless steel balls and sealed under Ar. Mechanical alloying was executed for a duration of two hours. To incorporate MgB_2, varying quantities (0.05, 0.1, 0.2, 0.3 and 0.4 wt. %) of MgB_2 powder were added to achieved $Mg_{3.2}Sb_{1.5}Bi_{0.49}Te_{0.01}$ powder within a stainless steel vial under Ar atmosphere, followed by an additional hour of ball milling to obtain the composite material. Following, the resulted powders were transferred into a graphite die and pressed by cold press under Ar. SPS was applied under a uniaxial pressure of 50 MPa for 2 minutes at 1023 K under vacuum conditions, to consolidate the achieved powders.

To analyse the phase purity and the chemical composition, X-ray diffraction (XRD) analysis via Rigaku Mini Flex 600 (Cu K_α (λ= 1.5406 °A), 40 kV voltage and 15 mA current). was employed. Scanning Electron Microscopy (SEM) and Energy Dispersive X-ray Spectroscopy (EDS) analyses were utilized for identification of the morphology and elemental compositions of the samples, respectively, utilizing a Zeiss Ultra Plus Field Emission Scanning Electron Microscope. Wavelength dispersive X-ray spectroscopy

(WDS) analysis was conducted on an electron microprobe (Cameca SX 100, tungsten cathode) taking into account the line compound Mg_2Si and certificated elements of Sb, Bi and Te as references, to determine the accurate chemical compositions. The high-resolution transmission electron microscopy (HR-TEM) and selected area electron diffraction (SAED) were adopted on samples using the Talos F200S scanning/transmission electron microscope (S/TEM) operating with a maximum acceleration voltage of 200 kV.

The electrical and thermal transport properties of the samples were examined within a temperature range 330-623 K. For the thermal diffusivity, D, measurements, Netzsch LFA 467 equipment was employed on disc-shaped samples (10 mm in diameter). Seebeck coefficient and electrical conductivity measurements were measured using an Ulvac ZEM-3 device on bar-shaped samples.

4.7 Characterization

4.7.1 Crystal structure and phase analysis

The crystal structure and phase purity characterizations were performed for $Mg_{3.2}Sb_{1.5}Bi_{0.49}Te_{0.01}$ samples processed by spark plasma sintering, along with various proportions of MgB_2 addition (wt.% = 0, 0.05, 0.1, 0.2, 0.3, 0.4). Figure 4.7 represents the XRD pattern of pristine and MgB_2 incorporated samples. The peaks corresponding to the main phase for all samples are indicative of the trigonal Mg_3Sb_2 crystal structure within the $P\bar{3}m1$ space group. The results indicate that both the pristine and those with MgB_2 added samples were obtained in a pure state, as no secondary phase was observed in either sample set. On the other hand, because of the larger ionic radii of Bi^{3-} (1.93 Å) in comparison to Sb^{3-} (1.88 Å), the substitution of Bi^{3-} into the Sb^{3-} sites shifts peak positions towards lower 2θ values resulting in higher lattice parameters.

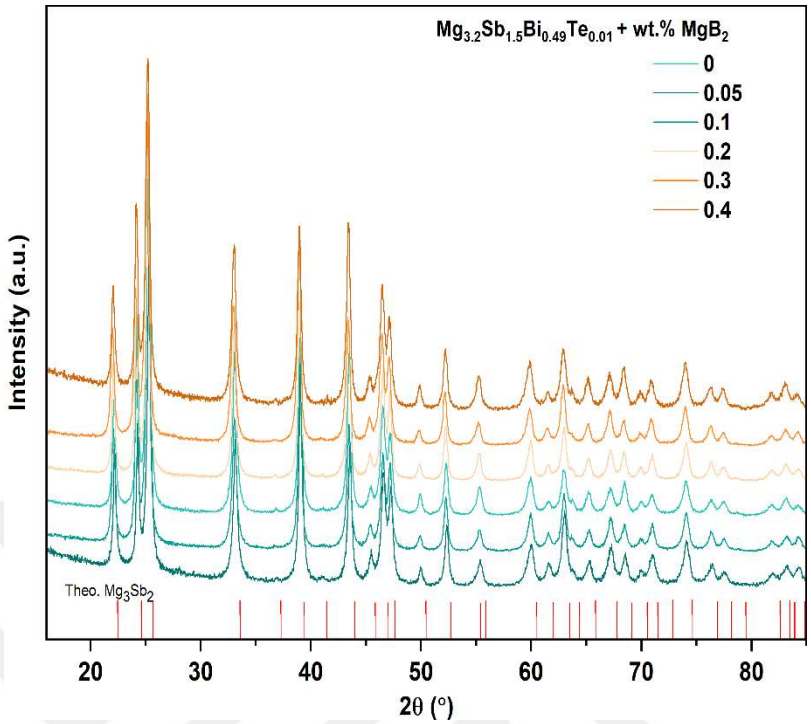

Figure 4.7. XRD patterns (Cu-K_α radiation) of MgB_2 incorporated $Mg_{3.2}Sb_{1.5}Bi_{0.49}Te_{0.01}$ (wt.% = 0, 0.05, 0.1, 0.2, 0.3, 0.4).

4.7.2 Phase and Microstructure Analysis

SEM, EDX, HR-TEM and WDX analyses were performed for further examination of the microstructure and chemical composition. SEM measurements were applied for microstructural analysis. Figure 4.8 presents BS-SEM images of pristine $Mg_{3.2}Sb_{1.5}Bi_{0.49}Te_{0.01}$ samples before and after etching, as well as samples containing 0.1 and 0.3 wt.% MgB_2. From the images without etching process (Figure 4.8a, b, c) the grain sizes are observed to be approximately 6-7 μm. However, larger grains and more grain boundary like structures are detected after etching (Figure 4.8d, e and f). In addition, irregularly shaped oval impurities are present, believed to originate from oxidized Mg on the surface. Acid etching, especially at high-energy grain boundaries and air-sensitive elemental Mg residues, has led to oxidation, causing spots and large grain boundaries observed in the SEM images. The contrast seen in the BSE-SEM images, show the existence of at least three different phase in the microstructure, which correspond to

individual phases of a slightly Bi-deficient phase, a slightly Bi-excess phase and impurity phase as small black spots.

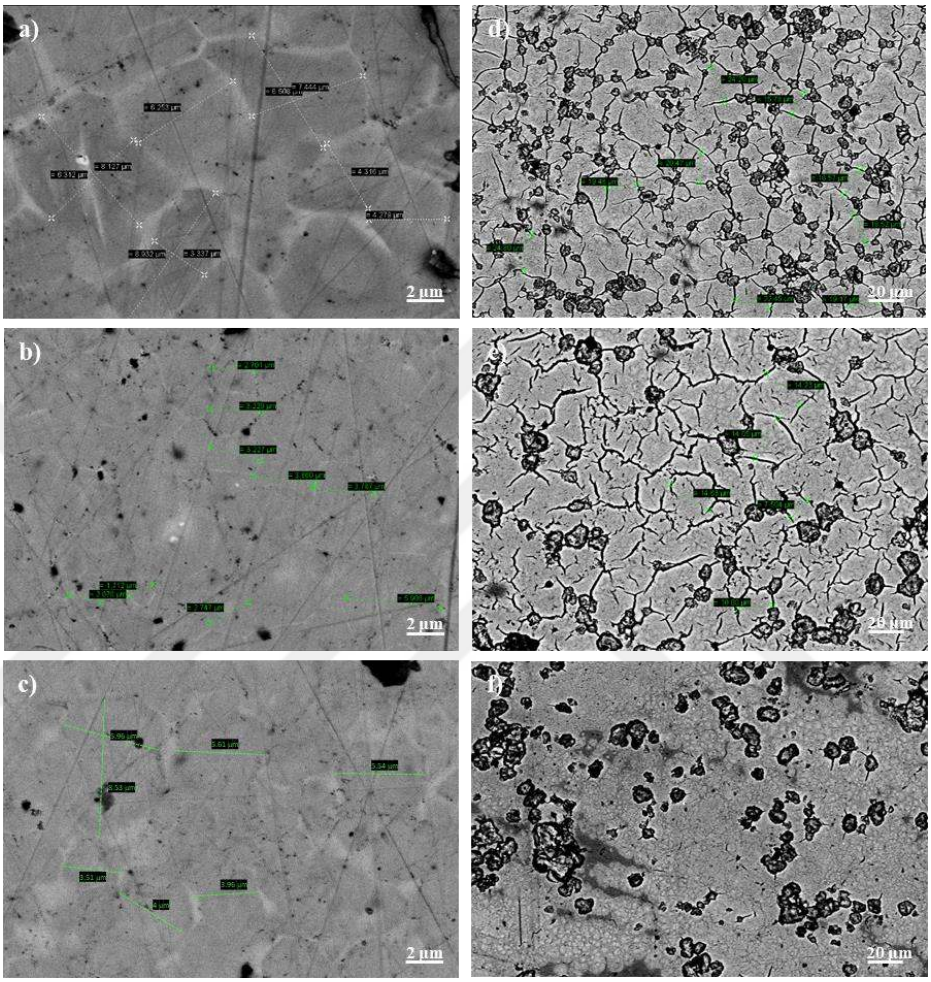

Figure 4.8. BSE-SEM images of a,b,c) MgB_2 incorporated $Mg_{3.2}Sb_{1.5}Bi_{0.49}Te_{0.01}$ before etching (wt.% = 0, 0.1, 0.3) and d, e, f) after etching (wt.% =0, 0.1, 0,3).

Because of the difficulty to observe grain boundaries and grains via SEM analysis, polarized light optical microscopy images were taken to be able to obtain more recognizable grain size determination for composite samples where x= 0, 0.1 and 0.3 as shown in Figure 4.9 a, b and c. The change in the grain sizes are clearly noticeable with alternating amounts of MgB_2 addition. The average grain sizes of samples are calculated by applying the line intercept method, d=l/N, where d is the grain size, l is length of test line and N is the number of grains intercept. As a result, grain size of 8, 4.5 and 6.7 µm are achieved for x wt.% MgB_2 (x=0, 0.1 and 0.3) incorporated samples, respectively.

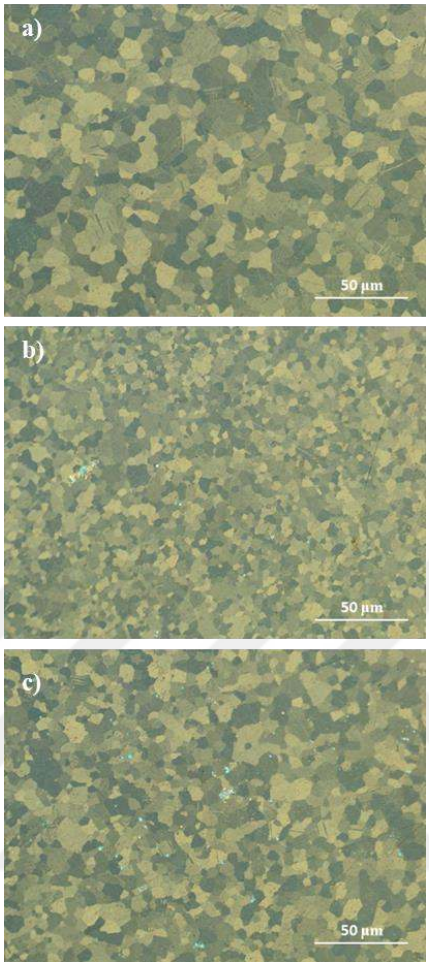

Figure 4.9. Polarized light optical microscopy images of pristine and MgB_2 incorporated (wt.% = 0, 0.1, 0.3) samples.

For further investigation of the different phases observed from the BS-SEM images, EDX analysis and mapping was employed. The EDX analysis was taken from the spots given in Figure 4.10 from the $Mg_{3.2}Sb_{1.5}Bi_{0.49}Te_{0.01}$ sample, with 0.1 wt. % MgB_2 addition. Mg, Sb, Bi and O atoms are detected from the overall map. Since Mg is air sensitive, the waiting time under air and metallographic treatments result in a slight oxidation for Mg_3Sb_2 based materials.

The atomic percentage of each element in the selected areas are examined in the Table 4.1. The first and second point selected from the, the black points observed in BS-SEM images mostly contains elemental Mg, since the atomic weight of it relatively light compared to other elements in the microstructure, it presents as darker spot. Compared to

the grains, it is observed that brighter areas of grain boundaries contain more Bi amount compared to the Sb amount.

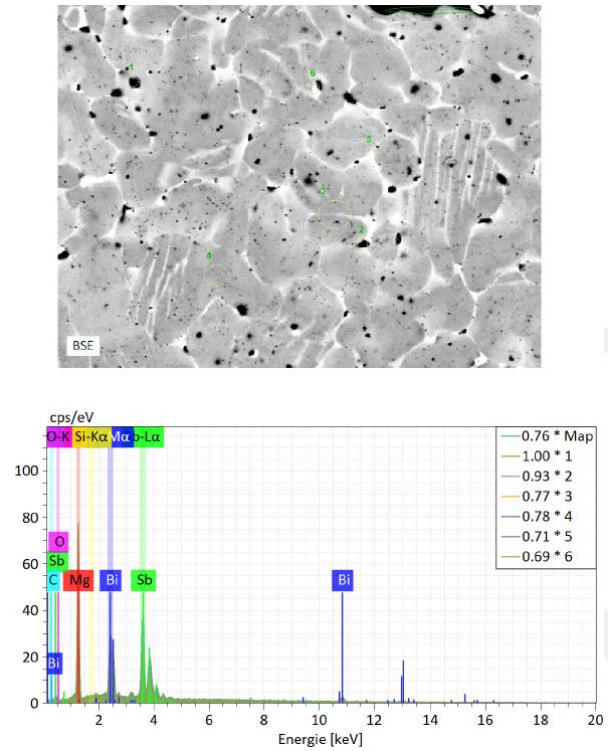

Figure 4.10. Selected spots where EDX analysis applied and EDX graph corresponding to the achieved elemental energy levels for the $Mg_{3.2}Sb_{1.5}Bi_{0.49}Te_{0.01}$ sample, with 0.1 wt.% MgB_2 addition.

Table 4.1. The EDX analysis results of $Mg_{3.2}Sb_{1.5}Bi_{0.49}Te_{0.01}$ sample.

Nominal $Mg_{3.2}Sb_{1.5}Bi_{0.49}Te_{0.01}$			
Spot #	**At. %**		
	Mg	**Sb**	**Bi**
1	73.61	20.60	5.79
2	75.78	19.23	5
3	61.52	31.02	7.47
4	62.13	30.57	7.30
5	61.44	27.66	10.90
6	63.18	24.89	11.93

SEM images and EDS elemental mapping of $Mg_{3.2}Sb_{1.5}Bi_{0.49}Te_{0.01}$ sample, with 0.1 wt. % MgB_2 addition given in Figure 4.11 reveal the elemental distribution of Mg, Sb, Bi, with black spots corresponding to the lightweight elements of Mg. The detection of B was not possible because of its low concentration and low weight. The elemental secondary phases are primarily detected around grain boundaries which contains elemental Mg. It is assumed that it comes from the addition of MgB_2. On the other hand, for the pristine sample while the phase differences are observable between the grain boundaries and grains, there was no obvious precipitation of Mg element in the EDS elemental mapping Figure A 1.

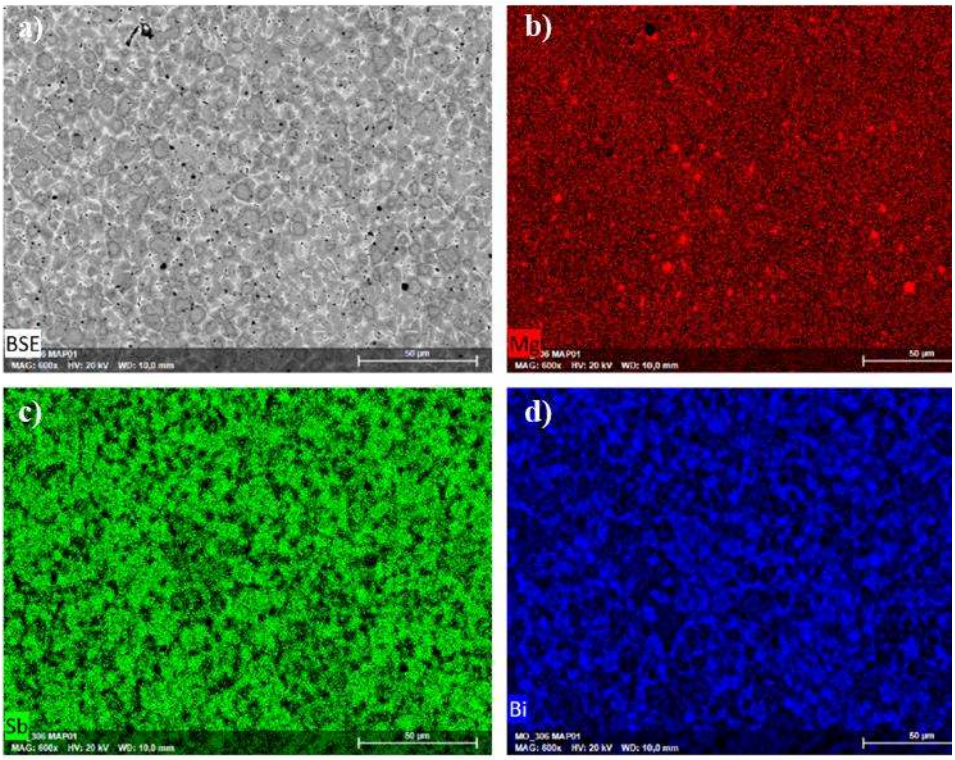

Figure 4.11. EDS elemental mapping of the $Mg_{3.2}Sb_{1.5}Bi_{0.49}Te_{0.01}$ sample, with 0.1 wt.% MgB_2 addition.

WDS analysis was applied for pristine and $Mg_{3.2}Sb_{1.5}Bi_{0.49}Te_{0.01}$ sample, with 0.1 wt. % MgB_2 samples as well for a more accurate identification of the composition. Figure 4.12 represents the BSE images of $Mg_{3.2}Sb_{1.5}Bi_{0.49}Te_{0.01}$ with 0.1 wt.% MgB_2 sample with the selected ten different points as an example. To ascertain the overall composition,

WDS analysis was conducted in ten different areas across the sample. Consequently, the average chemical composition was determined to be $Mg_{3.15}Sb_{1.56}Bi_{0.48}Te_{0.01}$ for 0.1 wt.% MgB_2 added sample, and for the pristine sample it is achieved as $Mg_{3.12}Sb_{1.59}Bi_{0.47}Te_{0.01}$ (Figure A 2).

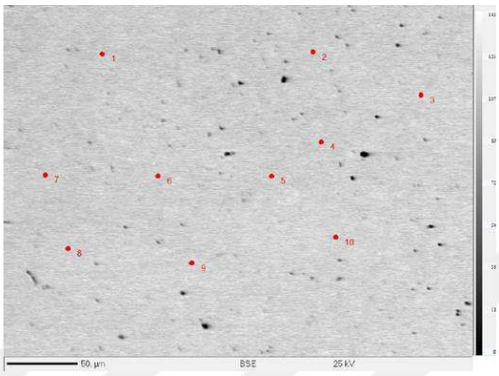

Average on 10 points								
	Weight%	Dev_Wt	NormWeight %	Dev Norm Wt	Atomic%	Dev_At	Det.Lim (Ancey)	StdDev wt%
Sb	51.80	0.71	51.57	0.55	30.02	0.46	180.	0.13
Mg	20.85	0.23	20.75	0.25	60.51	0.41	63.	0.06
Bi	27.39	0.37	27.27	0.36	9.25	0.11	378.	0.09
Te	0.42		0.41		0.23		39.	
Total	100.46		100.00		100.00			

Figure 4.12. Ten different spots that WDS analysis was conducted on $Mg_{3.2}Sb_{1.5}Bi_{0.49}Te_{0.01}$ with 0.1 wt.% MgB_2 addition.

STEM images of samples with 0.1 wt.% MgB_2 incorporation and $Mg_{3.2}Sb_{1.5}Bi_{0.49}Te_{0.01}$ without addition are provided in Figure 4.13a and b for further examination of microstructure and secondary phases. Following the inclusion of MgB_2, distinct grains are observed in the material, with grain sizes approximately 1 µm in diameter. In the sample without addition, elongated grains are visible, with smaller grain sizes compared to the sample with MgB_2 addition. Additionally, Figure 4.13a highlights the grouping of secondary phases, particularly at grain boundaries. This observation points out the idea of the dispersion of MgB_2 addition throughout the microstructure, especially along grain boundaries. Consequently, lower thermal conductivity values are expected due to phonon scattering in the secondary phases.

Figure 4.13c and d the HR-TEM image of $Mg_{3.2}Sb_{1.5}Bi_{0.49}Te_{0.01}$ sample with 0.1 wt.% MgB_2 incorporation is presented. Depending on the phase difference HR-TEM

image reveals different lattice spacing. A lattice fringe with spacing of around 0.34nm was achieved from the Figure 4.13c, corresponding to the (011) plane of Bi-deficient phase of $Mg_{3.2}Sb_{1.5}Bi_{0.49}Te_{0.01}$.

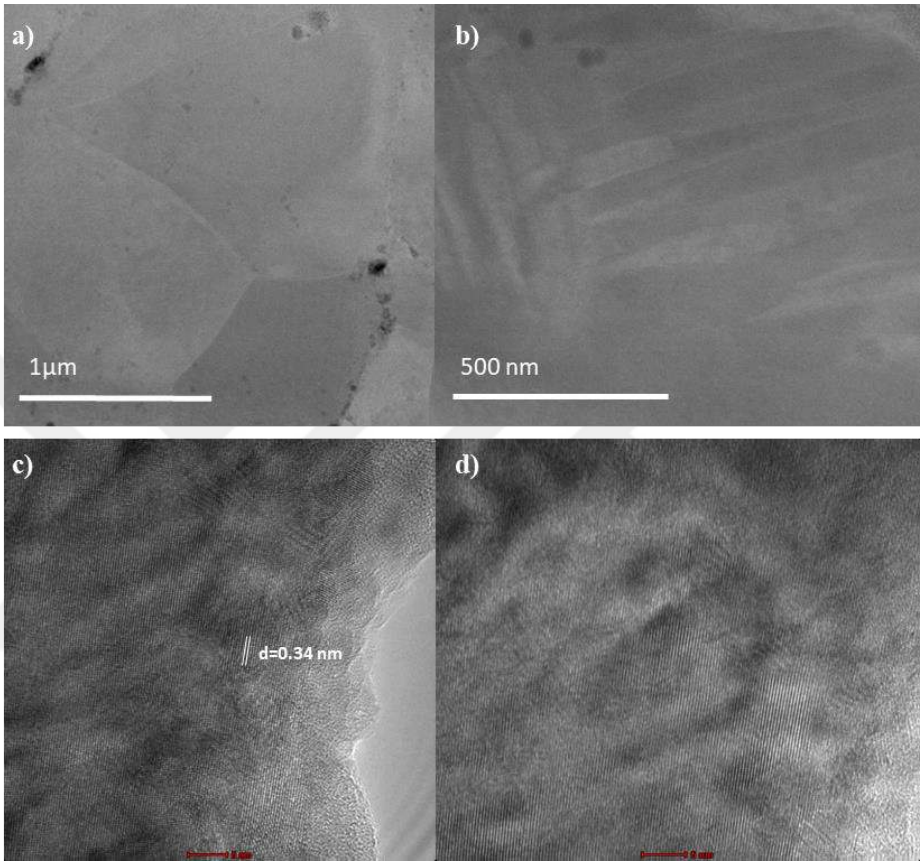

Figure 4.13. STEM images of a, b) (0.1 wt.% MgB_2 incorporated and pristine $Mg_{3.2}Sb_{1.5}Bi_{0.49}Te_{0.01}$) and c, d) HR-TEM image of 0.1 wt.% MgB_2 incorporated sample.

4.8 Transport Property Measurements

Figure 4.14a present the electrical resistivity values of the materials. The electrical resistivity values of the pristine material vary between approximately 2.5 and 4 mOhm.cm as the temperature increases from room temperature to intermediate temperatures. Relying on the temperature dependence of electrical conductivities, the pristine material shows an acoustic phonon scattering mechanism with the temperature dependence between $T^{-1.69}$-$T^{-1.82}$, and is not affected by the grain boundary resistance at low temperatures[59]. An increase in resistivity values at low temperatures is observed with

increasing temperature for pristine and 0.05, 0.1 wt.% MgB_2 incorporated samples, which is an examination of the electrical resistivity behavior of the material reveals that grain boundary resistivity is almost negligible. The temperature dependence of 0.05 and 0.1 wt.% MgB_2 composite materials also belongs the acoustic phonon scattering region with the dependence of $T^{-1.52}$-$T^{-1.76}$. This may be attributed to the change in the carrier scattering because of the secondary phases generated around grain boundaries. Spark plasma sintering at 1073 K has facilitated the attainment of higher grain sizes in the material[62]. Upon addition of MgB_2, an increase in electrical resistivity values is observed. This may be attributed to the reflective mechanism of a secondary phase and the creation of additional resistivity and decrease in the grain sizes. Additionally, microstructure analysis indicates lower grain size and a greater number of grain boundary-like defects in the composite materials. Previous studies have concentrated on investigating the effects of phenomena related to resistance at grain boundaries, where grains and grain boundaries behave like two different phases, resulting in a potential barrier and elevated electrical resistivity values, especially at room temperatures[65]. Moreover, the occurrence of high resistivity values at low temperatures, followed by a decrease and subsequent increase in resistivity at intermediate temperatures, is observed in samples with grain boundary resistivity[115, 116]. It is evident that after 0.2 wt.% MgB_2 incorporation, resistivity values start from higher values until 500K, following with an increasing trend. With the increased amount of MgB_2 incorporation, these impurities create potential barriers, particularly leading to an increase in electrical resistivity at low temperatures.

Figure 4.14b displays the Seebeck coefficients of $Mg_{3.2}Sb_{1.5}Bi_{0.49}Te_{0.01}$ materials with different weight percentages (wt. %) of MgB_2 addition (0, 0.05, 0.1, 0.2, 0.3, 0.4). The *n*-type behavior is indicated from Seebeck values for all samples. To see the effect of heating on the electronic performance of MgB_2 added samples heating-cooling cycle is also given in Figure A 3 for 0.1 wt.% addition. An increase in Seebeck coefficient is observed in the materials with MgB_2 incorporation compared to the pristine material, aligning with the increase in resistivity values and pointing to a decrease in carrier concentration. As evidence, Hall measurements are examined for pristine and 0.05, 0.1 and 0.2 wt.% MgB_2 incorporated samples, however, no diminution is observed in the carrier concentrations as given in Figure 4.14b. This correlation between the Seebeck coefficient and carrier concentration implies an effect similar to energy filtering. Also,

similar Seebeck coefficient values for materials with 0.2 and higher amounts of wt.% MgB_2 additions was achieved especially at elevated temperatures, where grain boundary scattering effect has a weak effect. This finding suggests that while the variance in electrical resistivity at low temperatures is connected to microstructure rather than carrier concentration, the overall reduction in resistivity could be attributed to the energy filtering effect. To investigate further, correlation between Seebeck coefficient and thermal conductivity is analyzed as given in Figure 4.14e. As discussed by Lin et al., samples exhibiting lower thermal conductivity demonstrate a greater Seebeck coefficient, indicating the significance of grain boundary Kapitza resistance in the energy filtering phenomenon[73].

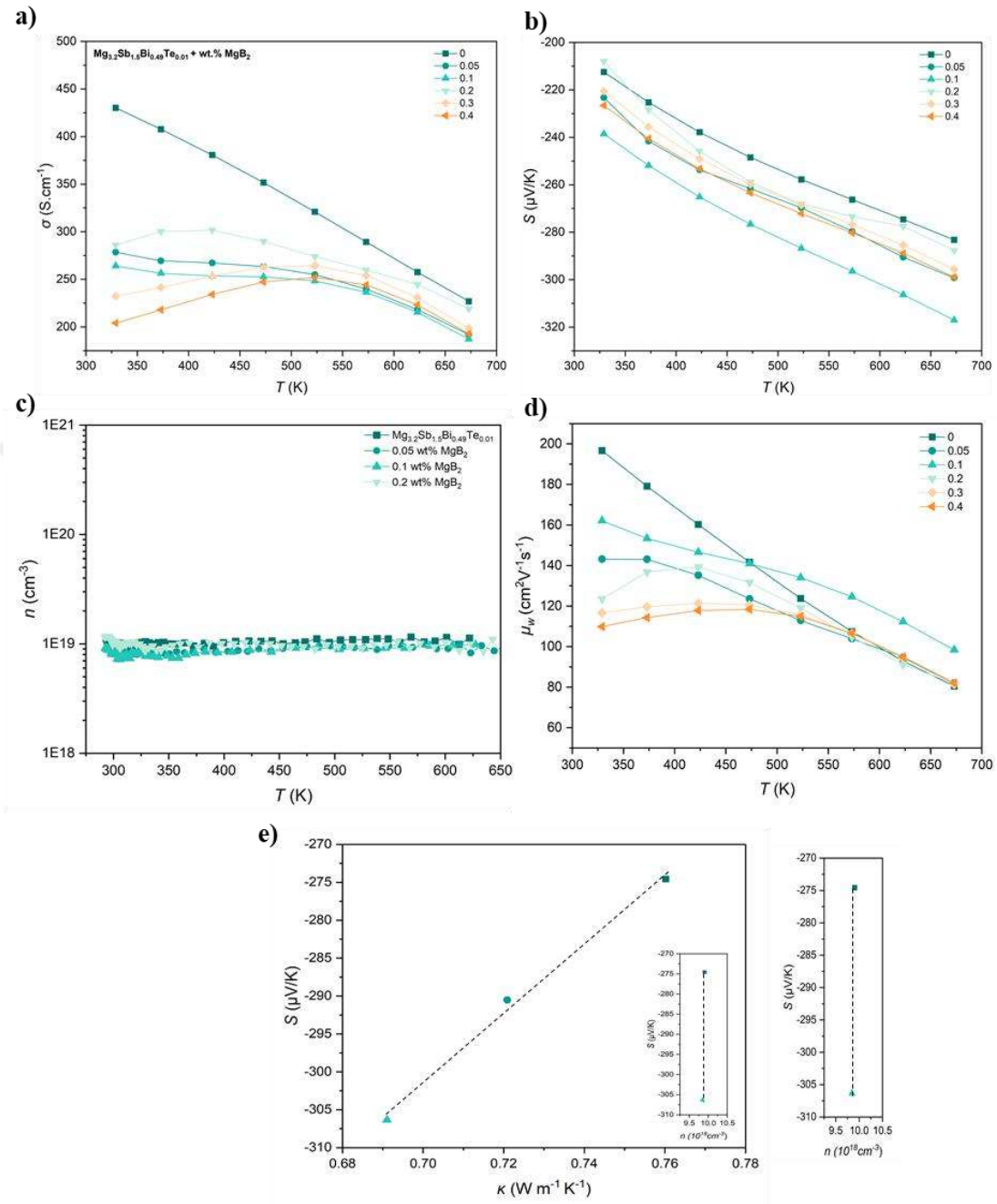

Figure 4.14. a) Electrical conductivity, b) Seebeck coefficient, c) carrier concentration (pristine and MgB_2 incorporated samples), d) weighted mobilitiy of pristine and x wt.% MgB_2 incorporated $Mg_{3.2}Sb_{1.5}Bi_{0.49}Te_{0.01}$ (x=0, 0.05, 0.1, 0.2, 0.3 and 0.4) samples, e) linear correlation between thermal conductivity and Seebeck coefficient of samples (x=0, 0.05, 0.1).

Using the Drude-Sommerfeld free electron model approximation the weighted mobility values of the samples were estimated from the experimental Seebeck coefficient

and resistivity data (Figure 4.14d) [117]. The weighted mobility is a substantial property to determine the electronic properties of thermoelectric materials [4, 117, 118]. After MgB_2 incorporation, there was a consistent decrease in all weighted mobility values, reaching a range of 110-165 $cm^2V^{-1}s^{-1}$ at 323 K. This is mostly related to the change in the scattering mechanism as observed from the Figure 4.14a, where the conductivity values become more dependent to the temperature with addition of MgB_2. On the other hand, after 473 K the weighted mobility of MgB_2 (0.1 wt.%) is superior compared to the pristine sample, which supports the enhancement of electronic properties. The Hall mobility measurements show similar trend after 473 K, however, while measurement is stable for MgB_2 added samples, it shows instability for the pristine sample (Figure A 4).

Figure 4.15 presents total, electronic and lattice thermal conductivities of the samples. The thermal conductivity values of samples with and without MgB_2 are in tendency to decrease with increasing temperature. Measurements indicate that additions up to 0.3 wt.% reduce the thermal conductivity of the material, while an increase in thermal conductivity is observed with 0.3 wt.% and 0.4 wt.% additions. Similar disturbance of the trend is observed by Lin et al., which stated as the achievement of a threshold after a certain amount of addition, where supported by the results of other studies conducted with energy-filtering strategy[76, 78]. As a result, low electrical conductivity, and high thermal conductivity values are achieved due to thermal shorting related aggregation or percolation of nano-materials addition[73]. Since the MgB_2 has notable thermal conductivity, reaching 25 $Wm^{-1}K^{-1}$, the integration of higher concentrations of MgB_2 into composite materials leads to elevated thermal conductivities by fostering the development of continuous networks[119]. Figure 4.15b and c show lattice thermal conductivity and electronic thermal conductivity values, respectively. Lattice thermal conductivity values contribute more dominantly to the total thermal conductivity values. A decrease in electronic thermal conductivity is observed proportional to the decrease in resistivity, which can be attributed to carrier scattering/filtering stemmed from created interfaces between MgB_2 and main phase[85]. In addition, while additions up to 0.3 wt.% are ineffective for phonon scattering, an increase in lattice thermal conductivity values is observed after that point. This can be explained using SEM images of etched samples. In the sample of the main material in Figure 4.8d, impurities and defects that would act more like reflective mechanisms are observed, especially line defects are

almost absent for the sample with 0.3 wt.% MgB_2 addition shown in Figure 4.8f. Therefore, lattice thermal conductivity and total thermal conductivity increase after the 0.3 wt.% level. In samples with 0.1 wt.% MgB_2 addition, total thermal conductivity values show approximately a 10% decrease at intermediate temperatures. This reduction can be attributed to mainly energy filtering/carrier scattering effect.

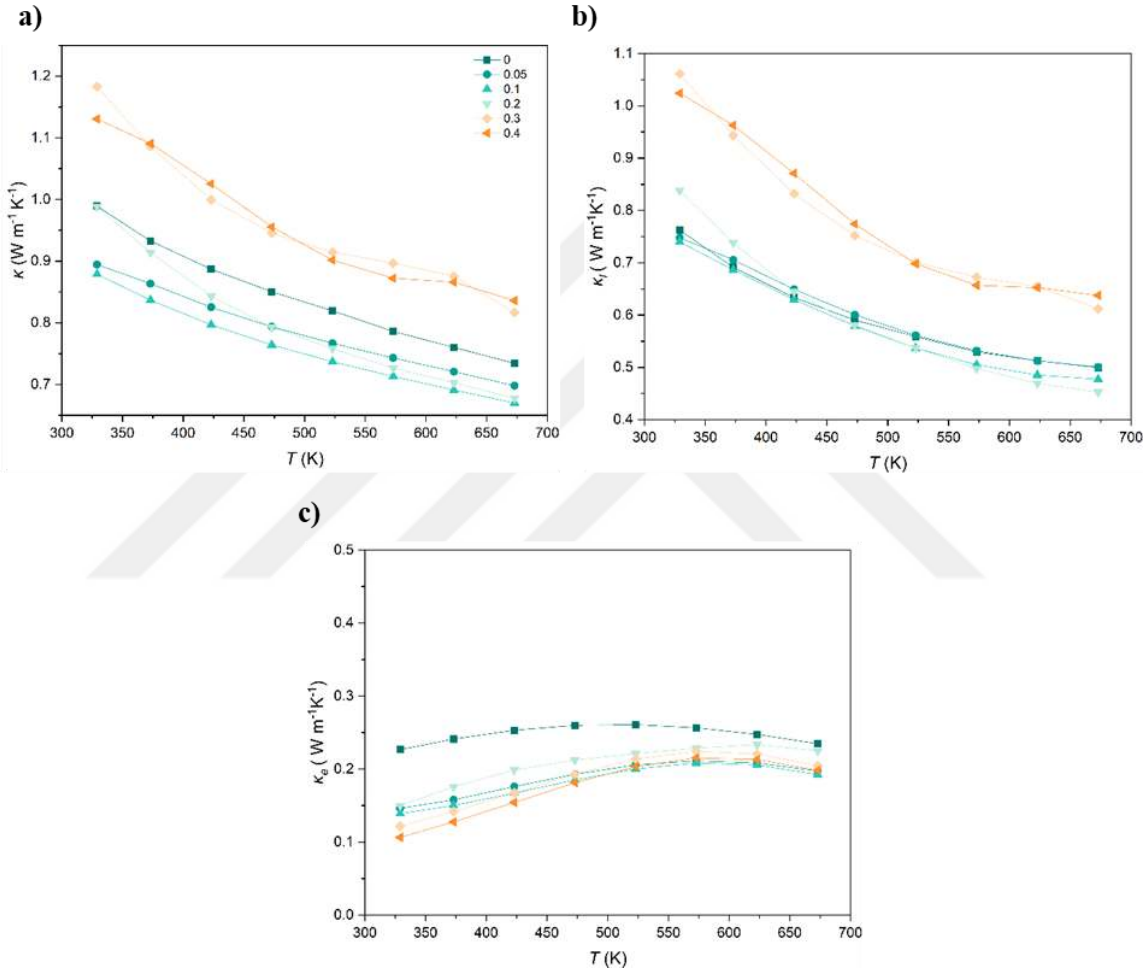

Figure 4.15. a) Total b) lattice and c) electronic thermal conductivity of pristine and x wt.% MgB_2 incorporated $Mg_{3.2}Sb_{1.5}Bi_{0.49}Te_{0.01}$ (x=0, 0.05, 0.1, 0.2, 0.3 and 0.4) samples.

Figure 4.16 illustrates the temperature-dependent thermoelectric figure of merit (zT) and quality factor (B) values of samples. All samples reach higher zT values as the temperature increases. The highest zT value for the main material is approximately 1.67 at 673 K. The synergy of diminished thermal conductivity and enhanced Seebeck coefficient results in a substantial enhancement of zT between 523 and 673K, reaching a record value of around 1.9 with 0.1 wt.% MgB_2-$Mg_{3.2}Sb_{1.5}Bi_{0.49}Te_{0.01}$ composite material.

This accomplishment is mainly attributed to the energy filtering effect. As a result, an approximately 14% improvement in thermoelectric performance is achieved. As plotted in Figure 4.16a and b, there is an exact correlation between the zT and B values, where B is the quality factor value, $B \propto \mu_w/\kappa_l$. Since the effect on the lattice component of the thermal conductivity is negligible, the increase in the weighted mobility at elevated temperatures, resulted in an encouraging enhancement for both B and zT values.

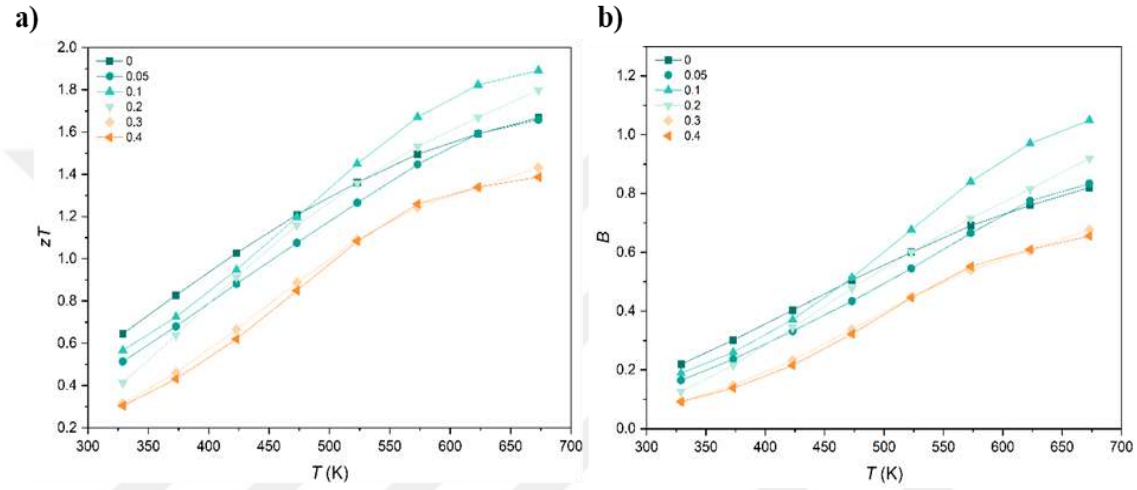

Figure 4.16. a) Thermoelectric figure of merit and b) quality factor of pristine and x wt.% MgB_2 incorporated $Mg_{3.2}Sb_{1.5}Bi_{0.49}Te_{0.01}$ (x=0, 0.05, 0.1, 0.2, 0.3 and 0.4) samples.

4.9 Mechanical Property Measurements

Figure 4.17 displays images of Vickers hardness measurements and average hardness values for x wt.% MgB_2-$Mg_{3.2}Sb_{1.5}Bi_{0.49}Te_{0.01}$ composite materials. Hardness measurements were taken from at least 10 different points for each sample, and the average values were calculated to obtain the hardness values of the materials. According to the results shown in Figure 4.17a, the best hardness value, 67 HV (657 MPa), is attributed to 0.1 wt.% MgB_2–added sample. Contrary to the reported papers, a remarkable enhancement is not achieved with the help of MgB_2[120, 121].

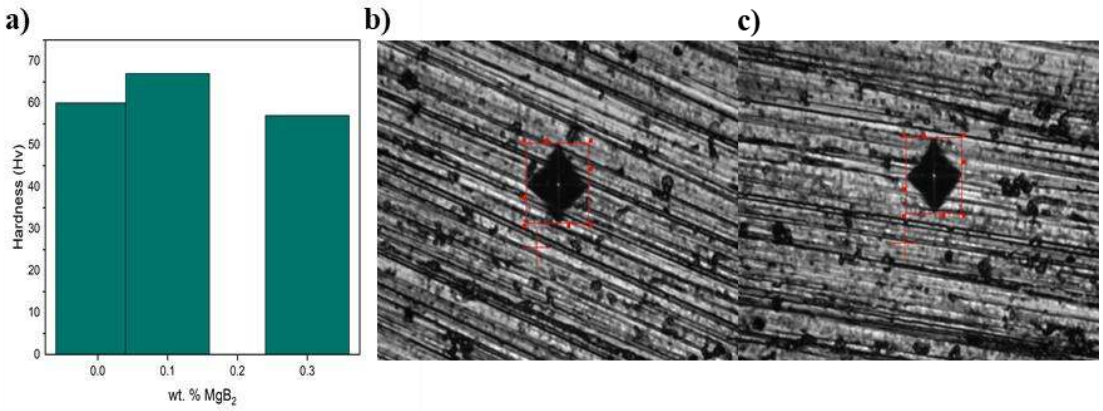

Figure 4.17. a) Vickers hardness, b, c) microscope images taken from the measurements of pristine and 0.1 wt.% MgB_2-$Mg_{3.2}Sb_{1.5}Bi_{0.49}Te_{0.01}$.

4.10 Conclusions

As a consequence of incorporating MgB_2 into composites, alterations in the microstructure and transport properties of the $Mg_3(Sb,Bi)_2$ system have been observed. Previous research utilizing highly conductive nano-carbon alternatives like graphene and carbon nanotubes has demonstrated the energy filtering effect of external additives on thermoelectric materials. Our study reveals a similar outcome with superconductive MgB_2, achieved by adjusting carrier scattering. While the addition of MgB_2 up to a certain threshold (0.3 wt.%) minimally affects the lattice thermal conductivity of the composite material, it induces a reduction in the electronic component of thermal conductivity, resulting in a κ value of 0.67 W m^{-1} K^{-1} for 0.1 wt.% MgB_2 at 673 K.

Despite negligible changes in carrier concentration determined from Hall measurements, a significant increase in the Seebeck coefficient of composite materials is observed. This phenomenon is attributed to energy filtering, where carriers are selectively scattered. The correlation between decreasing thermal conductivity and increasing Seebeck coefficient supports this notion. The achievement of a high Seebeck coefficient of 317 μV K^{-1}, coupled with low thermal conductivity, contributes to high zT values. Notably, our study demonstrates a record-high zT of 1.9 at 673 K. Considering the recent studies on $Mg_3(Sb,Bi)_2$ system for mid-temperature ranges, a significant enhancement (%8-18) was achieved in comparison with the zT values of 1.75[122], 1.75[123], 1.74[101], 1.6[3]

at 673 K. The homogeneous distribution of nanomaterials and elimination of percolations could potentially lead to even better results. This outcome underscores the potential of implementing an energy filtering strategy for $Mg_3(Sb,Bi)_2$ systems to further enhance thermoelectric properties.

Chapter 5

INVESTIGATING THERMOELECTRIC PERFORMANCE OF *N*-TYPE Mg_3Sb_2 – Mg_3Bi_2 THROUGH Nb INCORPORATION

5.1 Introduction

Despite decades of research on thermoelectric materials, Bi_2Te_3 alloys continue to dominate low-temperature module applications. Compared to the high-quality waste heat (above 573 K), recovering low-grade waste heat, which makes up to ca.90% of the source, is challenging due to its lower energy density[2, 4, 69]. So far, thermoelectric cooling market has been essentially dominated by the Bi_2Te_3-based materials[124]. However, the diminishing availability and toxicity of the Te element are reducing the practicality of Bi_2Te_3, prompting a shift in focus toward alternative materials[125]. Therefore, an extensive research for alternative thermoelectric materials have been conducted.

Recent years have shown promising advancements in alternative candidates, particularly Mg_3Sb_2 – Mg_3Bi_2 alloyed materials for low to mid-temperature ranges. Mg_3Sb_2 is known as a great candidate for thermoelectric applications due to the characteristic properties obeying phonon-glass electron-crystal concept, displaying inherently low thermal conductivity along with favorable electronic transport behaviour[53, 112, 126]. To date various strategies have been applied to enhance the thermoelectric efficiency of Mg_3Sb_2 system such as microstructure engineering, carrier concentration optimization, band structure modification, annealing etc.[4, 47-51, 57, 58, 64, 92, 112, 118, 127, 128]Among these studies alloying with Mg_3Bi_2 has notably enhanced the thermoelectric figure of merit by achieving an optimum band structure and modifying scattering mechanisms[4, 58-61, 64, 124, 127, 129]. A new strategy involved promoting grain growth by introducing wetting phases or layers along the grain boundaries. Liu et al. have achieved highest zT value of ~1.1 for $Mg_{3.2}Bi_{1.5}Sb_{0.48}Te_{0.002}Cu_{0.01}$ utilizing a Mg_2Cu wetting phase introduced during the sintering process. In this study, by creating conductive channels

along the solid grains, the mobilities of charge carriers could be drastically enhanced [3, 69]. Recent studies suggest a weak doping effect of Nb metal for Mg_3Sb_2 systems, aligning with the concept of wetting grain boundaries [51, 59, 130]

Despite their potential, the room temperature thermoelectric properties of Mg_3Sb_2- and Mg_3Bi_2-based thermoelectric materials are known to be severely limited due to grain boundary electrical resistance. Originally thought to be due to ionized impurity scattering[59] that could be modified by incorporation of other elements such as Nb, it was discovered that a thermally activated grain boundary electrical resistance leads to low σ and therefore low zT at room temperature[128]. The hopping-like conductivity at the grain boundaries leads to a dramatic reduction in grain boundary electrical resistance at higher temperatures allowing decent thermoelectric performance at high temperature in *n*-type Mg_3Sb_2. However, for good room temperature performance the grain boundary resistance must be reduced, usually by growing large grains[50, 68, 128]. In Mg_3Sb_2 the incorporation of Nb was found to increase grain size without significantly diffusing into the grains.[131] Thus it has been assumed that Nb and other transition metal impurities such as Cu, Ta, Co, Mn, and Hf function primarily to increase grain size[3, 48, 55, 128, 132].

A recent study revealed a maximum zT of 2.04 at 798 K for $Mg_{3.1}Nb_{0.1}Sb_{1.5}Bi_{0.49}Te_{0.01}$,[133] which shows great potential for mid-temperature applications. Another study on the addition of Nb to Mg_3Sb_2 with a higher proportion of Mg_3Bi_2 achieved a room temperature zT of 1.02.[134] This improvement is attributed to Nb's optimization mechanisms within the grains and at the grain boundaries, which prevent Mg vacancy accumulation and facilitate electron transmission both within and across grains.

In this study, the impact of different amounts of Nb metal addition to the Mg_3Bi_2-Mg_3Sb_2 system were investigated to enhance the thermoelectric performance at low and mid-temperature ranges. The influence of Nb-addition on the microstructure and transport properties was examined through chemical and structural characterizations.

5.2 Sample Preparation

In this study, $Mg_{3.2-x}Nb_x(Sb_{0.3}Bi_{0.7})_{1.996}Te_{0.004}$ (x=0, 0,025, 0.05, 0.1, and 0.15) samples were synthesized through mechanical alloying using high energy ball milling process (SPEX 8000D Mixer/Mill, 1425 rpm). All the high purity raw materials of magnesium powder (Mg, 99.8%; Alfa Aesar), bismuth pieces (Bi, 99.999%; Alfa Aesar), antimony shots (Sb, 99.999%; Alfa Aesar), tellurium pieces (Te, 99.9999%; AlfaAesar), and niobium powder (99.98%, Alfa Aesar) were used without further purification and weighed under Ar atmosphere to avoid oxidation during and after high energy ball milling. The stoichiometric amounts of elements according to the nominal composition were loaded with two half-inch stainless steel balls into a stainless-steel vial and sealed under Ar. The mechanical alloying technique was applied for a duration of two hours. Following that the resultant powders were loaded into a graphite die under Ar atmosphere and compressed via cold press. For consolidation, spark plasma sintering (SPS) was applied under a uniaxial pressure of 50 MPa for 2 minutes at 1073 K under vacuum.

The phase purity analysis and the chemical composition analysis were conducted through X-ray diffraction (XRD) analysis by using Rigaku Mini Flex 600 (Cu K_α (λ= 1.5406 °A), 40 kV voltage and 15 mA current). Scanning Electron Microscopy (SEM) and Energy Dispersive X-ray Spectroscopy (EDS) analyses were applied to determine the morphology and elemental compositions of the samples, respectively, using a Zeiss Ultra Plus Field Emission Scanning Electron Microscope. To examine the accurate chemical compositions, wavelength dispersive X-ray spectroscopy (WDS) analysis was conducted on an electron microprobe (Cameca SX 100, tungsten cathode) considering the line compound Mg2Si and certificated elements of Sb, Bi and Te as references. HR-TEM and SAED were adopted on samples using the Talos F200S S/TEM operating with a maximum acceleration voltage of 200 kV.

The electrical and thermal transport property analyses was applied between the temperature range of 50-400°C. For the thermal diffusivity, D, measurements, Netzsch LFA 467 equipment was employed on disc-shaped samples (10 mm in diameter). The electronic transport properties were measured by Ulvac ZEM-3 device on bar-shaped samples.

5.3 Characterization

5.3.1 Crystal structure and phase analysis

The crystal structure and phase purity analyses were carried out for the consolidated Nb-incorporated $Mg_{3.2-x}Nb_x(Sb_{0.3}Bi_{0.7})_{1.996}Te_{0.004}$ (x=0, 0.025, 0.05, 0.1 and 0.15) samples. The XRD pattern of pristine and Nb-incorporated samples were given in Figure 5.1a. In accordance with the theoretical peak positions, the XRD pattern of pristine sample conforms to the trigonal Mg_3Bi_2 crystal structure (in space group: $P\bar{3}m1$, Figure 5.1b). Although, because of the smaller ionic radii of Sb^{3-} (1.88 Å) in comparison to Bi^{3-} (1.93 Å), the substitution of Sb^{3-} into the B^{i3-} sites shifts peak positions towards higher 2θ values.

On the other hand, no detectable shift in peak positions is observed for the Nb-added samples due to similar ionic radii of Mg^{2+} and Nb cations. However, the increase in the Nb content to 0.1 and 0.15 led to an observation of secondary peaks at around 38º (a shoulder peak) and 42º a low-intensity peak, which correspond to the cubic Nb_3Sb phase (in space group $Pm\bar{3}n$). In the light of this result, it is indicated that the amount of Nb addition is considerably higher than the solubility limit of Nb in the intended phase. This is reliable with the results from Nb-mediated grain boundary study for Mg_3Sb_2 phase where no detectable incorporation observed in the grains other than the metallic Nb[51].

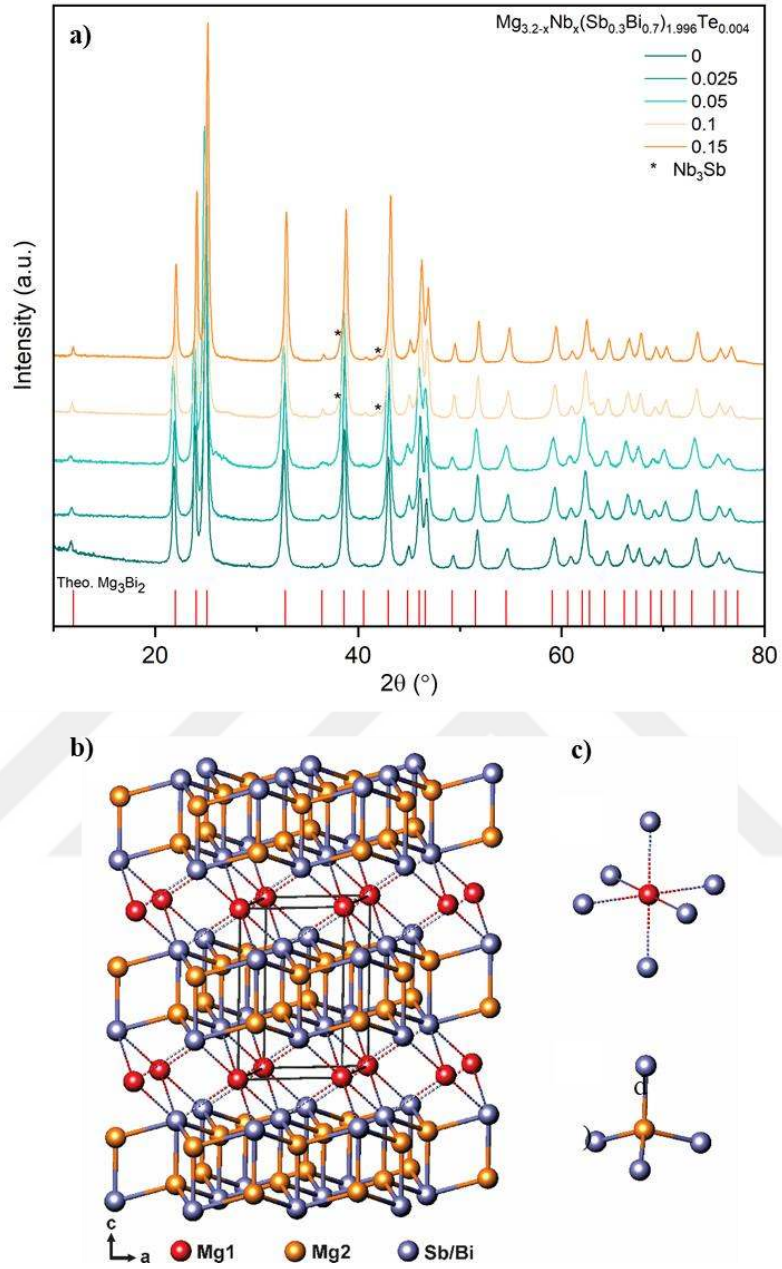

Figure 5.1. a) XRD patterns of Nb-incorporated $Mg_{3.2-x}Nb_x(Sb_{0.3}Bi_{0.7})_{1.996}Te_{0.004}$ (x=0, 0.025, 0.05, 0.1 and 0.15) samples, b) the crystal structure of $Mg_3(Sb,Bi)_2$ with labelled doping atom positions.

For further investigation of the effect of Nb addition on the crystal structure, lattice parameter refinement and texture analysis were performed by WinCSD program package. To determine the lattice parameters, LaB_6 was used as a reference material. The identified lattice parameters of $Mg_{3.2-x}Nb_x(Sb_{0.3}Bi_{0.7})_{1.996}Te_{0.004}$ (x=0, 0.025, 0.05, 0.1, 0.15)

samples were listed in Table 5.1. The theoretical lattice parameters of Mg_3Bi_2 and Mg_3Sb_2 were also given for comparison.

Table 5.1. Lattice parameters of $Mg_{3.2-x}Nb_x(Sb_{0.3}Bi_{0.7})_{1.996}Te_{0.004}$ (x=0, 0.025, 0,05, 0.1, 0.15).

With LaB_6 reference						**Mg_3Bi_2[135]**	**Mg_3Sb_2[136]**
	0	**0.025**	**0.05**	**0.1**	**0.15**		
***a* (Å)**	4.625(1)	4.6252(3)	4.6250(7)	4.6285(8)	4.6267(5)	4.666	4.5636(11)
***c* (Å)**	7.346(3)	7.3457(7)	7.350(2)	7.343(1)	7.351(1)	7.401	7.228(2)

For a rigid comparison of the achieved lattice parameters the values were illustrated in Figure 5.2. Taking into account the standard deviations, no significant peak shift is detected in the Nb added samples.

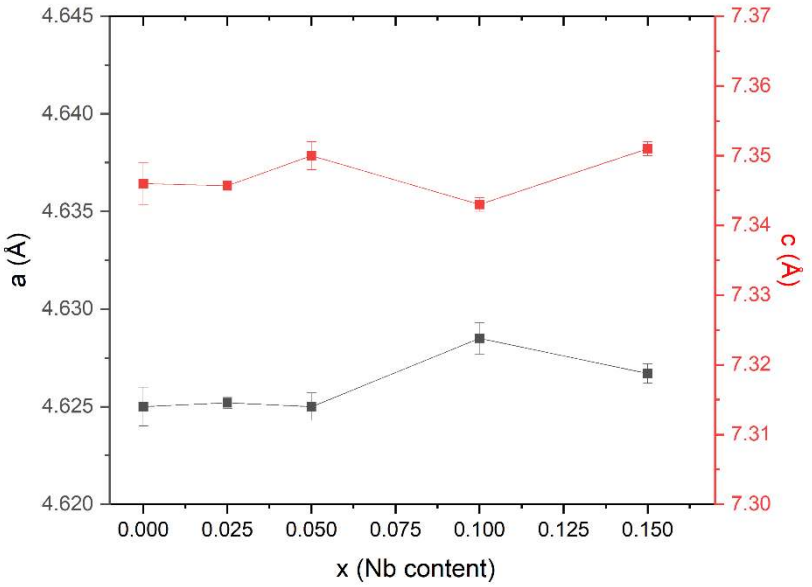

Figure 5.2. Lattice parameters of of $Mg_{3.2-x}Nb_x(Sb_{0.3}Bi_{0.7})_{1.996}Te_{0.004}$ (x=0, 0.025, 0,05, 0.1, 0.15) measured with LaB_6 reference.

5.4 Phase and Microstructure Analysis

For further investigation of the chemical composition and microstructure, EDX, SEM and WDX analyses were employed. In Figure 5.3a and b, the microstructure examination was performed on the backscattered electron (BS) – SEM images of both Nb-incorporated $Mg_{3.1}Nb_{0.1}(Sb_{0.3}Bi_{0.7})_{1.996}Te_{0.004}$ and pristine sample. Depending on the

contrast observed in BSE-SEM images, there are three individual phases in both samples exist: a slightly Bi-deficient phase, a slightly Bi-excess phase and secondary impurity phase as small black spots. In Figure 5.3c, the HR-TEM image of the $Mg_{3.1}Nb_{0.1}(Sb_{0.3}Bi_{0.7})_{1.996}Te_{0.004}$ sample reveals different lattice spacings corresponding to the different phases. Where the evaluated lattice fringe with spacing of around 0.34 nm corresponding to the (011) planes of Bi deficient phase, the spacing of approximately 0.37 nm corresponding to the Bi excess phase with (002) plane. This outcome also shows that nanometer-sized sub grains were observable in the microstructure, in addition to the micron-sized target phase. Furthermore, in Figure 5.3d, the diffraction pattern of the same sample was achieved from the SAED analysis. According to the presented diffraction pattern, the well-defined spots were reliable with the trigonal crystal structure of $Mg_3(Sb,Bi)_2$ along the [-111] zone axis.

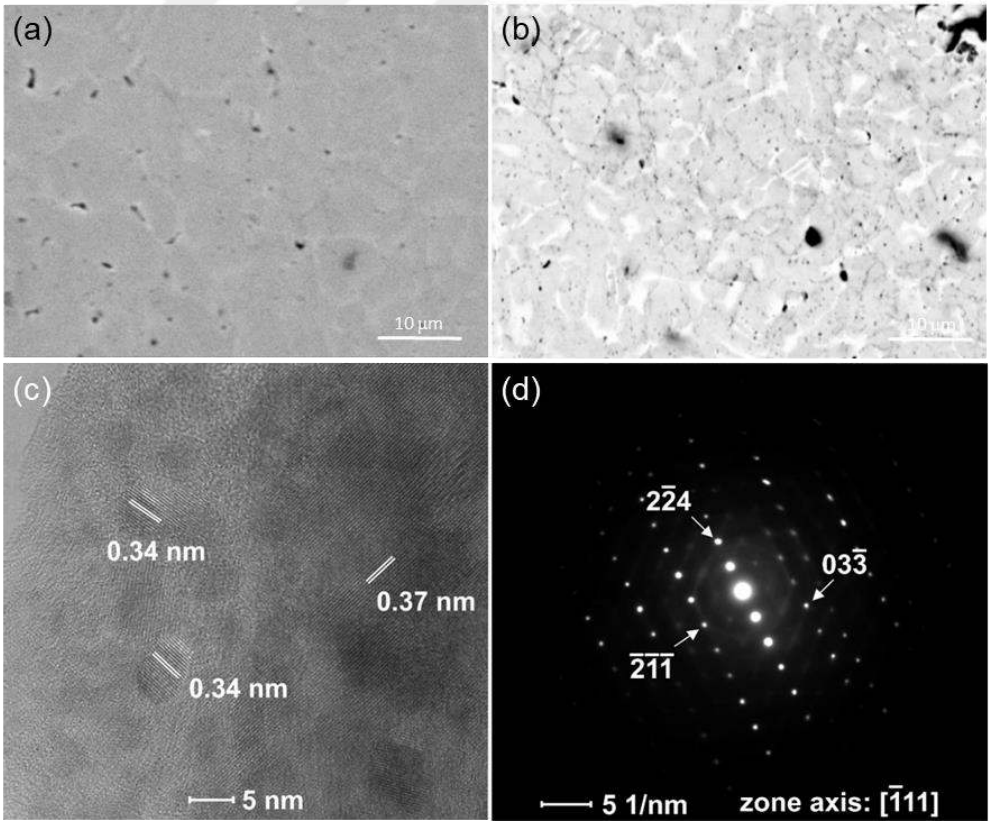

Figure 5.3. BSE-SEM images of $Mg_{3.2-x}Nb_x(Sb_{0.3}Bi_{0.7})_{1.996}Te_{0.004}$ for a) x=0 and b) x=0.1. c) HR-TEM and d) SAED images for x = 0.1 sample.

For identification of the different phases observed from the BS-SEM images, EDX analysis and mapping was applied. Figure 5.4 represents the EDX mapping areas taken from the $Mg_{3.2}(Sb_{0.3}Bi_{0.7})_{1.996}Te_{0.004}$ sample, without any Nb addition. As depicted in Figure 5.3a, different contrasts and points were selected particularly. Overall map indicates the existence of Mg, Sb, Bi and O atoms. Since Mg is air-sensitive, oxygen is observable especially from the spots where Mg stayed as element. However, the metallographic treatments and waiting time under air atmosphere led to a slight oxidation. Table 5.2 examines the atomic percentage of each element in the selected areas.

As given in Table 5.2, the black points observed in BS-SEM images mostly coming from the Mg element which is relatively light compared to other elements in the microstructure, therefore represents a darker spot. Other than the excess Mg in the microstructure, the spot #5 which is likewise an impurity, contains additional elements such as Si, Cr, Mn, and Fe which is post probably coming from the stainless steel vial. Therefore, the vial has been changed after achieving this result. The composition in the grains has been detected as $Mg_{3.14}Bi_{1.397}Sb_{0.6}$, which is similar to the nominal composition of $Mg_{3.2}(Sb_{0.3}Bi_{0.7})_{1.996}$.

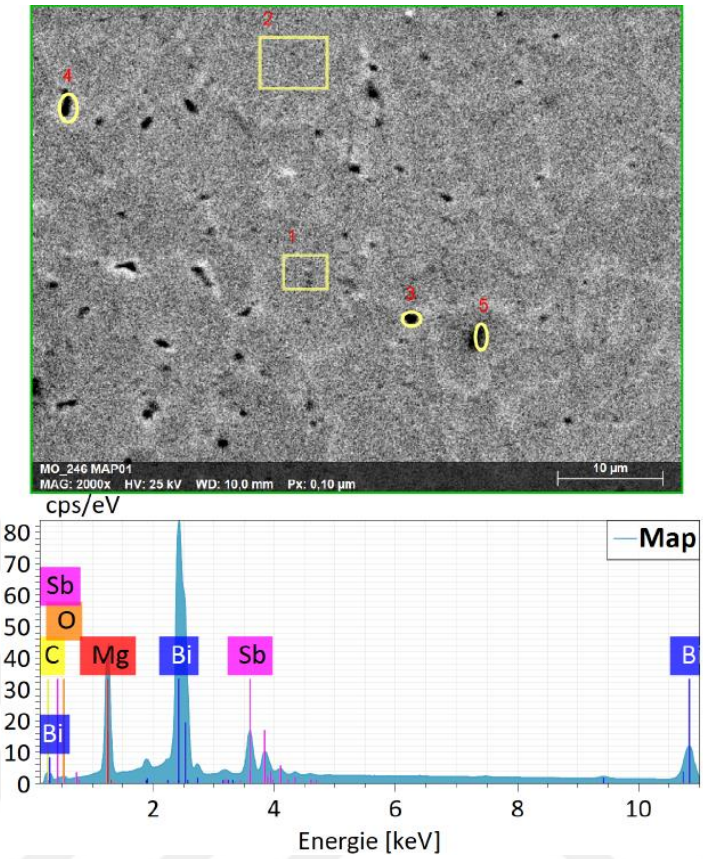

Figure 5.4. Selected spots where EDX analysis applied and EDX graph corresponding to the achieved elemental energy levels for the $Mg_{3.2}(Sb_{0.3}Bi_{0.7})_{1.996}Te_{0.004}$ sample.

Table 5.2. The EDX analysis results of $Mg_{3.2}(Sb_{0.3}Bi_{0.7})_{1.996}Te_{0.004}$ sample.

Nominal $Mg_{3.2}(Sb_{0.3}Bi_{0.7})_{1.996}Te_{0.004}$			
Spot #	**At. %**		
	Mg	**Bi**	**Sb**
1	61.57	25.44	12.99
2	61.06	27.25	11.69
3	71.93	19.39	8.69
4	67.91	23.14	8.96
5*	27.30	12.86	6.40
Map	61.13	26.97	11.90

As presented in Figure 5.3b, the phase differences become more obvious for the composition of $Mg_{3.1}Nb_1(Sb_{0.3}Bi_{0.7})_{1.996}Te_{0.004}$. To determine the phases EDX analysis

was applied for $Mg_{3.1}Nb_1(Sb_{0.3}Bi_{0.7})_{1.996}Te_{0.004}$ sample as well. SEM images reveal a homogeneous elemental distribution of Sb, Bi, and Te, with black spots corresponding to the lightweight elements of Mg and Nb. The elemental secondary phases are predominantly observed around grain boundaries but within the grains as well. The detection of Te was not possible because of its low concentration. Elemental mapping shows that a significant portion of Nb remains in its elemental form rather than incorporating into the crystal structure.

Furthermore, distinct phase differences are discernible in the microstructure, highlighted by variations in contrast. Through EDS analysis, the elemental distribution is elucidated: the darker grey areas correspond to 59.88, 25.79, 11.98, and 2.36 at. % of Mg, Bi, Sb, and Nb, respectively. In contrast, brighter areas exhibit concentrations of 59.04, 28.37, 10.59, and 2 at. % of Mg, Bi, Sb, and Nb. Thus, a meaningful difference is observed in the amounts of Bi for the bright and grey areas. The brighter areas creating inner grain boundaries possess a higher Bi content compared to the main grains with grey color. This observation aligns with the study conducted by Sepheri-Amin et al., discussing the brighter contrast of grain boundaries due to a higher concentration of heavier elements in Mg_3Sb_2-Mg_3Bi_2 alloys[118]. According to the EDX mapping, the overall composition of the pristine sample is $Mg_{3.13}Sb_{0.64}Bi_{1.43}$ and the Nb-added samples is $Mg_{3.09}Nb_{0.098}Sb_{0.62}Bi_{1.39}$.

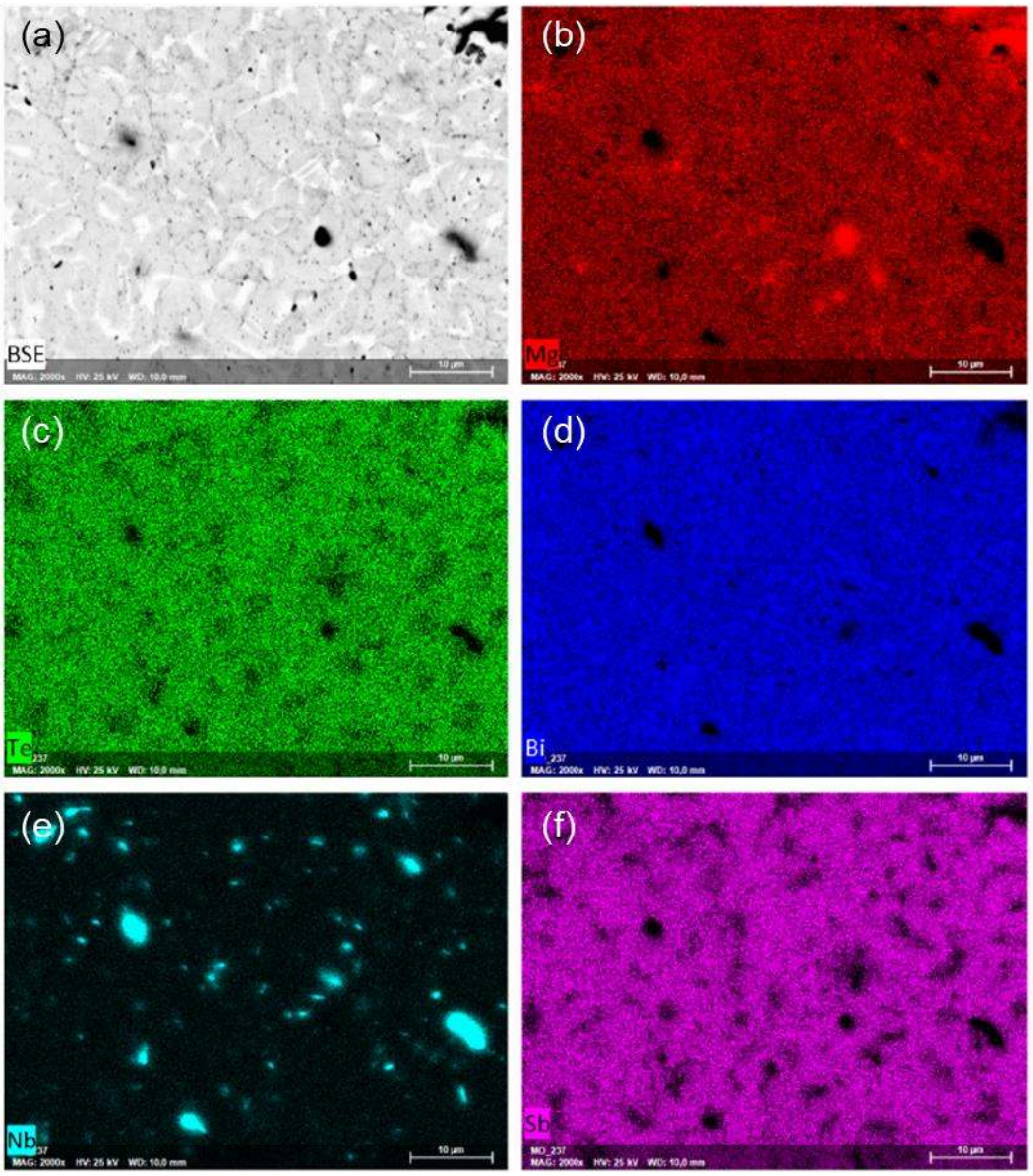

Figure 5.5. EDS elemental mapping of the $Mg_{3.1}Nb_1(Sb_{0.3}Bi_{0.7})_{1.996}Te_{0.004}$ sample.

For further investigation of secondary phases and microstructure, STEM image was captured from $Mg_{3.05}Nb_{0.15}(Sb_{0.3}Bi_{0.7})_{1.996}Te_{0.004}$ sample, to highlight changes more prominently. In Figure 5.6, the STEM image along with EDS layered images elucidates the generation of the Nb_3Sb phase within the microstructure. While the secondary phase of elemental Nb remained as small-grain precipitates, the Nb_3Sb phase manifested as distinct lines within the microstructure. Secondary phases manifest as lines and minute particles, approximately 100 nm in size, are dispersed within the sample. Particularly

noteworthy are the findings from Figure 5.6c and d, where it becomes evident that the secondary phases in the form of lines specifically correspond to the Nb_3Sb phase.

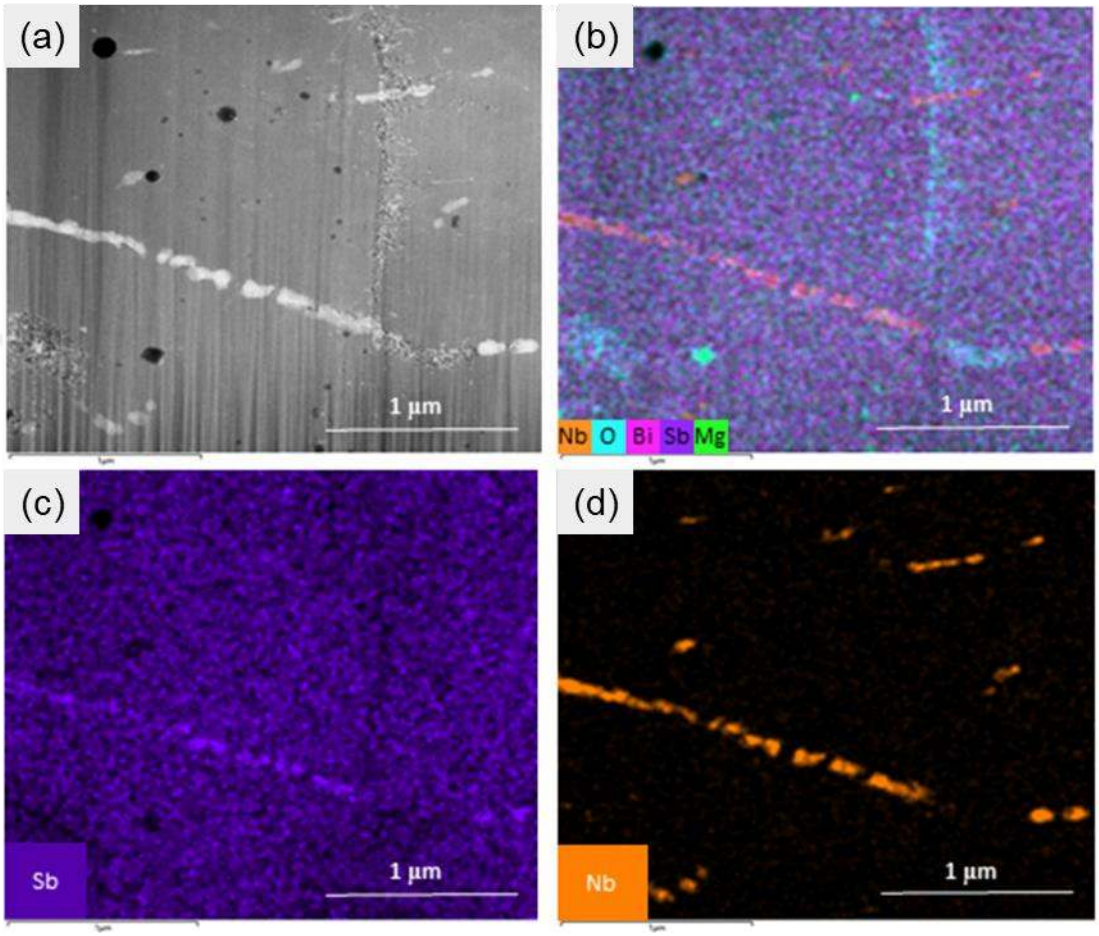

Figure 5.6. STEM image of $Mg_{3.05}Nb_{0.15}(Sb_{0.3}Bi_{0.7})_{1.996}Te_{0.004}$, b) EDS overall elemental mapping, c) Sb $L_{\alpha 1}$ and d) Nb $K_{\alpha 1}$.

For a more accurate identification of the compositional analysis WDS analysis was applied on ten different spots. In Figure 5.7, BSE images of $Mg_{3.1}Nb_{0.1}(Sb_{0.3}Bi_{0.7})_{1.996}Te_{0.004}$ sample are presented. The red crosses mark the location where EDS analysis was performed. Examining the results presented in Figure 5.5c and d, it becomes evident that lighter areas correspond to the main phase, while darker regions are predominantly composed of elemental Nb. To ascertain the overall composition, WDS analysis was conducted in ten different areas across the sample. Consequently, the

average chemical composition was determined to be $Mg_{3.13}Nb_{0.09}Sb_{0.6}Bi_{1.37}Te_{0.003}$, which is quite similar with the calculated composition from the EDX mapping.

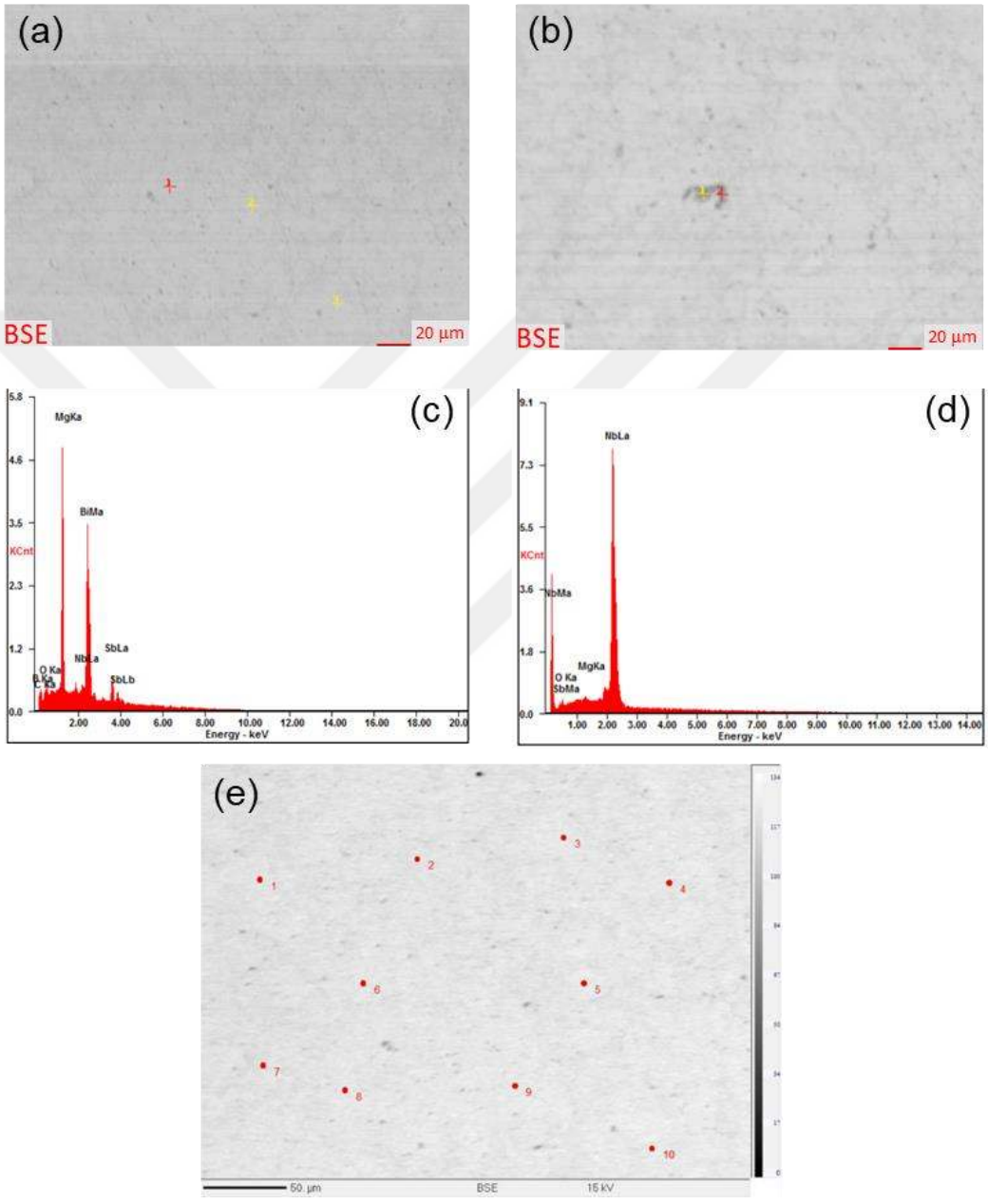

Figure 5.7. a, b) BSE images, c, d) EDS analysis of $Mg_{3.1}Nb_{0.1}(Sb_{0.3}Bi_{0.7})_{1.996}Te_{0.004}$ from bright and dark areas, and e) ten different spots that WDS analysis was conducted on $Mg_{3.1}Nb_{0.1}(Sb_{0.3}Bi_{0.7})_{1.996}Te_{0.004}$ sample.

Since clear estimations of grain boundaries and grains are challenging through SEM analysis, polarized light optical microscopy images were obtained both for the pristine and Nb-added samples. For quantitative average grain size analysis, the images shown in Figure 5.8a-e were generated using the image analysis software MIPAR. The results revealed that the grain sizes were approximately the same, in the range of around 14 μm and 15 μm for the $Mg_{3.2-x}Nb_x(Sb_{0.3}Bi_{0.7})_{1.996}Te_{0.004}$ samples. Unlike the pristine sample, the Nb-added sample exhibited twin formations, outlined with dashed lines, in the microstructure.

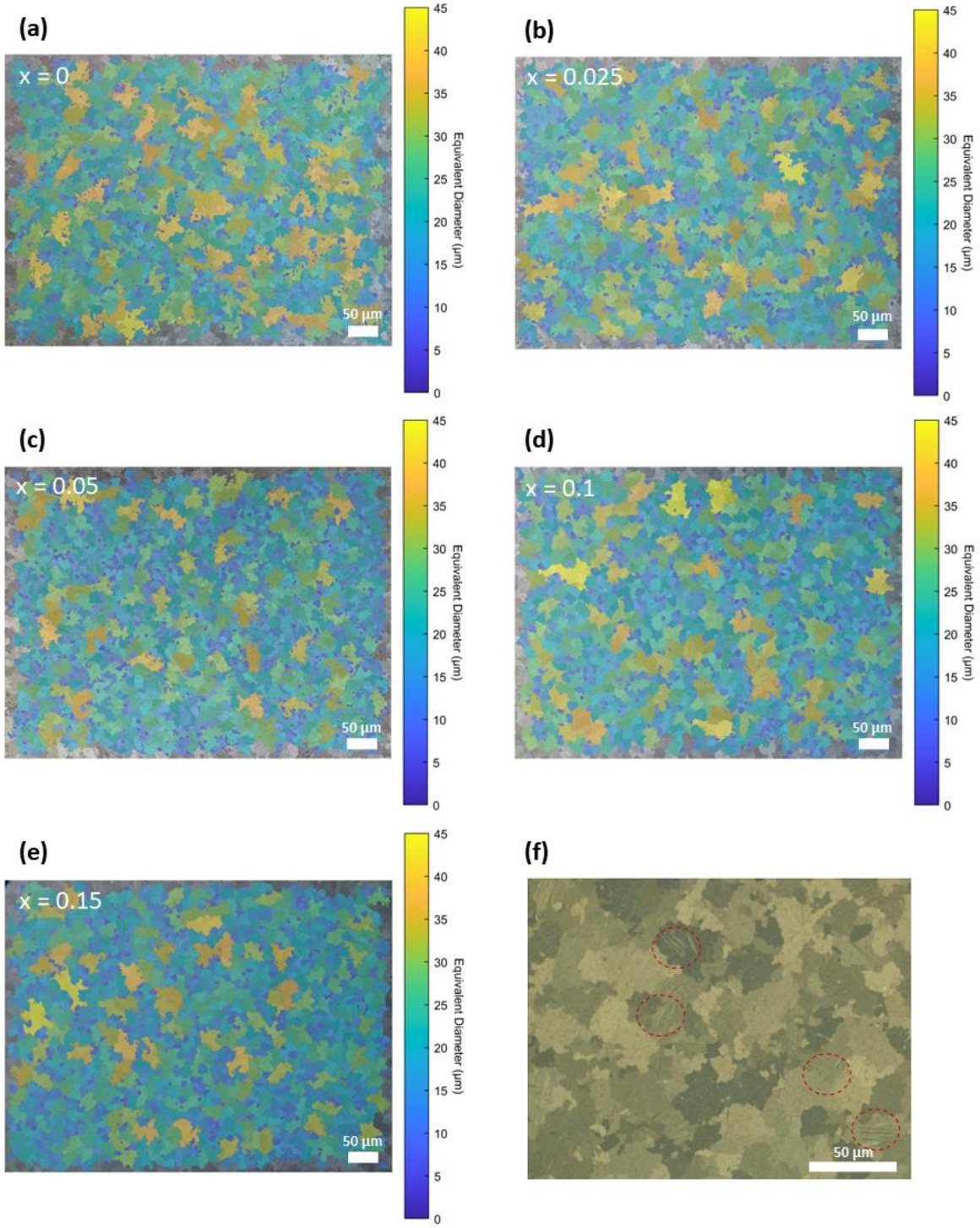

Figure 5.8. a-e) Grain size analysis of the pristine and Nb incorporated $Mg_{3.2-x}Nb_x(Sb_{0.3}Bi_{0.7})_{1.996}Te_{0.004}$ (x=0, 0.025, 0.05, 0.1 and 0.15) samples. f) Polarized light optical microscopy image of Nb-added (x=0.1) sample displaying twin formations.

5.5 Transport Property Measurements

The electrical resistivity (ρ) values of all Nb incorporated samples present an ascending behaviour as given in Figure 5.9a with increasing temperature in parallel with metal-like behaviour. Similar resistivity results are also achieved through Hall effect measurement which presents the consistency Figure B 1. U-shaped temperature dependence of ρ is slightly observable for the sample without Nb, because of the competition between different carrier scattering mechanisms. A thermally activated scattering mechanism is dominant for the low temperature regions. Although this is mostly attributed to ionized impurity scattering, it has been revealed conclusively in Mg_2Sb_3 to be due to charged grain boundaries[65]. The characteristics here are quite similar: samples with and without Nb exhibit comparable temperature dependent Seebeck coefficient, which indicates similar doping levels and electron scattering within the grains. Additionally, an increase in weighted mobility at low temperatures is observable, while a transition to decrease in weighted mobility with increasing temperature is demonstrated as expected for phonon scattering at high temperatures[65].

This result is mainly related to the grain boundary complexions and a concurrent reduction in the influence of grain boundary scattering. Since the polarized light images in Figure 5.8 illustrating no significant change of grain size upon Nb-incorporation (13.97 and 15.21 μm for pristine and $Mg_{3.1}Nb_{0.1}(Sb_{0.3}Bi_{0.7})_{1.996}Te_{0.004}$ samples), the main factor is grain boundary complexions, rather than the decrease in grain boundaries. As a result of Nb addition, grain boundary complexions lead to reduced grain boundary resistance and subsequently lower resistivity values compared to the pristine sample. After Nb addition, resistivity values of the samples are notably low at lower temperatures, a departure from the typical grain boundary resistance scenario where resistivity starts higher and decreases with temperature up to mid-temperature ranges. The detection of secondary phases, such as Nb_3Sb, through XRD and TEM images, doesn't seem to adversely impact resistivity values. In fact, the high electrical conductivity of Nb_3Sb, known to exhibit superconductivity at very low temperatures, and a room temperature resistivity of only 18 μOhm.cm, suggests a positive influence on overall electrical conductivity as a grain boundary complexion[137, 138]. Similarly, the presence of Nb as another secondary phase, characterized by high electrical conductivity, further supports

the notion that these secondary phases might not have a detrimental effect on resistivity values.

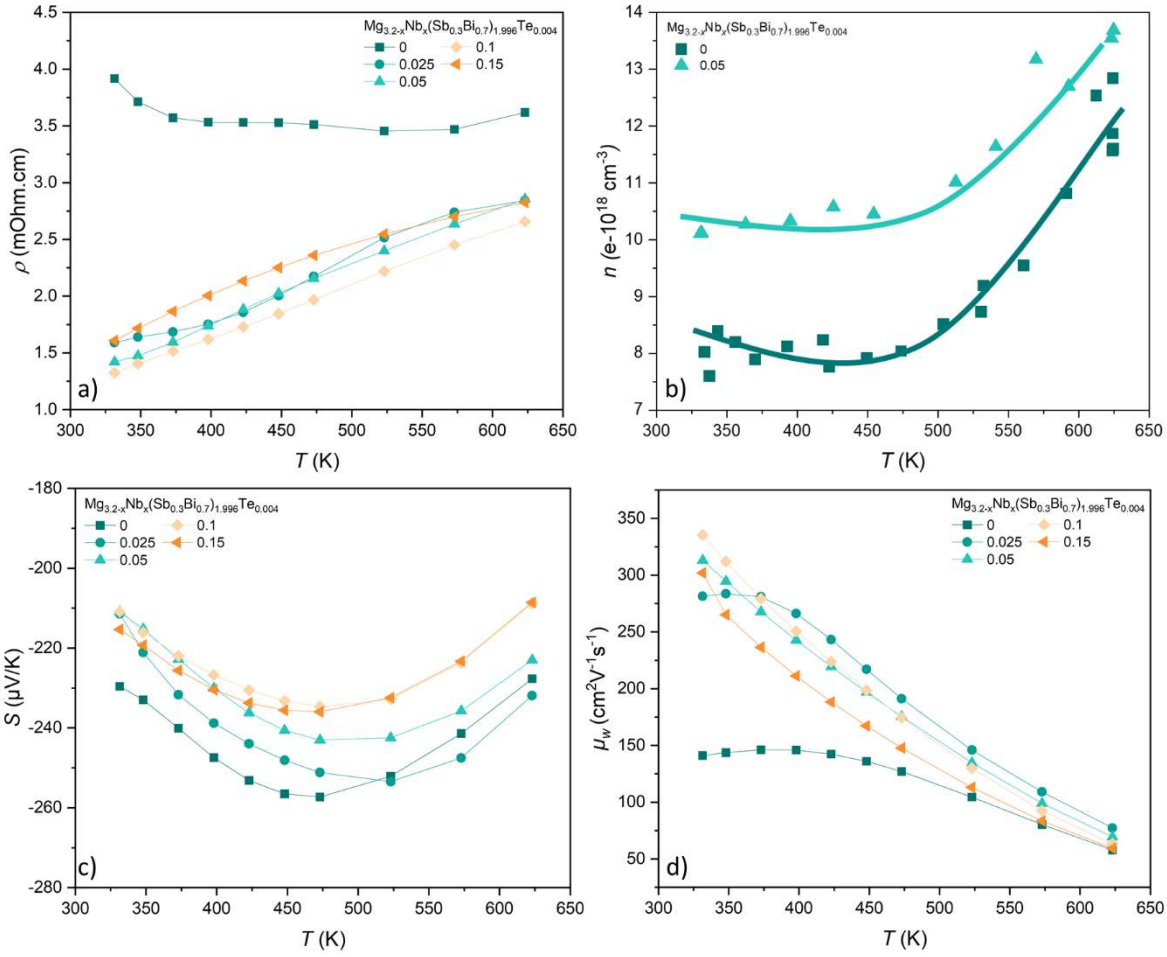

Figure 5.9. a) Electrical resistivity, b) Carrier concentration (pristine and Nb added (x=0.05) samples), c) Seebeck coefficient, d) weighted mobility of pristine and Nb added $Mg_{3.2-x}Nb_x(Sb_{0.3}Bi_{0.7})_{1.996}Te_{0.004}$ (x=0, 0.025, 0.05, 0.1 and 0.15) samples.

The effect of the distribution of low energy grain boundaries on physical properties can be significant as seen in this study. The structure and chemistry of grain boundaries depend on the type and orientation of the neighboring grains but also on the thermodynamic conditions such as Temperature and Chemical Potential. Thus, grain boundary phases are often called “complexions” to distinguish them from bulk 3-D phases. In principle, the properties of complexions phases should also depend on chemistry but this has not been conclusively demonstrated in $Mg_3(Sb,Bi)_2$ until now. There are some examples in Half Heusler thermoelectrics where complexion phases are

engineered to have low resistance and improve thermoelectric performance. In NbCoSn-Pt doped with Pt, for example the addition of Pt goes primarily to the grain boundary complexion phase and changes it from being insulating to metallic[139]. In NbFeSb doped with small amounts of Ti the complexion phase is insulating but with greater amounts of Ti there is a complexion transition where it becomes metallic and makes Ti-NbFeSb a competitive thermoelectric material[140]. In similar, recently grain boundary complexion effect is achieved for the Cu doped *p*-type MgAgSb phase. As a result, Mg-Cu binary complexions eliminated the thermally activated electrical conductivity behavior, and enhanced the carrier mobility values[3].

The carrier concentration measurements were conducted on both pristine and Nb-added (x=0.05) samples. As depicted in Figure 5.9b, the carrier concentration exhibited an increase following Nb addition. This finding aligns with the observed enhancement in electrical conductivity and the corresponding reduction in Seebeck coefficients (Figure 5.9c). The decrease in ρ with Nb doping cannot be solely attributed to the increased carrier concentration. The Hall mobility (μH) of the x = 0.05 sample (440.5 cm²/Vs) is significantly higher than that of the pristine sample (196.4 cm²/Vs) (Figure B 3), suggesting an additional factor influencing conductivity.

The change in σ is mainly related to the characteristics of the grain boundary complexions and a simultaneous decrease in the effect of grain boundary scattering. It is well-known that grain boundaries have a remarkable impact on electrical properties, especially in Mg_3Sb_2-based thermoelectric materials. This has been presented by examining the variation in properties with different grain size from BSE-SEM images. Several studies have confirmed the effect of grain boundary resistance, particularly their contribution to elevated ρ values, notably at room temperature.[17,22,24,38-42] The presence of Mg deficiencies around grain boundaries further clarifies the observed higher resistivity values.[42]

However, in this study the decrease in grain boundary resistance is associated not to grain growth but to a reduction in the resistance of the average grain boundary. Polarized light images in Figure 5.8 ascertain this, by representing no substantial change of grain size upon Nb incorporation. Since there is no strong noticeable change in grain size correlates with the decrease in grain boundary scattering after Nb addition, Nb must be the key factor to make the boundaries less resistive.

The extent of grain boundary scattering is discerned by the space charge region that develops, which may result from a mismatch in conduction or valence band energies between the grain and the grain boundary.[141, 142] For instance, if dopant segregation occurs or if grain boundary wetting phases are formed, the band energies of the grain boundary region will be affected, altering the mismatch between the bulk and boundary conduction or valence bands. This change can either reduce the conduction barrier if the mismatch is lower or increase it if the mismatch is greater. Since Nb has been observed to form a grain boundary wetting phase in Mg_3Sb_2,[51] this could explain the observed reduction in grain boundary scattering in samples with Nb compared to those without.

This band energy discrepancy between the boundaries and bulk, or band offset ΔE, can be modelled using a two-phase approach similar with the method that used by Kuo *et al.*[128] In this scenario, a series circuit representation of grain boundary scattering can be used to differentiate the contributions of grain and grain boundary to conductivity:

$$\sigma^{-1} = \left(1 - f_{gb}\right)\sigma_g^{-1} + f_{gb}\sigma_{gb}^{-1} \tag{5.1}$$

where σ_g and σ_{gb} are the contributions to σ from grain and grain boundaries, respectively, and f_{gb} is the volume fraction of grain boundaries, which can be estimated from the grain size as depicted by Chookajorn *et al.*[143] This equation can be combined with the band transport equation for conductivity:

$$\sigma = \sigma_{E_0}(T)sF_j(\eta) \tag{5.2}$$

where σ_{E_0} is the transport coefficient, s is a conduction mechanism-dependent parameter, F_j is the Fermi-Dirac integral of order j, and η is the reduced fermi level, E_f/k_BT (E_f and k_B are the fermi level and Boltzmann constant, respectively) for the bulk (grain) and $\left(E_f - \Delta E\right)/k_BT$ for the grain boundary phase. Phonon scattering parameters (s = 1 and $\sigma_{E_0} \propto T^0$) were used for both the grain and grain boundary phase.

Single crystal σ values (σ_g in Equation 5.1) for $Mg_{3.2}(Sb_{0.3}Bi_{0.7})_{1.996}Te_{0.004}$ can be calculated at different fermi levels by Equation 5.1, employing data from two samples with different grain sizes. This single crystal σ can be used to calculate a single crystal

μ_W, which is applicable to all samples with the same Bi-Sb ratio regardless of doping level until the onset of bipolar conduction.[117] Using the calculated single crystal conductivity values (σ_g), Equation 5.1 is applied to examine the grain boundary conductivity (σ_{gb}). The parameter *s* in Equation 5.2 is treated as a constant, chosen by minimizing the root mean square error of Equation 5.1 for $Mg_{3.2}(Sb_{0.3}Bi_{0.7})_{1.996}Te_{0.004}$ without added Nb. Figure 5a shows a series of temperature-dependent μ_W plots comparing values calculated using the two-phase method (dotted lines) with those derived from measured *S* and σ (solid dots).[117] The η value used to calculate the σ_{gb} can also be used to find the ΔE between the bulk and the grain boundaries. Figure B 4 presents the results of this calculation, demonstrating that samples containing Nb exhibit a significantly lower ΔE compared to pristine samples. To show that this relationship is independent of grain size, we included data from Li *et al.*[134] for a $Mg_{3.2}Bi_{1.49}Sb_{0.5}Te_{0.01}$ sample with a much smaller grain size of 2.9 μm and E_f of 37 meV. This sample exhibits a similar ΔE to the two samples synthesized in this study, both of which have larger grain sizes (>10 μm). The model results show that the incorporation of Nb decreases ΔE, hence decreasing the scattering strength of grain boundaries in Mg_3Sb_2. This effect is consistent across different grain sizes and doping levels, suggesting that the formation of the Nb wetting phase and resulting reduction in ΔE are the main factors driving the decrease in grain boundary scattering with Nb addition.

Figure 5.9c represents a consistent *n*-type behavior across all specimens, regardless of the extent of Nb incorporation. Notably, the absolute values of Seebeck coefficients decrease following Nb addition, aligning with the observed decrease in resistivity values and pointing to an increase in carrier concentration. This upsurge in carrier concentration could be attributed to subtle Nb substitutions or Nb interstitials. The decrease in Seebeck coefficients observed after 473 K is interpreted as compelling evidence of a bipolar effect. Figure B 2 presents the resistivity and Seebeck coefficient of $Mg_{3.1}Nb_{0.1}(Sb_{0.3}Bi_{0.7})_{1.996}Te_{0.004}$ during the heating cooling cycles.

The weighted mobility values of the samples were estimated from the experimental Seebeck coefficient and resistivity data[117]. The weighted mobility which is independent of the chemical potential and carrier concentration or the doping element, is an important property to determine the electronic properties of thermoelectric materials. The emergence of bipolar conduction in the Seebeck coefficient data after 473 K, attributed

to the establishment of a smaller band gap, results in a decrease in the weighted mobility values. Therefore, it is more meaningful to compare the weighted mobility values below this temperature. Notably, after Nb metal addition, there was a consistent increase in all weighted mobility values, reaching a range of 280-330 $cm^2V^{-1}s^{-1}$ at 330 K, regardless of the quantity of the added Nb. In the temperature range of 330-450 K, the weighted mobility values exhibited a consistent increase with Nb addition (0.025, 0.05, and 0.1 at. %), surpassing those of other promising low-temperature Mg_3Sb_2-Mg_3Bi_2 alloys where weighted mobilities change between 180 and 250 $cm^2V^{-1}s^{-1}$. This is mostly related to the grain boundary scattering mechanism as discussed above. The increase in the weighted mobility, might be related to increase in the Hall carrier mobility, where the GB-scattering of carriers is diminished because of the Nb addition, through formation of grain boundary complexions. For example, at 330 K, the μ_w of the Nb-added sample with $x = 0.1$ (330 $cm^2\ V^{-1}\ s^{-1}$) shows approximately 130 % improvement over the pristine sample (142 $cm^2\ V^{-1}\ s^{-1}$). Similar behavior is observed for Pt-doped NbCoSn.

Since the quality factor (*B*-factor, $B = 4.33 \times 10^{-10} \frac{\mu_W T^{5/2}}{\kappa_l}$) is associated to the weighted mobility values[144, 145], the substantial improvement approximately 140 % compared to pristine sample is a remarkable achievement for higher thermoelectric performances.

Figure 5.10a presents experimental κ as a function of temperature. Both pristine and Nb-doped samples exhibit a rising trend in κ with increasing temperature. Especially, the pronounced increase in κ observed above 450 K coincides with the onset of the bipolar conduction demonstrated by the temperature-dependent *S* given in Figure 5.9c. The dominant carrier scattering mechanism in Nb-doped samples was predicted as acoustic phonon scattering as across all temperatures. For pristine sample, the dominant carrier scattering mechanism is assumed to vary with temperature. Grain boundary scattering was considered up to 400 K, followed by a mixed scattering regime between 400 K and 500 K. Finally, with higher temperatures exceeding 500 K, acoustic phonon scattering became dominant consistent with the observed trend in μ_H with temperature (Figure B 5). The combined κ_l and κ_{bi} were isolated by subtracting the κ_e from the κ (Figure 5.10 a-c). The Effective Mass (EM) model was used to estimate the κ_e of pristine and Nb-doped samples (Figure 5.10b). The apparent lower κ_e of the pristine sample compared to the Nb-

added samples near room temperature is attributed to the low σ_{gb} of the pristine sample, as demonstrated by Kuo *et al.*[146] Given that the *S* is essentially the same for all samples (Figure 5.10c), it can be inferred that the σ_g is similar, and consequently, the κ_e is also comparable across samples. Figure 5.10b also presents the κ_e estimated by using σ_g instead of experimental σ in Equation 2.7 (empty symbols). The close agreement between these values supports our inference about the similarity of σ_g across samples. The κ_e (Figure 5.10b) was subtracted from the κ (Figure 5.10a), to obtain the sum of lattice thermal conductivity (κ_l) and bipolar thermal conductivity (κ_{bi}), as shown in Figure 5.10c. The sum of κ_l and κ_{bi} estimated using κ_e derived from σ_g is also presented (empty symbols). After accounting for grain boundary scattering, the apparent higher κ_l of the pristine sample (filled symbols) becomes comparable to other Nb-added samples (empty symbols). Nb and Nb_3Sb phases (observed in $x \geqslant 0.1$ samples) were ineffective in suppressing κ_l.

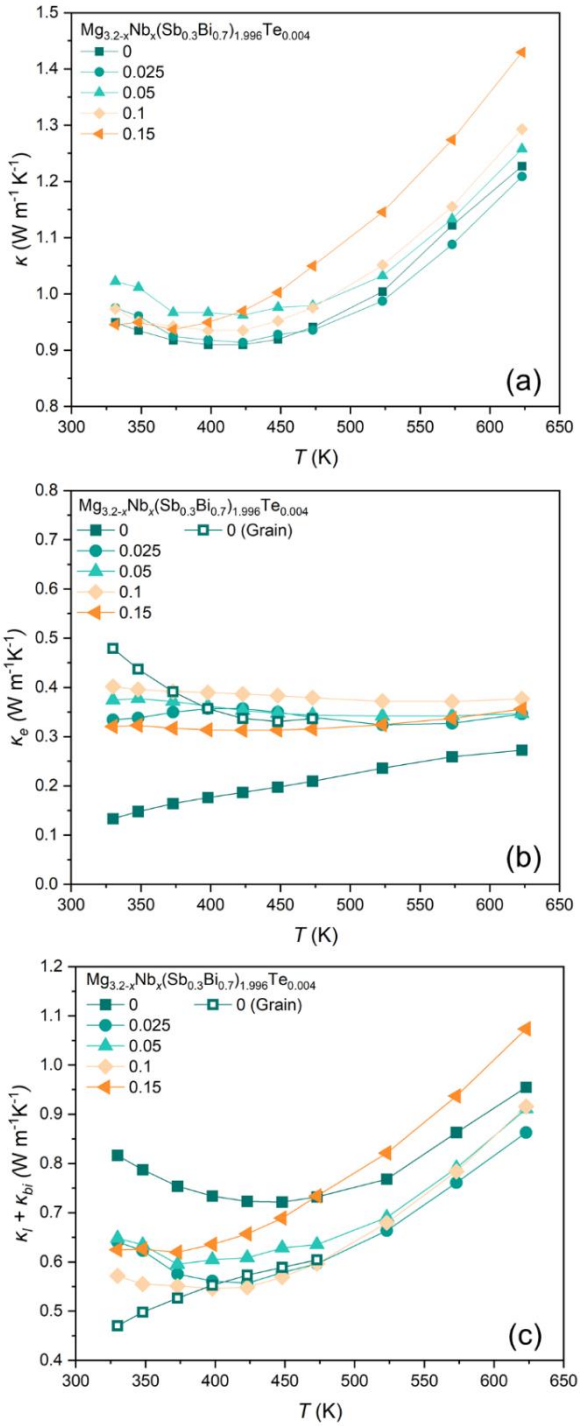

Figure 5.10. a) Total b) electronic c) summation of lattice and bipolar and d) estimated (symbols), Debye callaway model (lines), 330 K (inset) lattice thermal conductivity of pristine and Nb-added $Mg_{3.2-x}Nb_x(Sb_{0.3}Bi_{0.7})_{1.996}Te_{0.004}$ (x=0, 0.025, 0.05, 0.1 and 0.1 5) sample.

Figure 5.11 presents the temperature-dependent *B*-factor and the *zT*, along with the theoretically achievable *zT* as a function of carrier concentration. The combined effect of

low κ_l and high μ_W without GB scattering leads to a zT of Nb-doped samples between 330 and 423 K, exceeding 1 that is competitive with state-of-the-art Bi_2Te_3 alloys.

The B-factor (proportional to μ_W/κ_l), reflects the theoretical maximum zT. As shown in Figure 5.11a, the $x = 0.025$ sample exhibits a peak zT of 1.5 at 450 K, the highest among all investigated compositions. Notably, the zT of the $x = 0.1$ sample reaches 1.15 near room temperature, surpassing all reported $Mg_3(Sb,Bi)_2$-based materials. For comparison, the high zT of Cu-doped $Mg_3(Sb,Bi)_2$ by Liu *et al*. (dashed line) is included. To ensure reproducibility, an additional sample with identical composition was prepared, demonstrating comparable zT (Figure B 6). The $x = 0.025$ sample achieves an average zT of 1.26 between 330 - 573 K. Figure 5.11b confirms the correlation between Nb doping and increased B-factors.

Figure 5.11c presents the calculated carrier concentration-dependent zT for pristine and Nb-doped ($x = 0.05$) samples. The lines represent the theoretically achievable zT calculated using the EM model. Notably, the zT of the Nb-doped sample could potentially reach ~1.05 at a carrier concentration of 7×10^{18} cm^{-3}. However, the measured zT already approaches 1.02 at 330 K, suggesting near-optimal carrier concentration in Nb-doped samples. Also, the calculated device ZT value for $Mg_{3.1}Nb_{0.1}(Sb_{0.3}Bi_{0.7})_{1.996}Te_{0.004}$ ranges between 1.04-1.15 within the temperature range of 350 to 623 as given in Figure 5.11d. Eventually, the theoretical maximum device efficiency (η_{max}) reaches an impressive 11%, showing highly competitive performance.

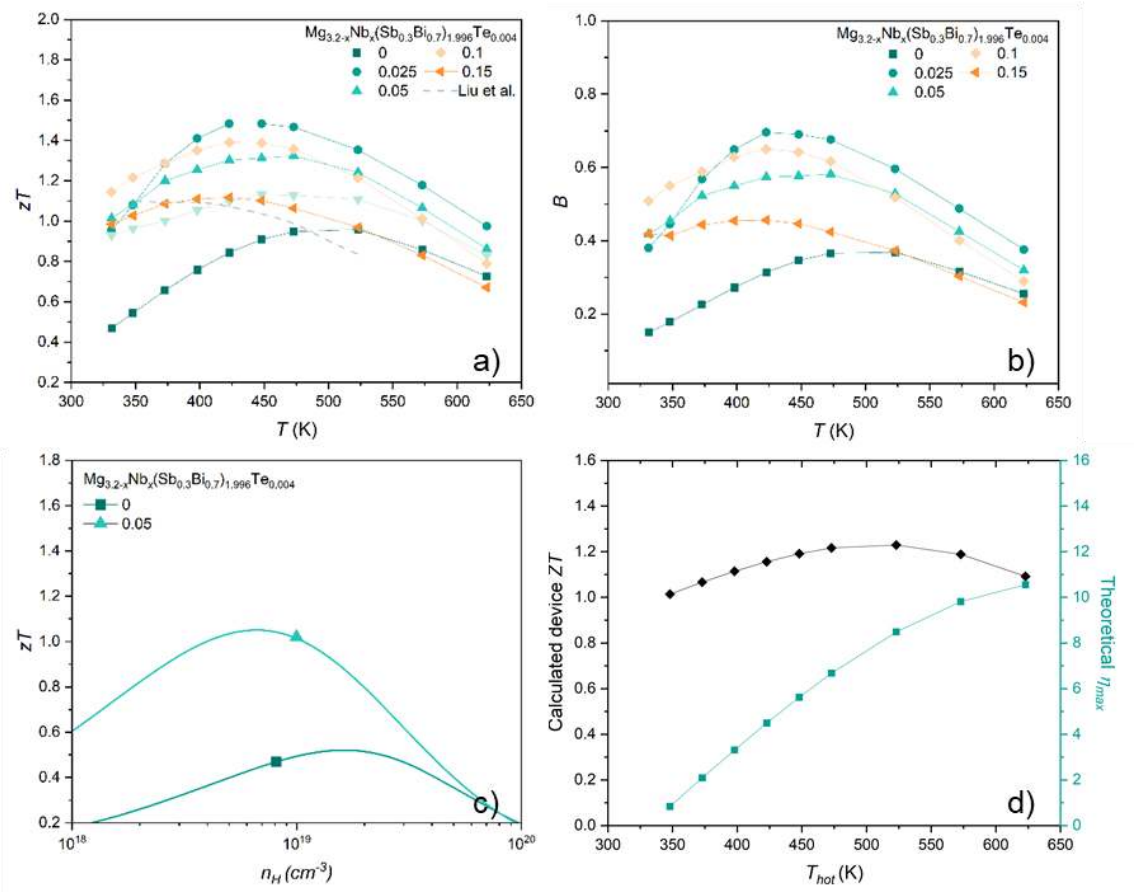

Figure 5.11. Temperature-dependent a) zT (Liu et al.[69] in dashed line) and b) B-factor of pristine and Nb-added $Mg_{3.2-x}Nb_x(Sb_{0.3}Bi_{0.7})_{1.996}Te_{0.004}$ (x = 0, 0.025, 0.05, 0.1 and 0.15) samples. c) Calculated and measured n_H-dependent zT of pristine and x = 0.05 samples, and d) calculated device ZT and η_{max} of x = 0.1 sample.

5.6 Mechanical Property Measurements

Mechanical properties of Nb-added and pristine $Mg_{3.2-x}Nb_x(Sb_{0.3}Bi_{0.7})_{1.996}Te_{0.004}$ (x=0, x=0.1) are analyzed via Vickers hardness test. The measurement is utilized at least ten different points from each samples to be able to achieve an average value for the overall sample. Then achieved results calculated through the system to obtain the hardness values. According to the results, the hardness value of 70.39 HV (690 MPa) and 71.475 HV (701 MPa) are achieved for pristine and Nb-added sample, respectively. It is concluded that, no significant improvement is observable on the hardness values through Nb addition.

5.7 Conclusions

The $Mg_3(Sb,Bi)_2$ system has been modified through the incorporation of Nb. While in Mg_3Sb_2 the primary effect of Nb is to facilitate grain growth, the samples prepared in this study presents a little change in grain size. Instead, the resistivity of the grain boundaries themselves is dramatically reduced. The reduction is so significant, that the conductivity and mobility have little indication of grain boundary resistance. The achievement of low thermal conductivity in the range of 0.9-1 W m^{-1} K^{-1}, coupled with low resistivity values and elevated carrier mobility, contributed to the attainment of high zT values, particularly in low-temperature regimes. Notably, a record-high zT of 1.15 at 330 K and 1.20 at 350 K, with a device ZT of 1.04 at 350 K, reaching 1.27 at 523 K, and a η_{max} of 11 % at 623 K was achieved highlighting a competitive performance. Compared to previous studies with enhanced zT values (0.86[147], 0.95[4], 0.98[148], 1.1[69] at 350 K) for low temperatures, a considering improvement ranging from 10 to 39% is achieved with a zT of 1.20 at 350 K. This work encourages the exploration of $Mg_3(Sb,Bi)_2$ as an alternative thermoelectric material for room-temperature applications. The emphasis on microstructure engineering, specifically the chemistry of grain boundary complexion phases, emerges as a promising avenue for further enhancing the thermoelectric properties of these materials.

Chapter 6

INVESTIGATING PERFORMANCE OF *P*-TYPE MgAgSb FOR LOW TEMPERATURE THERMOELECTRIC APPLICATIONS

6.1 Introduction

In general, thermoelectric studies and thermoelectric materials present good performance at middle and high temperature ranges. Only a few material groups have been studied for low temperatures (RT-550 K). One of the most famous material groups for the low temperature applications is Bi_3Te_2 family. However, Te element has high cost and low abundancy (0.001 ppm in the Earth crust[149]) besides its hazards on the environment. Therefore, there is an investigation on alternative low temperature, relatively low cost, and abundant thermoelectric materials. In this sense, α-MgAgSb shows up as a good candidate, because of its good thermoelectric performance around room temperature and abundance of elements. Also, recent studies have been showed that Mg_3Bi_2 thermoelectric materials have good thermoelectric performance at low temperatures as a *n*-type material. Considering the mechanical and thermoelectric property compatibilities of these materials, MgAgSb can be efficiently paired with Mg_3Sb_2-Mg_3Bi_2 family as a *p*-type material[150]. Recent studies have demonstrated promising outcomes indicating that TEGs have achieved impressive energy conversion efficiencies of approximately 8.5-10% by utilizing non-harmful materials, specifically based on magnesium[148, 151, 152].

6.1.1 Crystal Structure

The understanding of the crystal structure is important to examine the thermoelectric properties of the materials. MgAgSb presents three different crystal structures. First one

is a half-Heusler γ phase (space group F-43m) at high temperatures (630−700 K), second is a Cu_2Sb-related β phase (space group P4/*nmm*) at intermediate temperatures (560−630 K), and last one is a tetragonal structure α phase (space group $I\bar{4}c2$) with a = 9.1761 Å and c =12.6960 Å at low temperatures (RT ~ 560 K)[153]. Figure 6.1 shows the three different crystal structures for low, mid and high temperature phases, respectively. For all three crystal structure, Mg and Sb atoms built an undistorted or distorted rocksalt-type sublattices with Ag located on the tetrahedral or polyhedron sites.

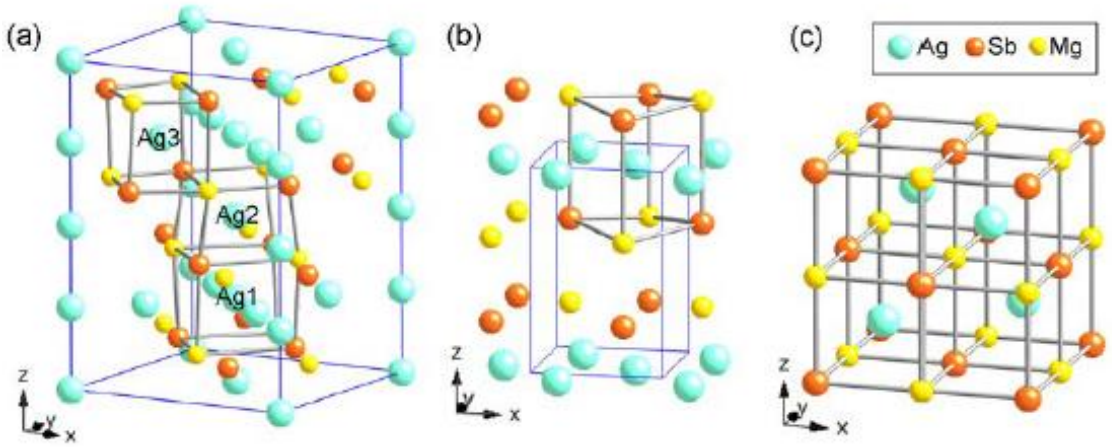

Figure 6.1. Crystal structures of the (a) low-temperature α-MgAgSb, (b) intermediate β-MgAgSb, and (c) high-temperature γ-MgAgSb, showing Ag atoms located on half of the Mg−Sb polyhedron sites of the distorted or undistorted Mg−Sb rocksalt-type sublattice[154].

For high-temperature γ-MgAgSb as known for the Half-Heusler crystal structures, the most and least electronegative atoms which are magnesium and antimony in this case, creates an undistorted rocksalt-type sublattice, with bond length of 3.28 Å between Mg and Sb. Meanwhile, the Ag atoms locates on the half of the tetrahedral sites, switching back and forth between occupied and vacant locations, bonding with Mg and Sb with bond length of 2.84 and 2.82 Å respectively. As shown in Figure 6.1c, each Ag atom is encompassed by four antimony and four magnesium atoms. The unit cell comprises 4 Mg, 4 Sb and 4 Ag atoms, in total[155].

Diverging from the high-temperature crystal structure, for the mid-temperature β-MgAgSb phase, antimony and magnesium atoms forms a distorted rocksalt-type sublattice along the ab plane, where the tetragonal unit cell lattice and rocksalt lattice

exhibit a relationship achieved through a 45° rotation around the c-axis. The silver atoms fill the half of the distorted Mg-Sb pseudo-cubes and connecting the Mg-Sb cubes along the c-axis. Mg-Sb, Ag-Mg, and Ag-Sb bond lengths are 2.91, 3.02, 2.95 Å correspondingly. The unit cell overall contains 6 atoms coming from 2 Mg, 2 Sb and 2 Ag atoms[155].

As examined in Figure 6.1a, the room temperature phase comprises a distorted rocksalt lattice of Mg-Sb which is rotated by 45° around the c-axis in similar with the intermediate phase. The bond lengths Mg-Sb rocksalt substructure is 2.97-3.03 Å. Additionally, the Ag atoms occupied on the half of the Mg-Sb pseudo-cubes, bonded with Mg and Sb atoms with bond lengths of 2.90 and 2.88 Å, respectively. The unit cell parameters are doubled along a and c axis for room temperature phase to adjust a distinct ordering of silver atoms. The most distinct alteration of α-phase from the β-phase is the Ag rearrangement. It differs the layer spacing and coordination number of atoms. While β-phase present a sandwich layer of MgSb-Ag-MgSb layers, through the transformation of α-phase sandwich layer spacing is decreasing from 3.97 to 3.43 Å, intercalating some of the Ag atoms in MgSb layer. Consuming this route incurs an energy barrier exceeding 1.2 eV per MgAgSb formula unit. The substantial energy obstacle aligns with the observed phenomenon that achieving the pure α-phase necessitates a low-temperature annealing process. Table 6.1 gives the refined structural parameters of three different phases[155].

Table 6.1. Refined structural parameters of the room-temperature, intermediate and high-temperature phases (α-, β- and γ-MgAgSb, respectively)[154].

Phase	γ-MgAgSb	β-MgAgSb	α-MgAgSb
Temperature (°C)	420	330	room
Space group	$F4^{-}3m$ (216)	P4/nmm (129)	$I4^{-}c2$ (120)
a (Å)	6.7004(1)	4.4199(1)	9.1761(4)
c (Å)	-	6.8896(2)	12.6960(7)
Theor. density (g/cm^3)	5.61	6.26	6.31

6.2 Phase Diagram

The published studies indicate that obtaining MgAgSb as a single phase is very challenging and difficult. Thus, the thermoelectric properties of MgAgSb also depend on the impurity phases and the amount of impurities. Figure 6.2 presents the ternary phase diagram of Mg-Ag-Sb. The phase diagram is studied around 1950 and no significant studies have been reported so far. The phase diagram corresponds to the system at 450 °C[156]. However, the material is studied for lower temperatures and synthesized at low temperatures. Nevertheless, it is certain that the MgAgSb monophase occurs only in a narrow region. This explains the difficulty of the synthesis phase pure MgAgSb[157]. The most common impurity is the Ag_3Sb dyscrasite phase, which is shown in the recent studies[153, 158, 159].

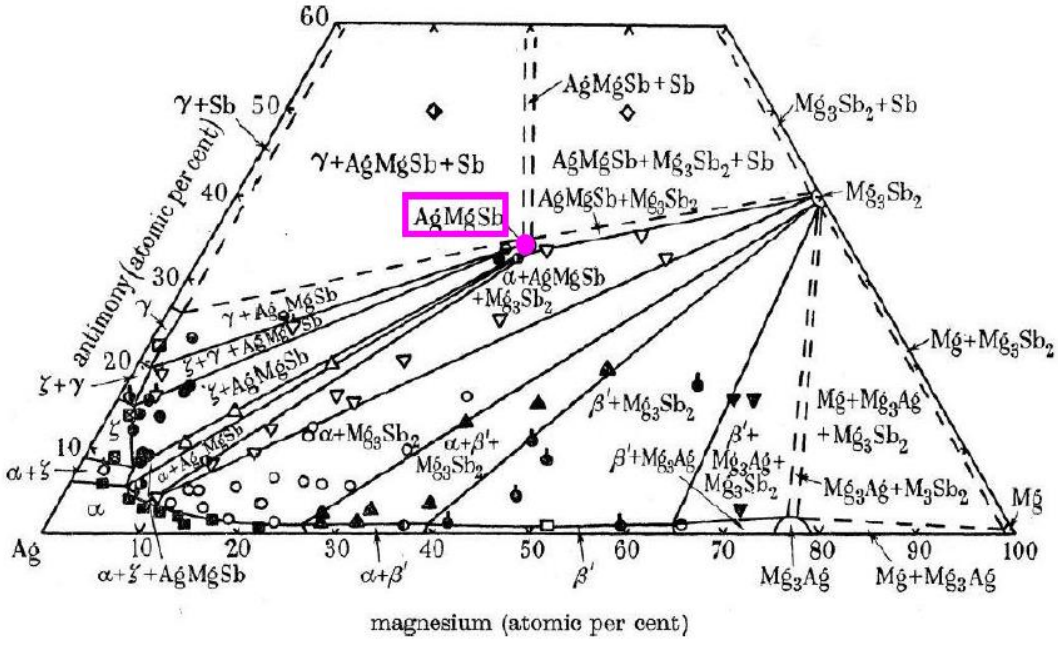

Figure 6.2. Ternary phase diagram for the system Mg-Ag-Sb at 450°C.

The most recent study about the phase diagram of Mg-Ag-Sb system is conducted by Materials Project through DFT calculations. The accuracy of the thermodynamic data has been enhanced by calculating the formation energies with the r2SCAN metaGGA functional. The extracted ternary phase diagram at 300 K is given in Figure 6.3. As illustrated by green circles, there are more than ten phases included in stable materials in

addition to the unstable secondary phases. Although in Figure 6.3a, the MgAgSb phase in the middle of the diagram seems to be a stable phase, it corresponds to the high-temperature γ-MgAgSb phase. And the more promising low-temperature α- MgAgSb phase for thermoelectric purposes is stays 0.01 eV/atom above hull in Figure 6.3b, which predicted as unstable thermodynamically by the Materials Project group. In addition, 7 regions with different impurity phases emphasized in the diagram with various colors. They correspond respectively: Mg-Mg_3Sb_2-MgAg (pink), Mg_3Sb_2-MgAg-$MgAg_3$ (purple), Mg_3Sb_2-$MgAg_3$-MgAgSb (yellow), Mg_3Sb_2-MgAgSb-Sb (blue), Ag-$MgAg_3$-MgAgSb (grey), Ag-Ag_3Sb-MgAgSb (green) and Ag_3Sb-MgAgSb-Sb (red).

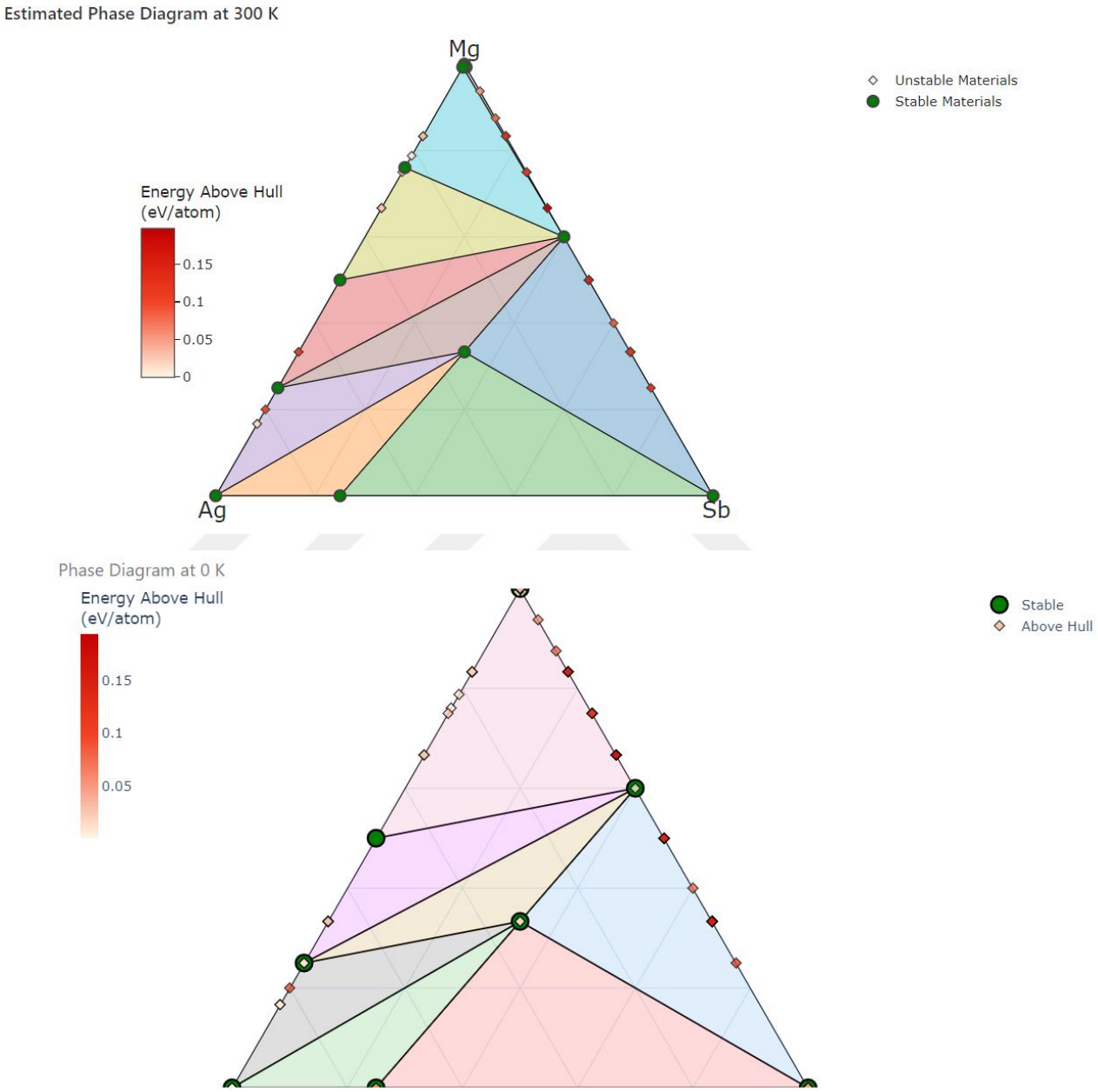

Figure 6.3. The calculated ternary phase diagram for the system Mg-Ag-Sb at a) 300 K and b) at 0 K for α- MgAgSb phase.

6.3 Band Structure and electronic properties

Zhang et al. calculated the band gap and band structure of MgAgSb phases through using the modified Becke-Johnson method[160]. The results of the calculations shows the α-phase MgAgSb has an indirect band gap around 0.22 eV, which is also close to the experimental band gap value of 0.16 eV[161]. Figure 6.4a and b illustrates the calculated band structures of the α- and β-phase.

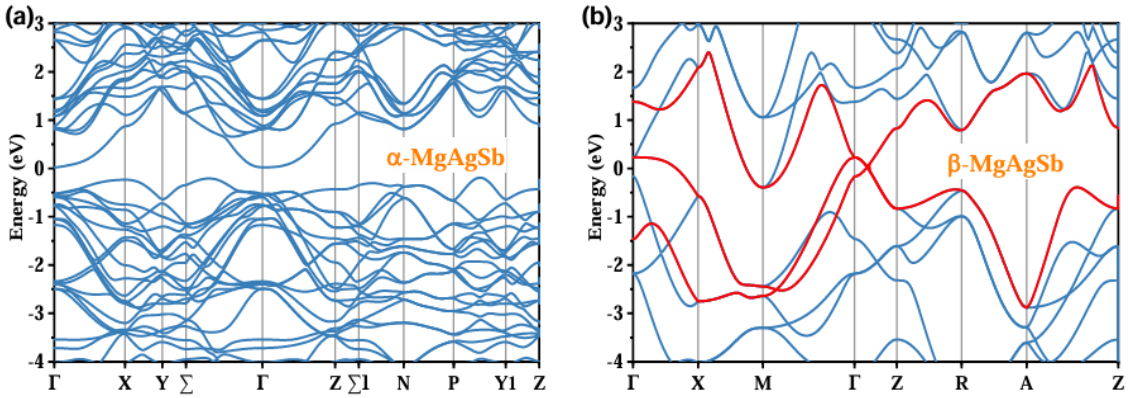

Figure 6.4. Calculated band structure of primitive cell: (a) α-MgAgSb, (b) β-MgAgSb. The Fermi level in each compound is set as the zero energy point.

According to Figure 6.4a, the valence band maximum (VBM) lies in the P-Y1 direction with a pocket degeneracy of 8, suggesting favorable *p*-type electrical transport characteristics, even under conditions of low carrier concentrations. On the other hand, the β-phase exhibits no discernible band gap; rather, it manifests clear metallicity owing to the existence of bands ranging from -3 eV below the Fermi level to +2 eV, as illustrated by the red lines in Figure 6.4b. The difference in the band structures of α- and β-phase affect both electronic and thermal transport properties, as a result the overall thermoelectric properties.

To further investigation for the fundamental reason behind the no band gap of β-phase element projected band structure were presented taking the Fermi level within the given compound as the reference point for zero energy. Figure 6.5 represents the element projected band structures of the α- and β-phases.

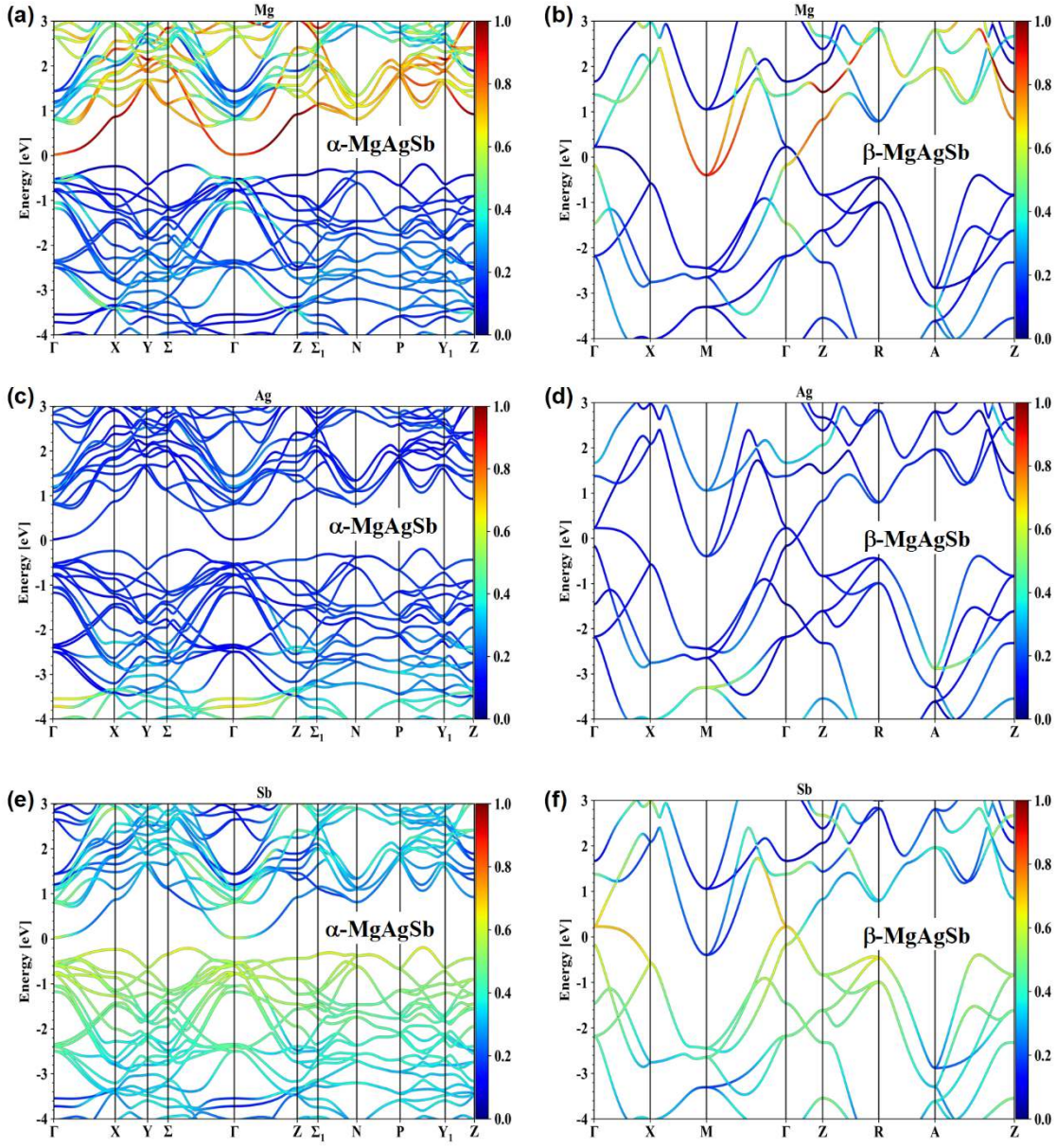

Figure 6.5. Projected band structures for the α-phase are depicted in panels (a, c, and e), while those for the β-phase are shown in panels (b, d, and f). The colour scheme represents the characteristic weight of Mg, Ag, and Sb elements. The zero energy point is aligned with the Fermi level in each respective compound[160].

In the α-phase, main contribution to the conduction band minimum (CBM) is coming from the Mg atoms, while Sb atoms contributing to the valence band maximum(VBM). Likewise, Mg and Sb atoms are responsible from the contributions to the band around Fermi level for the β-phase. Although, Mg atoms exhibit a greater contribution to the bands below the Fermi level, while Sb atoms contribute more to the bands above the

Fermi level for the β-phase in comparison with their counterparts in the α-phase. This distinction is particularly evident in the metallic bands mentioned earlier. Notably, Ag atoms do not directly contribute to the projected bands near the Fermi levels in both phases. Nevertheless, their impact on the band gap is not negligible, as well. The main effect of the Ag atoms coming from the interatomic interactions between Ag-Sb and Mg-Sb. For the β-phase, Ag–Sb represents an obvious antibonding interaction, Mg–Sb presents both s-s antibonding interaction and s-p bonding interaction. This behavior is attributed to the Ag-rearrangement and quasi two-dimensional structure. The metallic bands serve to elucidate the interlayer interactions within the sandwich structure, exhibiting enhanced electrical conductivity along the a/b axes, which is the case for the β-phase MgAgSb[160].

6.4 Thermal Properties

In general, the thermoelectric studies have been focused on enhanced electrical transport properties as well as reduced thermal conductivities. This phenomenon is related with "phonon-glass electron crystal concept (PGEC)"; where materials perform good electrical properties and high mobility such as electron crystals, combined with low thermal conductivities like glasses[162]. Materials with PGEC behavior show intrinsically low lattice thermal conductivities. To determine the reason behind the low lattice thermal conductivity, physical and chemical properties of the materials should be well-defined.

The bonding properties and strength gives information about phonon interactions as well. The weak chemical bonding characteristics led to low lattice thermal conductivity with low speed of sound, v_s. Additionally, low-frequency localized vibrations within a rigid lattice framework forces the reduced lattice thermal conductivities[163].

The phonon spectrum of the α- and β-phase MgAgSb is illustrated in Figure 6.6a and c. A phonon gap between 4–5 THz is observable for α-MgAgSb, while it is smaller for the β-phase MgAgSb. Also, when density of states was compared with each other for two phases, at around 1 THz a small bump becomes observable for α-MgAgSb differing from the β-phase. This result is related with Ag and Sb atoms, where Ag1 atoms migrated (Wyckoff site 4b) in α-MgAgSb local atomic disorders are created and resulted in low κ_L.

In the crystal structure of α-MgAgSb, three center bonding is observable for Mg-Ag-Sb with the bond lengths around 2.9–3.0 Å[164]. Three-center bonding scheme led to vibration of correlated atoms at highly low frequencies. The multicenter bonding interactions effective on electron and phonon dispersion. It causes low lying optical phonons. As a result, the larger scattering phase space as given in Figure 6.7b. are achieved with the contribution of optical phonons. The β-phase is lack of these phonon behaviors because the Ag1 atoms are eliminated from the three-center bonding structure[160].

The Figure 6.7a illustrates the group velocities of all phonons in both phases. As shown, in the α-phase the lower group velocity, which is 438 ms^{-1} within the 0–2 THz, promotes the lower lattice thermal conductivity. Since the α-phase presents a looser crystal structure than of the β-phase, it features a significant distortion and a reduced atomic coordination number, which consequently leads to a lower sound velocity than β-phase (728 ms^{-1}).

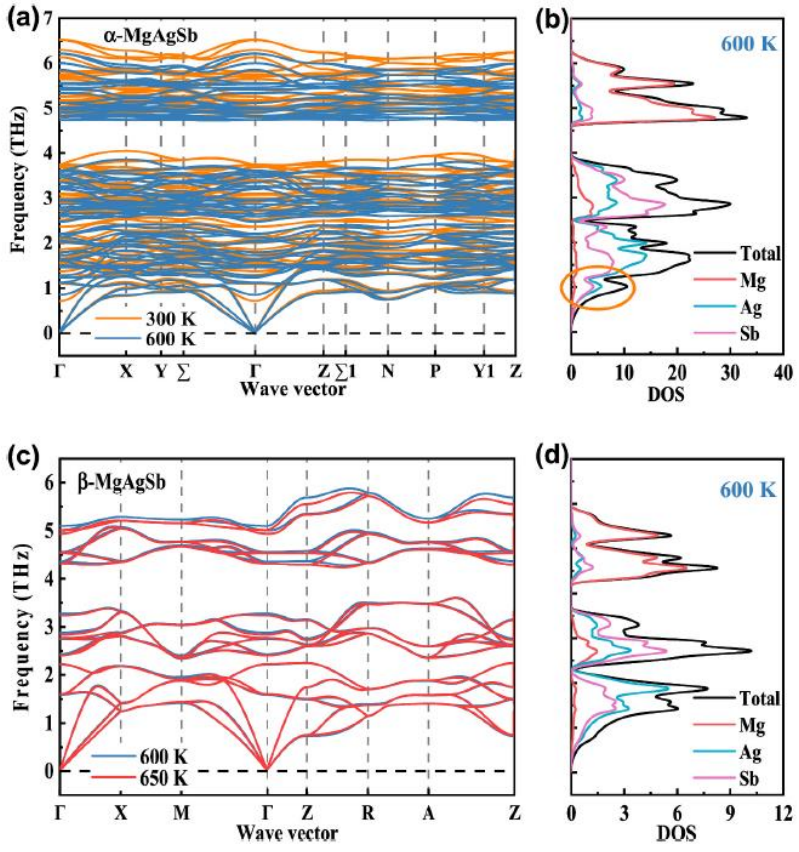

Figure 6.6. a) and c) calculated phonon dispersions, b) and d) partial phonon densities of states of α- and β-phase MgAgSb.

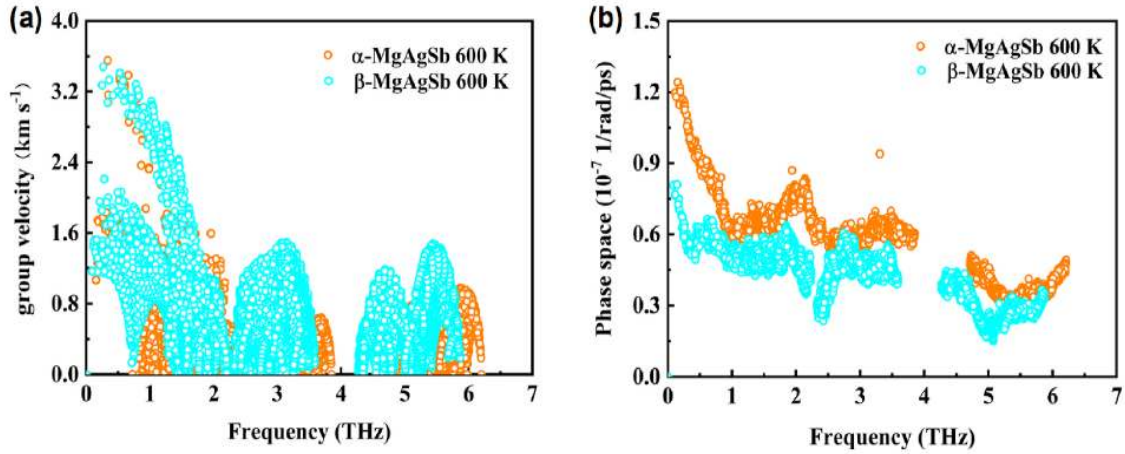

Figure 6.7. a) Phonon group velocities and b) 3-phonon scattering phase spaces of α-MgAgSb and β-MgAgSb dependent on the frequency.

As a result, the main responsible of the changes between α- and β-phase MgAgSb is the rearrangement of the Ag atoms within the crystal structure. The β-phase MgAgSb presents a more intricate interatomic connection between Mg–Sb and Ag–Sb, leading to the formation of multiple bands intersecting at the Fermi level and inducing metallization in the β-phase. The higher sound velocities together with the lower scattering phase spaces results in higher κ_L values for β-phase. On the other hand, weaker chemical bondings, low symmetry in crystal structure and vibrations of three-centered Mg-Ag-Sb bonds causes low thermal conductivity values for α-phase MgAgSb, caused by the rattling-like" thermal damping.

6.5 Sample Preparation

In this study, $MgAg_{0.97}Sb$ was synthesized through mechanical alloying by 2 step high energy ball milling process (SPEX 8000D Mixer/Mill, 1425 rpm). All the high purity raw materials of magnesium powder (Mg, 99.8%; Alfa Aesar), Ag powder (Bi, 99.999%; Alfa Aesar) and antimony shots (Sb, 99.999%; Alfa Aesar), were weighed under Ar atmosphere. To avoid oxidation during and after high energy ball milling, all sample handlings were carried out in an Ar-filled glove box. The stoichiometric amounts of elements according to the nominal composition of $MgAg_{0.97}$ were loaded with two half-

inch stainless steel balls into a stainless-steel vial and sealed under Ar. The mechanical alloying technique was applied for 8 hours. Following that the resultant powders were loaded into a graphite die under Ar atmosphere and compressed via cold press. For consolidation, spark plasma sintering (SPS) was applied under a uniaxial pressure of 85 MPa for 8 minutes at 673 K in vacuum. After controlling the purity of $MgAg_{0.97}$ phase, the consolidated $MgAg_{0.97}$ crushed into powder form through high energy ball milling process for 20 min. The achieved powder was loaded into a stainless-steel vial with the corresponding stoichiometric amount of Sb, and sealed under Ar. The second synthesis step was applied through mechanical alloying technique for 5 hours. The achieved powder was loaded into a graphite die under Ar atmosphere and compressed via cold press. Spark plasma sintering (SPS) was applied under a uniaxial pressure of 85 MPa for 8 minutes at 573 K in vacuum. The final SPS temperature hold especially bellow the phase transition temperature of 588 K [165]. To be able to see the effect of first SPS step, the same synthesis steps were followed without sintering the achieved $MgAg_{0.97}$ powder. The results have shown that with and without SPS step, the pure $MgAg_{0.97}$ phase was able to be synthesized. Also, to be able to investigate the effect of Sb amount in the composition, same synthesis processes were followed for $MgAg_{0.97}Sb_x$, where x corresponds to 1, 0.995, 0.9 and 0.975.

After achieving the consolidated $MgAg_{0.97}Sb_x$ samples, a low temperature annealing at 553 K was applied to eliminate the formation of β-phase MgAgSb. Before the annealing process, the surface of the samples was grinded through sandpapers to remove the graphite layer around the sample. After achieving a clear surface, the pellets were placed into a quartz tube which has 12 mm diameter. Then, the quartz tubes connected to a vacuum system to remove the oxygen and prevent the risks of oxidations during the annealing. After that, quartz tubes were sealed and placed into a muffle furnace. The detailed synthesis conditions were given in the Table 6.2.

The phase purity analysis and the chemical composition analysis were conducted through XRD analysis and WDS and the phase transition temperature was determined by DSC analysis. The electrical and thermal transport property analyses was applied between the temperature range of 50-300 °C. During the very first analysis, it has been observed that the electrical and thermal properties of the materials were in tendency to change the

characteristics during the cooling process. Besides, it has been approved that after the cooling process, the material behavior became more stable. Therefore, it has been determined that during the analyses, applied temperature acts like an annealing process and changes the characteristics of materials. As a result, an additional annealing step has been added to the entire synthesis procedure as described in detail above.

Table 6.2. Synthesis conditions of $MgAg_{0.97}Sb_X$ samples.

Composition	**Precursor**	**BM**	**Precursor**	**BM**	**SPS**	**Anneal**	**T** (°C)
$MgAg_{0.97}Sb$	$MgAg_{0.97}$	8 h	$MgAg_{0.97}$+ Sb	5 h	80 MPa 8 min 573 K	3 d	280
$MgAg_{0.97}Sb$	$MgAg_{0.97}$	8 h	$MgAg_{0.97}$+ Sb	5 h	80 MPa 8 min 573 K	3h	280
$MgAg_{0.97}Sb_{0.995}$	$MgAg_{0.97}$	8h	$MgAg_{0.97}$+ Sb	5 h	80 MPa 8 min 573 K	3 d	280
$MgAg_{0.97}Sb_{0.975}$	$MgAg_{0.97}$	8h	$MgAg_{0.97}$+ Sb	5 h	80 MPa 8 min 573 K	3d	280
$MgAg_{0.97}Sb_{0.99}$	$MgAg_{0.97}$	8h	$MgAg_{0.97}$+ Sb	5 h	80 MPa 8 min 573 K	3d	280
$MgAg_{0.97}Sb$	$MgAg_{0.97}$	8h	$MgAg_{0.97}$+ Sb	5 h	80 MPa 8 min 573 K	7d	280
$MgAg_{0.97}Sb$	$MgAg_{0.97}$	8h	$MgAg_{0.97}$+ Sb	5 h	80 MPa 8 min 573 K	15d	280

[1]The precursor sintered by SPS under 85 MPa pressure, for 8 min. at 673K, then ball milled for 20 min.

6.6 Characterization

6.6.1 Crystal structure and phase analysis

The crystal structure and phase purity analyses were carried out with room temperature X-ray diffraction (XRD, Rigaku Mini Flex 600, Cu Kα (λ= 1.5406 °A), 40 kV voltage and 15 mA current). First, to investigate the sintering process on the formation of $MgAg_{0.97}$, the XRD patterns of only ball milled (BM) and spark plasma sintered (SPS) $MgAg_{0.97}$ were compared as given in Figure 6.8a.

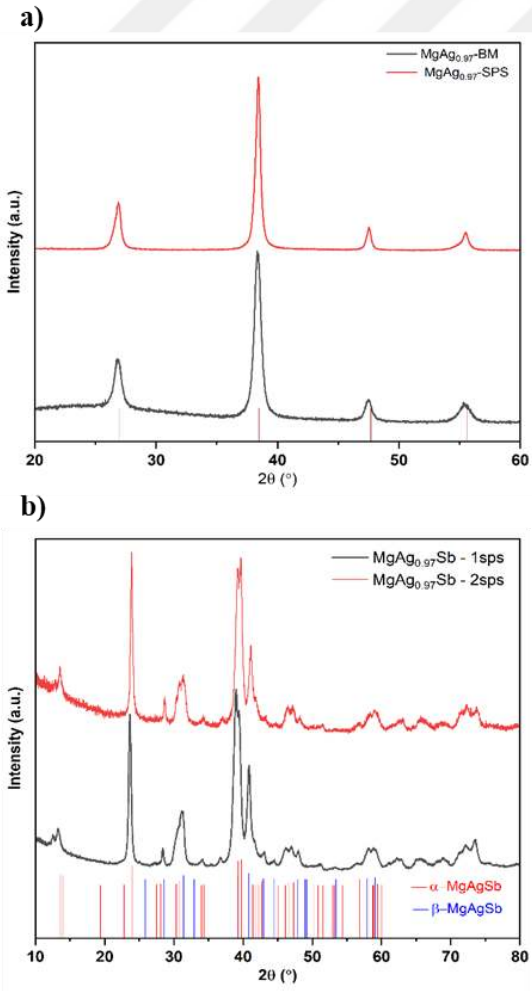

Figure 6.8. XRD patterns of a) ball milled (BM) and sintered (SPS) $MgAg_{0.97}$ and b) sintered $MgAg_{0.97}Sb$ pellets produced with only ball milled $MgAg_{0.97}$ precursor (1sps) and sintered $MgAg_{0.97}$ precursor (2sps).

Both of the BM and SPS- $MgAg_{0.97}$ patterns were in accordance with the cubic crystal structure of MgAg phase (in Pm-3m space group). No observable effect was detected by the sintering process, therefore, the experiments were followed without applying additional SPS process to the MgAg precursors.

The XRD patterns of sintered $MgAg_{0.97}Sb$ based samples synthesized with two different $MgAg_{0.97}$ precursors are given in Figure 6.8b. The XRD pattern of the samples are mainly in compliance relative to the tetragonal crystal structure of α-MgAgSb phase (in I-4c2 space group). However, after the spark plasma sintering process, the low intensity peak around at 2θ=12.5 is observed, which corresponds to one of the main peaks of Cu_2Sb-related β phase (space group P4/nmm). Also, additional peaks are observable at 2θ=13, 28.47, 38.94 and 40.9 which belong to the secondary phases of Sb and Ag_3Sb, respectively.

Since the XRD results of sintered pellets represent β phase in addition to the α-MgAgSb phase, additional annealing step was added to the synthesis process. The XRD pattern given in Figure 6.9a, shows the results belong to only sintered and 3 days anneal $MgAg_{0.97}Sb$ samples. It is clear that, after the annealing at 553 K for 3 days, the XRD peaks coming from the β phase were eliminated, especially observable around 2θ=13, 38.94 and 40.9. In addition, the broadening effect coming from the overlapped peaks of α and β-phase also diminished, and more distinct peaks were observed. When secondary phases of Sb and Ag_3Sb compared with the un-annealed sample, a decrease in the intensity of Ag_3Sb peak was achieved, although the intensity of the Sb peak seemed to be similar.

Depending on the XRD results, the effect of the composition on the purity of MgAgSb was considered. To eliminate the secondary phases of Sb and Ag_3Sb, the Sb amount of the nominal composition is taken as a variable. The XRD patterns of $MgAg_{0.97}Sb_x$, (x=1, 0.995, 0.99, 0.975) were examined and presented in Figure 6.9b. When compared with theoretical peaks, the peak positions belonging to the main phase overlap with the α-phase MgAgSb. Despite the change of the Sb amount in the nominal composition, Sb and Ag_3Sb secondary phases are still observable.

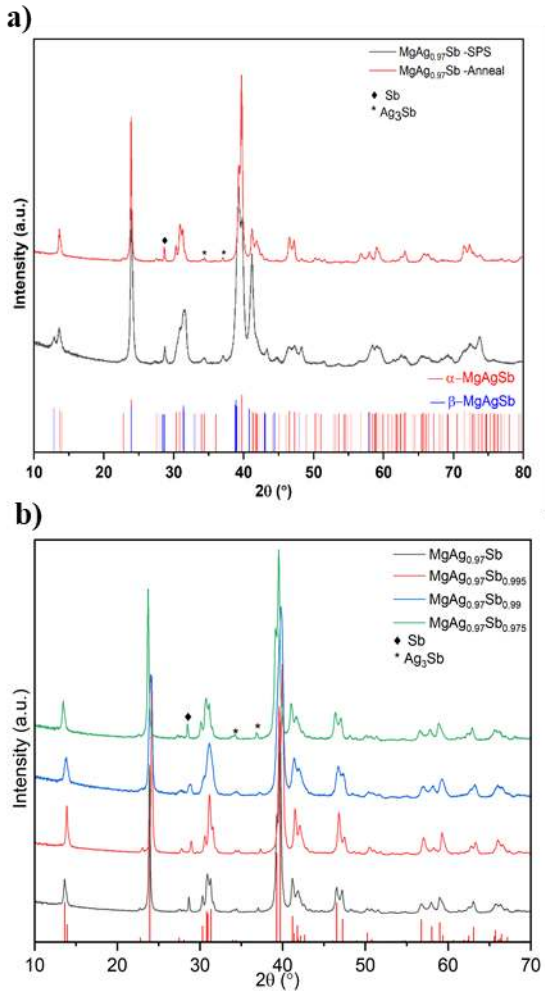

Figure 6.9. XRD patterns of a) spark plasma sintered and 3 days annealed $MgAg_{0.97}Sb$ and b) 3 days annealed $MgAg_{0.97}Sb_x$ (x=1, 0.995, 0.99 and 0.975) pellets.

6.7 Phase analysis

To investigate the thermal stability and phase transition characteristic of MgAgSb, DSC/TG analysis was applied to the consolidated samples. Figure 6.10 indicates three major endothermic effects, first a phase transition at around 588 K was observed corresponding to phase transition from α-MgAgSb to β-MgAgSb, and, second phase transition from β-MgAgSb to γ-MgAgSb at around 655 K, finally, melting peak of Ag_3Sb

impurities at around 738 K. These phase transition temperatures are related with the data reported before[154, 166]. According to TG data, no weight loss was observed.

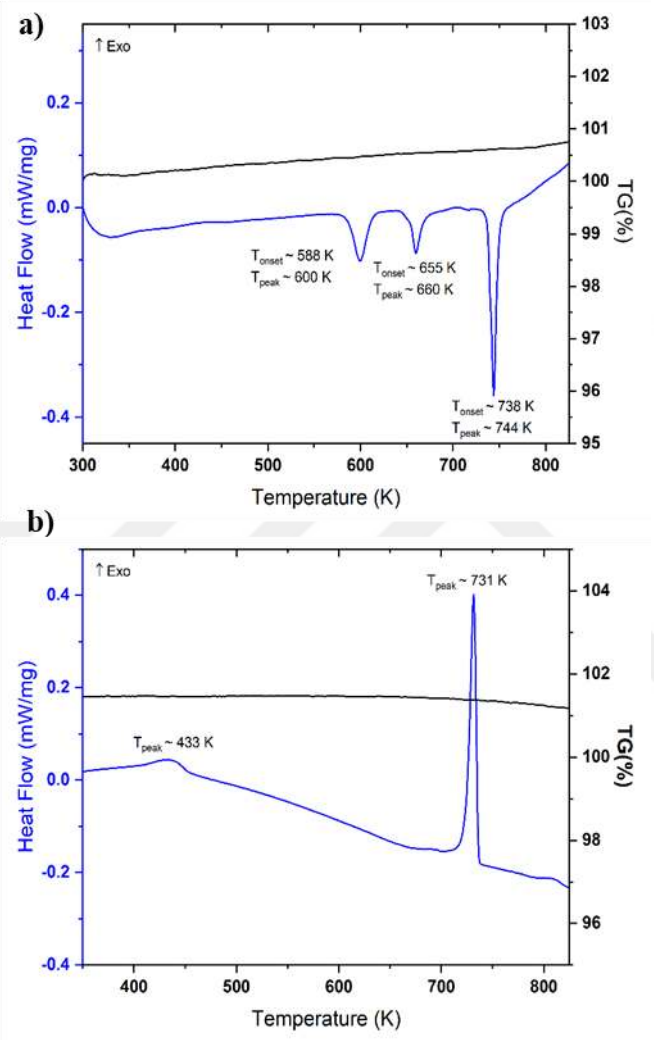

Figure 6.10. DSC/TG graphs of a) MgAgSb (scanning rate 10 K min^{-1}) showing three endothermic peaks at T_{peak}≈600, 660 and 744 K (heating) and b) cooling.

The cooling data given in the Figure 6.10b shows that after 800 K, the MgAgSb is almost completely decomposed. After DSC/TG analysis, annealing process was applied for the next batches under the phase transition temperature at 553 K.

For further investigation of the phase distribution in the microstructure, EDX analysis was applied to the $MgAg_{0.97}Sb_x$ (x=1, 0.995, and 0.975) samples. Depending on the contrast difference observed in the BSE images (Figure 6.11), it is depicted that in some points secondary phases such as Sb and Ag_2Sb presents. For all of the $MgAg_{0.97}Sb_x$

(x=1, 0.995, and 0.975) samples, the brighter areas mostly correspond to the Sb and Ag_2Sb phases.

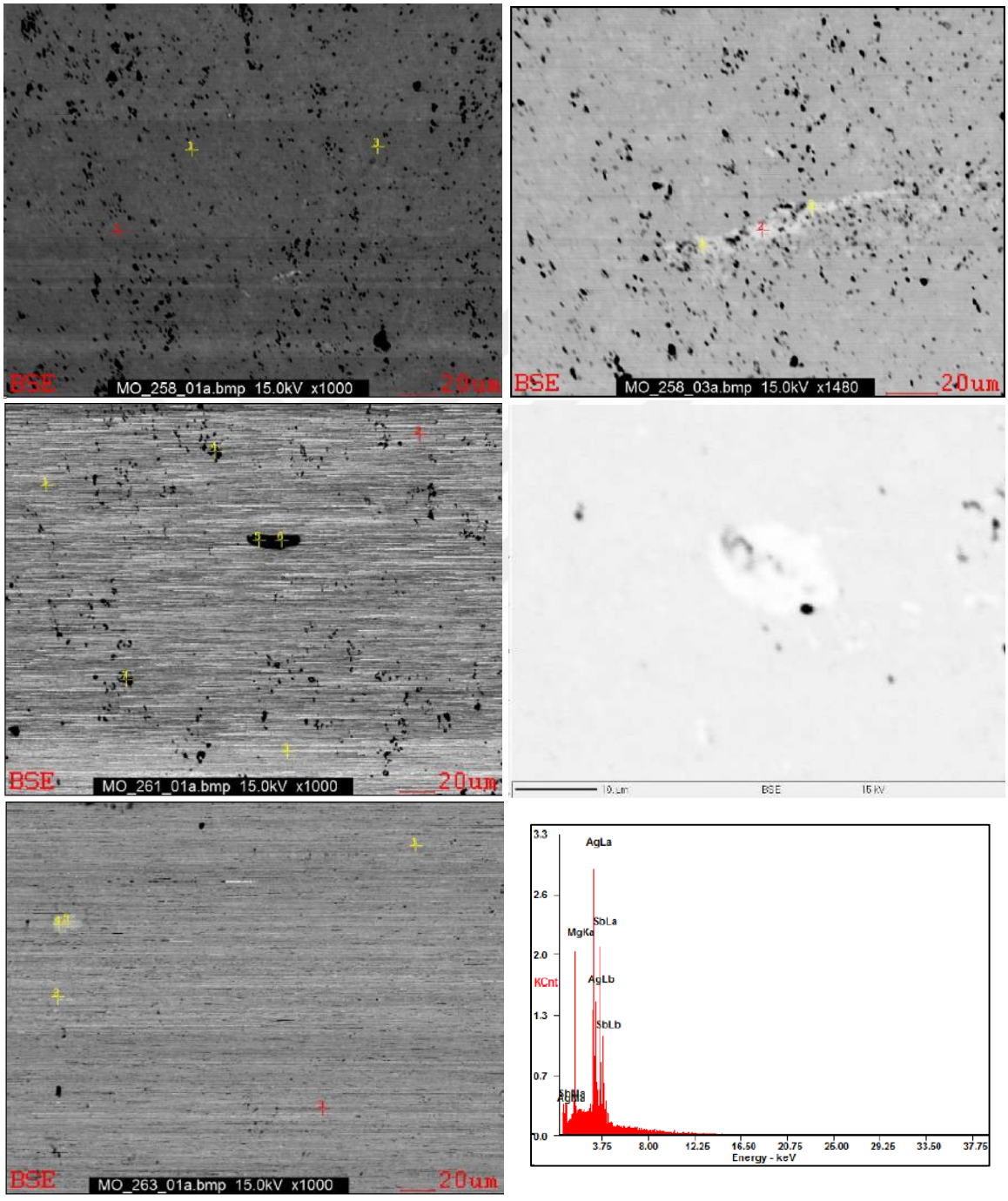

Figure 6.11. Backscattered electron (BSE) images and the selected points for EDX analysis of a,b) $MgAg_{0.97}Sb$, c,d) $MgAg_{0.97}Sb_{0.975}$, e) $MgAg_{0.97}Sb_{0.995}$ and an EDX graph taken from the main phase according to contrast.

As given in the Table 6.3 the EDX analyses taken from 7 different spots reveal the actual chemical compositions main and secondary phases observed in the structure. According to the EDS analysis, the main phase of nominal $MgAg_{0.97}Sb_x$ (x=1, 0.995, and 0.975) compositions which are taken from the homogenously distributed areas, correspond to $Mg_{1.056}Ag_{0.976}Sb_{0.938}$, $Mg_{1.063}Ag_{0.947}Sb_{0.959}$, and, $Mg_{1.069}Ag_{0.932}Sb_{0.969}$, respectively. Also, the composition selected in the Figure 6.11b, has the atomic distribution of Mg, Ag and Sb given in Table 6.3, spot #4, 5 and 6 for nominal $MgAg_{0.97}Sb$ sample, which proves the secondary phases with higher Sb amounts. The atomic distribution of Mg, Ag and Sb atoms from the selected area given in Figure 6.11c, is detected as given Table 6.3 spot #4, for the $MgAg_{0.97}Sb_{0.975}$ sample. Lastly, for the $MgAg_{0.97}Sb_{0.995}$ some points only corresponded to the Sb_{La} and Sb_{Lb} specific energy values, which proves the existence of the elemental Sb in the microstructure.

Table 6.3. The EDX analysis results of $MgAg_{0.97}Sb_x$ (x=1, 0.995, and 0.975).

Nominal $MgAg_{0.97}Sb$				**Nominal $MgAg_{0.97}Sb_{0.975}$**				**Nominal $MgAg_{0.97}Sb_{0.995}$**			
Spot #	**At. %**			#	**At. %**			#	**At. %**		
	Mg	**Ag**	**Sb**		**Mg**	**Ag**	**Sb**		**Mg**	**Ag**	**Sb**
1	35.94	32.56	31.50	1	36.14	31.03	32.82	1	36.14	30.55	33.31
2	34.40	33.80	31.80	2	36	31.92	32.09	2	36.07	31.72	32.21
3	36.32	32.21	31.47	3	35.85	31.18	32.97	3	35.17	33.43	31.41
4*	20.12	14.40	65.49	4*	05.38	60.29	34.34	4*	-	-	100
5*	08.19	08.03	83.78					5*	-	-	100
6*	13.70	11.06	75.25								
7*		03.09	96.91								

Enhanced compositional accuracy was attained via WDS analysis through the aggregation of ten individual measurement data points (Figure 6.12 and Table 6.4). The compositions were calculated by estimating the nominal total number of atoms in the composition as 2.97. The Ag content is increasing slightly with the decrease in the Sb content in nominal composition. While the amount of Ag is far from the nominal Ag

content $Mg_{1.01}Ag_{0.911}Sb_{1.045}$(for $MgAg_{0.97}Sb$), with the decrease in the Sb content from 1 to 0.995, the nominal composition converges to approximately $MgAg_{0.945}Sb$ (for $MgAg_{0.97}Sb_{0.995}$). However, when the content of Sb is further decreased from 0.995 to 0.975, the content of Mg slightly increases $Mg_{1.025}Ag_{0.945}Sb_{0.999}$ (for $MgAg_{0.97}Sb_{0.975}$), which might be related to formation of Ag_3Sb secondary phase.

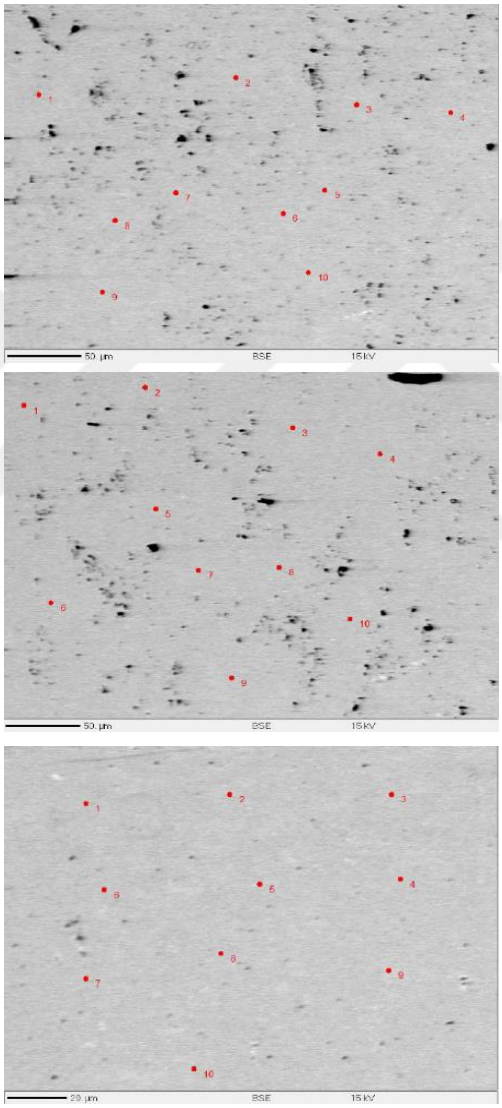

Figure 6.12. SEM images of a) $MgAg_{0.97}Sb$, b) $MgAg_{0.97}Sb_{0.975}$ and c) $MgAg_{0.97}Sb_{0.995}$ with corresponding 10 different spots used for WDS analysis.

Table 6.4. The WDS analysis results of $MgAg_{0.97}Sb$, $MgAg_{0.97}Sb_{0.975}$ and $MgAg_{0.97}Sb_{0.995}$.

Nominal $MgAg_{0.97}Sb$				**Nominal $MgAg_{0.97}Sb_{0.975}$**			**Nominal $MgAg_{0.97}Sb_{0.995}$**		
	At.%	**Wt.%**	**StdDev wt.%**	**At.%**	**Wt.%**	**StdDev wt.%**	**At.%**	**Wt.%**	**StdDev wt.%**
Mg	34.09	9.83	0.03	34.52	10.01	0.03	33.85	9.73	0.03
Ag	30.69	39.27	0.14	31.82	40.97	0.14	31.83	40.61	0.14
Sb	35.21	50.84	0.13	33.66	48.91	0.13	34.31	49.41	0.14
Total	100	99.94		100	99.89		100	99.75	
	$Mg_{1.01}Ag_{0.911}Sb_{1.045}$			$Mg_{1.025}Ag_{0.945}Sb_{0.999}$			$Mg_{1.005}Ag_{0.945}Sb_{1.019}$		

6.8 Transport Property Measurements

In Figure 6.13a and b, the electrical resistivity values and Seebeck coefficients of $MgAg_{0.97}Sb_x$ (x=1, 0.995, and 0.975) samples are plotted as a function of temperature. The samples show a semi-conducting behavior, where electrical resistivity values tend to decrease with the increasing temperature. Similarly, the Seebeck coefficients decrease with the increase in temperature. The positive value of the Seebeck coefficient proves that holes are the main charge carriers, and, the material has *p*-type character. The electrical properties of the samples are similar to the literature without any doping strategies. To obtain the optimum composition, the amount of Sb element was taken as a variable.

In Figure 6.13a, the electrical resistivity increase with the decreased amount of Sb. Considering the ternary phase diagram given in Figure 6.3, the both compositions are in the blue region. Considering the real composition of the samples it seems like the carrier concentration of the samples are mostly related to the amount of Ag in the stoichiometry. However, the change in the amounts of secondary phases and the distribution of them in the microstructure might be effective on the resistivity values. Since it is difficult to control the distribution and formation of secondary phases. The change in the stoichiometry affects the resistivity values remarkably. As discussed by Iqbal et.al, the dyscrasite Ag_3Sb phase can play a role in introducing positive carriers, which have an effect on the decrease in electrical resistivity values especially at low temperatures as given in Figure 6.13a for the $MgAg_{0.97}Sb$ composition[158, 167, 168]. In accordance with the

compositions given in Table 6.4, the lowest electrical resistivity value is achieved for the $Mg_{1.01}Ag_{0.911}Sb_{1.045}$, where Ag-Sb related secondary phases were observed from the EDX analysis. Also, the highest resistivity value is obtained for the $MgAg_{0.97}Sb_{0.995}$ composition, which has the highest Ag content in the main composition, and no observable Ag_3Sb phase is observed from the EDX analysis compared to other samples. Basically, in solid-state chemistry, in line with the typical valence state MgAgSb can be expressed as $Mg^{+2}Ag^{+1}Sb^{-3}$, therefore, the decrease in the Ag amount or an increase in the Sb amount in the crystal structure would led to an increase in the hole concentration. In accordance with that, the electrical resistivity value is highest for the $MgAg_{0.97}Sb_{0.995}$ composition. And, the lowest resistivity value was achieved as 2.4 mOhm.cm at 330 K similar with the result achieved by Liu et. al[169].

As illustrated in Figure 6.13b, only a slight change was observed for Seebeck coefficients. For the samples with Sb amounts of 0.975 and 1, the Seebeck coefficient values were almost the same. Only a slight increase in Seebeck coefficient is observed with the content of Sb (0.995). Interestingly, this phenomenon is not compatible with the change in resistivity values. Therefore, the decrease in the resistivity with the increased amount of secondary phases, might be related to grain boundary phases. In the case of Ag_3Sb phases placed on the grain boundaries, the decrease in resistivity values might be coming from the chemically altered grain boundary complexions with Ag_3Sb. Hall effect measurements also show that the carrier concentration is almost same for the samples with different amounts of Sb (1 and 0.975), however, the Hall mobility differ from each other (Figure C 1). This support the idea of variation in resistivity values most probably come from the change in the carrier scattering. On the other hand, after first measurement of the electronic transport properties, an enhancement is observable while measuring during the cooling (Figure C 2).

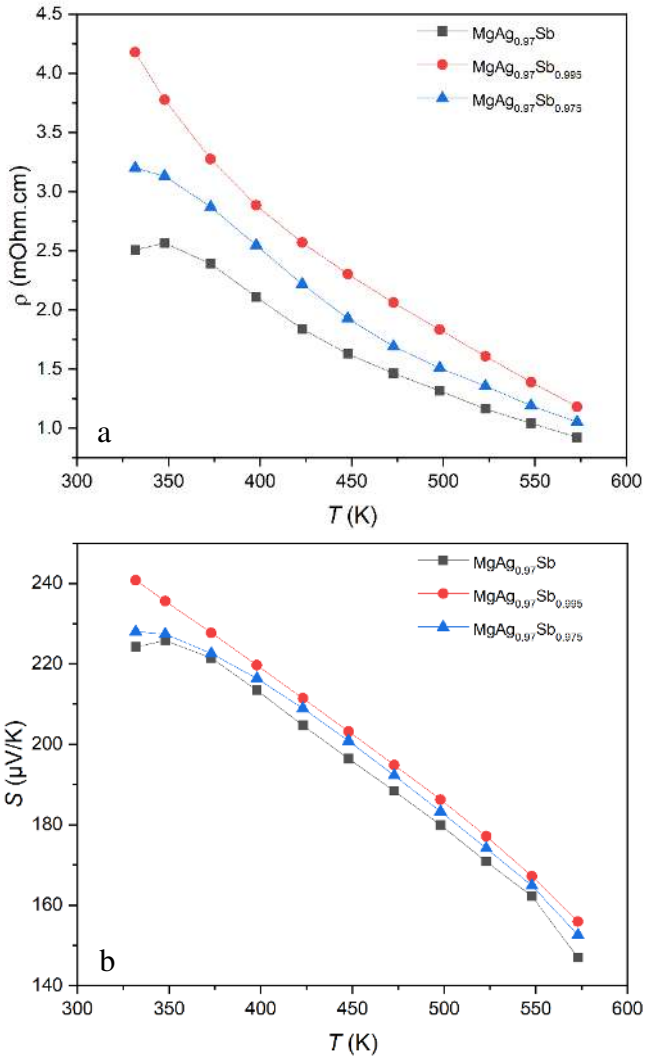

Figure 6.13. a) Electrical resistivity and b) Seebeck coefficient of $MgAg_{0.97}Sb_x$ (x=1, 0.995, and 0.975) as a function of temperature.

The temperature-dependent behavior of thermal conductivity is presented in Figure 6.14. All the thermal conductivity values increase with increasing temperature. This behavior is consistent with the literature. In the literature, the thermal conductivity values are between 0.7 ile 0.9 W/mK[170-172]. In this study, similarly lowest thermal conductivity of 0.75 W/mK was achieved at 330 K. Regardless the Sb content, all the thermal conductivity values were observed similar to each other. Interestingly, a jump was obtained for $MgAg_{0.97}Sb$ phase at 573 K. Although the onset of the phase transition temperature was achieved as 588 K, this increase in the thermal conductivity is seem to

be related with the phase transition. In relation with the deviations in the measurement temperatures and the measurement atmosphere, it is possible to trigger the onset phase change.

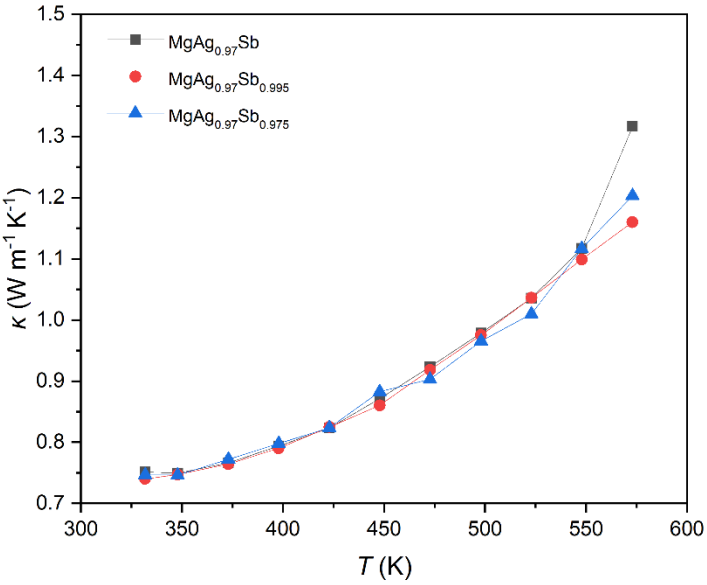

Figure 6.14. Total thermal conductivity values of $MgAg_{0.97}Sb_x$ (x=1, 0.995, and 0.975) as a function of temperature.

In Figure 6.15, the dimensionless thermoelectric figure of merit (zT) values of different $MgAg_{0.97}Sb_{1-x}$ (x=0,995, 0,975 ve 1) samples are presented. According to measurements, the low temperature zT values differ between 0.6 to 0.9, while the highest zT value was achieved at 523 K as 1.21. Combining the low thermal conductivity, lowest resistivity with optimum Seebeck coefficient the highest zT observed for $MgAg_{0.97}Sb$ composition. However, because of the complex phase diagram, secondary phases and transport properties of the materials, it is difficult to say that the optimum composition was produced.

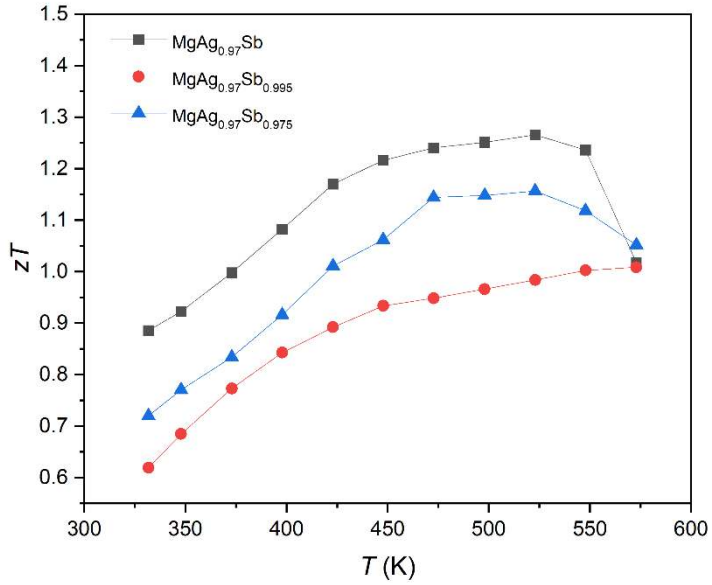

Figure 6.15. Temperature dependence of zT curves of $MgAg_{0.97}Sb_x$ (x=1, 0.995, and 0.975).

6.9 Conclusions

Polycrystalline thermoelectric materials with nominal compositions of $MgAg_{0.97}Sb_x$ (x=1, 0.995, and 0.975) were synthesized through high-energy ball milling process and consolidated by spark plasma sintering method. The phase transition behavior of MgAgSb-based materials was investigated by differential scanning calorimetry measurements, and phase transitions at around 588 K (α- to β-MgAgSb) and 655 K (β- to γ-MgAgSb) were detected. To investigate the effect of MgAg precursor, two different routes with and without sintering the MgAg powder were followed. As a result of no difference between the XRD patterns, the further experiments proceeded without additional SPS step. Although the low sintering temperature of 573 K, additional XRD peaks coming from the β-MgAgSb phase was observed. Therefore, an extra annealing step at 553 K for 3 days was incorporated into the synthesis methodology. Following the annealing process, a significant difference in the XRD patterns was noted, particularly regarding the elimination of secondary phases. Afterwards, the effect of the content of Sb on the purity and transport properties of $MgAg_{0.97}Sb$ was investigated. Based on the

assessment of electronic transport properties, it was deduced that variations in the quantities of secondary phases, namely Ag_3Sb and Sb, exert an influence on the transport characteristics. Optimal electronic transport properties were attained with the nominal composition of $MgAg_{0.97}Sb$. The effect of the amount of Sb and Ag in the crystal structure was observed from the electrical transport properties. However, it is difficult to achieve the exact composition as nominal composition for the MgAgSb system. On the other hand, no notable alteration was discerned in the thermal conductivity. By integrating the thermal and electronic transport properties, a peak figure of merit (zT) of 1.21 was achieved at 523 K, while a lower temperature zT of 0.89 was observed at 332 K.

Further investigations have been planned based on insights from both DSC analysis and XRD patterns. It has been determined that an additional annealing process is necessary to enhance the purification of the MgAgSb phase from secondary phases. With this aim in mind, the impact of the synthesis parameters outlined in Table 6.2 on the purity of MgAgSb was examined in the next chapter.

Chapter 7

THE EFFECT OF SYNTHESIS PARAMETERS ON THERMOELECTRIC TRANSPORT IN MgAgSb

7.1 Introduction

Lately, MgAgSb system became attractive for thermoelectric devices, because of their good thermoelectric performance at low temperature ranges with environmental friendly behaviour in addition to their low cost[173]. However, the phase transition and impurities generates a challenge for the achievement of high zT values at RT[153, 174]. The thermoelectric transport properties are in relation with the residual impurity phases, drastically[161]. Different synthesis methods, as well as different annealing procedures play an important role on the synthesis of MgAgSb with varying thermoelectric performances[159, 175-179].

As discussed previous chapter, as sintered MgAgSb contains both α and β phases together. After annealing process, XRD patterns show that α-MgAgSb achievable, and no detectable β phase observed. However, there are still some secondary phases exist. On the other hand, there are arguments on the effect of Ag_3Sb secondary phases, that because the metallic character of it, Ag_3Sb might have an effective role on the increase of carrier concentration[168]. To be able to enhance the thermoelectric performance, several studies have been conducted on annealing process with different temperature and holding times. Ying et al. applied an annealing step at 553 K with a heating rate of 5/min for 2 weeks, and claimed and achieved α-MgAgSb with a zT value of around 0.5 at RT, however, still included Sb and Ag_3Sb phases as well[175]. Zheng et al. applied the annealing process at 573 K for durations of 3, 10 and 30 days. For the un-doped sample with 10 days of annealing process, they claimed to achieve a zT near 1 at 325 K[170]. Contrary, Iqbal et al. reported a zT value of 0.4 at 350 K with annealing at 575 K for two weeks[158]. The zT of

0.1 to 0.7 at 325 K is reported by Lei et al. with annealing at 575 K for two weeks[180]. They also argued the obtain pure MgAgSb without impurities with increased sintering temperature at 723 K. Zihang et al., also discussed the effect of temperature on the hot press, and concluded that at high temperatures, a recovery effect come forward and decrease the formation of Ag vacancies, resulting in an increase in electrical resistivity values[168]. Contradictory, Xie et al., also studied the effect of sintering temperature in between 423-573 K, and resulted in higher zT of around 1 at 325 K with low sintering temperature of 473 K. They suggested that the increasing sintering temperature causes proliferation of Ag vacancies by breaking the unstable Ag atoms from the lattice[181]. Interestingly, Zhao et al., declared obtaining a high zT of 0.85 for $MgAg_{0.97}Sb_{0.99}$ at 325 K, with annealing for 30 minutes[161]. However, all those studies differ from each other in terms of some compositional differences or synthesis procedures. Yet, it is difficult to attribute the thermoelectric performance of MgAgSb based materials to specific synthesis conditions or starting composition. Every study result in different transport properties even some conditions remain same. Therefore, it is challenging to achieve a distinct thermoelectric performance for *p*-type MgAgSb.

In this chapter, sintering temperature, time and annealing time has been studied for enhancement of thermoelectric properties, as well as stabilizing the achieved result. As discussed previous chapter, annealing process enhanced the purity of the samples. Beyond that, sintering temperature is studied to eliminate the effect of secondary phases observed from the XRD patterns.

7.2 Sample Preparation

In this chapter, same method mentioned in Chapter 6 was utilized to prepare $MgAg_{0.97}Sb$. However, by examination of the achieved transport properties, the parameters of synthesis process were altered. 2 step high energy ball milling process (SPEX 8000D Mixer/Mill, 1425 rpm) remained same. Raw materials with high purities of magnesium powder (Mg, 99.8%; Alfa Aesar), Ag powder (Bi, 99.999%; Alfa Aesar) and antimony shots (Sb, 99.999%; Alfa Aesar) were handled under Ar atmosphere, during all weighing and preparation steps. The mechanical alloying technique was applied for 8

hours and 5 hours as mentioned in Chapter 6. Following that the resultant powders were loaded into a graphite die under Ar atmosphere and compressed via cold press. For consolidation, spark plasma sintering (SPS) was applied under a uniaxial pressure of 80 MPa for 8 minutes at 523, 573 and 673 K in vacuum. The effect of the sintering temperature was investigated.

The consolidated $MgAg_{0.97}Sb$ samples, then annealed at low temperature of 553 K for the elimination of β-phase MgAgSb. Before the anneal process, the surface of the samples was grinded through sandpapers to remove the graphite layer around the sample. After achieving a clear surface, the pellets were placed into a quartz tube which has 12 mm diameter. Then, the quartz tubes connected to a vacuum system to remove the oxygen and prevent the risks of oxidations during the annealing. After that, quartz tubes were sealed and placed into a muffle furnace. The sealed tubes were kept in the furnace at 553 K for several times; 3 h, 3 days, 7 days and 15 days. And the effect of the annealing time was examined. For further investigation, additional heat treatment was applied for the samples ball milled and sintered with the same synthesis parameters as mentioned above annealed for 3 days. An additional heat treatment was applied with the profile of heating up to 300°C in 260 min. and waited at that temperature for 10 min. and then cooled down to the room temperature. The detailed synthesis conditions were given in the Table 7.1.

Table 7.1. The synthesis conditions with varying SPS temperature and annealing time.

Composition	**BM**	**SPS conditions**	**Anneal**	**T** (°C)	**HT**
$MgAg_{0.97}Sb$	8+5 h	80 MPa 8 min 573 K	**3 h**	280	-
$MgAg_{0.97}Sb$	8+5 h	80 MPa 8 min 573 K	**3 d**	280	-
$MgAg_{0.97}Sb$	8+5 h	80 MPa 8 min 573 K	**7 d**	280	-
$MgAg_{0.97}Sb$	8+5 h	80 MPa 8 min 573 K	**15 d**	280	-
$MgAg_{0.97}Sb$	8+5 h	80 MPa 8 min **523** K	3d	280	-
$MgAg_{0.97}Sb$	8+5 h	80 MPa 8 min **573** K	3d	280	-
$MgAg_{0.97}Sb$	8+5 h	80 MPa 8 min **673** K	3d	280	-
$MgAg_{0.97}Sb$*	8+5 h	80 MPa 8 min 673 K	3d	280	300 °C 260 min.

7.3 Characterization

7.3.1 Crystal Structure Analysis

The XRD graphs of $MgAg_{0.97}Sb$ samples with different sintering temperatures of 523, 573 and 673 K are plotted in Figure 7.1 after annealing process. The main peaks observed from the XRD patterns correspond to the tetragonal crystal structure of α phase with the $I\bar{4}c2$ space group. At 523 K, a small intensity additional peak is observed around 11.5°. With the increase in sintering temperature a decrease is obtained for elemental Sb peak, especially. As discussed in the introduction, there are studies have been conducted on the increase of the temperature during the sintering, and discussed the idea of recovery effect of high temperatures in terms of eliminating the vacancies and suppressing the formation of secondary phases[168]. The relatively, low intensities of the secondary phases observed for the 673 K, compared to main phase, supports this idea.

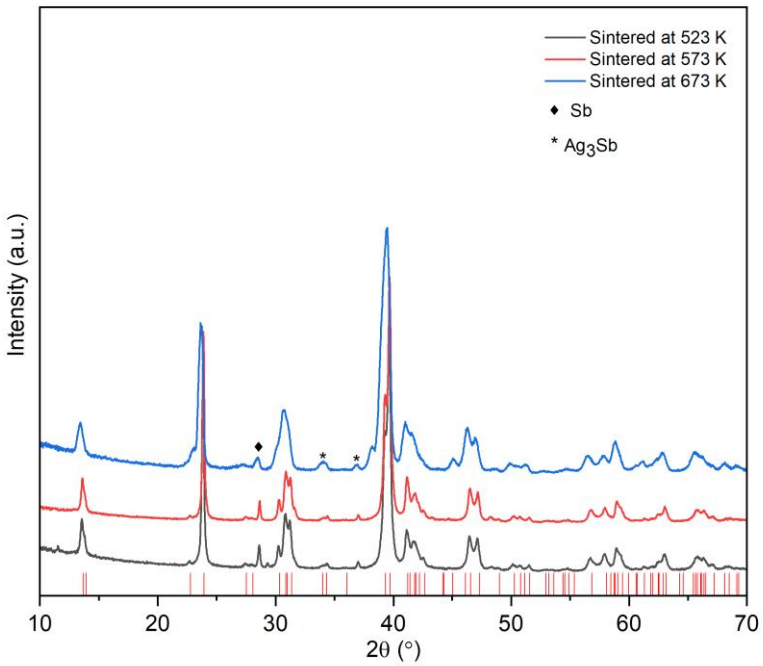

Figure 7.1. XRD patterns of 3 days annealed $MgAg_{0.97}Sb$ samples sintered at 523, 573 and 673 K, respectively.

For further investigations, the effect of the annealing temperature is studied. Figure 7.2 presents the XRD graphs of $MgAg_{0.97}Sb$ samples with different anneal durations of 3 hours, 3 days, 7 day and 15 days, respectively. The main peaks observed from the XRD patterns correspond to the tetragonal crystal structure of α phase with the $I\bar{4}c2$ space group. The crystallinity of sample with 3 hours annealing is weaker than the other samples. All the samples contain Sb and Ag_3Sb secondary phases regardless of annealing time. However, the longer annealing process has an effect on the peak positions as observed from the XRD patterns. Through the 7 days of annealing, peaks shift toward higher 2θ values, while the 15 days of treatment resulted in a shift towards lower 2θ values. It might be related to change of intrinsic vacancy or anti-site defects in the crystal structure, with the applied temperature. Similar behavior was observed by Li et al., connected to lattice expansion in the crystal structure because of the anti-site defects[182].

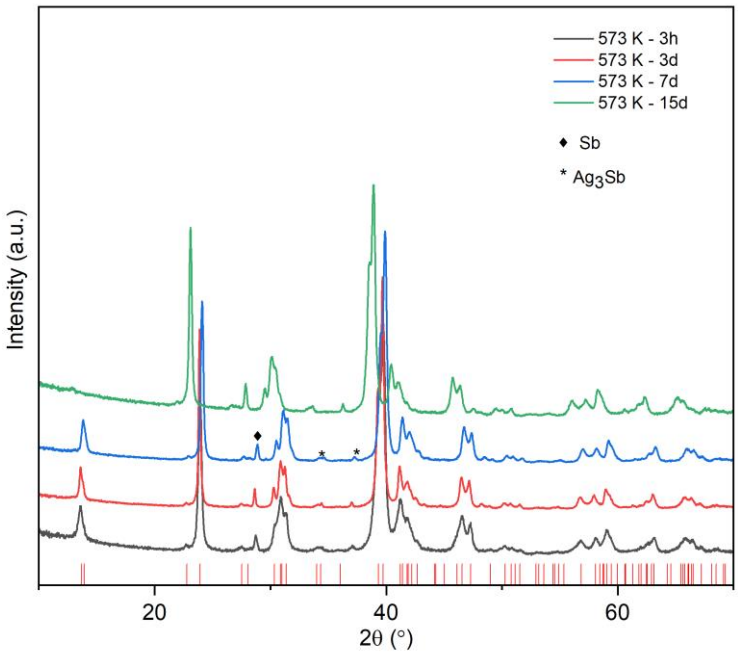

Figure 7.2. XRD patterns of $MgAg_{0.97}Sb$ samples sintered at 573 K, with different annealing durations of 3h, 3d, 7d and 15 days respectively.

After examining the transport properties an interesting phenomenon was observed from the electrical transport properties, which will be discussed in transport property characterization. As reported from another study before, the transport properties seem to be enhanced after the first measurement[158]. While analysing the transport properties samples are heated up to 300°C, while taking measurements every 25°C. Therefore, it is decided to apply a similar heat treatment procedure for following samples. For the samples sintered at 673 K and annealed for 3 days, additional heat treatment was performed by heating them to 300°C in 4.5 h and keeping for 10 minutes. This procedure was applied several times to be able to discuss the stability of the procedure. The achieved XRD patterns of heat treated samples are given in Figure 7.3. Each samples show secondary phases of Ag_3Sb and Sb in the XRD patterns, also with increased sintering temperature a small neck formation was observed near the main peak of α-MgAgSb, which correspond to the β-phase MgAgSb, since the sintering temperature was higher than the phase transition temperature, 3 days of annealing might not be sufficient to reinforce the phase transition. However, after applying the special heat treatment, the

peak intensity observed from the β-phase is decreased for each HT1, HT2 and HT3 samples. Annealing time is also increased from 3 days to 15 days for the samples sintered at 673 K. The results are given in the Appendix C (Figure C 3).

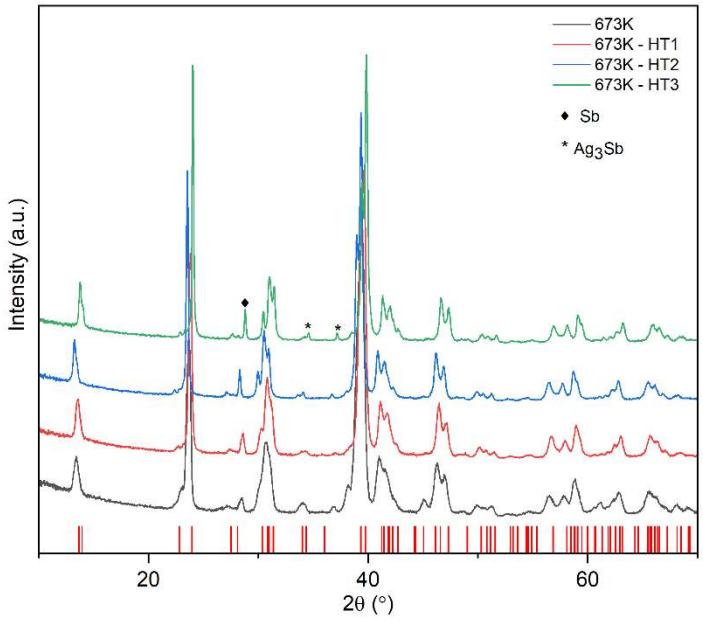

Figure 7.3. XRD patterns of 3 days annealed $MgAg_{0.97}Sb$ samples sintered at 673 K and heat treated samples for 3 different benches as HT1, HT2 and HT3.

Lattice parameters of the heat treated and un-treated sample is also calculated using WinCSD for lattice parameter refinement. The achieved parameters are represented in Table 7.2. Previous studies reported the lattice parameters of α-MgAgSb as a=b=9.163Å and c=12.701Å, and a=b=9.1761 and c=12.6960Å using Rietveld refinement[153, 154]. Another study conducted by Li et al., calculated the lattice parameters for $MgAg_{0.97}Sb_{0.99}$ as a=b=9.1687(2), c=12.7075(3) Å, respectively[182]. The lattice parameters achieved in this study are quite similar to each other considering the standard deviation. After heat treatment both a and c tend to decrease compared to un-treated sample. Also, to be able to see the effect of heating during the ZEM-3 measurement, lattice parameters of the heat treated sample is calculated. Compared to pristine lattice parameters, almost no noticeable change is observed after ZEM-3 measurements which suggest the idea that the effect of the applied temperature profile on the crystal structure is negligible after the heat treatment. Previously, Li et al., has discussed the effect of Ag^{+} and Mg^{2+} migrations. As

a result of these ion migrations, local atomic disorders are observable for MgAgSb. Normally, Ag atoms are occupied in the half of Sb tetrahedrons, while Mg atoms are placed in the centers of all the Sb octahedrons. However, it creates a contradictory because of the higher ionic radius of Ag^{+}(1.26 Å) and lower ionic radius of Mg^{2+}(0.66 Å). Therefore, a distorted energy is obtained because of the size mismatch. Through the heat treatment at 573 K, mutual ion migration tends to take a place with the increase of temperature[182]. As a result, cell parameters changes after heat treatment.

Table 7.2. Lattice parameters of heat treated and only annealed $MgAg_{0.97}Sb$ samples.

	a (Å)	**c (Å)**	**V(Å^3)**
Without heat treatment	9.18(3)	12.74(4)	1073.89
With heat treatment	9.15(1)	12.72(2)	1065.32
After ZEM-3 for sample_HT	9.152(7)	12.72(1)	1065.36

7.3.2 Phase Analysis

To investigate the thermal stability and phase transition characteristic of MgAgSb, DSC/TG analysis was applied to both the sample annealed for 3 days and sample heat treated after the annealing step. Figure 7.4 illustrates the DSC/TG analysis which taken as 2 heating/cooling cycle to be able to see the effect of heating and cooling process on the phase transition during the transport property measurements. Therefore, the measurement applied up to 300°C, which is the highest temperature of the ZEM-3 measurement. According to DSC graphs, no notable peaks are observed. This result may that there is no phase transition occurring in either sample. Therefore, there is no expectation for any phase transition under the conditions of transport property measurements. The DSC graphs with scanning rate of 10 K min^{-1}, with and without holding time also given in Figure C 4.

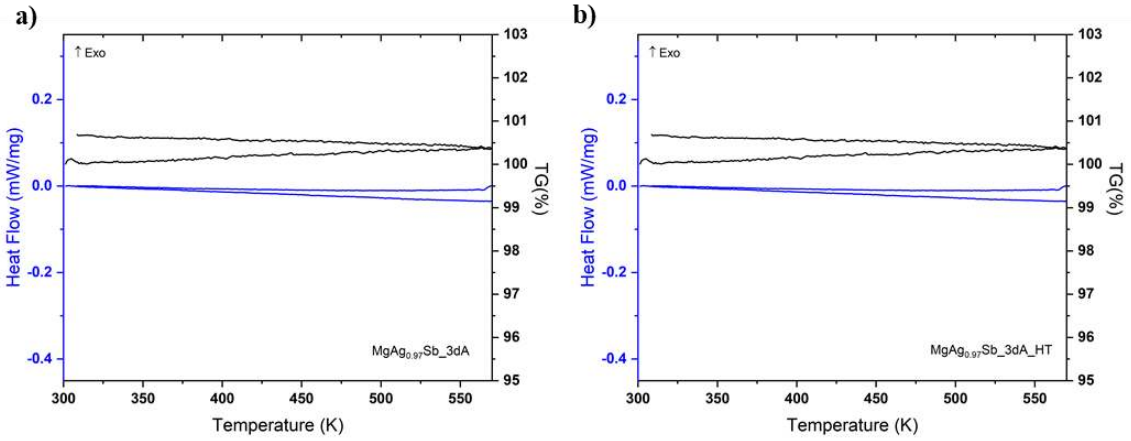

Figure 7.4. DSC/TG (scanning rate 2 K min^{-1}) graphs of a) $MgAg_{0.97}Sb$ sample after annealing for 3 days and b) heat treated $MgAg_{0.97}Sb$ sample after annealing.

EDX analysis is also utilized for further investigation of the phases in the microstructure, to the $MgAg_{0.97}Sb$ samples sintered at 673K with and without heat treatment. To investigate the different phases obtained through the contrast, the EDX analysis is applied for different spots as given in Figure 7.5. The corresponding amounts of the elements are given in Table 7.3. Especially, the secondary phases in the microstructure is investigated. The brighter areas (#1, 2 for un-treated and treated samples) selected from the BSE images mostly correspond to the higher amounts of Ag element, which is consistent with the XRD peaks achieved for Ag_3Sb phases. On the other hand, small brighter spots numbered as 7, 8 and 3, 4 respectively, correspond to higher Sb amounts for both sample with similar atomic percentages of Mg and Ag elements. This result is related to elemental Sb peak observed from the XRD results, in addition to the main phase MgAgSb phase. Other than that, the main phases examined from the spots 5 and 6 from the un-treated sample correspond to the chemical composition of $MgAg_{0.965}Sb_{0.996}$. And, #7 and 8 from the heat treated sample align with the composition of $Mg_{0.97}Ag_{0.98}Sb_{1.01}$. Both samples present similar chemical composition with starting composition with small deviations. However, it might play a role on the electronic and thermal transport properties.

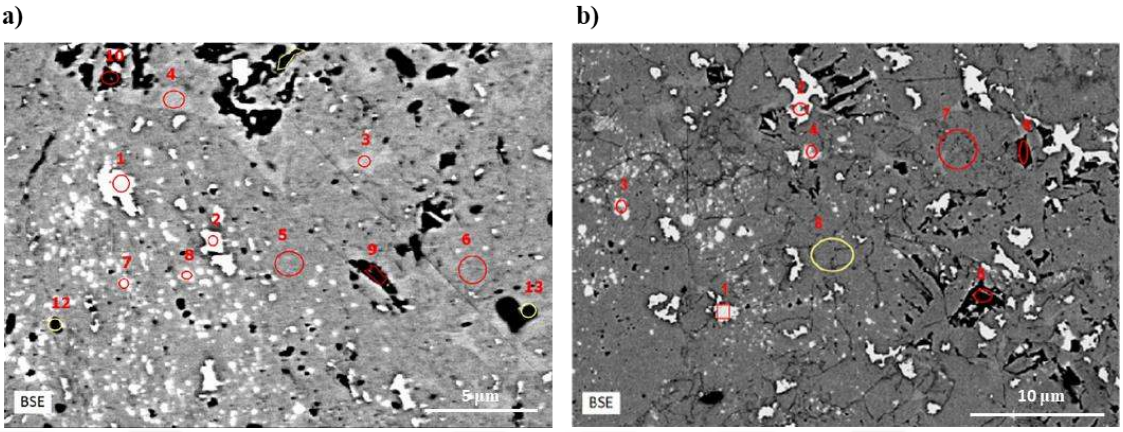

Figure 7.5. BSE images (HV=10 kW, WD=10 mm) of a) $MgAg_{0.97}Sb$ without heat treatment and b) after heat treatment.

Table 7.3. The EDX analysis results of $MgAg_{0.97}Sb$ with and without heat treatment.

Nominal $MgAg_{0.97}Sb$				**Nominal $MgAg_{0.97}Sb$ (HT)**			
Spot #	**At. %**			#	**At. %**		
	Mg	**Ag**	**Sb**		**Mg**	**Ag**	**Sb**
1	4.53	67.14	28.33	1	4.72	70.82	24.46
2	7.06	62.60	30.34	2	7.59	66.74	25.67
3	30.80	34.75	34.46	3	17.33	17.33	65.34
4	32.51	33.71	33.78	4	15.61	11.76	72.63
5	34.01	32.50	33.49	5	45.35	14.28	40.37
6	33.94	32.53	33.53	6	47.13	13.97	38.90
7	23.19	22.42	54.39	7	32.73	33.02	34.26
8	23.59	21.88	54.53	8	32.47	33.27	34.26
9	46.36	17.27	36.38				
10	47.09	16.40	36.51				
Mean	28.31	34.12	37.57	Mean	25.37	32.65	41.99

7.3.3 Transport Property Measurements

Transport Properties of Samples with Different Sintering Temperature

First, the effect of the sintering temperature on the thermoelectric properties have been investigated. Figure 7.6a and b provide the graphs of the electrical resistance and Seebeck coefficient of the materials. The electrical resistivity and Seebeck values show a decrease with increasing temperature. This behavior is in accordance with the semiconducting-like transport properties. The resistivity values of the samples sintered at 523 and 673 K are very similar to each other, while a significant decrease is observed for the sample sintered at 573 K. The achieved resistivity value of 2.4 mOhm.cm is similar to the result reported by Liu et al., where applied sintering temperature of 573K under 90 MPa pressure. However, the Seebeck coefficient of 197 μVK^{-1} is smaller than the value they have obtained[169]. The difference may come from the different amounts of secondary phases. However, the Seebeck coefficient shows an increase after cooling while taking ZEM-3 measurement and reaches 215 μVK^{-1}. However, the stability of the transport properties is important for the applications, where several heating and cooling steps take a place. The transport properties are measured during the heating and cooling. The resistivity and Seebeck coefficients of same samples while cooling are given in Figure 7.6c and d, respectively. As represented, the resistivity values are changed after cooling for the samples sintered at 673 and 573K. In parallel with the decrease in the electrical resistivity of samples sintered at 673K, the Seebeck coefficient is decreased also slightly. On the other hand, Seebeck coefficients of samples sintered at 573 and 523 K, are increased after the cooling cycle. The carrier concentration of those samples are tend to increase after a heating-cooling cycle. Although the measurements are conducted at a temperature range lower than the phase transition. They are affected after heating process.

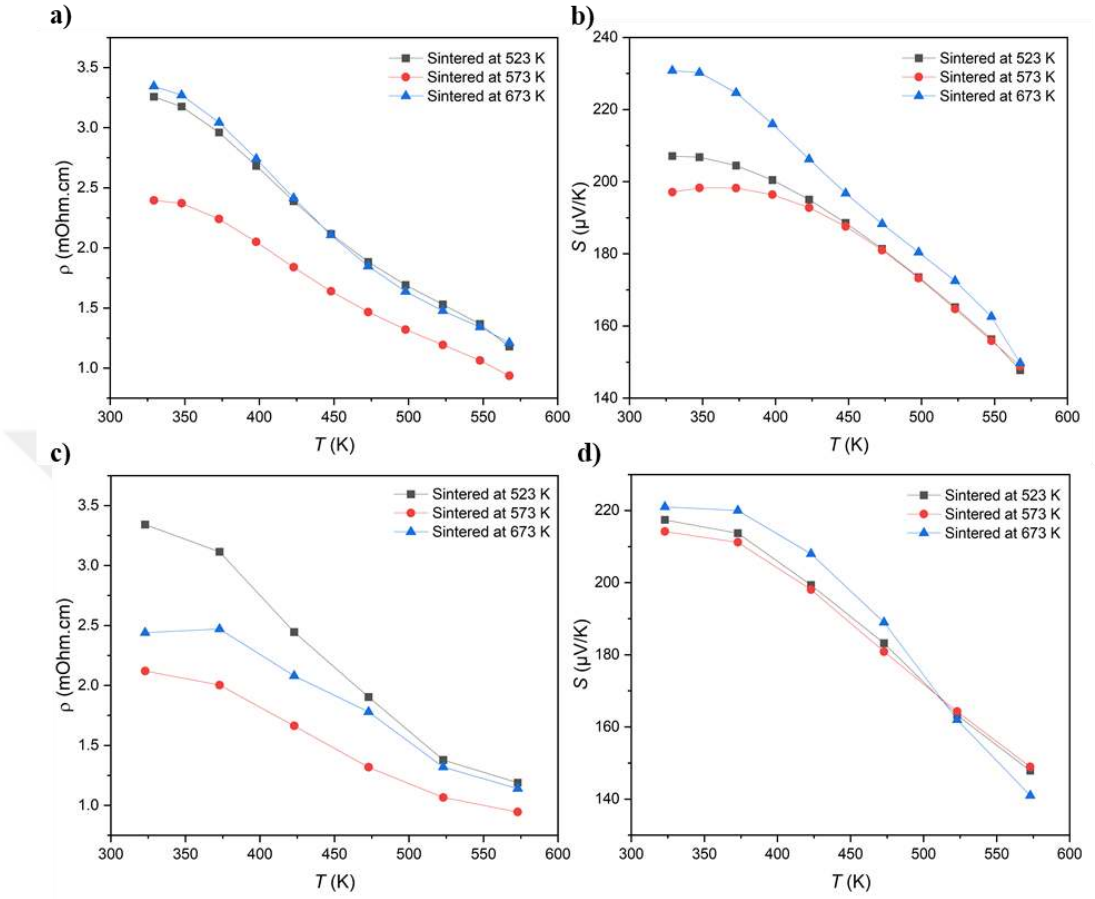

Figure 7.6. a) Electrical resistivity and b) Seebeck coefficient of $MgAg_{0.97}Sb$ samples sintered at 523, 573 and 673 K, and c,d) cooling graphs of resistivity and Seebeck coefficients, respectively.

Figure 7.7 presents the total thermal conductivity values for $MgAg_{0.97}Sb$ compounds with different sintering temperatures. The thermal conductivity values exhibit an increasing trend with increasing temperature. As discussed for the electronic transport properties, the effect of the temperature during the measurements become more obvious while LFA measurement. Especially for the one sintered at 523 K, thermal conductivity changes dramatically after heating to 550K and higher temperatures. The low sintering temperature might be play a role on the instability of the α-phase MgAgSb. Even after cooling cycle the lowest thermal conductivity of 1.23 $Wm^{-1}K^{-1}$ is observed, which is twofold of the value achieved before heating the sample. For the samples sintered at 573

and 673 K, the total thermal conductivity values follow the same trend with the heating cycle.

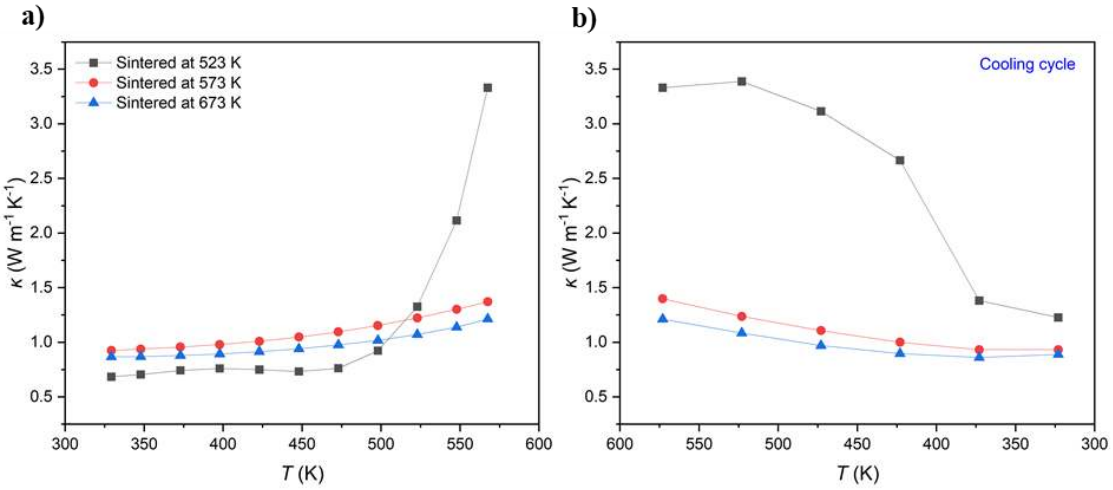

Figure 7.7. Total thermal conductivity values of $MgAg_{0.97}Sb$ samples sintered at 523, 573 and 673 K during a) heating and b) cooling cycles.

The temperature-dependent zT values of $MgAg_{0.97}Sb$ samples with different sintering temperatures are illustrated in Figure 7.8. According to these data, zT values are very similar to each other at the beginning of the measurement. However, after applying temperature, the zT value of the sample sintered at 523 K is decreased tremendously, while the zT of the samples sintered at 573 and 673 K is increased. A considerably high zT values of 0.75 and 0.76 at 325 K are achieved for those samples.

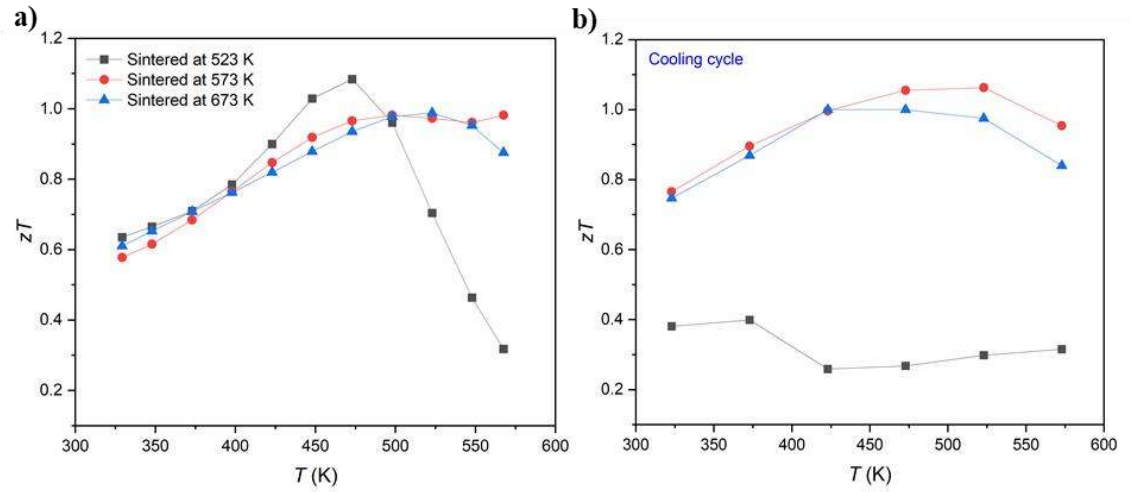

Figure 7.8. Temperature dependent *zT* values of samples sintered at 523, 573 and 673 K during a) heating and b) cooling cycles.

After the examination of transport properties, it is concluded that sintering at 523 K is not sufficient to achieve a stable thermoelectric MgAgSb, and reproducibility is not possible. Therefore, the coming experiments are considered to be applied by sintering either 573 or 673 K. Since the main purpose of this study is achieving a good thermoelectric material for cooling applications at low temperatures, durability is an important issue. Therefore, samples with same conditions are synthesized and characterized during this study. In Figure 7.9, the thermoelectric transport properties of 3 different batches of the samples sintered at 573 K are presented. The transport properties are varying between the different batches, for second and third samples the Seebeck coefficient is changed significantly after 550 K. Although the thermal conductivities are similar for those samples, because of the high resistivity achieved for second trial and low Seebeck coefficient achieved for third trial, total thermoelectric figure of merit values are stayed smaller than the first sample. Through the sintering temperature of 573 K and annealing process for 3 days, the reproducibility was not attainable.

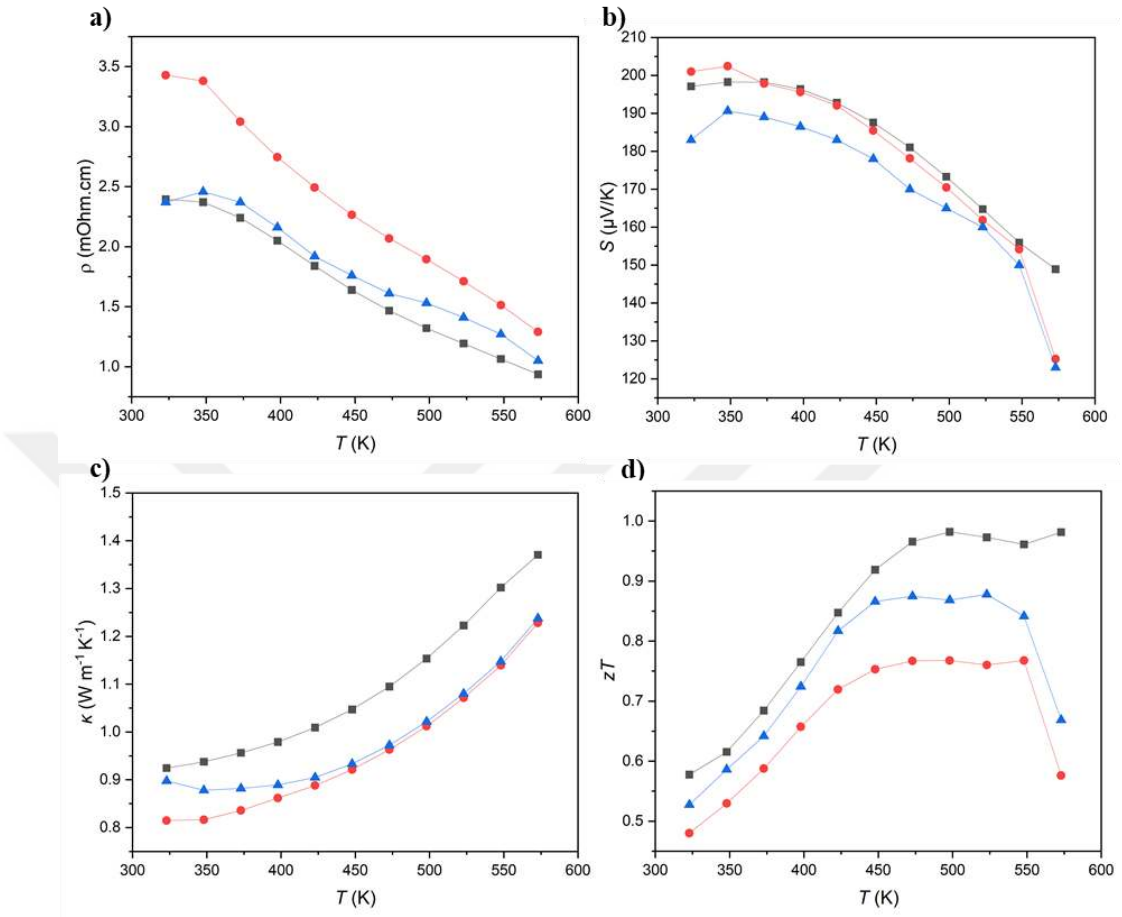

Figure 7.9. a) Electrical resistivity, b) Seebeck coefficient, c) total thermal conductivity and d) zT values of $MgAg_{0.97}Sb$ samples sintered at 573 K.

Transport Properties of Samples with Heat Treatment

After the observation of instability for the sample sintered at 573 K, and increase in the thermoelectric performance through the cooling cycles, the electronic transport properties of the sample sintered at 673 K repeated for several times. After each measurement, it is observed that the thermoelectric performance tends to enhance with the heating cooling cycle of ZEM-3 measurement. Therefore, it is decided to apply a new heat treatment for the as-synthesized bulk samples. The details of the heat treatment are given in the synthesis part. The electronic transport properties for each heating cooling cycle is illustrated in Figure 7.10. After the first measurement cycle, a significant change is observed especially for low temperature transport properties. And overall power factor was enhanced after the measurement. Second measurement of the cooling cycle seems to

be stabilized for the electrical transport properties. The increasing temperature during the measurement, led to initiation of Ag^{+} and Mg^{2+} ion migrations in the crystal structure, as a result, a decrease in the electrical resistivity and Seebeck coefficient is observed.

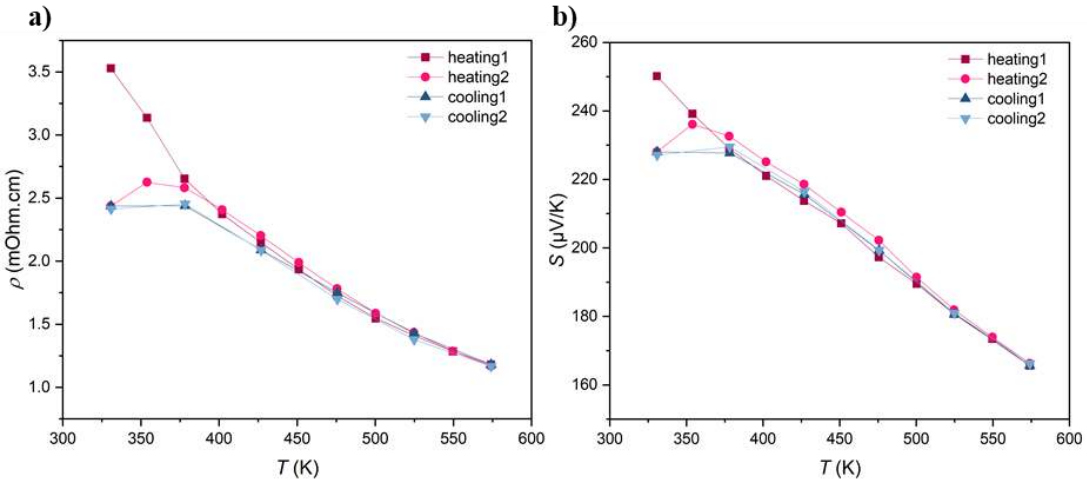

Figure 7.10. a) Resistivity and b) Seebeck coefficient of $MgAg_{0.97}Sb$ sample sintered at 673 K, during the heating and cooling cycles.

The electronic transport properties of heat treated samples in comparison with the un-treated sample are given in Figure 7.11. To ensure the achievability of the similar thermoelectric performance, several batches were prepared with the same conditions. Figure 7.11a and b represents resistivity and Seebeck coefficient values of heat treated samples in comparison with the sample only annealed for 3 days (discussed above). The heating cycles are compared. A decrease in the electrical resistivity with the increase in Seebeck coefficient is observed. Normally those parameters are proportional to each other, due to the relation of carrier concentration. If the reason would be the increase in the carrier concentration it would be expected to see a decrease in the Seebeck coefficient as well, however, the situation is the opposite in this case. The carrier concentration plotted in Figure 7.11e remains almost same with the un-treated sample. The weighted mobility values are also calculated through the resistivity and Seebeck coefficient values, and given in Figure 7.11c. After the heat treatment an increase was observed for the weighted mobility values. To investigate the Hall mobility and carrier concentration values experimentally, Hall measurement is applied for both heat treated and un-treated

samples. As a result, a slight increase in the Hall mobility is achieved after the heat treatment procedure as given in Figure 7.11d. This result proves that the enhancement after heat treatment is not related to carrier concentration values. Other than that, the scattering mechanism of the carriers tend to change with the heat treatment resulting in a higher carrier mobility.

The enhancement in both mobility and Seebeck coefficient might also be explained through band engineering and strain engineering strategies[183-186]. As given in the Table 7.2, after the heat treatment lattice constants are changing with an expansion. Because of the formation of anti-site defects, lattice strains which affect the electronic band structure can be created in the crystal structure. Through enhancing the band convergence and increasing the density of states the Seebeck coefficient might increase, while modifying the band curvature leading to an increase in mobility. Combining those effects, a reliable achievement can be obtained for both electrical conductivity, Seebeck coefficient and mobility.

To be able to see the overall effect on the electronic transport properties the power factor is calculated using the resistivity and Seebeck coefficient. A relatively high power factor is achieved for the heat treated samples with an enhancement of 8 and 14% compared to the sample without heat treatment step.

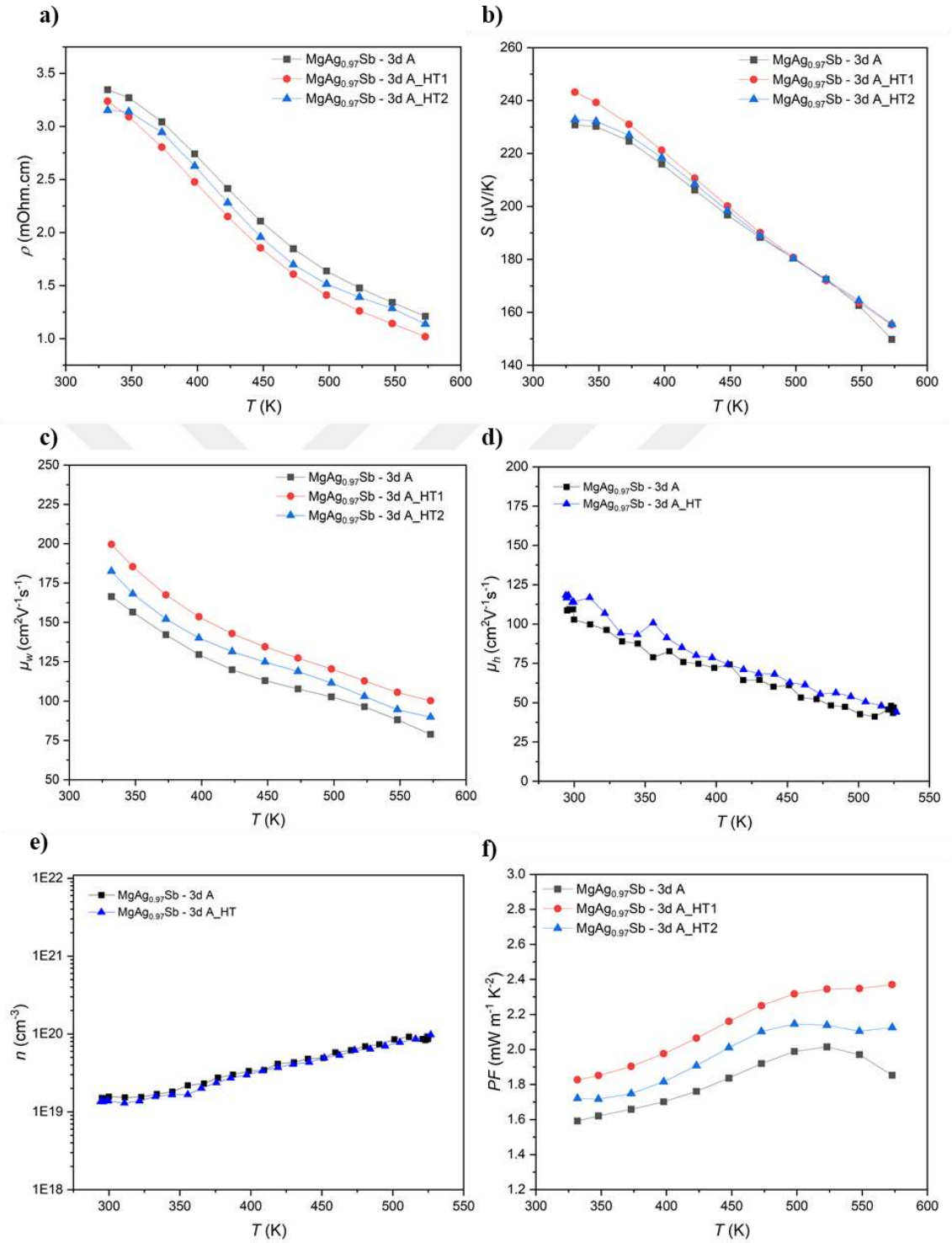

Figure 7.11. a) Resistivity, b) Seebeck coefficient, c) weighted mobility, f) power factor of $MgAg_{0.97}Sb$ samples with and without heat treatment annealed for 3 days and d) Hall mobility, e) carrier concentration of $MgAg_{0.97}Sb$ with and without heat treatment.

The thermal transport properties of heat treated and only annealed samples are given in Figure 7.12. The total thermal conductivities of the samples tend to decrease after additional heat treatment. Especially, both of the heat treated samples presents relatively low thermal conductivities around 0.7 W $m^{-1}K^{-1}$ at low temperatures, which is 15% lower than the untreated thermal conductivity of 0.86 W $m^{-1}K^{-1}$. Through the Wiedemann-Franz law, the electronic contribution on the thermal conductivity is achieved, and plotted in Figure 7.12b. Despite the significant difference in thermal conductivities, the electronic thermal conductivity values are quite similar, which is consistent with the Hall measurements showing that carrier concentrations are nearly identical across all samples. By extracting the electronic contribution from total thermal conductivities, the lattice thermal conductivities are achieved as plotted in Figure 7.12c. It is examined that after heat treatment as well as the difference observed in carrier scattering, phonon scattering is also affected by the treatment. Due to the formation of defects in the crystal structure as well as the impurities, the phonon scattering increases after heat-treatment. The ion migration facilitation also enhances the phonon scattering leading to a decrease in the lattice thermal conductivity[182]. In addition, any possible lattice strains in the crystal structure would affect the relaxation of phonons resulting in a reduced lattice thermal conductivity. In the light of those effects, lower lattice thermal conductivities achieved, with a decrease of around 20% at low temperatures.

Overall, by combination of the electronic and thermal transport properties, the *zT* values are calculated. As given in Figure 7.12d, after the heat treatment a significant increase in the *zT* values are achieved. The highest *zT* for low temperature is obtained as 0.82 for heat treated samples. A substantial improvement of *zT* around 32% is attained with the elevation of electronic contribution of power factor with the diminished thermal conductivity values. And, similar results for thermoelectric performance is achievable for the both heat treated samples.

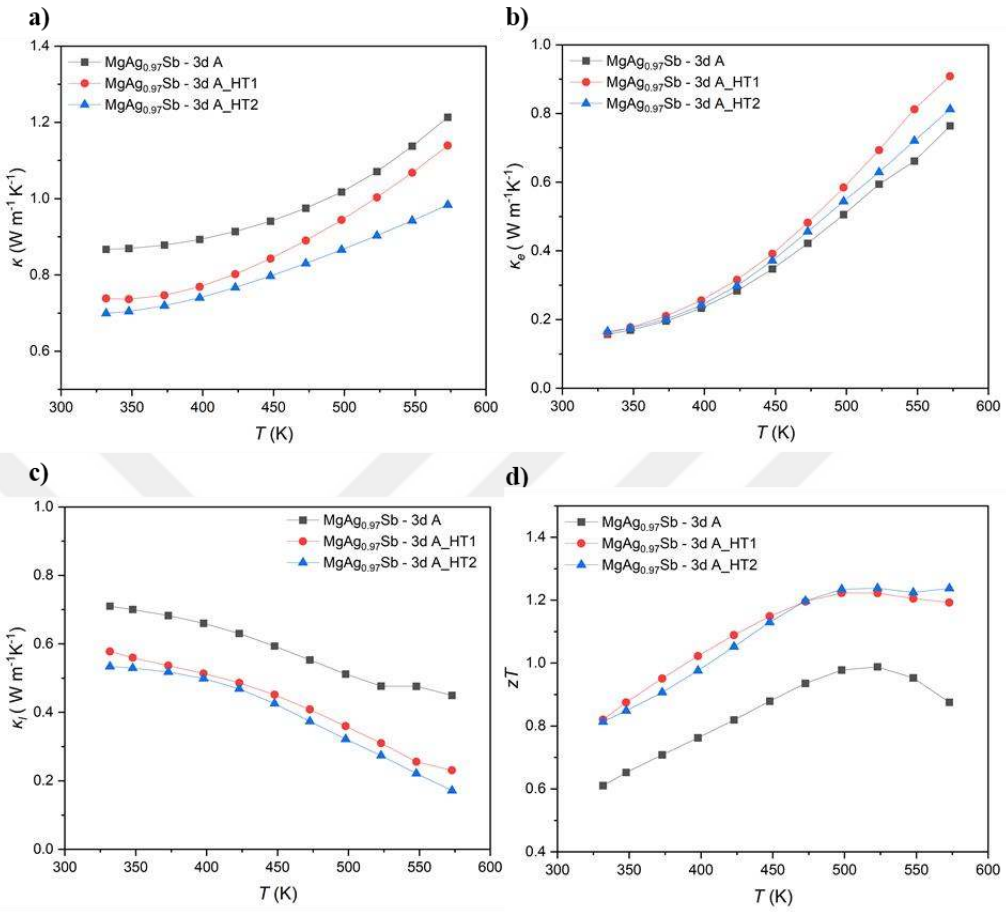

Figure 7.12. a) Total thermal conductivity, b) electronic thermal conductivity, c) lattice thermal conductivity and d) zT value of $MgAg_{0.97}Sb$ samples with and without heat treatment annealed for 3 days.

7.4 Conclusion

$MgAg_{0.97}Sb$ thermoelectric materials were synthesized through high-energy ball milling process and consolidated by spark plasma sintering method. Sintering and annealing parameters were investigated. The phase transition behavior of MgAgSb-based materials was investigated by differential scanning calorimetry measurements for both heat treated and pristine sample. In the temperature range of the measurement conditions no peaks which might relate with a phase transition were observed. Lattice parameters were calculated from the XRD patterns, resulting in a change for both a and c lattice constants with an expansion. It is connected to Mg-Ag anti-site defects observed for

MgAgSb phases[168, 182, 187]. As a result of the change in the lattice constant strain defects can be created. Strain engineering is an effective strategy for optimization of thermal and electronic transport properties of the thermoelectric materials. From the Seebeck coefficient and electrical resistivity values, a change in the behavior is observable especially at low temperatures. Implementing a heat treatment or heat coming from the measurement conditions trigger atoms to relocate in the crystal structure. During the heating cooling cycles, this behavior stabilizes after first cycling. As a result of the strain defects, relaxation time increases and led to a decrease in the lattice thermal conductivity. Besides, the change of the atomic positions modifies the electronic band structure of the material. Although no remarkable change is observed for the carrier concentrations, electrical conductivity and Hall mobility increases. This is connected to change in the band curvature which enhances the mobility resulting in a higher electrical conductivity. On the other hand, enhanced band convergence and the DOS improves the Seebeck coefficient. As a result, high Seebeck coefficient of 243 μV/K, high Hall and weighted mobilities of 116 and 200 $cm^2V^{-1}s^{-1}$ were achieved. Also, combining the low lattice thermal conductivity of 0.57 $Wm^{-1}K^{-1}$, a high zT of 0.82 at 330K was obtained after the heat treatment.

Further investigations might focus on the strain engineering strategy for both advancement of optimum transport properties and stabilization of the MgAgSb characteristic. Since thermoelectric materials would face high temperatures in operation, the heat applied would help to relocation of the atoms in the crystal structure and enhance the thermoelectric properties. After that, the material tends to be stable for further temperature cycles.

Chapter 8

THE EFFECT OF DIFFERENT DOPING ELEMENTS ON THERMOELECTRIC TRANSPORT PROPERTIES OF MgAgSb

8.1 Introduction

After achieving high thermoelectric figure of merit values at low temperatures for MgAgSb system, many studies have been focused on the enhancement of thermoelectric performance of MgAgSb thermoelectric materials as an alternative to the Bi_2Te_3 system[161, 168, 169, 175, 188] . To achieve a high *ZT* value, it is crucial to minimize heat transport while also preserving good electronic transport properties. Two advanced approaches for boosting the *ZT* of thermoelectric materials involve improving the power factor (PF) and decreasing lattice thermal conductivity. To enhance the PF, methods such as band engineering, optimizing carrier concentration, enhancing carrier mobility can be employed. While, for the second, nano-structuring, microstructure engineering and alloying or doping strategies can be effective for further reduce the lattice thermal conductivity. As an example, point-defects can be created as a phonon scattering centers through doping strategies while improving the electronic transport properties. Sheng et. al. computationally studied the possible dopants for the MgAgSb system, and, revealed the feasible doping elements as Li, Na, K and Rb on Mg site; Ni, Pd, Pt, Co, Rh, Ir on Ag site and Si, Ge, Sn, Pb, Al, Ga, In and Tl on Sb site for the *p*-type MgAgSb thermoelectric materials[189].

Previous doping studies have been applied experimentally for MgAgSb system, for each element positions. For instance, Li and Na doping on Mg site was studied, however the overall *zT* was not affected significantly because of the small decrease in K_{lat}[190, 191]. Another study was focused on the Yb doping on Mg site, as a result, the carrier concentration and power factor were enhanced, while the total thermal conductivity

stayed still, the lattice thermal conductivity was decreased[171]. For Mg site, calcium (Ca) was also selected as a doping element by Liu et. al., and, the power factor value was enhanced while the thermal conductivity was also increasing due to the bipolar effect[192]. Also doping of zinc (Zn) element on Mg site with long annealing time (10 days) was investigated by Yanyan et. al. An increase in the electrical resistivity value and thermal conductivity was observed. On the other hand, they have claimed that the power factor was also enhanced due to the optimized carrier concentration[170]. However, another study conducted by Zheng et. al, also presented the thermoelectric properties of Zn doping on Mg site, with a very similar composition have shown a very low thermoelectric figure of merit zT value of 0.3 at 325 K[176]. Lastly, Cu doping on Mg site was studied by Liu et. al, showed a decrease in electrical resistivity values with an increase in total thermal conductivity. As a result, an increase in the zT was achieved with value of 0.8 at 325 K[3].

Besides, Mg site doping researches, doping on the Ag site was also studied to enhance the thermoelectric properties of MgAgSb system. The effect of the Cu concentration was investigated by Siu et. al, by doping Ag site with Cu. The electrical resistivity and lattice thermal conductivity values were diminished after Cu doping, and overall thermoelectric figure of merit value was increased almost 0.95 at 300 K. That result was attributed to the increase in carrier concentration with reduced lattice thermal conductivity coming from the difference in the mass of Cu and Ag[172]. Alternatively, the investigation of Ni doping on the Ag site was revealed that Ni doping boosted the electrical resistivity while decreasing the thermal conductivity. Combining the enhanced power factor with low thermal conductivity, the zT of 0.9 was achieved at 300 K[161].

Lastly, the effect of doping elements such as In, B, As, Bi on the Sb site was investigated experimentally. While As doping expanded the power factor, Bi doping lowered the power factor[192]. The boron (B) doping affected the zT values negatively for high amounts or was ineffective to improve the thermoelectric properties. However, it was effective on the enhancement of hardness of the MgAgSb[193]. Ying et al., discussed the effect of In doping on Sb site. The carrier concentration was increased through In doping, with increased thermal conductivity and power factor. As a result, they were able to achieve a zT of 0.58 at 325 K[175]. Because of the complexity of the MgAgSb system, although some studies have shown an improvement in their own set of experiments, it is difficult to achieve similar results from different resources.

In view of different doping strategies considered above, to enhance the carrier concentration and explore the impact of substitution, a comprehensive study was carried out on $MgAg_{0.97}Sb$, through different substitutions such as Zn and Co elements on Ag site, Y and Nb on Mg site and finally Ge and Te elements on Sb site.

8.2 Sample Preparation

The same method outlined in the Chapter 6 was applied to prepare the pristine and the doped samples. The Zn and Co substituted $MgAg_{0.97-x}SbM_x$ samples were synthesized in two step. First, the high purity raw materials of magnesium powder (Mg, 99.8%; Alfa Aesar), Ag powder (Bi, 99.999%; Alfa Aesar) and dopant elements (Zn or Co) were weighted according to the stoichiometry ($MgAg_{0.97-x}M_x$; M=Zn, Co; x= 0.005, 0.01 and 0.03 without doping element) and loaded into a stainless-steel vial with two half-inch stainless steel balls under Ar atmosphere to avoid oxidation. Mechanical alloying technique was applied for 8 hours through high-energy ball milling. The achieved powder was loaded into a stainless-steel vial with the corresponding stoichiometric amount of Sb, and sealed under Ar. The second synthesis step was applied through mechanical alloying technique for 5 hours. The achieved powder was loaded into a graphite die under Ar atmosphere and compressed via cold press. SPS was applied to obtain dense cylindrical pellets under a uniaxial pressure of 85 MPa for 8 minutes at 573 K in vacuum.

8.3 Characterization

8.3.1 Crystal Structure Analysis

Crystal Structure of Ag-doped Samples

In the ongoing studies aimed at examining the thermoelectric properties of materials, research has been conducted on the amount of silver (Ag) element and its doping with different alternative elements. XRD analysis was applied in each steps; including $MgAg_{0.97-x}$ powder, $MgAg_{0.97-x}SbM_x$ powders, $MgAg_{0.97-x}SbM_x$ pellets and finally annealed $MgAg_{0.97-x}SbM_x$ pellets.

The XRD graphs of compounds synthesized in these studies, namely $MgAg_{0.97}Sb$, $MgAg_{0.94}Sb$, $MgAg_{0.96}Co_{0.01}Sb$, $MgAg_{0.965}Zn_{0.005}Sb$, and $MgAg_{0.96}Zn_{0.01}Sb$, are shown in Figure 8.1 after annealing process. According to the evaluations, the main peaks correspond to the tetragonal crystal structure of α phase with the $I\bar{4}c2$ space group. After cobalt (Co) doping, a slight decrease in the intensity of the secondary phase peak of antimony (Sb) is observed (dark blue pattern). It was anticipated that reducing the amount of Ag without the doping element would decrease the formation of Ag_3Sb, but XRD peaks of $MgAg_{0.94}Sb$ (red line) showed no decrease in the amount of Ag_3Sb, conversely, an increase in the amount of unreacted Sb phase was observed. Also, due to the decrease in the amount of Sb within the crystal structure, a shift to the left was observed in the peaks of the $MgAg_{0.94}Sb$ composition. Peaks obtained with the doping of zinc (Zn) instead of silver (Ag) show similar characteristics to the peaks of the $MgAg_{0.97}Sb$ phase.

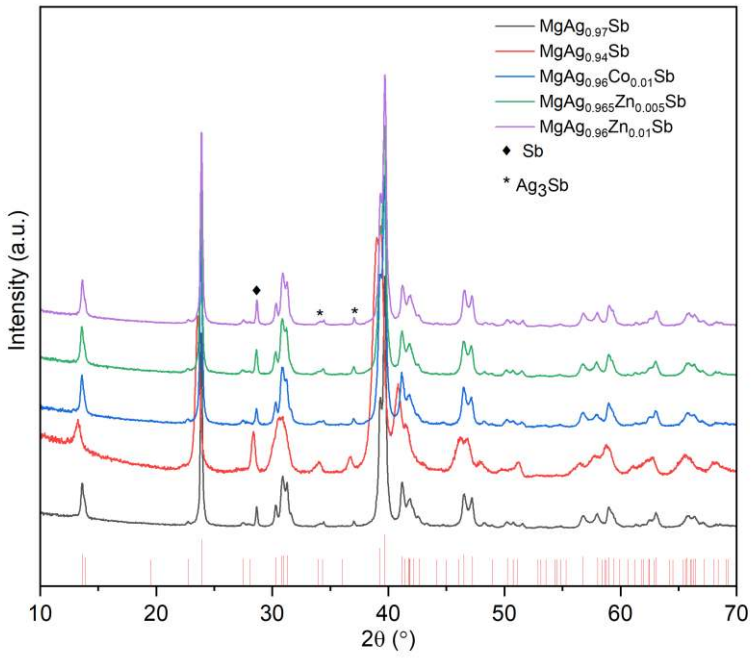

Figure 8.1. XRD patterns of 3 days annealed $MgAg_{0.97}Sb$, $MgAg_{0.94}Sb$, $MgAg_{0.96}Co_{0.01}Sb$, $MgAg_{0.965}Zn_{0.005}Sb$, and $MgAg_{0.96}Zn_{0.01}Sb$ samples.

Crystal Structure of Mg-doped Samples

Secondly, to observe the effect on the thermoelectric properties of materials, research has been conducted on the doping of magnesium (Mg) element with different alternative

elements (Nb and Y). XRD analysis was applied in each steps; including powders, pellets and finally annealed samples.

XRD graphs of compounds synthesized in these studies, namely $MgAg_{0.97}Sb$, $Mg_{0.99}Nb_{0.01}Ag_{0.97}Sb$, $Mg_{0.995}Y_{0.005}Ag_{0.97}Sb$, and $Mg_{0.99}Y_{0.01}Ag_{0.97}Sb$, are shown inFigure 8.2. Evaluation indicates that the primary peaks correspond to the tetragonal crystal structure of α phase with the $I\bar{4}c2$ space group. Following the introduction of element Y, there is a noticeable increase in the intensity of peaks associated with the Sb and Ag_3Sb secondary phases. This phenomenon could be linked to the diminished presence of Mg within the crystal structure, as a decrease in Mg ratio correlates with heightened secondary phase quantities. However, in the doping study involving the Nb element, new peaks unrelated to the primary phase, alongside those of Ag and Ag_3Sb phases, were observed. This suggests that the doping attempt with Nb was unsuccessful, as indicated by an escalation in impurity levels.

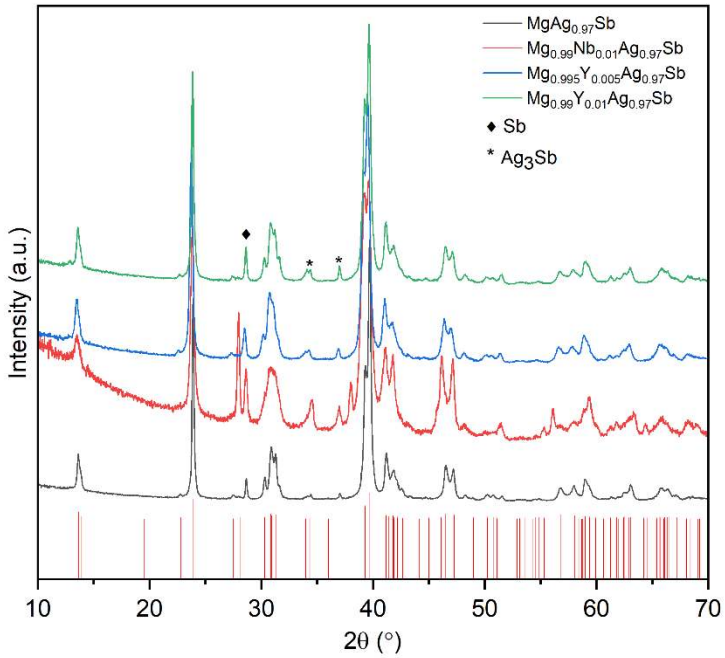

Figure 8.2. XRD patterns of 3 days annealed $MgAg_{0.97}Sb$, $Mg_{0.99}Nb_{0.01}Ag_{0.97}Sb$, $Mg_{0.995}Y_{0.005}Ag_{0.97}Sb$, and $Mg_{0.99}Y_{0.01}Ag_{0.97}Sb$ samples.

Crystal Structure of Sb-doped Samples

Secondly, to observe the effect on the thermoelectric properties of materials, research has been conducted on the doping of silver (Sb) element with different alternative elements (Te and Ge). XRD analysis was applied in each steps; including powders, pellets and finally annealed samples. The XRD graphs of compounds synthesized in these studies, namely $MgAg_{0.97}Sb$, $MgAg_{0.94}Sb$, $MgAg_{0.96}Co_{0.01}Sb$, $MgAg_{0.965}Zn_{0.005}Sb$, and $MgAg_{0.96}Zn_{0.01}Sb$ are shown in Figure 8.3. after annealing process. According to the evaluations, the main peaks correspond to the tetragonal crystal structure of α phase with the $I\bar{4}c2$ space group. After tellurium (Te) doping, a slight increase in the intensity of the secondary phase peaks of antimony (Sb) and Ag_3Sb was observed (green and purple lines). It was anticipated that introducing the Te instead of Sb led to formation of secondary phases. The reason behind this results might be related to decrease in the Sb amount within the crystal structure. Since the ionic radius of Te^{2-} (207 pm) and Te^{4+} (111 pm) is higher than the ionic radius of Sb^{3-} (90 pm), it might force the formation of secondary Sb phases instead of substitution defect. On the other hand, germanium (Ge) doped samples presents similar XRD patterns with the un-doped material.

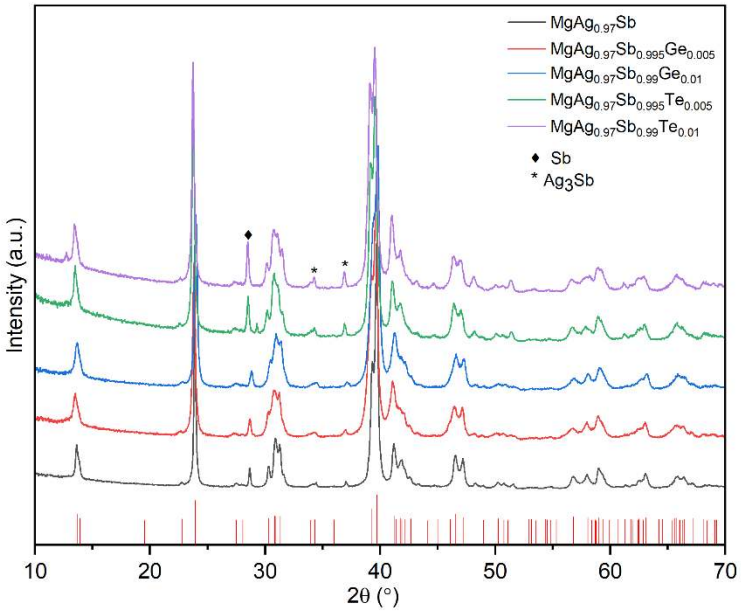

Figure 8.3. XRD patterns of 3 days annealed $MgAg_{0.97}Sb$, $MgAg_{0.97}Sb_{0.995}Ge_{0.005}$, $MgAg_{0.97}Sb_{0.99}Ge_{0.01}$, $MgAg_{0.97}Sb_{0.995}Te_{0.005}$, and $MgAg_{0.97}Sb_{0.99}Te_{0.01}$samples.

8.3.2 Transport Property Measurements

Transport Properties of Ag-doped Samples

First studies have been conducted on changes in the Ag ratio and different doping strategies for the examination of thermoelectric transport properties. In these studies, the thermoelectric properties of materials synthesized as $MgAg_{0.97}Sb$, $MgAg_{0.94}Sb$, $MgAg_{0.96}Co_{0.01}Sb$, $MgAg_{0.965}Zn_{0.005}Sb$ ve $MgAg_{0.96}Zn_{0.01}Sb$ compounds have been investigated. Figure 8.4a and b provide the graphs of the electrical resistance and Seebeck coefficient of the materials. The electrical resistance values show a decrease with increasing temperature. Similarly, the Seebeck coefficient values also decrease with increasing temperature. This behavior is in accordance with the semiconducting-like transport properties.

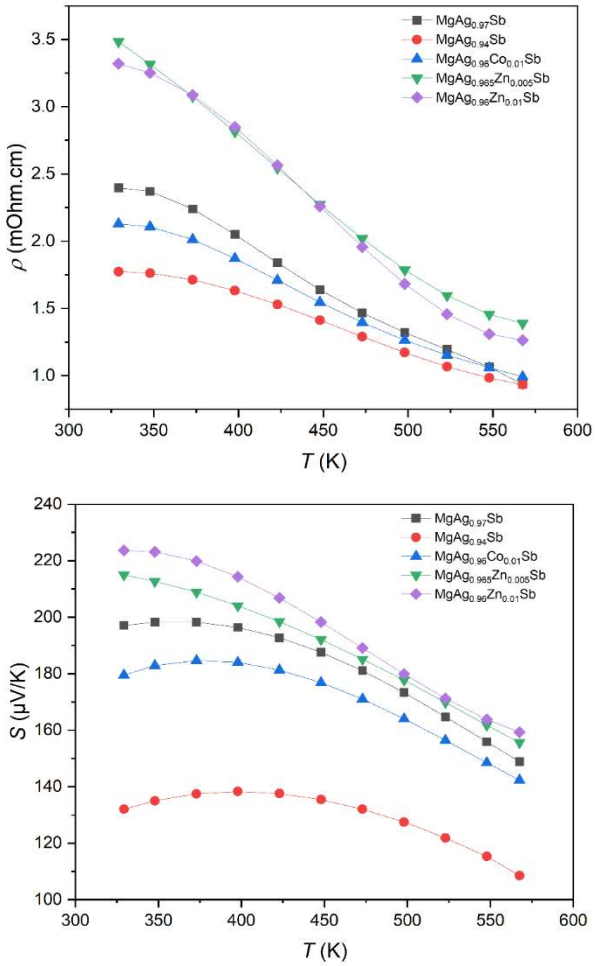

Figure 8.4. a) Electrical resistivity and b) Seebeck coefficient of $MgAg_{0.97}Sb$, $MgAg_{0.94}Sb$, $MgAg_{0.96}Co_{0.01}Sb$, $MgAg_{0.965}Zn_{0.005}Sb$, and $MgAg_{0.96}Zn_{0.01}Sb$ samples.

With the decrease in the Ag ratio in the $MgAg_{0.94}Sb$ phase, an increase in the carrier concentration is observed. The reduction of Ag, which acts as an electron donor, leads to an increase in the concentration of holes in the *p*-type material and consequently a decrease in electrical resistivity. However, the significant change in carrier concentration results in a substantial decrease in the Seebeck coefficient as well, as shown in Figure 8.4b. Toh et al., also have studied the effect of Ag amount on the transport properties. Although the values are different from this study which might be related to synthesis conditions, a decrease in resistivity and Seebeck coefficient was observed with decrease in the Ag amount[194]. Also, this behavior can be related with the study conducted by Zheng et al., which Seebeck coefficient diminished even 60 $\mu V\ K^{-1}$, with decrease of Ag amount to 0.9 instead of 0.97. In similar with the reducing Ag amount concept, when the Co element is doped instead of Ag, the electrical resistivity and Seebeck coefficient decreased. Although the electron donor character of the Co^{2+} or Co^{3+} ion, the resistivity value was slightly decreased compared to the un-doped sample. It might be coming from the decrease in the Ag^{+} concentration in the crystal structure. In that case, Co might not be acted as a dopant. On the other hand, Sui et al., has discussed the effect of Cu substitution into Ag position, and similarly they have concluded that Cu doping decreases the electrical resistivity and Seebeck coefficient by increasing the carrier concentration. However, there was no further explanation for that behaviour[172].

When the Zn element is doped instead of Ag in different ratios, the electrical resistivity values increase while the Seebeck coefficient values increase. Since the Zn^{+2} ion provides additional electrons compared to the Ag^{+} ion, this behavior might be expected in a *p*-type material, and thus this study has been conducted to optimize the carrier concentration and power factor. For the doped samples, a bipolar effect was observed after 525 K, where electrons are becoming also effective on the electronic transport, in addition to the holes.

By correlating the findings of electrical resistivity and Seebeck coefficient, Figure 20 presents the calculated power factor of the materials. For $MgAg_{0.94}Sb$, although the decrease in the electrical resistivity values around 26%, the Seebeck coefficient was also decreased around 33%. Since the power factor is proportional to twice the Seebeck coefficient, the overall power factor was decreased compared to the pristine sample. For Co doping strategy, the decrease in the resistivity and Seebeck coefficient values were

calculated around 11 and 9%, respectively. Combining those values overall power factor was decreased compared with the pristine sample. For the Zn doped samples, additional electron donors were placed in the crystal structure to be able to see the effect on the electronic transport properties. Although the high amount of increase in the resistivity values, the change in the Seebeck coefficient was relatively small. Therefore, the power factor of those samples were lower compared to the pristine material. After 500 K, bipolar effect was observed from resistivity and power factor graphs (Figure 8.4a and Figure 8.5).

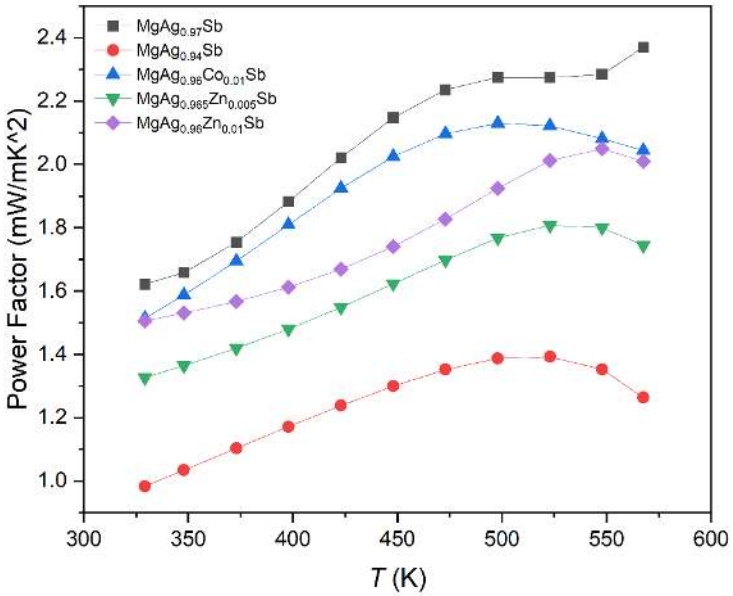

Figure 8.5. Power factor of $MgAg_{0.97}Sb$, $MgAg_{0.94}Sb$, $MgAg_{0.96}Co_{0.01}Sb$, $MgAg_{0.965}Zn_{0.005}Sb$, and $MgAg_{0.96}Zn_{0.01}Sb$ samples.

Figure 8.6 presents the total thermal conductivity values for $MgAg_{0.97}Sb$, $MgAg_{0.94}Sb$, $MgAg_{0.96}Co_{0.01}Sb$, $MgAg_{0.965}Zn_{0.005}Sb$ ve $MgAg_{0.96}Zn_{0.01}Sb$ compounds. The thermal conductivity values exhibit an increasing trend with increasing temperature. Similar to the effect observed in electrical resistivity values, when the Ag ratio is reduced, an increase in the thermal conductivity values was observed. Despite the changes in electrical properties with the addition of Co, no significant changes were observed in thermal conductivity values. With the addition of Zn, however, a slight decreasing trend in thermal conductivity is observed, especially at low temperatures.

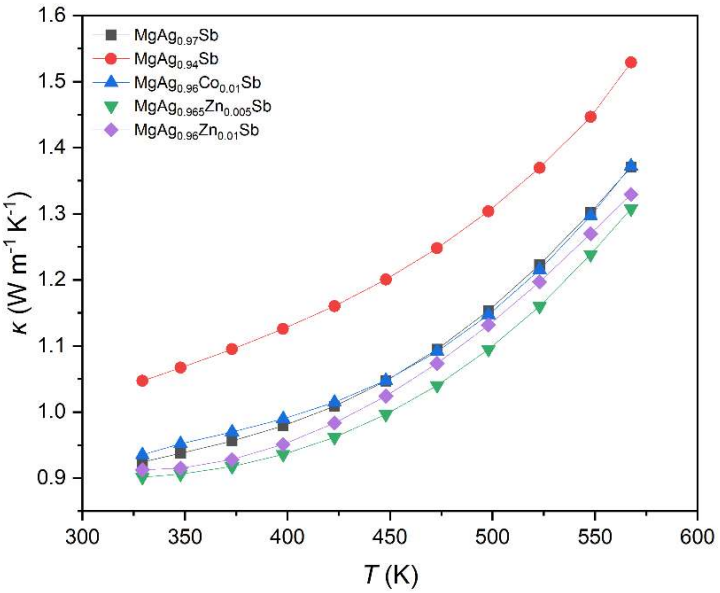

Figure 8.6. Total thermal conductivity values of $MgAg_{0.97}Sb$, $MgAg_{0.94}Sb$, $MgAg_{0.96}Co_{0.01}Sb$, $MgAg_{0.965}Zn_{0.005}Sb$, and $MgAg_{0.96}Zn_{0.01}Sb$ samples as a function of temperature.

In Figure 8.7, the temperature-dependent zT values of $MgAg_{0.97-x}M_x$ samples (where M=Zn, Co; x= 0.005, 0.01 and 0.03 without a doping element) were illustrated. According to these data, the change in the amount of Ag element generally led to a decrease in zT values. Particularly, the significant decrease in the Seebeck coefficient adversely affects the zT value. A decrease in zT value is observed when the electrical resistivity reaches values around 3.5 mOhm.cm.

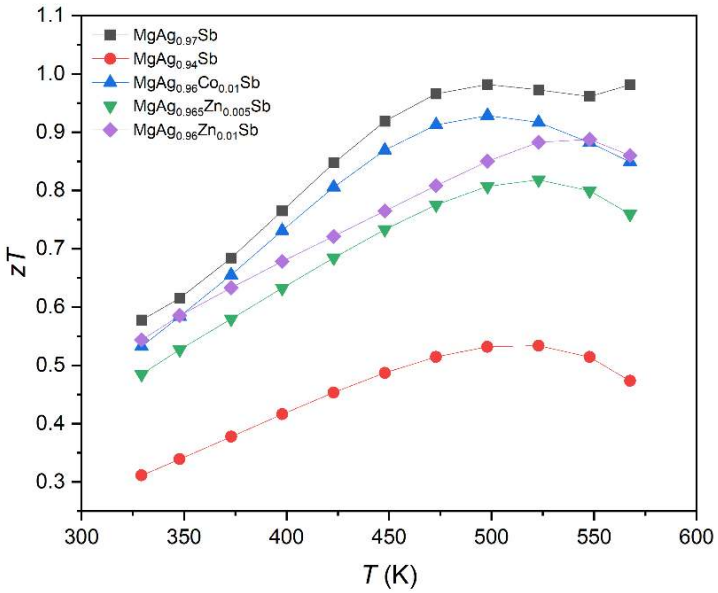

Figure 8.7. The thermoelectric figure of merit, zT, values of $MgAg_{0.97}Sb$, $MgAg_{0.94}Sb$, $MgAg_{0.96}Co_{0.01}Sb$, $MgAg_{0.965}Zn_{0.005}Sb$, and $MgAg_{0.96}Zn_{0.01}Sb$ samples as a function of temperature.

Transport Properties of Mg-doped Samples

In the second study, experiments were conducted regarding the quantity of magnesium (Mg) and its doping with various additional elements (Nb and Y). In these studies, the thermoelectric properties of materials synthesized as $MgAg_{0.97}Sb$, $Mg_{0.99}Nb_{0.01}Ag_{0.97}Sb$, $Mg_{0.995}Y_{0.005}Ag_{0.97}Sb$, and $Mg_{0.99}Y_{0.01}Ag_{0.97}Sb$ have been investigated. Figure 8.8a and b presents the electrical resistivity and Seebeck coefficient of the materials depending on the temperature.

As the temperature increases, both the electrical resistivity and Seebeck coefficient values decrease. Even small variations in the Mg ratio have been observed to significantly affect the electronic properties. Generally, a decrease in the Mg element, which provides electrons, leads to a decrease in electrical resistivity and Seebeck coefficient values. Since $MgAg_{0.97}Sb$ phase represents a *p*-type character, the decrease in the electron concentration led to an increase in the hole carrier concentrations. Previous studies have shown that Nb incorporation instead of Mg might decrease the carrier concentration for *n*-type Mg_3Sb_2[59]. In view of this result, it is predicted to increase the carrier concentration as a dopant of Mg site for a *p*-type material.

In this study with the Nb element, a decrease in the electrical resistivity values from 2.4 to 1.65 mOhm.cm was observed. However, the impurity phases that observed from the XRD analysis, might be effective on causing a decrease in the Mg content in the composition leading to an increase in the hole carrier concentration. In similar with the decrease in electrical resistivity, there was an approximately 37% decrease in the Seebeck coefficient.

In the other alternative, Y was used as a dopant instead of Mg. Upon using Y, it was observed that the Seebeck coefficients decreased by approximately 30% in both compositions with the Y content of 0.05 and 0.1. Additionally, there was a decrease in electrical resistivity values, especially at low temperature values. Under normal conditions, since Y is at a +3 valence, an increase in resistivity values and Seebeck coefficients would be expected in *p*-type materials. Similarly, yttrium (Y) has been used as a dopant for the *n*-type Mg_3Sb_2 material before, and, an increase in the carrier concentration was observed as expected[195-197]. However, in this study, the opposite was observed. This decrease is most likely resulted from a decrease in the amount of Mg in the crystal structure, and Y doping probably a weak counter element for Mg in the MgAgSb system.

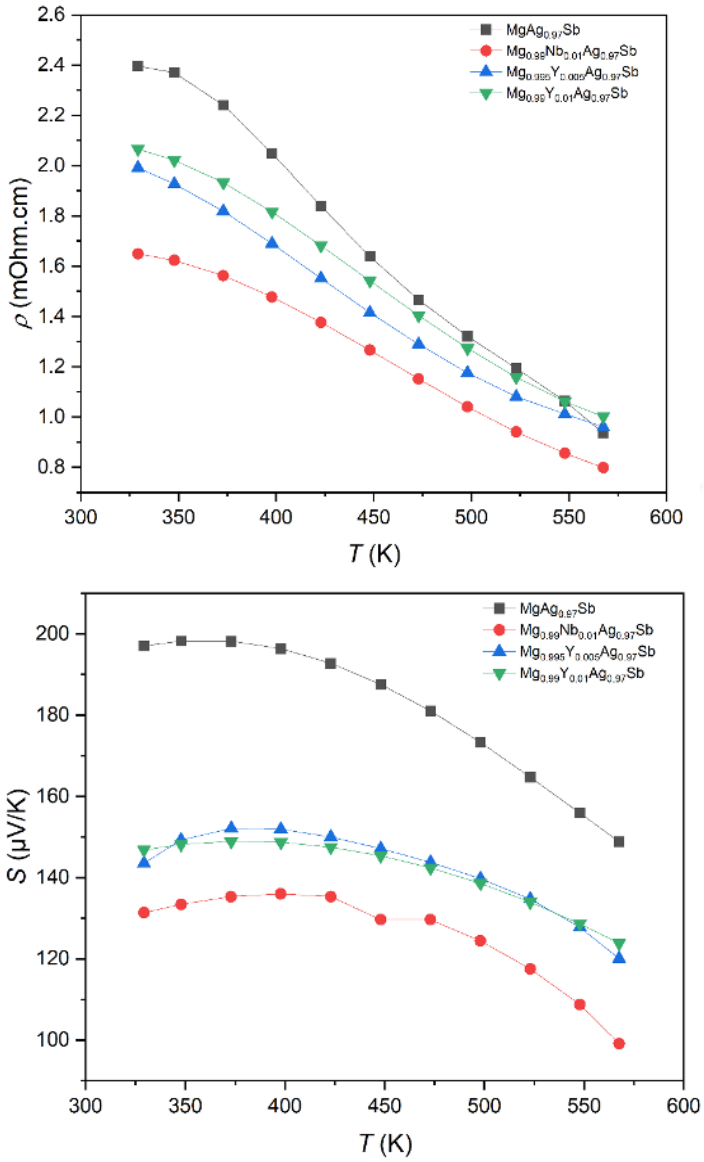

Figure 8.8. a) Electrical resistivity and b) Seebeck coefficient of $MgAg_{0.97}Sb$, $Mg_{0.99}Nb_{0.01}Ag_{0.97}Sb$, $Mg_{0.995}Y_{0.005}Ag_{0.97}Sb$, and $Mg_{0.99}Y_{0.01}Ag_{0.97}Sb$ samples.

Figure 8.9 shows the total thermal conductivity values as a function of temperature for compounds $MgAg_{0.97}Sb$, $Mg_{0.99}Nb_{0.01}Ag_{0.97}Sb$, $Mg_{0.995}Y_{0.005}Ag_{0.97}Sb$, and $Mg_{0.99}Y_{0.01}Ag_{0.97}Sb$. The thermal conductivity values exhibit an increasing behavior. Similar to the effect observed in electrical resistivity values when the Mg ratio is reduced, an increase in thermal conductivity values was observed. In samples with 0.01 ratio of Nb and 0.005 ratio of Y added, a jump in thermal conductivity values was observed after 550K. This indicates a phase transition in the MgAgSb phase, which typically exhibits a

β phase between 560-630 K under normal conditions. The change in the Mg content might be effective on the phase stability, also the sensitivity of temperature of the measurement device might be effective on the phase transition.

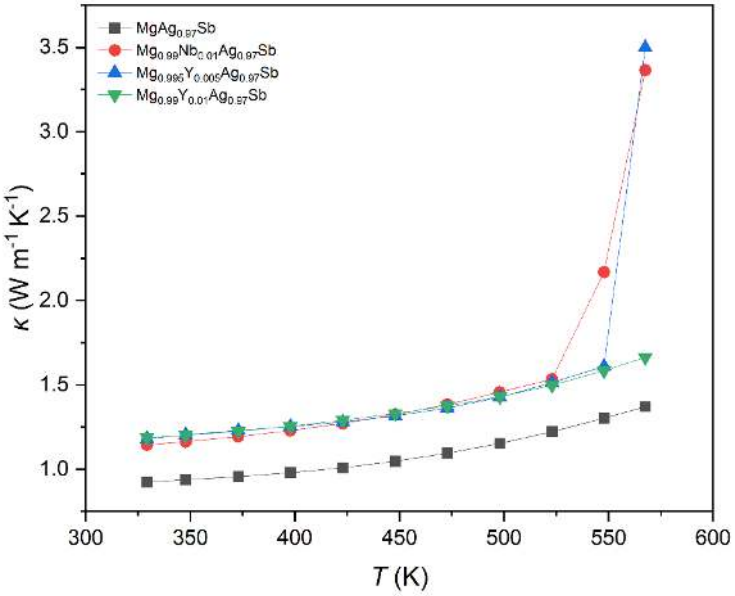

Figure 8.9. Total thermal conductivity values of $MgAg_{0.97}Sb$, $Mg_{0.99}Nb_{0.01}Ag_{0.97}Sb$, $Mg_{0.995}Y_{0.005}Ag_{0.97}Sb$, and $Mg_{0.99}Y_{0.01}Ag_{0.97}Sb$ samples as a function of temperature.

Figure 8.10 provides the temperature-dependent thermoelectric figure of merit (zT) values for $MgAg_{0.97}Sb$, $Mg_{0.99}Nb_{0.01}Ag_{0.97}Sb$, $Mg_{0.995}Y_{0.005}Ag_{0.97}Sb$, and $Mg_{0.99}Y_{0.01}Ag_{0.97}Sb$ materials. According to these data, changes in the Mg content generally lead to a remarkable decrease in the zT value. Especially, the significant decrease in the Seebeck coefficient negatively impacts the zT value, similar to the effect observed in the Ag study. There is a noticeable decrease in zT at temperatures where phase transitions occur.

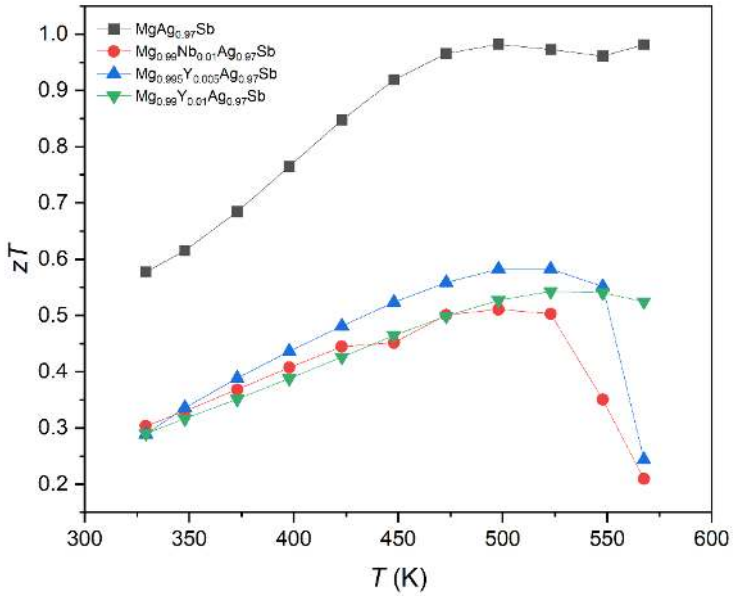

Figure 8.10. The thermoelectric figure of merit, *Zt*, values of $MgAg_{0.97}Sb$, $Mg_{0.99}Nb_{0.01}Ag_{0.97}Sb$, $Mg_{0.995}Y_{0.005}Ag_{0.97}Sb$, and $Mg_{0.99}Y_{0.01}Ag_{0.97}Sb$ samples as a function of temperature.

Transport Properties of Sb-doped Samples

Lastly, studies have been conducted on the doping on silver (Sb) element site with different alternative elements (Te and Ge). Previously, Sheng et al., have presented the Ge element as a possible doping element for *p*-type character with the amount of 0.0053 Ge, however, it was not studied experimentally before[189]. In this chapter, the thermoelectric properties of materials synthesized as $MgAg_{0.97}Sb$, $MgAg_{0.97}Sb_{0.995}Ge_{0.005}$, $MgAg_{0.97}Sb_{0.99}Ge_{0.01}$, $MgAg_{0.97}Sb_{0.995}Te_{0.005}$, and $MgAg_{0.97}Sb_{0.99}Te_{0.01}$ samples have been investigated. Figure 8.11a and b presents the electrical resistance and Seebeck coefficient of the materials depending on the temperature.

As the temperature increases, both the electrical resistivity and Seebeck coefficient values decrease. For the germanium (Ge) doped samples, the resistivity values are similar for the content of 0.005 with the un-doped samples from around 400 K. However, a significant increase in the resistivity value was observed with increasing the content of Ge from 0.005 to 0.1. The low temperature resistivity values were increased about 27%. The similar phenomenon was observed before with the Cu incorporation study instead of Ag element. The resistivity value was first decrease with the content of 0.003 and 0.007 and then elevated with the increased content of Cu up to 0.1[172]. This behavior was

attributed to formation of minor secondary phases which are not detectable through XRD spectrometry. Because of the solubility limit of the doping element, after a certain amount, transport properties were affected differently. Analogous to electrical resistivity values, the Seebeck coefficient was not affected effectively with the content of 0.005 Ge doping, and then increased with elevated content of Ge at low temperatures.

With the tellurium incorporation, the resistivity value was first decreased about 22%, and then reached to the un-doped sample with the increased amount of Te from 0.005 to 0.1. As discussed above, the increased amount of dopant element up to 0.01 most probably reaches the solubility limits and changes the transport character immediately. Although the *n*-type dopant characteristic of the Te element, it has been studied in this research to be able to see the effect of carrier concentration on the overall electronic transport properties. The study conducted by Duparchy et al. presented the relation between Seebeck coefficient, electrical resistivity and thermoelectric figure of merit value on the Mg-Ag-Sb phase map, through experimentally investigating over 30 samples with different synthesis conditions[178]. According to the experimental results, the higher thermoelectric figure of merit values was achieved in the region where electrical resistivity is in between 2.85 – 3.8 mOhm.cm. Therefore, *n*-type dopant was also substituted with Sb element in this study. However, compared to the results derived in the phase map, the Seebeck coefficient values achieved in this study were much lower. Most probably the secondary phases obtained in the microstructure are responsible from the difference in electronic transport properties.

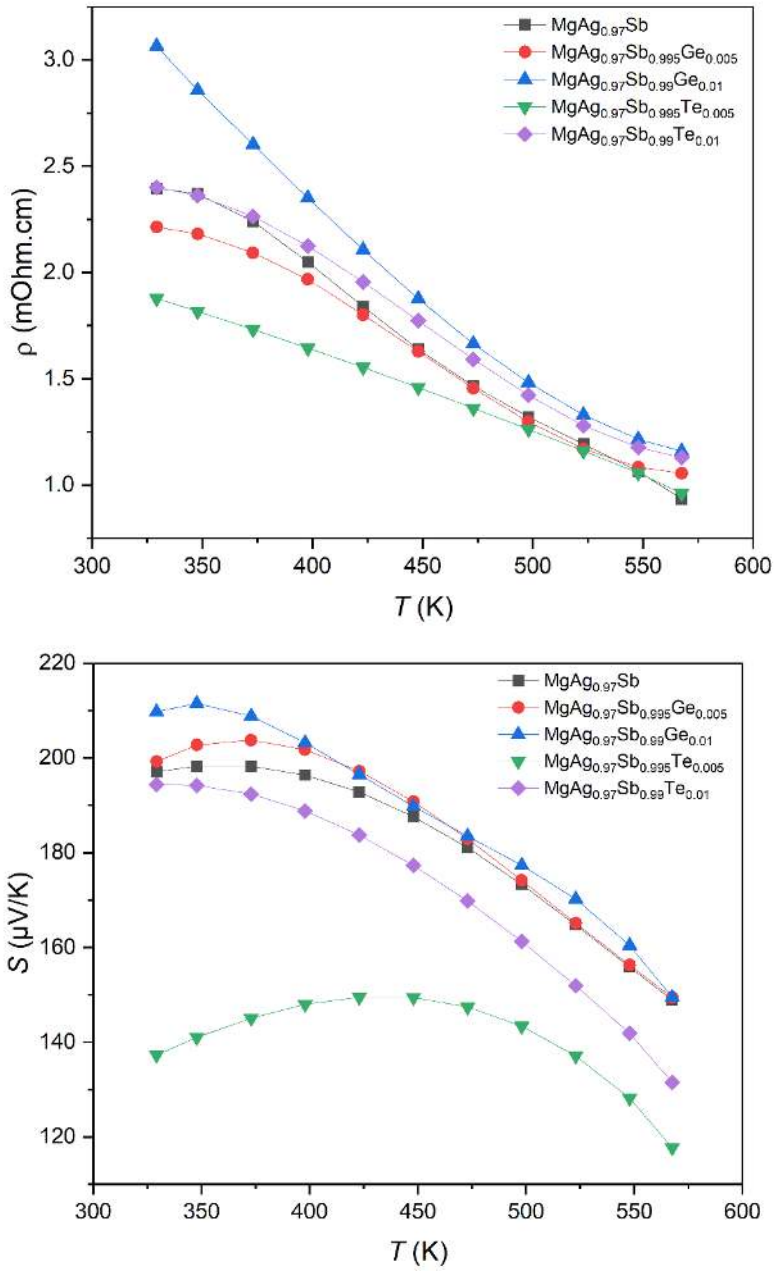

Figure 8.11. a) Electrical resistivity and b) Seebeck coefficient of $MgAg_{0.97}Sb$, $MgAg_{0.97}Sb_{0.995}Ge_{0.005}$, $MgAg_{0.97}Sb_{0.99}Ge_{0.01}$, $MgAg_{0.97}Sb_{0.995}Te_{0.005}$, and $MgAg_{0.97}Sb_{0.99}Te_{0.01}$.

Figure 8.12 presents the total thermal conductivity values as a function of temperature for compounds $MgAg_{0.97}Sb$, $MgAg_{0.97}Sb_{0.995}Ge_{0.005}$, $MgAg_{0.97}Sb_{0.99}Ge_{0.01}$, $MgAg_{0.97}Sb_{0.995}Te_{0.005}$, and $MgAg_{0.97}Sb_{0.99}Te_{0.01}$. The thermal conductivity values slightly increase with elevated temperatures. Although the noticeable change in the

electrical resistivity values, the overall thermal conductivity values were less affected by Sb substitution. Even the amplified electrical resistivity with Ge amount of 0.01, the Ge-doped samples displayed the thermal conductivity values were same with the pristine sample. For the $MgAg_{0.97}Sb_{0.995}Te_{0.005}$ sample, a jump in thermal conductivity values was observed after 525 K. This behavior might be related with a phase transition in the MgAgSb phase, where typically β phase-transition occurred between 560-630 K under normal conditions. Since β phase MgAgSb has a higher thermal conductivity, it might be resulted in enhanced thermal conductivity at high temperature. Although the electrical resistivity was similar for the Te content of 0.01, a slight raise was observed for the thermal conductivity.

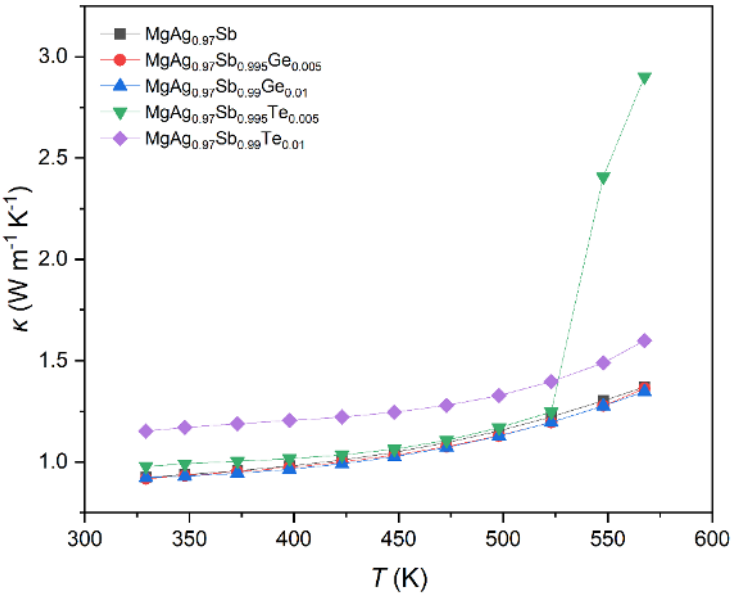

Figure 8.12. Total thermal conductivity values of $MgAg_{0.97}Sb$, $MgAg_{0.97}Sb_{0.995}Ge_{0.005}$, $MgAg_{0.97}Sb_{0.99}Ge_{0.01}$, $MgAg_{0.97}Sb_{0.995}Te_{0.005}$, and $MgAg_{0.97}Sb_{0.99}Te_{0.01}$ samples as a function of temperature.

The thermoelectric figure of merit (zT) values for $MgAg_{0.97}Sb$, $MgAg_{0.97}Sb_{0.995}Ge_{0.005}$, $MgAg_{0.97}Sb_{0.99}Ge_{0.01}$, $MgAg_{0.97}Sb_{0.995}Te_{0.005}$, and $MgAg_{0.97}Sb_{0.99}Te_{0.01}$ materials are displayed in Figure 8.13. Because of the tremendous decrease in the carrier concentration, which is predicted from the enormously low Seebeck coefficients, the zT value for Te-doped samples diminished. On the other hand, the zT value of Ge-doped sample with the composition of $MgAg_{0.97}Sb_{0.995}Ge_{0.005}$ was enhanced to 0.65 at 325 K and the highest value was achieved at 500 K with the zT of

1.03. In the lines of synthesis parameters and environment of this study, Ge element might an effective dopant on Sb-site, as suggested by Sheng et al[189].

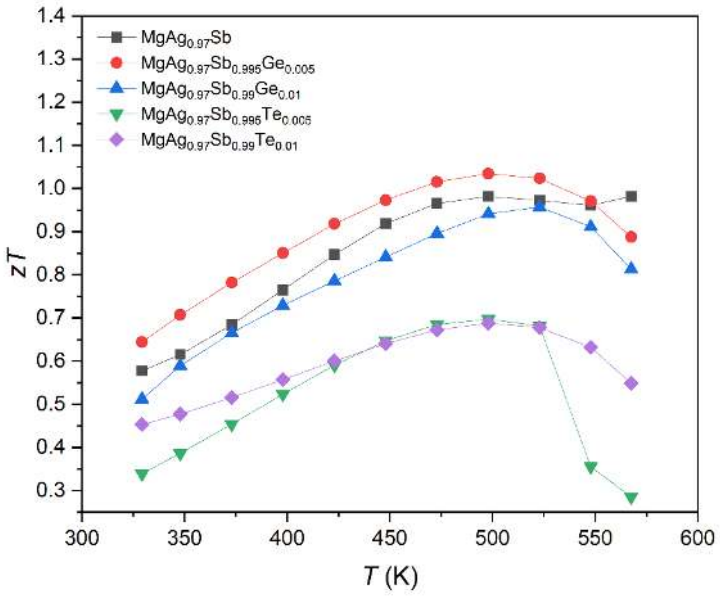

Figure 8.13. The thermoelectric figure of merit, zT, values of $MgAg_{0.97}Sb$, $MgAg_{0.97}Sb_{0.995}Ge_{0.005}$, $MgAg_{0.97}Sb_{0.99}Ge_{0.01}$, $MgAg_{0.97}Sb_{0.995}Te_{0.005}$, and $MgAg_{0.97}Sb_{0.99}Te_{0.01}$ samples as a function of temperature.

8.4 Conclusions

To investigate the effect of carrier concentration on the thermoelectric performance of $MgAg_{0.97}Sb$, an extensive examination was performed through different dopant elements like Y and Nb elements on Mg site, Zn and Co elements on Ag site, and finally Ge and Te elements on Sb site. All the experimental procedure retained same as the preparation methods of pristine $MgAg_{0.97}Sb$ sample.

Through the doping of the Ag site, it is noticed that Ag plays an important role for electron donation and a decrease in the Ag concentration in the chemical composition led to an increase in carrier concentration and Seebeck coefficients. To optimize the carrier concentration, different dopants have been utilized as electron donor and acceptor character. However, the optimum carrier concentration couldn't be achieved, and power factor values were decreased.

As discussed in previous chapters, Nb incorporation plays an effective role for enhancing the transport properties for Mg-containing phases. And if can be doped instead of Mg, it could increase the carrier concentration. However, this study reveals that Nb element is not acting like a dopant inside the structure and impurities are observable from the XRD analysis. Through the Nb addition, resistivity value is decreased as decreasing the Seebeck coefficient. In similar, Y-doping is also resulted in a decrease in Seebeck coefficient and resistivity. It is concluded that, the decrease in Mg content resulted in worse thermoelectric properties, overall.

For Sb-site doping, Ge addition initially resulted in a decrease in the Seebeck coefficient and resistivity, while maintaining the thermal conductivity. However, beyond the solubility limit, Ge doping caused an increase in resistivity. Despite this, the overall zT value increased with 0.005 at. % Ge addition, reaching a value of 0.65 at 330 K. In contrast, Te doping was found to be ineffective in improving the thermoelectric performance of $MgAg_{0.97}Sb$.

BIBLIOGRAPHY

1. P. Fragkos, N. Tasios, L. Paroussos, P. Capros and S. Tsani, *Energy Policy*, 2017, **100**, 216-226.
2. Z. Liang, C. Xu, S. Song, X. Shi, W. Ren and Z. Ren, *Advanced Functional Materials*, 2023, **33**, 2210016.
3. Z. Liu, N. Sato, W. Gao, K. Yubuta, N. Kawamoto, M. Mitome, K. Kurashima, Y. Owada, K. Nagase and C.-H. Lee, *Joule*, 2021, **5**, 1196-1208.
4. K. Imasato, S. D. Kang and G. J. Snyder, *Energy & Environmental Science*, 2019, **12**, 965-971.
5. R. Freer, D. Ekren, T. Ghosh, K. Biswas, P. Qiu, S. Wan, L. Chen, S. Han, C. Fu and T. Zhu, *Journal of Physics: Energy*, 2022, **4**, 022002.
6. X. Zhang and L.-D. Zhao, *Journal of Materiomics*, 2015, **1**, 92-105.
7. T. M. Tritt, *Annual review of materials research*, 2011, **41**, 433-448.
8. J. G. R. Sereni, 2016.
9. G. S. Nolas, J. Sharp and J. Goldsmid, *Thermoelectrics: basic principles and new materials developments*, Springer Science & Business Media, 2013.
10. J.-F. Li, W.-S. Liu, L.-D. Zhao and M. Zhou, *NPG Asia Materials*, 2010, **2**, 152-158.
11. G. J. Snyder and E. S. Toberer, *Nature materials*, 2008, **7**, 105-114.
12. H.-S. Kim, Z. M. Gibbs, Y. Tang, H. Wang and G. J. Snyder, *APL materials*, 2015, **3**.
13. J. R. Sootsman, D. Y. Chung and M. G. Kanatzidis, *Angewandte Chemie International Edition*, 2009, **48**, 8616-8639.
14. R. Taherian and A. Kausar, *Electrical Conductivity in polymer-based composites: experiments, modelling, and applications*, William Andrew, 2018.
15. J. R. Christman, *(No Title)*, 1988.
16. C. J. Vineis, A. Shakouri, A. Majumdar and M. G. Kanatzidis, *Advanced materials*, 2010, **22**, 3970-3980.
17. J. Zhai, T. Wang, H. Wang, W. Su, X. Wang, T. Chen and C. Wang, *Chinese Physics B*, 2018, **27**, 047306.
18. J. Hook and H. Hall, *Journal*, 2001.
19. K. H. Lee and S. W. Kim, *Journal of the Korean Ceramic Society*, 2017, **54**, 75-85.
20. L. E. Bell, *science*, 2008, **321**, 1457-1461.
21. H. Goldsmid, *Thermoelectric refrigeration*, Springer, 2013.
22. J. He and T. M. Tritt, *Science*, 2017, **357**, eaak9997.
23. R. He, G. Schierning and K. Nielsch, *Advanced Materials Technologies*, 2018, **3**, 1700256.
24. C. Han, Z. Li and S. Dou, *Chinese science bulletin*, 2014, **59**, 2073-2091.
25. M.-L. Pykälä, K. Sipilä, U.-M. Mroueh, M. Wahlström, H. Huovila, T. Tynell and J. Tervo, *Susterel energy harvesting Roadmap for societal applications*, VTT Research Report VTT: Espoo, Finland, 2012.
26. L.-D. Zhao, S.-H. Lo, Y. Zhang, H. Sun, G. Tan, C. Uher, C. Wolverton, V. P. Dravid and M. G. Kanatzidis, *nature*, 2014, **508**, 373-377.
27. M. Suárez, A. Fernández, J. Menéndez, R. Torrecillas, H. Kessel, J. Hennicke, R. Kirchner and T. Kessel, *Sintering applications*, 2013, **13**, 319-342.

28. Z.-Y. Hu, Z.-H. Zhang, X.-W. Cheng, F.-C. Wang, Y.-F. Zhang and S.-L. Li, *Materials & Design*, 2020, **191**, 108662.
29. P. Cavaliere, B. Sadeghi and A. Shabani, *Spark plasma sintering of materials: advances in processing and applications*, 2019, 3-20.
30. A. A. Bunaciu, E. G. UdriŞTioiu and H. Y. Aboul-Enein, *Critical reviews in analytical chemistry*, 2015, **45**, 289-299.
31. L. Akselrud and Y. Grin, *Journal of Applied Crystallography*, 2014, **47**, 803-805.
32. B. J. Inkson, in *Materials characterization using nondestructive evaluation (NDE) methods*, Elsevier, 2016, pp. 17-43.
33. W. Zhou, R. Apkarian, Z. L. Wang and D. Joy, *Scanning microscopy for nanotechnology: techniques and applications*, 2007, 1-40.
34. R. F. Egerton, *Physical principles of electron microscopy*, Springer, 2005.
35. L. Reimer, *Transmission electron microscopy: physics of image formation and microanalysis*, Springer, 2013.
36. G. F. Vander Voort and R. Fowler, *AM&P Technical Articles*, 2012, **170**, 28-33.
37. E. S. Toberer, C. A. Cox, S. R. Brown, T. Ikeda, A. F. May, S. M. Kauzlarich and G. J. Snyder, *Advanced Functional Materials*, 2008, **18**, 2795-2800.
38. O. Janka and S. M. Kauzlarich, *Encyclopedia of Inorganic and Bioinorganic Chemistry*, 2011, 1-19.
39. S. M. Kauzlarich, S. R. Brown and G. J. Snyder, *Dalton Transactions*, 2007, 2099-2107.
40. J. Shuai, J. Mao, S. Song, Q. Zhang, G. Chen and Z. Ren, *Materials Today Physics*, 2017, **1**, 74-95.
41. S. Song, J. Mao, M. Bordelon, R. He, Y. Wang, J. Shuai, J. Sun, X. Lei, Z. Ren and S. Chen, *Materials Today Physics*, 2019, **8**, 25-33.
42. J. Zhang, L. Song, A. Mamakhel, M. R. V. Jørgensen and B. B. Iversen, *Chemistry of Materials*, 2017, **29**, 5371-5383.
43. P. Gorai, A. Goyal, E. S. Toberer and V. Stevanović, *Journal of Materials Chemistry A*, 2019, **7**, 19385-19395.
44. J. Shuai, B. Ge, J. Mao, S. Song, Y. Wang and Z. Ren, *Journal of the American Chemical Society*, 2018, **140**, 1910-1915.
45. S. Ohno, K. Imasato, S. Anand, H. Tamaki, S. D. Kang, P. Gorai, H. K. Sato, E. S. Toberer, T. Kanno and G. J. Snyder, *Joule*, 2018, **2**, 141-154.
46. H. Tamaki, H. K. Sato and T. Kanno, *Advanced Materials (Deerfield Beach, Fla.)*, 2016, **28**, 10182-10187.
47. X. Shi, C. Sun, X. Zhang, Z. Chen, S. Lin, W. Li and Y. Pei, *Chemistry of Materials*, 2019, **31**, 8987-8994.
48. T. Kanno, H. Tamaki, H. K. Sato, S. D. Kang, S. Ohno, K. Imasato, J. J. Kuo, G. J. Snyder and Y. Miyazaki, *Applied Physics Letters*, 2018, **112**.
49. M. Wood, J. J. Kuo, K. Imasato and G. J. Snyder, *Advanced Materials*, 2019, **31**, 1902337.
50. K. Imasato, C. Fu, Y. Pan, M. Wood, J. J. Kuo, C. Felser and G. J. Snyder, *Advanced Materials*, 2020, **32**, 1908218.
51. T. Luo, J. J. Kuo, K. J. Griffith, K. Imasato, O. Cojocaru-Mirédin, M. Wuttig, B. Gault, Y. Yu and G. J. Snyder, *Advanced Functional Materials*, 2021, **31**, 2100258.
52. L. Yu, S.-t. Wei, L.-j. Wang, Z.-p. Zhang, Z. Ji, S.-t. Luo, J.-x. Liang, W.-y. Song and S.-Q. Zheng, *ACS Applied Materials & Interfaces*, 2023, **15**, 53594-53603.

53. X. Sun, X. Li, J. Yang, J. Xi, R. Nelson, C. Ertural, R. Dronskowski, W. Liu, G. J. Snyder and D. J. Singh, *Journal of computational chemistry*, 2019, **40**, 1693-1700.
54. X. Tan, G.-Q. Liu, H. Hu, H. Shao, J. Xu and J. Jiang, *Journal of Materials Chemistry A*, 2019, **7**, 8922-8928.
55. J. Mao, J. Shuai, S. Song, Y. Wu, R. Dally, J. Zhou, Z. Liu, J. Sun, Q. Zhang and C. dela Cruz, *Proceedings of the National Academy of Sciences*, 2017, **114**, 10548-10553.
56. X. Li, C. Sun, K. Yang, D. Liang, X. Ye, W. Song, W. Xu, W. Zhao and Q. Zhang, *Small*, 2024, 2311478.
57. M. Ozen, M. Yahyaoglu, C. Candolfi, I. Veremchuk, F. Kaiser, U. Burkhardt, G. J. Snyder, Y. Grin and U. Aydemir, *Journal of Materials Chemistry A*, 2021, **9**, 1733-1742.
58. J. Yang, G. Li, H. Zhu, N. Chen, T. Lu, J. Gao, L. Guo, J. Xiang, P. Sun and Y. Yao, *Joule*, 2022, **6**, 193-204.
59. J. Shuai, J. Mao, S. Song, Q. Zhu, J. Sun, Y. Wang, R. He, J. Zhou, G. Chen and D. J. Singh, *Energy & Environmental Science*, 2017, **10**, 799-807.
60. R. Shu, Y. Zhou, Q. Wang, Z. Han, Y. Zhu, Y. Liu, Y. Chen, M. Gu, W. Xu and Y. Wang, *Advanced Functional Materials*, 2019, **29**, 1807235.
61. Z. Liang, C. Xu, H. Shang, Q. Zhu, F. Ding, J. Mao and Z. Ren, *Materials Today Physics*, 2021, **19**, 100413.
62. K. Imasato, M. Wood, S. Anand, J. J. Kuo and G. J. Snyder, *Advanced Energy and Sustainability Research*, 2022, **3**, 2100208.
63. K. Imasato, S. D. Kang, S. Ohno and G. J. Snyder, *Materials Horizons*, 2018, **5**, 59-64.
64. X. Shi, X. Zhang, A. Ganose, J. Park, C. Sun, Z. Chen, S. Lin, W. Li, A. Jain and Y. Pei, *Materials Today Physics*, 2021, **18**, 100362.
65. J. J. Kuo, S. D. Kang, K. Imasato, H. Tamaki, S. Ohno, T. Kanno and G. J. Snyder, *Energy & Environmental Science*, 2018, **11**, 429-434.
66. Q. Qiu, Y. Liu, K. Xia, T. Fang, J. Yu, X. Zhao and T. Zhu, *Advanced Energy Materials*, 2019, **9**, 1803447.
67. J.-W. Li, Z. Han, J. Yu, H.-L. Zhuang, H. Hu, B. Su, H. Li, Y. Jiang, L. Chen and W. Liu, *Nature Communications*, 2023, **14**, 7428.
68. F. Zhang, D. Wu and J. He, *Materials Lab*, 2022, **1**, 220012-220011-220012-220016.
69. Z. Liu, W. Gao, H. Oshima, K. Nagase, C.-H. Lee and T. Mori, *Nature communications*, 2022, **13**, 1120.
70. C. Gayner and Y. Amouyal, *Advanced Functional Materials*, 2020, **30**, 1901789.
71. A. Minnich, M. S. Dresselhaus, Z. Ren and G. Chen, *Energy & Environmental Science*, 2009, **2**, 466-479.
72. Z. A. S. D. B. JL, *Phys. Rev*, 2018, **5**, 021303.
73. Y. Lin, M. Wood, K. Imasato, J. J. Kuo, D. Lam, A. N. Mortazavi, T. J. Slade, S. A. Hodge, K. Xi and M. G. Kanatzidis, *Energy & Environmental Science*, 2020, **13**, 4114-4121.
74. M. Zebarjadi, K. Esfarjani, M. Dresselhaus, Z. Ren and G. Chen, *Energy & Environmental Science*, 2012, **5**, 5147-5162.
75. L. Yang, Z. G. Chen, M. S. Dargusch and J. Zou, *Advanced Energy Materials*, 2018, **8**, 1701797.

76. Y. Lin, C. Norman, D. Srivastava, F. Azough, L. Wang, M. Robbins, K. Simpson, R. Freer and I. A. Kinloch, *ACS applied materials & interfaces*, 2015, **7**, 15898-15908.
77. R. Nunna, P. Qiu, M. Yin, H. Chen, R. Hanus, Q. Song, T. Zhang, M.-Y. Chou, M. T. Agne and J. He, *Energy & Environmental Science*, 2017, **10**, 1928-1935.
78. P.-a. Zong, R. Hanus, M. Dylla, Y. Tang, J. Liao, Q. Zhang, G. J. Snyder and L. Chen, *Energy & Environmental Science*, 2017, **10**, 183-191.
79. B. Madavali, H.-S. Kim, K.-H. Lee and S.-J. Hong, *Intermetallics*, 2017, **82**, 68-75.
80. Y. Dou, X. Qin, D. Li, L. Li, T. Zou and Q. Wang, *Journal of Applied Physics*, 2013, **114**.
81. J. Li, Q. Tan, J. F. Li, D. W. Liu, F. Li, Z. Y. Li, M. Zou and K. Wang, *Advanced Functional Materials*, 2013, **23**, 4317-4323.
82. D. Li, J. Li, J. Li, Y. Wang, J. Zhang, X. Qin, Y. Cao, Y. Li and G. Tang, *Journal of Materials Chemistry A*, 2018, **6**, 9642-9649.
83. Y. Li, Y. Dou, X. Qin, J. Zhang, H. Xin, D. Li, C. Song, T. Zou, Y. Liu and C. Li, *RSC Advances*, 2016, **6**, 12243-12248.
84. B. Madavali, C. H. Lee, H. S. Kim, K. H. Lee and S. J. Hong, *International Journal of Applied Ceramic Technology*, 2018, **15**, 125-131.
85. A. Pakdel, Q. Guo, V. Nicolosi and T. Mori, *Journal of Materials Chemistry A*, 2018, **6**, 21341-21349.
86. F. Li, X. Huang, Z. Sun, J. Ding, J. Jiang, W. Jiang and L. Chen, *Journal of Alloys and Compounds*, 2011, **509**, 4769-4773.
87. J. Wang, J. Mark, K. E. Woo, J. Voyles and K. Kovnir, *Chemistry of Materials*, 2019, **31**, 8286-8300.
88. W. Zhang, J.-F. Halet and T. Mori, *Journal of Materials Chemistry A*, 2023, **11**, 24228-24238.
89. J. Zhang, L. Song and B. B. Iversen, *Npj Computational Materials*, 2019, **5**, 76.
90. X. Shi, X. Wang, W. Li and Y. Pei, *Small Methods*, 2018, **2**, 1800022.
91. X. Chong, P.-W. Guan, Y. Wang, S.-L. Shang, J. Paz Soldan Palma, F. Drymiotis, V. A. Ravi, K. E. Star, J.-P. Fleurial and Z.-K. Liu, *ACS Applied Energy Materials*, 2018, **1**, 6600-6608.
92. J. Zhang, L. Song, M. Sist, K. Tolborg and B. B. Iversen, *Nature Communications*, 2018, **9**, 4716.
93. T. Balakumar and M. Medraj, *Calphad*, 2005, **29**, 24-36.
94. E. G. Seebauer and M. C. Kratzer, *Materials Science and Engineering: R: Reports*, 2006, **55**, 57-149.
95. J. Zhang, L. Song, S. H. Pedersen, H. Yin, L. T. Hung and B. B. Iversen, *Nature communications*, 2017, **8**, 13901.
96. J. Sun, J. Shuai, Z. Ren and D. J. Singh, *Materials Today Physics*, 2017, **2**, 40-45.
97. L. Song, J. Zhang and B. B. Iversen, *Journal of Materials Chemistry A*, 2017, **5**, 4932-4939.
98. S. Ning, S. Huang, Z. Zhang, N. Qi, M. Jiang, Z. Chen and X. Tang, *Journal of Materiomics*, 2022, **8**, 1086-1094.
99. M. K. Brod, S. Anand and G. J. Snyder, *Materials Today Physics*, 2023, **31**, 100959.
100. A. Li, C. Fu, X. Zhao and T. Zhu, *Research*, 2020.

101. X. Chen, H. Wu, J. Cui, Y. Xiao, Y. Zhang, J. He, Y. Chen, J. Cao, W. Cai and S. J. Pennycook, *Nano Energy*, 2018, **52**, 246-255.
102. J. Zhang and B. B. Iversen, *Journal of Applied Physics*, 2019, **126**.
103. H. J. Goldsmid, *Introduction to thermoelectricity*, Springer, 2010.
104. J. Zhang, L. Song, G. K. Madsen, K. F. Fischer, W. Zhang, X. Shi and B. B. Iversen, *Nature communications*, 2016, **7**, 10892.
105. S. Lee, K. Esfarjani, T. Luo, J. Zhou, Z. Tian and G. Chen, *Nature communications*, 2014, **5**, 3525.
106. C. W. Li, J. Hong, A. F. May, D. Bansal, S. Chi, T. Hong, G. Ehlers and O. Delaire, *Nature Physics*, 2015, **11**, 1063-1069.
107. G. A. Slack, *Solid state physics*, 1979, **34**, 1-71.
108. E. S. Toberer, A. Zevalkink and G. J. Snyder, *Journal of Materials Chemistry*, 2011, **21**, 15843-15852.
109. T. M. Tritt, *Thermal conductivity: theory, properties, and applications*, Springer Science & Business Media, 2005.
110. W. Peng, G. Petretto, G.-M. Rignanese, G. Hautier and A. Zevalkink, *Joule*, 2018, **2**, 1879-1893.
111. L.-D. Zhao, V. P. Dravid and M. G. Kanatzidis, *Energy & Environmental Science*, 2014, **7**, 251-268.
112. T. Kanno, H. Tamaki, M. Yoshiya, H. Uchiyama, S. Maki, M. Takata and Y. Miyazaki, *Advanced Functional Materials*, 2021, **31**, 2008469.
113. J. Hu, J. Zhu, X. Dong, M. Guo, Y. Sun, W. Shi, Y. Zhu, H. Wu, F. Guo and Y. X. Zhang, *Small*, 2023, **19**, 2301382.
114. J. Li, S. Zheng, T. Fang, L. Yue, S. Zhang and G. Lu, *Physical Chemistry Chemical Physics*, 2018, **20**, 7686-7693.
115. C. Zhang, G. Yan, Y. Wang, X. Wu, L. Hu, F. Liu, W. Ao, O. Cojocaru-Mirédin, M. Wuttig and G. J. Snyder, *Advanced Energy Materials*, 2023, **13**, 2203361.
116. T. J. Slade, J. A. Grovogui, J. J. Kuo, S. Anand, T. P. Bailey, M. Wood, C. Uher, G. J. Snyder, V. P. Dravid and M. G. Kanatzidis, *Energy & Environmental Science*, 2020, **13**, 1509-1518.
117. G. J. Snyder, A. H. Snyder, M. Wood, R. Gurunathan, B. H. Snyder and C. Niu, *Advanced Materials*, 2020, **32**, 2001537.
118. H. Sepehri-Amin, K. Imasato, M. Wood, J. J. Kuo and G. J. Snyder, *ACS applied materials & interfaces*, 2022, **14**, 37958-37966.
119. E. Bauer, C. Paul, S. Berger, S. Majumdar, H. Michor, M. Giovannini, A. Saccone and A. Bianconi, *Journal of Physics: Condensed Matter*, 2001, **13**, L487.
120. B. Chen, J. Li, M. Wu, L. Hu, F. Liu, W. Ao, Y. Li, H. Xie and C. Zhang, *ACS applied materials & interfaces*, 2019, **11**, 45746-45754.
121. H. Qin, B. Cui, W. Wang, S. Sun, D. Qin, M. Guo, L. Xie, F. Guo, W. Cai and J. Sui, *Advanced Electronic Materials*, 2021, **7**, 2100173.
122. F. Jiang, T. Feng, Y. Zhu, Z. Han, R. Shu, C. Chen, Y. Zhang, C. Xia, X. Wu and H. Yu, *Materials Today Physics*, 2022, **27**, 100835.
123. L. Wang, N. Sato, Y. Peng, R. Chetty, N. Kawamoto, D. H. Nguyen and T. Mori, *Advanced Energy Materials*, 2023, **13**, 2301667.
124. J. Mao, H. Zhu, Z. Ding, Z. Liu, G. A. Gamage, G. Chen and Z. Ren, *Science*, 2019, **365**, 495-498.
125. W. Liu, X. Yan, G. Chen and Z. Ren, *Nano Energy*, 2012, **1**, 42-56.
126. A. Bhardwaj and D. Misra, *Rsc Advances*, 2014, **4**, 34552-34560.

127. F. Zhang, C. Chen, H. Yao, F. Bai, L. Yin, X. Li, S. Li, W. Xue, Y. Wang and F. Cao, *Advanced Functional Materials*, 2020, **30**, 1906143.
128. K. Imasato, M. Wood, J. J. Kuo and G. J. Snyder, *Journal of Materials Chemistry A*, 2018, **6**, 19941-19946.
129. X. Shi, T. Zhao, X. Zhang, C. Sun, Z. Chen, S. Lin, W. Li, H. Gu and Y. Pei, *Advanced Materials*, 2019, **31**, 1903387.
130. P. Gorai, B. R. Ortiz, E. S. Toberer and V. Stevanović, *Journal of Materials Chemistry A*, 2018, **6**, 13806-13815.
131. T. Luo, J. J. Kuo, K. J. Griffith, K. Imasato, O. Cojocaru-Mirédin, M. Wuttig, B. Gault, Y. Yu and G. J. Snyder, *Advanced Functional Materials*, 2021, **31**, 2100258.
132. J. Mao, Y. Wu, S. Song, Q. Zhu, J. Shuai, Z. Liu, Y. Pei and Z. Ren, *ACS Energy Letters*, 2017, **2**, 2245-2250.
133. J.-W. Li, Z. Han, J. Yu, H.-L. Zhuang, H. Hu, B. Su, H. Li, Y. Jiang, L. Chen, W. Liu, Q. Zheng and J.-F. Li, *Nature Communications*, 2023, **14**, 7428.
134. H.-T. Liu, Q. Sun, Y. Zhong, Q. Deng, L. Gan, F.-L. Lv, X.-L. Shi, Z.-G. Chen and R. Ang, *Nano Energy*, 2022, **91**, 106706.
135. E. Wigner, *Aufbau der Materie*, 1932, **19**, 203-216.
136. M. Calderón-Cueva, W. Peng, S. M. Clarke, J. Ding, B. L. Brugman, G. Levental, A. Balodhi, M. Rylko, O. Delaire and J. P. Walsh, *Chemistry of Materials*, 2021, **33**, 567-573.
137. S. Williamson and M. Milewits, 1976.
138. Q. Chen, Y. Zhou, B. Xu, Z. Lou, H. Chen, S. Chen, C. Wu, J. Du, H. Wang and J. Yang, *Chinese Physics Letters*, 2021, **38**, 087501.
139. T. Luo, F. Serrano-Sánchez, H. Bishara, S. Zhang, R. B. Villoro, J. J. Kuo, C. Felser, C. Scheu, G. J. Snyder and J. P. Best, *Acta Materialia*, 2021, **217**, 117147.
140. R. Bueno Villoro, D. Zavanelli, C. Jung, D. A. Mattlat, R. Hatami Naderloo, N. Pérez, K. Nielsch, G. J. Snyder, C. Scheu and R. He, *Advanced Energy Materials*, 2023, **13**, 2204321.
141. J. Y. W. Seto, *Journal of Applied Physics*, 1975, **46**, 5247-5254.
142. C. Hu, K. Xia, C. Fu, X. Zhao and T. Zhu, *Energy & Environmental Science*, 2022, **15**, 1406-1422.
143. T. Chookajorn, H. A. Murdoch and C. A. Schuh, *Science*, 2012, **337**, 951-954.
144. H. Wang, Y. Pei, A. D. LaLonde and G. Jeffery Snyder, *Thermoelectric Nanomaterials: Materials Design and Applications*, 2013, 3-32.
145. I. T. Witting, T. C. Chasapis, F. Ricci, M. Peters, N. A. Heinz, G. Hautier and G. J. Snyder, *Advanced Electronic Materials*, 2019, **5**, 1800904.
146. J. J. Kuo, M. Wood, T. J. Slade, M. G. Kanatzidis and G. J. Snyder, *Energy & Environmental Science*, 2020, **13**, 1250-1258.
147. X. Shi, C. Sun, Z. Bu, X. Zhang, Y. Wu, S. Lin, W. Li, A. Faghaninia, A. Jain and Y. Pei, *Advanced science*, 2019, **6**, 1802286.
148. P. Ying, L. Wilkens, H. Reith, N. P. Rodriguez, X. Hong, Q. Lu, C. Hess, K. Nielsch and R. He, *Energy & Environmental Science*, 2022, **15**, 2557-2566.
149. R. Amatya and R. Ram, *Journal of electronic materials*, 2012, **41**, 1011-1019.
150. Y. Sun, J. Fu, Y. Ohishi, K. Toh, K. Suekuni, K. Kihou, U. Anazawa, C.-H. Lee and K. Kurosaki, *ACS Applied Materials & Interfaces*, 2023, **15**, 23246-23254.
151. Y. Sun, Y. k. Zhu, H. Wu, N. Qu, L. Xie, J. Zhu, Z. Liu, Q. Zhang, W. Cai and F. Guo, *Energy & Environmental Science*, 2024.

152. P. Ying, H. Reith, K. Nielsch and R. He, *Small*, 2022, **18**, 2201183.
153. M. J. Kirkham, A. M. dos Santos, C. J. Rawn, E. Lara-Curzio, J. W. Sharp and A. J. Thompson, *Physical Review B*, 2012, **85**, 144120.
154. J.-L. Mi, P.-J. Ying, M. Sist, H. Reardon, P. Zhang, T.-J. Zhu, X.-B. Zhao and B. B. Iversen, *Chemistry of Materials*, 2017, **29**, 6378-6388.
155. G. Li, Q. An, U. Aydemir, S. I. Morozov, B. Duan, P. Zhai, Q. Zhang and W. A. Goddard III, *Journal of Materiomics*, 2020, **6**, 24-32.
156. B. Frost and G. V. Raynor, *Proceedings of the Royal Society of London. Series A. Mathematical and Physical Sciences*, 1950, **203**, 132-147.
157. J. Camut, École Européenne d'Ingénieurs en Génie des Matériaux, 2018.
158. Y. Iqbal, C. Wang, J. Wang, L. Li, S. Li and Y. Chen, 2022.
159. Y. Liao, J.-L. Chen, C. Liu, J. Liang, Q. Zhou, P. Wang and L. Miao, *Journal of Materials Chemistry C*, 2022, **10**, 3360-3367.
160. Z. Zhang, Y. Zhu, J. Ji, J. Zhang, H. Luo, C. Fu, Q. Li, M. Brod, G. J. Snyder and Y. Zhang, *Materials Today Physics*, 2022, **25**, 100702.
161. H. Zhao, J. Sui, Z. Tang, Y. Lan, Q. Jie, D. Kraemer, K. McEnaney, A. Guloy, G. Chen and Z. Ren, *Nano Energy*, 2014, **7**, 97-103.
162. G. A. Slack, in *CRC handbook of thermoelectrics*, CRC press, 2018, pp. 407-440.
163. W. G. Zeier, A. Zevalkink, Z. M. Gibbs, G. Hautier, M. G. Kanatzidis and G. J. Snyder, *Angewandte Chemie International Edition*, 2016, **55**, 6826-6841.
164. P. Ying, X. Li, Y. Wang, J. Yang, C. Fu, W. Zhang, X. Zhao and T. Zhu, *Advanced Functional Materials*, 2017, **27**, 1604145.
165. J. Camut, I. Barber Rodriguez, H. Kamila, A. Cowley, R. Sottong, E. Mueller and J. de Boor, *Materials*, 2019, **12**, 1857.
166. S. Li, J. Yang, Y. Liu, J. Xin, S. Li, Q. Long and Q. Jiang, *Advances in Applied Ceramics*, 2020, **119**, 107-113.
167. K. Peng, L. Guo, G. Wang, X. Su, X. Zhou, X. Tang and C. Uher, *Science of Advanced Materials*, 2017, **9**, 682-687.
168. Z. Liu, H. Geng, J. Mao, J. Shuai, R. He, C. Wang, W. Cai, J. Sui and Z. Ren, *Journal of Materials Chemistry A*, 2016, **4**, 16834-16840.
169. Z. Liu, J. Shuai, J. Mao, Y. Wang, Z. Wang, W. Cai, J. Sui and Z. Ren, *Acta Materialia*, 2016, **102**, 17-23.
170. Y. Zheng, C. Liu, L. Miao, C. Li, R. Huang, J. Gao, X. Wang, J. Chen, Y. Zhou and E. Nishibori, *Nano Energy*, 2019, **59**, 311-320.
171. Z. Liu, Y. Zhang, J. Mao, W. Gao, Y. Wang, J. Shuai, W. Cai, J. Sui and Z. Ren, *Acta Materialia*, 2017, **128**, 227-234.
172. J. Sui, J. Shuai, Y. Lan, Y. Liu, R. He, D. Wang, Q. Jie and Z. Ren, *Acta Materialia*, 2015, **87**, 266-272.
173. X. Wu, Y. Lin, C. Liu, Y. Wang, H. Li, B. Ge and W. Liu, *Energy & Environmental Science*, 2024, **17**, 2879-2887.
174. Y. Huang, J. Lei, H. Chen, Z. Zhou, H. Dong, S. Yang, H. Gao, T.-R. Wei, K. Zhao and X. Shi, *Acta Materialia*, 2023, **249**, 118847.
175. P. Ying, X. Liu, C. Fu, X. Yue, H. Xie, X. Zhao, W. Zhang and T. Zhu, *Chemistry of Materials*, 2015, **27**, 909-913.
176. Y. Zheng, C. Liu, L. Miao, H. Lin, J. Gao, X. Wang, J. Chen, S. Wu, X. Li and H. Cai, *RSC advances*, 2018, **8**, 35353-35359.
177. J. Xin, J. Yang, S. Li, A. Basit, B. Sun, S. Li, Q. Long, X. Li, Y. Chen and Q. Jiang, *Chemistry of Materials*, 2019, **31**, 2421-2430.

178. A. Duparchy, L. Millerand, J. Camut, S. Tumminello, H. Kamila, R. Deshpande, A. Cowley, E. Mueller and J. de Boor, *Journal of Materials Chemistry A*, 2022, **10**, 21716-21726.
179. I. Rodriguez-Barber, J. Camut, L. Luhmann, A. Cowley, E. Mueller and J. de Boor, *Journal of Alloys and Compounds*, 2021, **860**, 158384.
180. J. Lei, D. Zhang, W. Guan, Z. Cheng, C. Wang and Y. Wang, *Physical Chemistry Chemical Physics*, 2018, **20**, 16729-16735.
181. L. Xie, J. Yang, Z. Liu, N. Qu, X. Dong, J. Zhu, W. Shi, H. Wu, G. Peng and F. Guo, *Materials Today*, 2023, **65**, 5-13.
182. D. Li, H. Zhao, S. Li, B. Wei, J. Shuai, C. Shi, X. Xi, P. Sun, S. Meng and L. Gu, *Advanced Functional Materials*, 2015, **25**, 6478-6488.
183. S. A. Khandy and J.-D. Chai, *Journal of Alloys and Compounds*, 2021, **850**, 156615.
184. Y. Wu, K. Xu, C. Ma, Y. Chen, Z. Lu, H. Zhang, Z. Fang and R. Zhang, *Nano Energy*, 2019, **63**, 103870.
185. X. Lou, S. Li, X. Chen, Q. Zhang, H. Deng, J. Zhang, D. Li, X. Zhang, Y. Zhang and H. Zeng, *ACS nano*, 2021, **15**, 8204-8215.
186. Y. Sun, A. Abbas, H. Wang, C. Tan, Z. Li, Y. Zong, H. Sun, C. Wang and H. Wang, *Chemical Engineering Journal*, 2024, **486**, 150158.
187. Z. Feng, J. Zhang, Y. Yan, G. Zhang, C. Wang, C. Peng, F. Ren, Y. Wang and Z. Cheng, *Scientific Reports*, 2017, **7**, 2572.
188. D. Kraemer, J. Sui, K. McEnaney, H. Zhao, Q. Jie, Z. Ren and G. Chen, *Energy & Environmental Science*, 2015, **8**, 1299-1308.
189. C. Sheng, H. Liu, D. Fan, L. Cheng, J. Zhang, J. Wei, J. Liang, P. Jiang and J. Shi, *Journal of Applied Physics*, 2016, **119**.
190. J. Shuai, H. S. Kim, Y. Lan, S. Chen, Y. Liu, H. Zhao, J. Sui and Z. Ren, *Nano Energy*, 2015, **11**, 640-646.
191. Z. Liu, Y. Wang, J. Mao, H. Geng, J. Shuai, Y. Wang, R. He, W. Cai, J. Sui and Z. Ren, *Advanced Energy Materials*, 2016, **6**, 1502269.
192. Z. Liu, Y. Wang, W. Gao, J. Mao, H. Geng, J. Shuai, W. Cai, J. Sui and Z. Ren, *Nano Energy*, 2017, **31**, 194-200.
193. W. Gao, X. Yi, B. Cui, Z. Wang, J. Huang, J. Sui and Z. Liu, *Journal of Materials Chemistry C*, 2018, **6**, 9821-9827.
194. K. Toh, K. Suekuni, K. Hashikuni, H. Nishiate, U. Anazawa, C.-H. Lee and M. Ohtaki, *Journal of Materials Science*, 2022, **57**, 11265-11273.
195. Y. Wang, X. Zhang, Y. Wang, N. Liu, Y. Liu and Q. Lu, *Journal of Materials Science*, 2022, **57**, 3183-3192.
196. J.-i. Tani and H. Ishikawa, *Materials Letters*, 2020, **262**, 127056.
197. K. Kihou, H. Kunioka, H. Nishiate and C. Lee, *Journal of Materials Research and Technology*, 2021, **10**, 438-444.

Appendix A

$Mg_{3.2}Sb_{1.5}Bi_{0.49}Te_{0.01} + MgB_2$

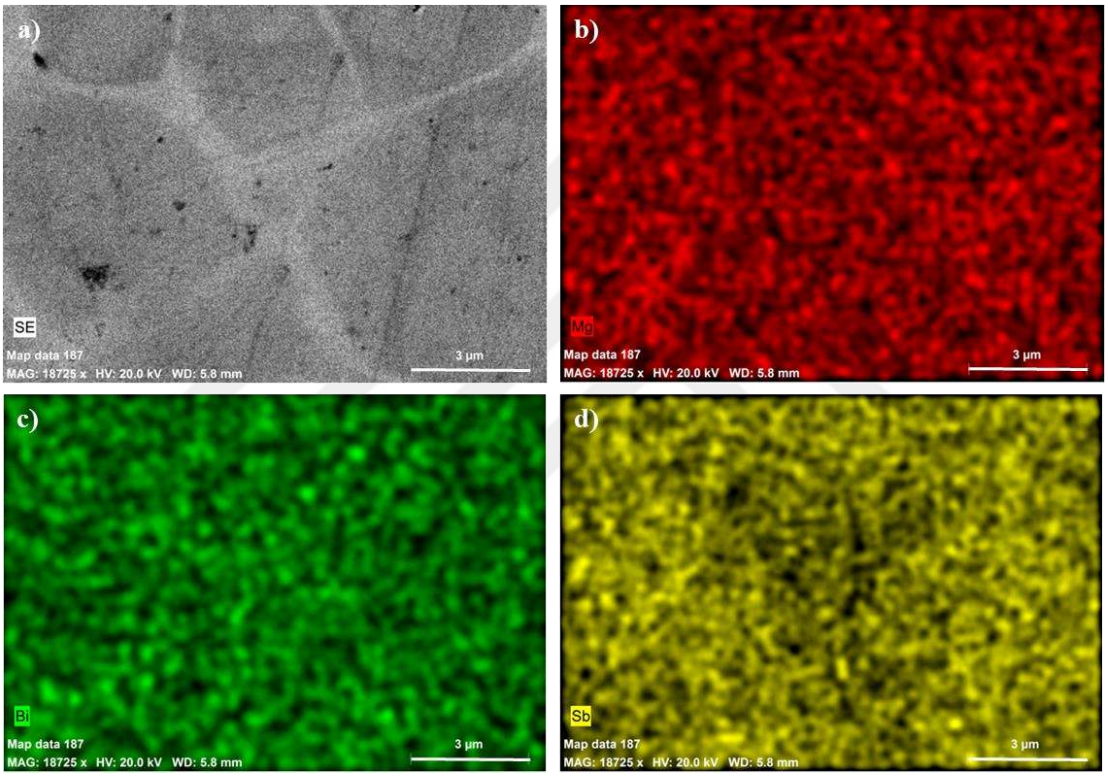

Figure A 1. EDS elemental mapping of the $Mg_{3.2}Sb_{1.5}Bi_{0.49}Te_{0.01}$ sample.

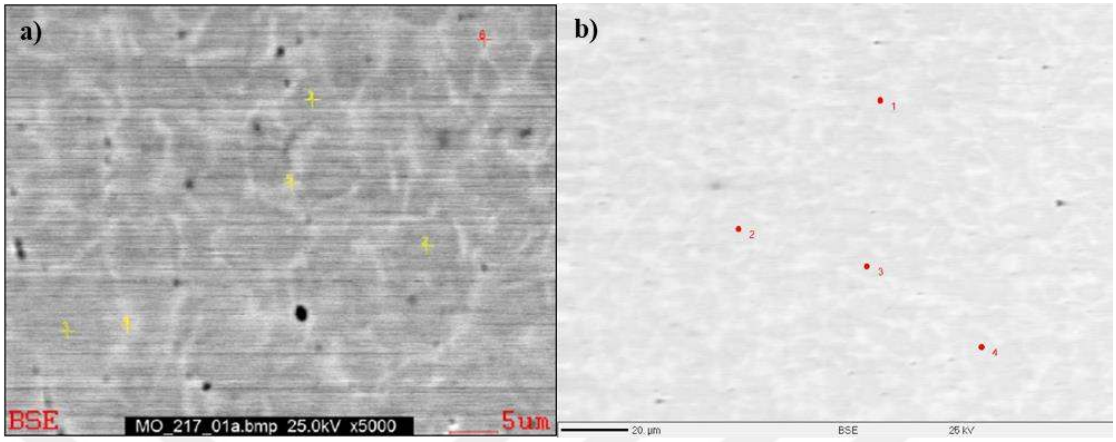

Average on 10 points								
	Weight%	Dev_Wt	NormWeight %	Dev Norm Wt	Atomic%	Dev_At	Det.Lim (Ancey)	StdDev wt%
Sb	53.71	1.62	52.55	1.53	30.69	0.68	178.	0.13
Mg	20.98	0.29	20.53	0.34	60.06	0.39	62.	0.06
Bi	27.09	1.85	26.50	1.73	9.02	0.68	374.	0.09
Te	0.42	0.01	0.41	0.01	0.23		38.	
Total	102.21		100.00		100.00			

Figure A 2. a, b) Ten different spots that WDS analysis was conducted on $Mg_{3.2}Sb_{1.5}Bi_{0.49}Te_{0.01}$ without MgB_2 addition and average atomic percentages of the elements.

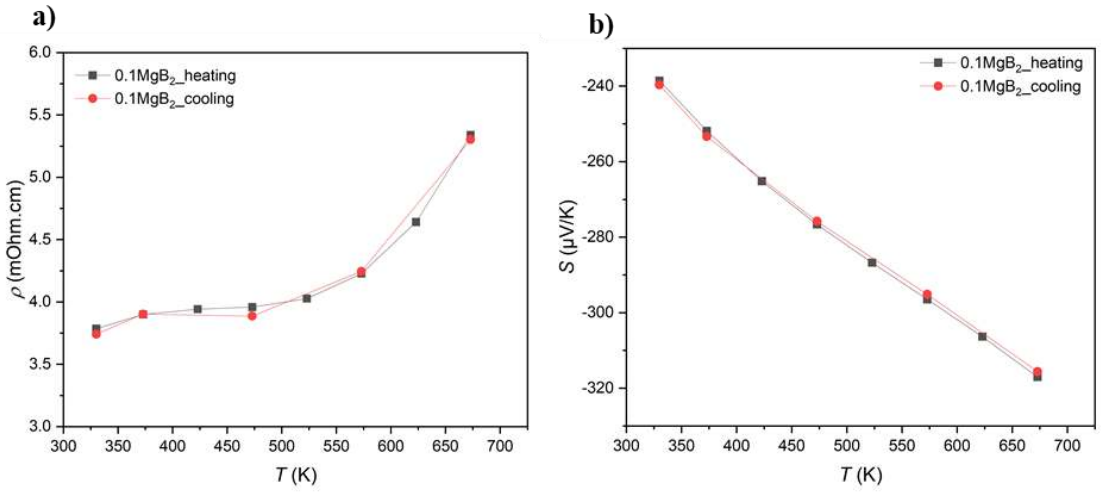

Figure A 3. a) Electrical resistivity and b) Seebeck coefficient of $Mg_{3.2}Sb_{1.5}Bi_{0.49}Te_{0.01}$ with 0.1 wt.% MgB_2 addition during heating and cooling cycles.

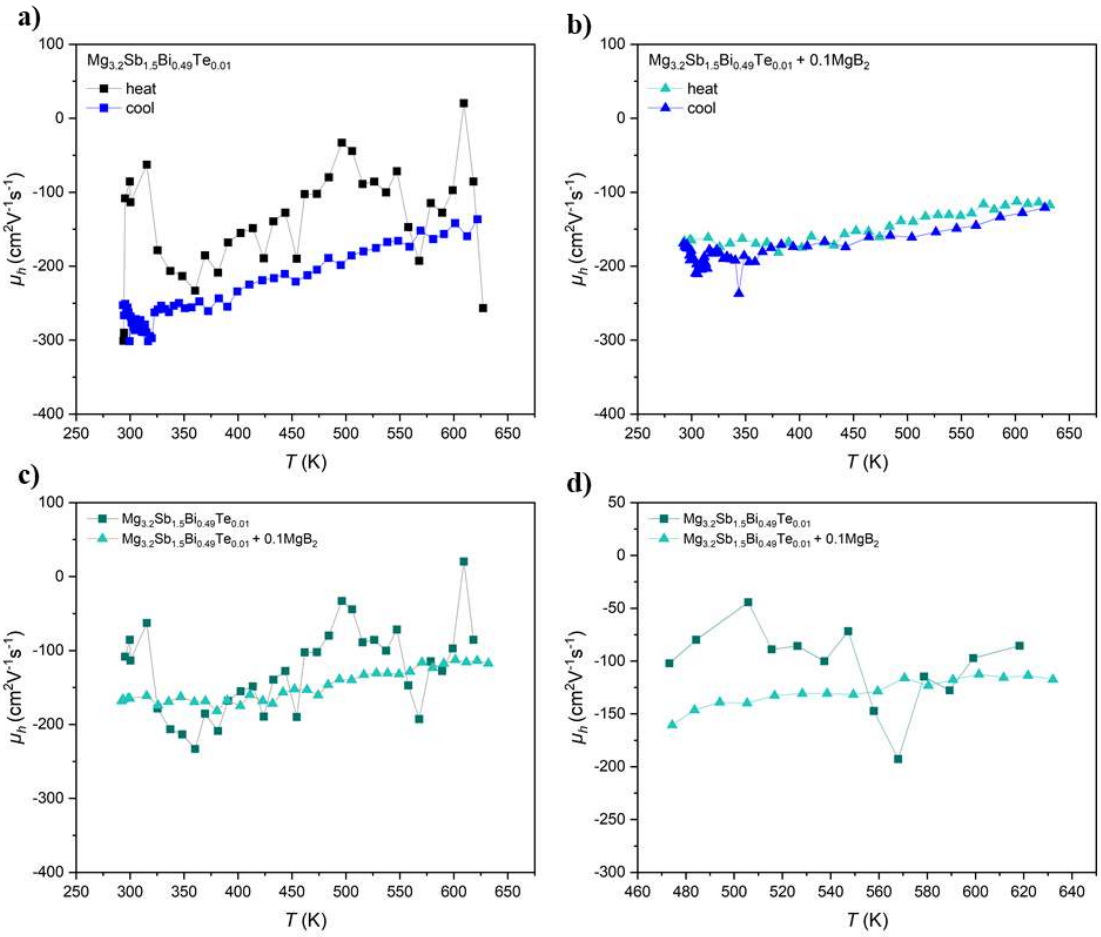

Figure A 4. Hall mobility of a) $Mg_{3.2}Sb_{1.5}Bi_{0.49}Te_{0.01}$ and b) $Mg_{3.2}Sb_{1.5}Bi_{0.49}Te_{0.01}$ with 0.1 wt.% MgB_2 addition measured during heating and cooling cycles, and c, d) comparison of Hall mobility values with and without MgB_2 addition for heating cycles.

Appendix B

$Mg_{3.2-x}Nb_x(Sb_{0.3}Bi_{0.7})_{1.996}Te_{0.004}$

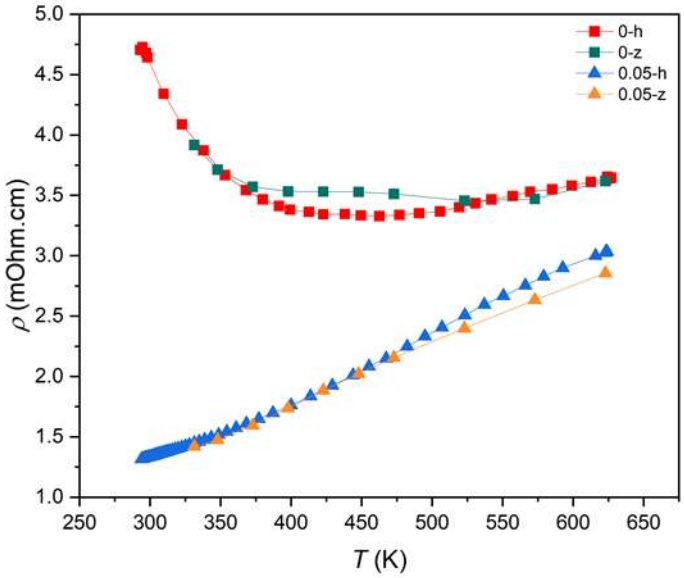

Figure B 1. Resistivity values of $Mg_{3.15}Nb_{0.05}(Sb_{0.3}Bi_{0.7})_{1.996}Te_{0.004}$ and $Mg_{3.2}Bi_{1.49}Sb_{0.5}Te_{0.01}$ measured by ZEM-3(z) and Hall effect (h).

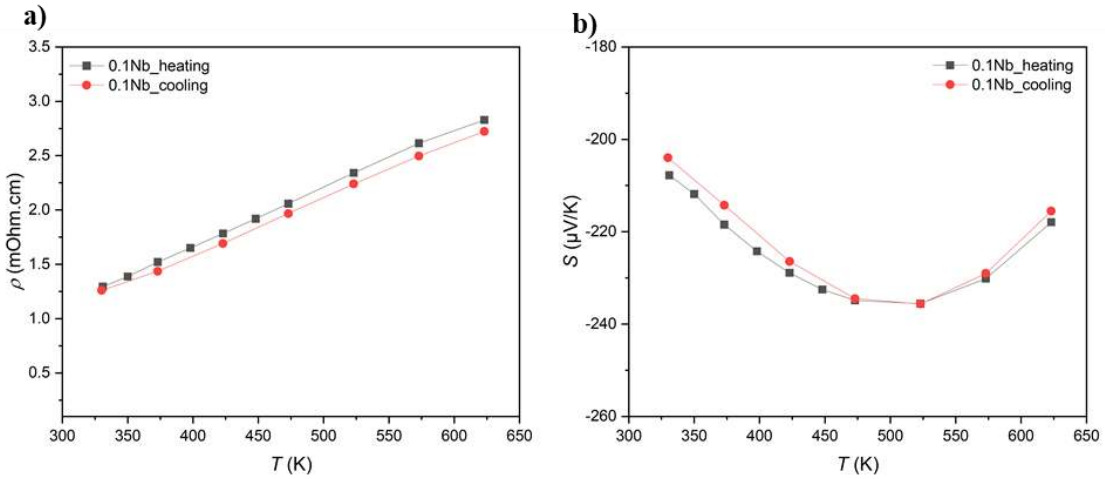

Figure B 2. Resistivity and Seebeck coefficient of $Mg_{3.1}Nb_{0.1}(Sb_{0.3}Bi_{0.7})_{1.996}Te_{0.004}$ during heating and cooling cycles.

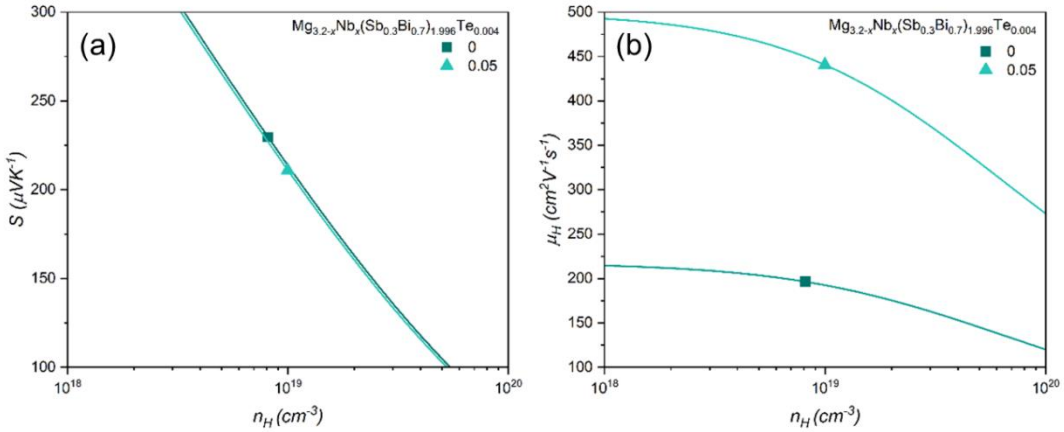

Figure B 3. Calculated (lines) and experimental (symbols) n_H-dependent a) S and b) μ_H of pristine and Nb-added $Mg_{3.15}Nb_{0.05}(Sb_{0.3}Bi_{0.7})_{1.996}Te_{0.004}$ (x = 0.05) samples at 330 K.

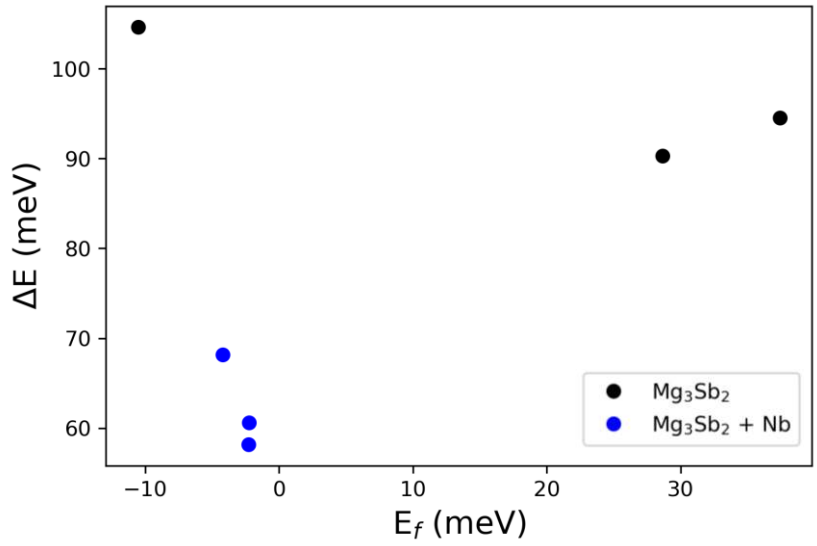

Figure B 4. The modeled ΔE versus bulk E_f for $Mg_{3.2-x}Nb_x(Sb_{0.3}Bi_{0.7})_{1.996}Te_{0.004}$ and one $Mg_{3.2}Bi_{1.49}Sb_{0.5}Te_{0.01}$ sample from Liu et al.[134].

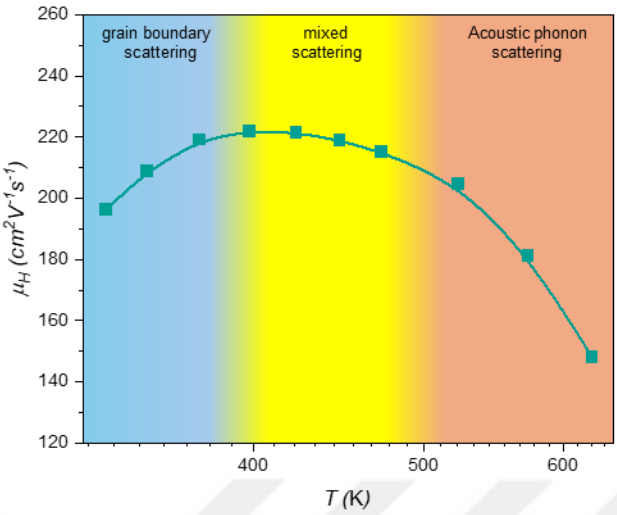

Figure B 5. Temperature dependent hall mobility of the pristine sample.

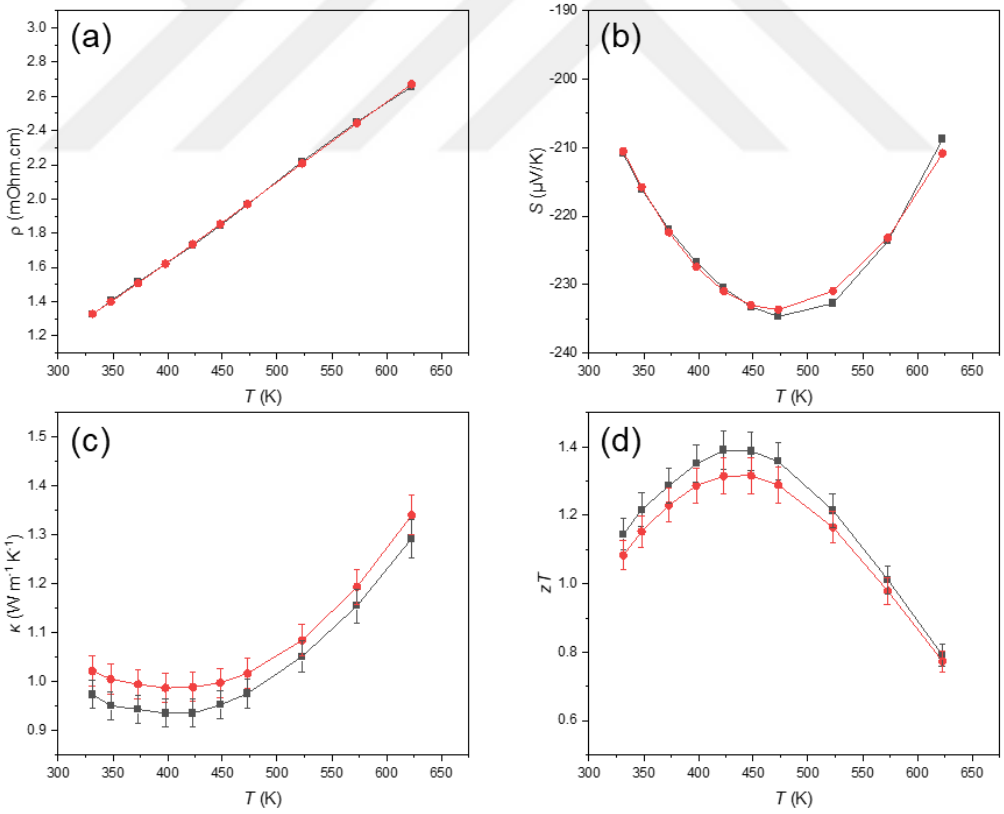

Figure B 6. Temperature-dependent a) ρ, b) S, c) κ and d) zT values of two different $Mg_{3.2}Nb_{0.1}(Sb_{0.3}Bi_{0.7})_{1.996}Te_{0.004}$ samples.

Appendix C

$MgAg_{0.97}Sb$

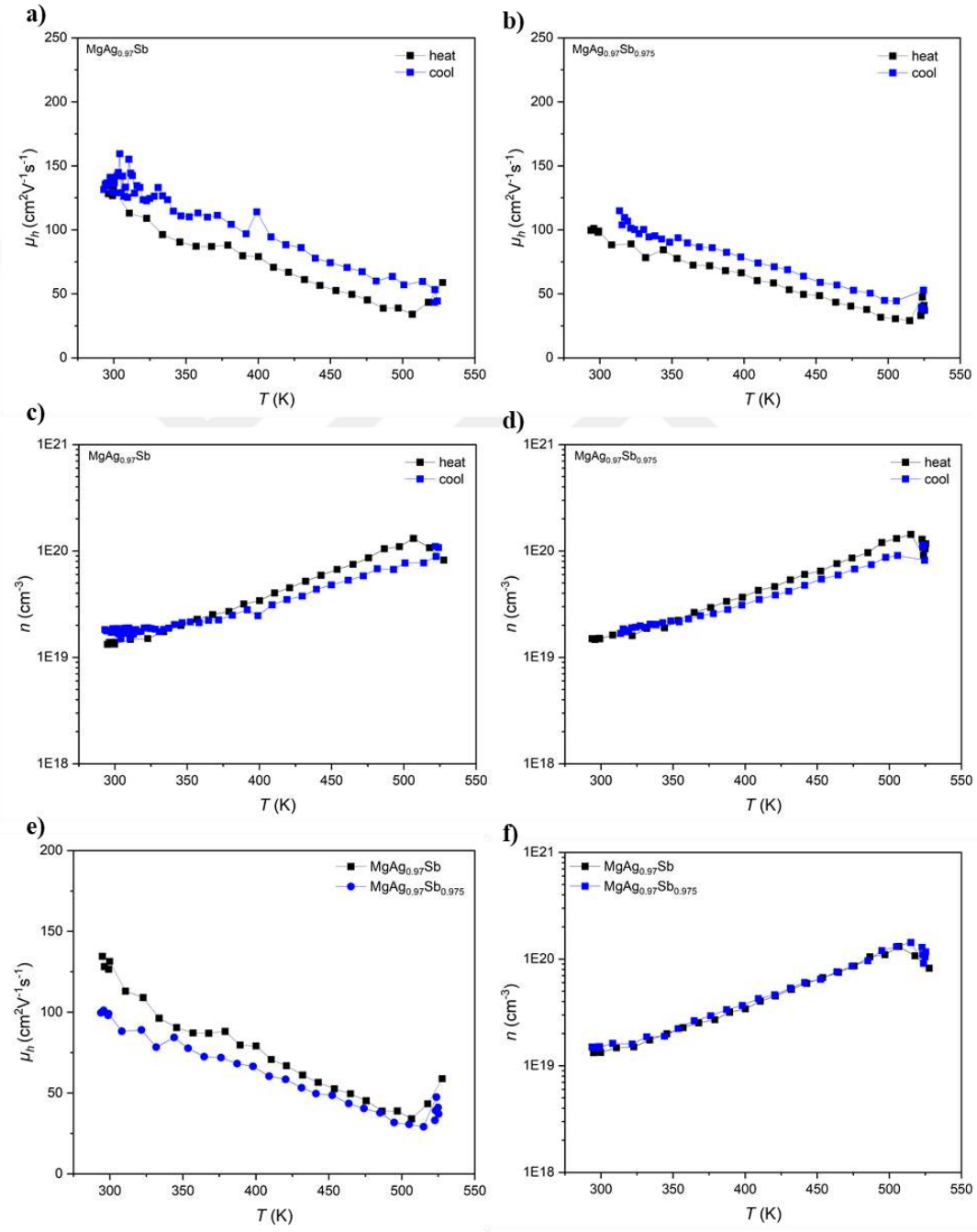

Figure C 1. a,b) Hall mobility values, c, d) carrier concentration of $MgAg_{0.97}Sb$ and $MgAg_{0.97}Sb_{0.975}$ and e,f) comparison of Hall mobility and carrier concentrations of $MgAg_{0.97}Sb$ and $MgAg_{0.97}Sb_{0.975}$ as a function of temperature.

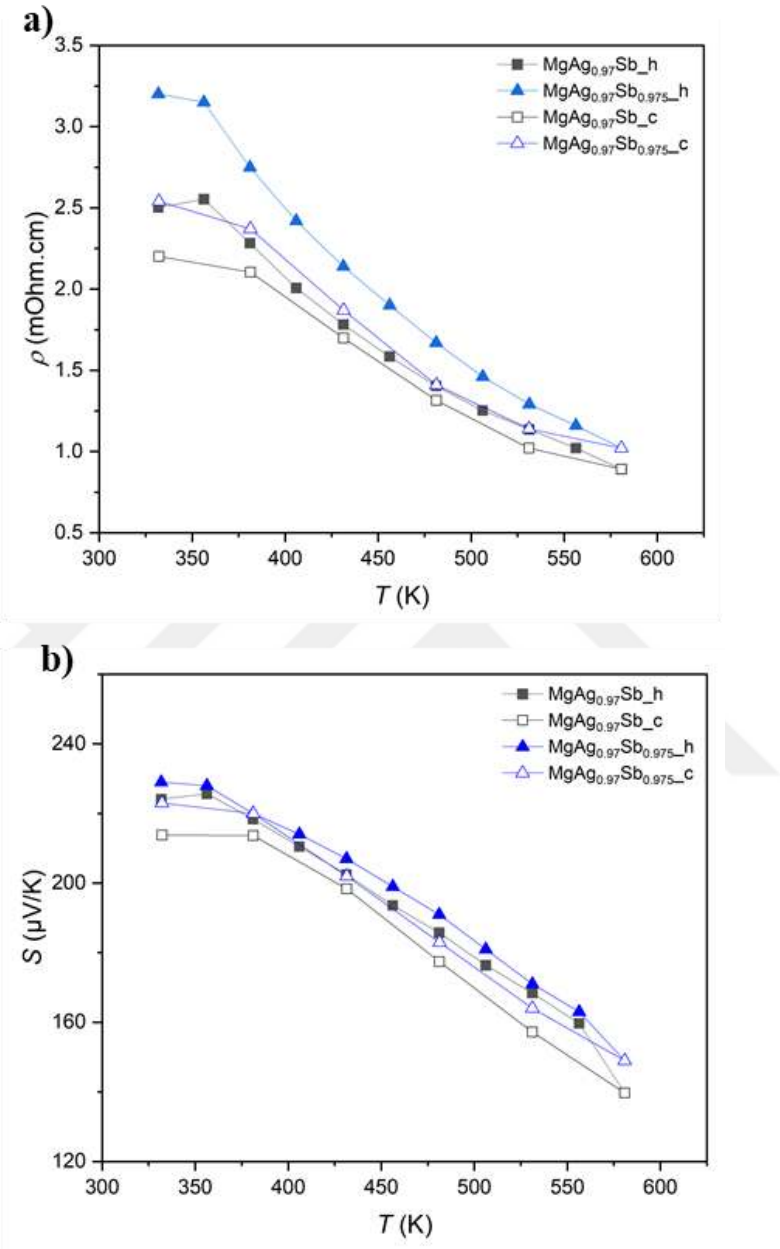

Figure C 2. a) electrical resistivity and b) Seebeck coefficient of $MgAg_{0.97}Sb$ and $MgAg_{0.97}Sb_{0.975}$ comparing the heating-cooling cycles as a function of temperature.

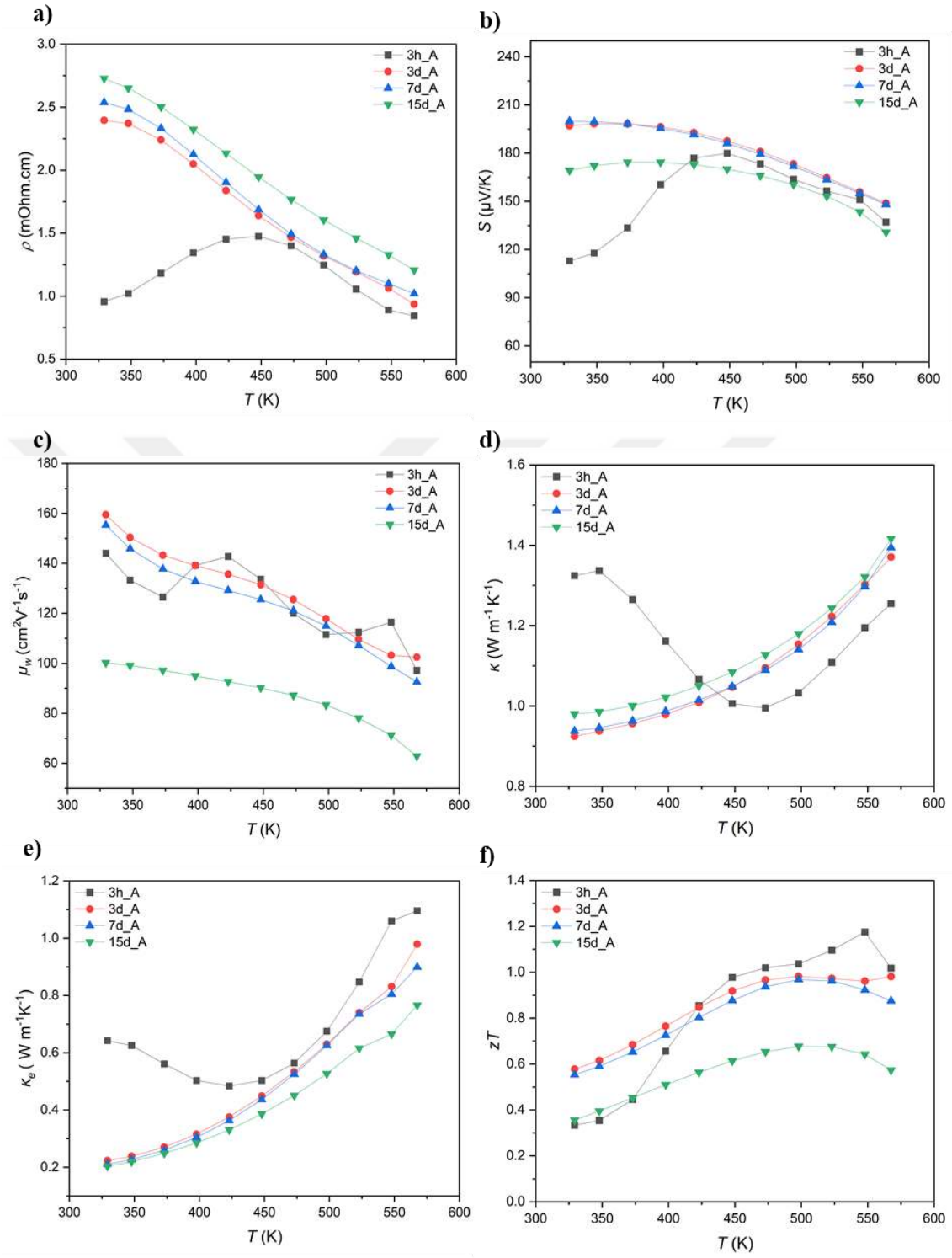

Figure C 3. a) Electrical resistivity, b) Seebeck coefficient, c) weighted mobility, d) total thermal conductivity, e) electronic thermal conductivity and f) zT values of $MgAg_{0.97}Sb$ annealed for 3h, 3d, 7d and 15 d.

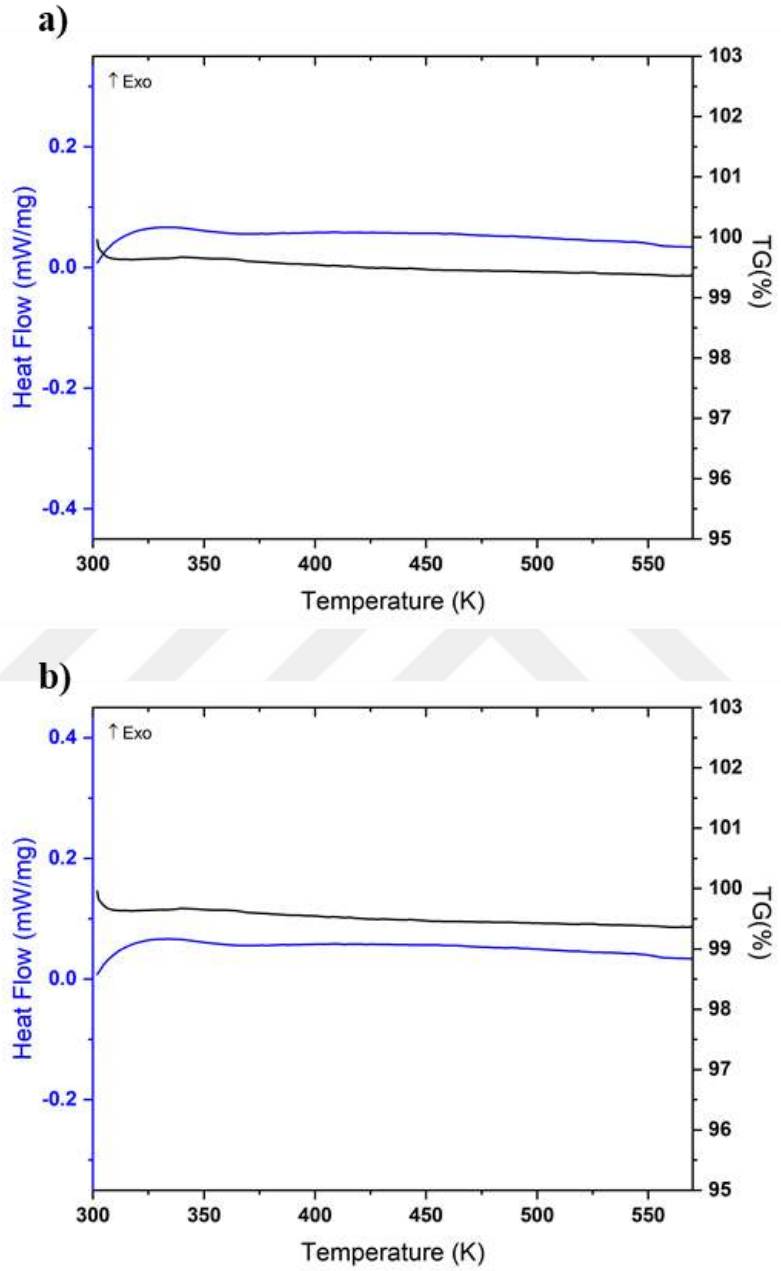

Figure C 4 . DSC/TG (scanning rate 10 K min^{-1}) graphs of a) holding time of 10 min. and b) without a holding time for the $MgAg_{0.97}Sb$ sample after annealing for 3 days.